

Spectroscopic Investigations of the Magnetic Anisotropy of Lanthanide- and Cobalt-Based Molecular Nanomagnets

Von der Fakultät Chemie der Universität Stuttgart zur Erlangung der Würde
eines Doktors der Naturwissenschaften (Dr. rer. nat.) genehmigte
Abhandlung

vorgelegt von

Dipl.-Chem. Yvonne Rechkemmer

aus Sinsheim

Hauptberichter: Prof. Dr. Joris van Slageren

Mitberichter: Prof. Dr. Peer Fischer

Prüfungsvorsitzender: Prof. Dr. Wolfgang Kaim

Tag der mündlichen Prüfung: 15. April 2016

Institut für Physikalische Chemie der Universität Stuttgart

2016

„Die Praxis sollte das Ergebnis des Nachdenkens sein, nicht umgekehrt.“

Hermann Hesse

Erklärung über die Eigenständigkeit der Dissertation

Ich versichere, dass ich die vorliegende Arbeit mit dem Titel

Spectroscopic Investigations of the Magnetic Anisotropy of Lanthanide- and Cobalt-Based Molecular Nanomagnets

selbstständig verfasst und keine anderen als die angegebenen Quellen und Hilfsmittel benutzt habe. Aus fremden Quellen entnommene Passagen und Gedanken sind als solche kenntlich gemacht.

Declaration of Authorship

I hereby certify that the dissertation entitled

Spectroscopic Investigations of the Magnetic Anisotropy of Lanthanide- and Cobalt-Based Molecular Nanomagnets

is entirely my own work except where otherwise indicated. Passages and ideas from other sources have been clearly indicated.

Name/Name:

Unterschrift/Signed:

Datum/Date:

With special thanks to

Prof. Dr. Joris van Slageren for providing the possibility to join his group and work on the multifaceted projects presented in this thesis. I strongly appreciate the useful scientific discussions and the high level of leeway in decision making. I experienced great science and acquired a lot of new skills. Many thanks of course to the entire work group for the pleasant working atmosphere and the great fun we had during our leisure activities.

Prof. Dr. Wolfgang Kaim and Prof. Dr. Peer Fischer for kindly agreeing to act as examiners for this thesis.

Jack Aviv, Dr. Glen Ramsay and Guy McCaffery for their support concerning the technical details of the MCD-spectrometer and their willingness to answer thousands of questions.

The members of the mechanical workshop for constructing the MCD sample cell as well as the table for positioning the magnet according to my drafts.

Prof. Dr. Harald Giessen, Dr. Timo Gissibl, Dominik Floess and Xinghui Yin for useful discussions concerning the optical setup and providing the optical design software. Thanks as well to Sinja Manck for her motivated assistance in adjusting the optics and in performing the very first MCD measurements.

Dr.-Ing. Petr Neugebauer, Jan Vaverka and especially Michal Kern for their great support in designing the light shielding box for the MCD-spectrometer and assembling it. Thanks as well to the members of the carpenter's workshop for cutting the required pieces.

Dr. Jiří Novák, Dr. Chennan Wang and Jakub Rozbořil for their effort in preparing monolayers for MCD measurements and Dr. Michael Waters for providing the required sample.

Claudio Eisele for his preliminary work concerning the synthesis of the lanthanide tetra-carbonates and Julia E. Fischer for doing a great job concerning the improved synthesis and the preliminary magnetic characterization.

Barbara Förtsch for performing the elemental analyses, Dr. Wolfgang Frey for his patience in performing the single crystal X-ray diffraction studies and Dr. Pierre Eckold for performing the X-ray powder diffraction studies.

Prof. Dr. Martin Dressel for access to the SQUID-magnetometer as well as the FIR-spectrometer and Dr. Shang-Da Jiang and Michael Slota for their help in solving technical issues.

Dr.-Ing. Petr Neugebauer again for spending a lot of time in measuring the HFEPR-spectra.

Raphael Marx for performing part of the FIR- and HFEPR-measurements and providing some of his scripts for data analysis. Thanks as well to Dr. María Dörfel for her contribution to the FIR measurements and to Philipp Lutz for providing some additional Matlab scripts.

Maren Gysler, Dr. Stergios Piligkos and Theis Brock-Nannestad for the luminescence measurements.

Prof. Dr. Michael F. Reid and Sebastian Horvath for providing their lanthanide crystal field software and kindly answering all my questions. Thanks also to Prof. Dr. Yau Yuen Yeung for kindly providing his crystal field software for d-block transition metal compounds.

Prof. Dr. Biprajit Sarkar, Dr. David Schweinfurth and Dr. Margarethe van der Meer for the fruitful collaboration, the synthesis of the studied cobalt systems and their structural identification.

Irina Peremykin for her contribution to the magnetic and EPR-spectroscopic characterization of the symmetric cobalt dimers and Frauke D. Breitgoff for her great work concerning the magnetic characterization of the mononuclear and asymmetrically bridged cobalt complexes.

Dr. Milan Orlita and Michael Hakl for performing the wide-range FIR measurements.

Prof. Dr. Frank Neese and Dr. Mihail Atanasov for theoretical calculations on one of the mononuclear cobalt complexes.

Dr. Stefan Jagiella for his help concerning computers and software, Birgit Feucht and Diana Zauser for their help concerning chemicals and consumables as well as Inge Blankenship for her help in handling administrative issues.

The members of the low temperature department for providing liquid helium whenever needed.

My family and friends who always supported me and proudly believed in me. Conny, thanks for finding typing mistakes and grammatical errors. Andi, thanks for always being there for me and for your patience when leisure time was scarce.

Table of Contents

Abbreviations and Symbols	XIII
Abstract	XIX
Zusammenfassung	XXV
1 Introduction	1
2 Background	3
2.1 Basic Concepts in Molecular Magnetism	3
2.1.1 Characteristics of Single-Molecule Magnets	3
2.1.2 Single-Ion Magnets	7
2.1.3 Magnetic Relaxation	8
2.2 Electronic Structure of Ln(III) Compounds	13
2.2.1 Free Ln(III) Ions	13
2.2.2 Ln(III) Ions in a Crystal Field	19
2.3 Electronic Structure and Magnetism of Co(II) Compounds	25
2.3.1 Octahedrally Coordinated Co(II)	25
2.3.2 Tetrahedrally Coordinated Co(II)	33
2.4 Experimental Methods for Studying SMMs	36
2.4.1 Magnetometry	36
2.4.2 EPR Spectroscopy	39
2.4.3 FIR Spectroscopy	40
2.4.4 Optical Spectroscopy	40
3 Aim of this Work	47
4 Results and Discussion	51
4.1 Design and Setup of the MCD-Spectrometer	51
4.1.1 General Considerations	51
4.1.2 The CD-Spectrometer	52

4.1.3	Magnet and Sample Holder	59
4.1.4	Optics and Optomechanics	61
4.1.5	Characterization of the MCD-Spectrometer	65
4.2	Molecular Lanthanide Tetra-Carbonates	74
4.2.1	Synthesis and Structural Characterization	74
4.2.2	Magnetic Properties	78
4.2.3	Spectroscopic Results	85
4.2.4	Crystal Field Analysis and Electronic Structure	92
4.3	Mononuclear Cobalt Complexes	101
4.3.1	Structures of the Mononuclear Co(II) Complexes	101
4.3.2	Magnetic Properties	102
4.3.3	Spectroscopic Results and Electronic Structure	111
4.4	Binuclear Cobalt Complexes	123
4.4.1	Structures of the Cobalt Dimers	123
4.4.2	Magnetic Properties	126
4.4.3	Spectroscopic Results and Discussion	135
5	Summary and Conclusion	143
6	Experimental Part	151
6.1	Film and Monolayer Preparation	151
6.1.1	Films of $K_3[Fe(CN)_6]$ in Poly(vinylalcohol)	151
6.1.2	Synthesis of $(NBu_4)[Dy(Pc)_2]$ for Film Preparation	151
6.1.3	Films of $[Dy(Pc)_2]$ in Polystyrene	151
6.1.4	$[Dy(Pc)_2]$ Monolayers	152
6.2	Synthesis and Structural Characterization	152
6.2.1	Synthesis and Characterization of the Lanthanide Tetra-Carbonates	152
6.2.2	Single Crystal X-Ray Analysis for the Lanthanide Tetra-Carbonates	153
6.2.3	X-Ray Powder Diffraction Studies on the Lanthanide Tetra-Carbonates	155
6.2.4	Synthesis and Characterization of the Mononuclear Co(II) Complexes	155

6.2.5	Synthesis and Characterization of the Cobalt Dimers.....	156
6.3	Magnetic and Spectroscopic Measurements.....	156
6.3.1	SQUID Magnetometry	156
6.3.2	Far-Infrared Spectroscopy	156
6.3.3	Luminescence Spectroscopy	157
6.3.4	Low Temperature Electronic Absorption and Magnetic Circular Dichroism..	157
6.3.5	Electron Paramagnetic Resonance	157
6.4	Analysis and Calculations	158
6.4.1	Simulation of Magnetic Data	158
6.4.2	Simulation of Spectroscopic Data	158
6.4.3	Crystal Field Analysis	159
6.4.4	Theoretical Calculations.....	159
7	References	161
8	Appendix	175
8.1	Appendix A: Background.....	175
8.1.1	Energy Level Calculations for Pr(III)	175
8.1.2	Free Ion Terms of Co(II).....	178
8.1.3	Lines Equations for Octahedral Co(II) Compounds	178
8.1.4	Coefficients for the Empirical Function $G(T)$ for Co(II) Compounds.....	180
8.1.5	Energy Levels of Axially Distorted Tetrahedral Co(II) Compounds.....	182
8.2	Appendix B: MCD Design and Setup	182
8.2.1	Optical Layout and Spot Diagrams for the First Version of the MCD Setup ..	182
8.2.2	CD Calibration Measurements on CSA	183
8.2.3	Electronic Absorption of [Dy(Pc) ₂] in Polystyrene.....	184
8.3	Appendix C: Lanthanide Tetra-Carbonates.....	184
8.3.1	Infrared Spectra	184
8.3.2	Ac Susceptibilities of Dried Samples.....	185
8.3.3	Parameters Extracted from the Argand Plots	186

8.3.4	Arrhenius Plots	188
8.3.5	Dc Field Dependence of the Relaxation Rates	188
8.3.6	Luminescence Spectroscopy	192
8.3.7	Electronic Absorption and MCD-Spectra	193
8.3.8	Energy Levels	195
8.4	Appendix D: Mononuclear Cobalt Complexes	201
8.4.1	Parameters Extracted from the Argand Plots	201
8.4.2	Energies of Spin-Allowed Transitions	205
8.5	Appendix E: Cobalt Dimers	206
8.5.1	Diamagnetic Susceptibility of $5[\text{OTf}]_2[\text{BF}_4]_2$	206
8.5.2	X-Band EPR-Spectroscopy	206
8.5.3	Analysis of HFEPR-Spectra	207
9	Curriculum Vitae	209

Abbreviations and Symbols

A	Absorption or hyperfine coupling constant, see context
A, B, C	Racah parameters
A_1, B_0, C_0	Parameters for Faraday A, B and C terms
A_{direct}	Coefficient for direct relaxation
A_{SO}	Angular part of the spin-orbit interaction
$A_k^q \langle r^k \rangle, B_k^q$	Crystal field parameters in the Stevens notation
AC, ac	Alternating Current
arb. u.	arbitrary units
A/D	Analog-to-digital
B	Magnetic field
B_1, B_2	Empirical parameters for quantum tunneling of magnetization
B_{kq}	Crystal field parameters in the Wybourne notation
Bu	Butyl
BW	Bandwidth
c	speed of light; $c = 2.998 \cdot 10^8 \text{ m s}^{-1}$
C_{Raman}	Raman coefficient
$C_q^{(k)}$	Spherical tensor operator
CASSCF	Complete Active Space Self-Consistent Field
CD	Circular Dichroism
CF	Crystal Field
CSA	(1S)-(+)-10-Camphor Sulfonic Acid
D	Axial zero-field splitting parameter
D_{MD}	Magnetic dipole strength
DC, dc	Direct Current
DFT	Density Functional Theory
Dq	Cubic crystal field parameter
Ds, Dt	Tetragonal radial parameters defined by Ballhausen
E	Energy or transverse zero-field splitting parameter; see context
e	Elementary charge; $e = 1.602 \cdot 10^{-19} \text{ C}$
E_{AVE}	Parameter describing the spherically symmetric part of the free-ion and crystal field perturbations

EPR	Electron Paramagnetic Resonance
ESO	Extended Stevens Operators
ESR	Electron Spin Resonance, Elektronenspin-Resonanz
Et	Ethyl
F^k	Electrostatic radial integrals
f_k	Angular parts of the electrostatic interaction
$f(E), f(\nu)$	Lineshape function
$F_m(T)$	Temperature-dependent factor appearing in the Lines model for Co(II)
FDMR	Frequency Domain Magnetic Resonance
FIR	Far-Infrared
g	Landé factor, g -value
g_0	Effective g -value in the ground Kramers doublet
$G(G_2), G(R_7)$	Casimir's operators for the groups G_2 and R_7
$G(T)$	Empirical function derived by Lloret <i>et al.</i>
$g(T)$	Temperature-dependent g -value appearing in the Lines model
H	Magnetic field strength
\mathcal{H}	Hamiltonian
h	Planck's constant, $h = 6.626 \cdot 10^{-34}$ J s
HFEPR	High-Field Electron Paramagnetic Resonance
H_2L^1	1,2-bis(methanesulfonamido)-benzene
H_2L^2	2,5-di-[2-(methoxy)-anilino]-1,4-benzoquinone
H_2L^3	2,5-di-[2-(trifluoromethyl)-anilino]-1,4-benzoquinone
H_2L^4	2-[4-(isopropyl)-anilino]-5-hydroxy-1,4-benzoquinone
HS	High-Spin
I	Intensity
IR	Infrared
InGaAs	Indium Gallium Arsenide
J	Total angular momentum quantum number
J_{ex}	Exchange coupling constant
k_B	Boltzmann constant; $k_B = 1.381 \cdot 10^{-23}$ J K ⁻¹
k_r	Orbital reduction factor in the Lines model for Co(II)
KD	Kramers Doublet
L	Total orbital angular momentum quantum number
l	Orbital angular momentum quantum number for a single electron

l_p	Direction cosines
\hat{L}	Total orbital angular momentum operator
lcp	Left circularly polarized light
Ln	Lanthanide
LS	Low-Spin
M	Magnetization
m_e	Electron mass, $m_e = 9.109 \cdot 10^{-31}$ kg
M^k	Marvin integrals
m_J	Magnetic total angular momentum quantum number
M_{mol}	Molar magnetization
M_{pp}	Effective polarization products
m_S	Magnetic spin quantum number for single-ion systems
M_S	Magnetic spin quantum number for exchange-coupled systems
m_k	Operators accounting for spin-spin and spin-other-orbit interactions
MCD	Magnetic Circular Dichroism
Me	Methyl
MM	Molar Mass
Mn_{12}ac	Manganese cluster with chemical formula $[\text{Mn}_{12}\text{O}_{12}(\text{OAc})_{16}(\text{H}_2\text{O})_4]$
N	Number of electrons within the d-shell or f-shell
n	Principal quantum number
N_A	Avogadro's constant; $N_A = 6.022 \cdot 10^{23}$ mol ⁻¹
N_i	Boltzmann population of the i^{th} sublevel
n_{direct}	Exponent for direct relaxation
n_{Raman}	Raman exponent
NEVPT2	Second-order N-Electron Valence State Perturbation Theory
NIR	Near-Infrared
NIST	National Institute of Standards and Technology
NMR	Nuclear Magnetic Resonance
O_k^q	Stevens operators
ODEPR	Optically Detected Electron Spin Resonance
OTf	Triflate anion
OVC	Outer Vacuum Chamber
P^k	Parameters describing electrostatic correlated spin-orbit interactions
p_k	Operators accounting for electrostatic correlated spin-orbit interactions

Pc ²⁻	Dianion of phthalocyanine
Ph	Phenyl
PEM	Photoelastic Modulator
PLX	plano-convex
PMT	Photomultiplier Tube
Pr	Propyl
PVA	Poly(Vinyl Alcohol)
PVC	Poly(Vinyl Chloride)
QTM	Quantum Tunneling of Magnetization
R	Substituent
r_{12}	Distance between two interacting electrons
rcp	Right circularly polarized light
rms	root mean squares
S	Total electron spin quantum number
s	Spin quantum number for a single electron
\hat{S}	Total spin operator
S_{eff}	Effective spin
SIM	Single-Ion Magnet
SMM	Single-Molecule Magnet
SQUID	Superconducting Quantum Interference Device
T	Temperature
T^i	Three-particle configuration interaction parameters
t_i	Three-particle operators
TIP	Temperature Independent Paramagnetism
tmpa	Tris(2-pyridylmethyl)amine
$U_q^{(k)}$	Unit tensor operator
U_{eff}	Effective energy barrier for spin reversal
UV	Ultra-Violet
V_{CF}	Crystal field potential
\hat{V}_{tet}	Tetragonal crystal field operator
vis	visible
VTI	Variable Temperature Insert
VTVH	Variable Temperature, Variable Field
Wyb	Wybourne notation

XRD	X-Ray Diffraction
ZFS	Zero-Field Splitting
α, β, γ	Two-body configuration interaction parameters
α	Additional quantum number for distinguishing terms with the same LS values or distribution parameter for relaxation times, see context
$\alpha_J, \beta_J, \gamma_J$	Stevens factors for $k = 2, 4, 6$
α_r	Orbital reduction factor in the model developed by Lloret <i>et al.</i>
γ	Collection of spectroscopic constants in MCD spectroscopy
ε	Extinction coefficient
Δ_{ax}	Axial distortion parameter
ζ	One-electron spin-orbit coupling constant
θ	Ellipticity
θ_k	Stevens factors
λ_{SO}	Spin-orbit coupling coefficient
$\hat{\mu}$	Dipole moment operator
μ_{B}	Bohr magneton; $\mu_{\text{B}} = 9.724 \cdot 10^{-24} \text{ J T}^{-1}$
ν	Frequency
ρ	Light polarization
τ	Relaxation time
χ	Magnetic susceptibility
χ_{dia}	Diamagnetic susceptibility
χ_{m}	Molar paramagnetic susceptibility
χ_{para}	Paramagnetic susceptibility
χ_0	Isothermal magnetic susceptibility
χ_{∞}	Adiabatic magnetic susceptibility
χ'	In-phase component of the magnetic susceptibility
χ''	Out-of-phase component of the magnetic susceptibility
ψ	Wave function
ω	Angular frequency

Abstract

Since the very first observation of magnetic hysteresis of purely molecular origin in 1993,¹ the field of molecular magnetism^{2,3} has become a versatile and flourishing area of scientific research. Single-molecule magnets²⁻⁸ are metal complexes exhibiting an energy barrier for spin reversal, leading to magnetic bistability and slow relaxation of the magnetization after having switched off an external magnetic field. Their potential for practical applications such as ultrahigh-density magnetic data storage devices was recognized early on¹ and with the goal of achieving higher and higher energy barriers, a wide range of different kinds of single-molecule magnets has been synthesized up to now.^{5,9-12} The first generation typically comprised clusters of exchange-coupled transition metal ions with high electron spins, with the manganese cluster $[\text{Mn}_{12}\text{O}_{12}(\text{OAc})_{16}(\text{H}_2\text{O})_4]^{13}$ exhibiting a total spin of $S = 10$ as the most prominent example.^{1,3-8,10,14} For integer spin systems the energy barrier is given by $|D| \cdot S^2$, where D describes the axial zero-field splitting, while the energy barrier for half-integer spin systems is given by $|D| \cdot (S^2 - 1/4)$.³ The quadratic dependence of the barrier height on the spin motivated chemists to synthesize metal complexes with very high total spins; however, with limited success.¹⁵⁻¹⁸ It was shown that high spins tend to come along with low anisotropies^{19,20} and increased interest thus focused on magnetic anisotropy. Magnetic anisotropy is mainly caused by spin-orbit coupling and special interest is currently focused on the synthesis and investigation of (mononuclear) complexes of highly anisotropic metal centers, e.g. lanthanide or cobalt complexes.^{9,11,21-24} Although rather high energy barriers can be achieved in such systems, practical application remains problematic and has not been realized yet. Reasons are for example the lack of rational design criteria and the complex interplay of different magnetic relaxation pathways, including under-barrier relaxation, which have not been fully understood yet.

The aim of this work was therefore the comprehensive magnetic and spectroscopic investigation of selected molecular lanthanide and cobalt compounds in order to obtain a deeper insight into the correlation of molecular and electronic structures as well as the corresponding magnetic properties. The applied spectroscopic methods included electron paramagnetic resonance spectroscopy, far-infrared spectroscopy and optical methods. Special emphasis was placed on magnetic circular dichroism (MCD) spectroscopy, which served as a main tool for electronic structure determination and unravelling magnetic relaxation mechanisms. However, since the MCD-spectrometer was not part of the available

experimental equipment at the University of Stuttgart, its design, setup and characterization were the first part of this work.

The successfully installed MCD-spectrometer essentially consists of an Aviv Model 42 circular dichroism spectrometer combined with an Oxford Instruments SM-4000-10 optical cryomagnet, providing magnetic field strengths up to 10 T. A variable temperature insert allows for temperature stabilization between 1.5 and 300 K. The circular dichroism spectrometer shows an excellent spectral resolution of up to 0.1 nm, which was crucial for the accurate determination of f-f-transition energies of the studied lanthanide compounds in the further course of this work. A Rochon polarizer combined with a photoelastic modulator generates alternately left and right circularly polarized light, which is focused onto the sample in the center of the magnetic field by using appropriate optics. A home-built sample cell allows for studying frozen solutions, mulls and thin films. A photomultiplier tube and an indium gallium arsenide photodiode are used for the detection of the resulting light intensity in the near UV-, visible- and near-IR regions. Worthwhile mentioning is the spectrometer's rather large wavelength range from 200 to 2000 nm, which has rarely been realized in MCD-spectroscopy up to now. MCD-experiments in the near-IR region proved to be essential for the electronic structure determination of the cobalt compounds in this work. The performance of the spectrometer was tested by recording CD- and MCD-spectra of literature-known samples and verified by excellent agreement between the obtained spectra and the published data. Special interest concerned the spectrometer's sensitivity and the possibility of employing MCD-spectroscopy for the investigation of monolayers. Indeed, preliminary measurements on Langmuir-Blodgett deposited monolayers of the well-known single-molecule magnet DyPc₂²⁵ showed very promising results, including not only the observation of clear spectra but also optical detection of magnetic hysteresis.

In the further course of this work MCD-spectroscopy was employed as one of the main tools for the electronic structure determination of selected lanthanide and cobalt compounds. The studied lanthanide compounds were literature-known molecular tetra-carbonates of erbium (**1-Er**) and dysprosium (**1-Dy**)^{26,27}, which were chosen mainly due to the colorlessness of the carbonate ligands allowing for optical detection of f-f-transitions. Successful synthesis and structural characterization were followed by detailed magnetometric studies. Both **1-Er** and **1-Dy** are field-induced single-molecule magnets with energy barriers of 52 cm⁻¹ and 29 cm⁻¹, respectively, according to spectroscopic data. However, **1-Er** and **1-Dy** show significant differences in their magnetic relaxation behavior. For **1-Dy**, a significant contribution of the Orbach relaxation, i.e. the thermally activated over-barrier

relaxation was observed, while for **1-Er** the barrier independent Raman as well as direct relaxation processes were shown to be dominant. The magnetic studies were complemented by detailed spectroscopic investigations which were far beyond what is usually done in the field of molecular magnetism. The combination of far-infrared-, luminescence- and MCD-spectroscopy allowed for the experimental determination of no fewer than 48 energy levels for **1-Er** and 55 levels for **1-Dy**, which built the foundation for the subsequent crystal field analysis for electronic structure determination. In addition, the results of EPR-spectroscopic studies were used for fine-tuning and verifying the respectively determined crystal field parameters. Crystal field analysis was performed by iterative fitting of calculated against experimentally determined energy levels and led to reliable sets of parameters that allowed for the satisfactory simulation of all the experimental data. The corresponding wave functions describe heavily mixed states and calculating the magnetic dipole strengths for transitions between the relevant states led to a quantitative understanding of the magnetic relaxation pathways. The combination of magnetometry and spectroscopy thus not only enabled the full electronic structure determination for the single-molecule magnets **1-Er** and **1-Dy**, but also provided a deeper insight into magnetic relaxation. Worthwhile mentioning is the finding that none of the applied methods is suitable on its own for the determination of reasonable crystal field parameters. Thus, this work provides a recipe for the electronic structure determination of low-symmetry mononuclear lanthanide complexes.

Besides the investigation of lanthanide compounds, this thesis deals with two classes of cobalt complexes. The first class comprises the mononuclear complexes **(HNEt₃)₂2** and **(NMe₄)₂2** in which one Co(II) ion is ligated by the nitrogen donors of two doubly deprotonated 1,2-bis(methanesulfonamido)-benzene-ligands. Rather acute N-Co-N bite angles indicate strong deviations from ideal tetrahedral symmetry. The static magnetic properties hint at very high energy barriers for spin reversal and with the help of far-infrared spectroscopy, the axial zero-field splitting parameters were determined as $D = -115 \text{ cm}^{-1}$ for **(HNEt₃)₂2** and $D = -112.5 \text{ cm}^{-1}$ for **(NMe₄)₂2**. The corresponding energy barriers belong to the highest ever reported for 3d-transition metal complexes,^{11,24,28} making **(HNEt₃)₂2** and **(NMe₄)₂2** extraordinarily interesting systems for probing single-molecule magnet behavior. Indeed, investigating the dynamic magnetic properties confirmed single-molecule magnet behavior. Slow relaxation of the magnetization in an alternating magnetic field was observed even in the absence of an external static field, which is rarely observed in mononuclear Co(II) complexes.^{11,24} The unique magnetic properties were fully explained by analyzing spectroscopic results. Multi-frequency EPR-spectra, recorded on **(HNEt₃)₂2** and **(NMe₄)₂2**,

displayed no signals. Taking into account the EPR selection rules, this finding confirms the high negative values for D and indicates rather axial, e.g. pure $m_S = \pm 3/2$ ground doublets. The MCD-spectra showed very intense signals that were assigned to spin-allowed d-d-transitions. Subsequent crystal field analysis assuming D_{2d} point symmetry revealed that the strong axial crystal field generated by the ligands leads to a large splitting of the electronic terms and thus in turn to a relatively small energy gap between the electronic 4B_1 ground state and the first excited state 4B_2 . The resulting increase in second-order spin-orbit coupling explains the high energy barriers observed in **(HNEt₃)₂2** and **(NMe₄)₂2**. The MCD-signal intensities show magnetic hysteresis with coercive fields of 0.24 T and 0.14 T, confirming the presence of significant magnetic bistability. Thus, this work shows that magnetic bistability in mononuclear complexes does not necessarily require linear coordination symmetries, in contrast to a current trend in related literature.²⁹⁻³¹ The key factors for the appearance of axial ground states seem to be acute N-Co-N angles as well as the presence of symmetry beyond the directly coordinated donor atoms. **(HNEt₃)₂2** and **(NMe₄)₂2** are thus promising starting points for the synthesis of improved single-molecule magnets.

The second class of cobalt compounds studied in this work included dimers of distorted octahedrally coordinated Co(II) ions bridged by quinone based bridging ligands.³² In the bridging ligands, one or two oxygen donors of 2,5-dihydroxy-1,4-benzoquinone were replaced by isoelectronic [NR] groups, leading to the asymmetrically bridged dimer **5[OTf]₂** in the former case and to the symmetrically bridged dimers **3[BF₄]₂** and **4[BPh₄]₂** in the latter case. The main focus of investigation lay on the impact of the bridging ligand on the magnetic coupling between the cobalt centers, since it was reported that exchange coupling might prevent undesired under-barrier relaxation of the magnetization.^{33,34} In view of the potential non-innocent behavior of the bridging ligands, another interesting question concerned the observation of valence tautomerism in the corresponding one-electron oxidized species, which could lead to interesting switchable properties.³⁵ However, no valence tautomerism was observed in the mixed-valent species **3[BF₄]₃** and **5[OTf]₃**. The magnetic properties of the complexes were studied with the help of static susceptibility and magnetization measurements and analyzed by means of different models. It was shown that due to the strong deviations from ideal octahedral coordination symmetry the application of a common spin Hamiltonian is appropriate. Weak antiferromagnetic exchange couplings were found for **5[OTf]₂** and **3[BF₄]₂** and the corresponding exchange coupling constants were determined as $J_{\text{ex}} = -0.47 \text{ cm}^{-1}$ and $J_{\text{ex}} = -0.52 \text{ cm}^{-1}$. In contrast, ferromagnetic exchange with $J_{\text{ex}} = +0.76 \text{ cm}^{-1}$ was found for **4[BPh₄]₂**. The different signs of the exchange coupling

constants can be explained by different relative contributions of possible exchange paths, influenced by the different substituents at the bridging ligands or slight geometry differences. The observations indicate that electron withdrawing substituents favor ferromagnetic couplings, which are preferred in the context of molecular magnetism. The magnetometric investigations were complemented by EPR-spectroscopic studies. Simulating the obtained spectra required assuming anisotropic exchange couplings; however, the isotropic mean values agreed excellently with the coupling constants determined by magnetometry.

All in all, it can be concluded that this work provides a significant contribution to the deeper understanding of the features relevant for single-molecule magnets. The electronic structure determination for selected lanthanide and cobalt complexes applying advanced magnetometric and spectroscopic techniques not only led to an understanding of the static and dynamic magnetic properties but also allowed for the development of design criteria and new approaches for improved single-molecule magnets in the future.

Zusammenfassung

Seit der erstmaligen Beobachtung magnetischer Hysterese rein molekularen Ursprungs im Jahr 1993¹ hat sich der Bereich des molekularen Magnetismus^{2,3} zu einem eigenständigen und vielseitigen Forschungsgebiet entwickelt. Als Einzelmolekülmagneten²⁻⁶ werden dabei Metall-Komplexe bezeichnet, welche aufgrund einer Energiebarriere für Spin-Umkehr magnetische Bistabilität aufweisen und somit auch nach Abschalten eines externen Magnetfelds für gewisse Zeit magnetisiert bleiben. Schnell wurde deren praktisches Potential im Gebiet der magnetischen Datenspeicherung erkannt¹ und mit dem Ziel hoher Energiebarrieren wurde bis heute eine Vielzahl verschiedenartiger Einzelmolekülmagnete synthetisiert.^{5,9-12} Die erste Generation umfasste dabei typischerweise Cluster von austauschgekoppelten Übergangsmetall-Ionen mit hohem Gesamtelektronenspin, wie zum Beispiel der in diesem Zusammenhang meist untersuchte Mangan-Komplex $[\text{Mn}_{12}\text{O}_{12}(\text{OAc})_{16}(\text{H}_2\text{O})_4]$ ¹³ mit einem Gesamtelektronenspin von $S = 10$, der als Prototyp der Einzelmolekülmagneten gilt.^{1,3-8,14} Für Systeme mit ganzzahligem Elektronenspin ergibt sich die Energiebarriere aus $|D| \cdot S^2$, wobei D die axiale Anisotropie des Systems wiedergibt, während die Energiebarriere für halbzahlige Spin-Systeme mit $|D| \cdot (S^2 - 1/4)$ beschrieben wird.³ Die quadratische Abhängigkeit vom Elektronenspin motivierte zur Synthese von Metall-Komplexen mit immer höheren Gesamtspins, allerdings mit lediglich mäßigem Erfolg.¹⁵⁻¹⁸ Es wurde gezeigt, dass hohe Spins tendenziell niedrige Anisotropien mit sich bringen,^{19,20} woraufhin sich vermehrtes Interesse der magnetischen Anisotropie zuwandte. Magnetische Anisotropie wird hauptsächlich durch die Stärke der Spin-Bahn-Kopplung beeinflusst und besonderes Interesse liegt momentan auf der Synthese und Untersuchung von Metall-Komplexen mit stark anisotropen Metall-Zentren, wie zum Beispiel Lanthanoid(III)- oder Cobalt(II)-Ionen.^{9,11,21-24} Obwohl in derartigen Systemen bereits sehr viel höhere Energiebarrieren erreicht werden konnten als in den Einzelmolekülmagneten der ersten Generation, ist die praktische Anwendung problematisch und bisher nicht realisiert. Gründe hierfür sind zum Beispiel das Fehlen rationaler Design-Kriterien und das komplexe Zusammenspiel verschiedener magnetischer Relaxationsmechanismen, die u.a. auch das Durchtunneln der Energiebarriere beinhalten und bisher nicht vollständig verstanden sind.

Ziel dieser Arbeit war deshalb die umfassende magnetische und spektroskopische Untersuchung ausgewählter molekularer Lanthanoid- und Cobalt-Verbindungen, um damit zum tieferen Verständnis der Zusammenhänge zwischen molekularer und elektronischer

Struktur sowie den magnetischen Eigenschaften beizutragen. Die zu diesem Zweck eingesetzten spektroskopischen Methoden umfassten Elektronenspinresonanz-Spektroskopie, Ferninfrarot-Spektroskopie sowie optische Methoden. Hervorzuheben ist hierbei die magnetische Zirkulardichroismus-Spektroskopie (MCD-Spektroskopie), die einen wesentlichen Beitrag zur Aufklärung der vorliegenden elektronischen Strukturen und der damit verbundenen magnetischen Relaxationsmechanismen lieferte. Da das verwendete MCD-Spektrometer nicht von Beginn an Teil der Ausstattung war, ist dessen Design, Aufbau sowie Charakterisierung als erster Teil der vorliegenden Arbeit anzusehen.

Das erfolgreich in Betrieb genommene MCD-Spektrometer besteht im Wesentlichen aus einem Aviv Model 42 Zirkulardichroismus-Spektrometer in Kombination mit einem Oxford Instruments SM-4000-10 optischen Kryomagneteten, welcher magnetische Feldstärken von bis zu 10 T ermöglicht. Ein Temperaturregelungs-Einsatz ermöglicht die Stabilisierung von Temperaturen zwischen 1.5 und 300 K. Das Zirkulardichroismus-Spektrometer besitzt eine exzellente spektrale Auflösung von bis zu 0.1 nm, was im weiteren Verlauf dieser Arbeit vor allem für die exakte Bestimmung von f-f-Übergangsenergien in den untersuchten Lanthanoid-Komplexen von Bedeutung war. Die Kombination eines Rochon-Polarisators mit einem photoelastischen Modulator erzeugt alternierend links und rechts zirkular polarisiertes Licht, welches mit Hilfe geeigneter Optik auf die Probe im Zentrum des Magnetfelds fokussiert wird. Eine eigens gestaltete Probenzelle erlaubt die Untersuchung von gefrorenen Lösungen, Verreibungen oder dünnen Filmen. Ein Photoelektronenvervielfacher sowie eine Indiumgalliumarsenid-Photodiode dienen zur Detektion der resultierenden Strahlungsintensität im nahen UV-, sichtbaren- und nahen IR-Bereich. Bemerkenswert ist der Wellenlängenbereich des Spektrometers, welcher mit 200 bis 2000 nm sehr breit ist und bisher in kaum einem anderen MCD-Spektrometer realisiert wurde. Vor allem die MCD-Untersuchungen im nahen Infrarot-Bereich erwiesen sich als ausschlaggebend für die Bestimmung der elektronischen Struktur in den hier untersuchten Cobalt(II)-Komplexen. Die Funktionstüchtigkeit des vollständig installierten MCD-Spektrometers wurde anhand von CD- und MCD-Untersuchungen an literaturbekannten Proben erprobt und durch gute Übereinstimmung der erhaltenen Spektren mit den vorliegenden Literaturdaten bestätigt. Ein besonders interessanter Aspekt im Zusammenhang mit der Charakterisierung des Spektrometers betraf dessen Sensitivität und den denkbaren Einsatz der MCD-Spektroskopie zur Untersuchung von Monolagen. Tatsächlich zeigten vorläufige Messungen an Monolagen des Einzelmolekülmagneteten DyPc₂²⁵ sehr vielversprechende Ergebnisse, die nicht nur die

Beobachtung deutlicher Spektren sondern auch optisch detektierter magnetischer Hysterese beinhalteten.

Im weiteren Verlauf dieser Arbeit wurde die MCD-Spektroskopie als eine der wesentlichen experimentellen Methoden zur Aufklärung der elektronischen Struktur ausgewählter Lanthanoid(III)- und Cobalt(II)-Komplexe eingesetzt. Bei den untersuchten Lanthanoid-Verbindungen handelte es sich um literaturbekannte molekulare Tetra-Carbonate des Erbiums (**1-Er**) und des Dysprosiums (**1-Dy**)^{26,27}, welche hauptsächlich aufgrund der Farblosigkeit des Carbonat-Liganden und der damit verbundenen Möglichkeit zur optischen Detektion von f-f-Übergängen gewählt wurden. Nach erfolgreicher Synthese und struktureller Charakterisierung wurden die magnetischen Eigenschaften im Detail untersucht. Sowohl **1-Er** als auch **1-Dy** sind sogenannte feld-induzierte Einzelmolekülmagneten mit Energiebarrieren von 52 cm^{-1} bzw. 29 cm^{-1} , basierend auf spektroskopischen Daten. **1-Er** und **1-Dy** zeigen gravierende Unterschiede im magnetischen Relaxationsverhalten: Während für **1-Dy** bei höheren Temperaturen ein signifikanter Beitrag des Orbach-Prozesses, d.h. der thermisch aktivierten Überwindung einer Energiebarriere nachgewiesen wurde, dominieren bei **1-Er** der sogenannte Raman-Prozess sowie die direkte Relaxation, welche in erster Näherung unabhängig von der Energiebarriere sind. Die magnetometrischen Messungen wurden durch detaillierte spektroskopische Untersuchungen ergänzt, die weit über die sonst im Bereich des molekularen Magnetismus üblichen Untersuchungen hinausgehen. Die Kombination von Ferninfrarot-, Lumineszenz- und MCD-Spektroskopie erlaubte die experimentelle Bestimmung von nicht weniger als 48 Energieniveaus für **1-Er** und 55 Niveaus für **1-Dy**, welche die Grundlage für die anschließende Kristallfeldanalyse zur Bestimmung der elektronischen Strukturen bildeten. Zusätzlich dienten die Ergebnisse ESR-spektroskopischer Untersuchungen zur Feinabstimmung und Verifizierung der jeweils bestimmten Kristallfeldparameter. Die Kristallfeldanalyse erfolgte durch iterative Anpassung berechneter an experimentell ermittelte Energien und führte zu verlässlichen Parametersätzen, die zufriedenstellende Simulationen aller experimentellen Daten erlaubten. Die zugehörigen Wellenfunktionen beschreiben stark gemischte Zustände und durch Berechnung der magnetischen Dipolstärken für Übergänge zwischen den relevanten Niveaus konnte ein quantitatives Verständnis des Relaxationsverhaltens gewonnen werden. Die Kombination magnetometrischer und spektroskopischer Methoden erlaubte somit nicht nur die vollständige Bestimmung der elektronischen Struktur der Einzelionenmagnete **1-Er** und **1-Dy**, sondern lieferte auch einen Beitrag zum tieferen Verständnis der magnetischen Relaxation. Erwähnenswert ist außerdem die Feststellung, dass keine der angewandten Methoden für sich

allein zur Bestimmung sinnvoller Parametersätze herangezogen werden konnte und diese Arbeit somit als Anleitung für die experimentelle Bestimmung der elektronischen Strukturen mononuklearer Lanthanoid-Komplexe mit niedriger Symmetrie dienen kann.

Neben der Untersuchung der Lanthanoid-Carbonate befasste sich diese Arbeit mit Cobalt-Komplexen, welche in zwei Klassen unterteilt werden können. Die erste Klasse beinhaltete die einkernigen Komplexe $(\text{HNEt}_3)_2\mathbf{2}$ und $(\text{NMe}_4)_2\mathbf{2}$, in welchen jeweils ein Co(II)-Ion von den Stickstoff-Donoren zweier zweifach deprotonierter 1,2-Bis(methansulfonamido)benzol-Liganden koordiniert wird. Mit verhältnismäßig kleinen N-Co-N-Winkeln sind die Koordinationssymmetrien im Vergleich zu idealer tetraedrischer Symmetrie stark verzerrt. Die statischen magnetischen Eigenschaften deuteten auf sehr hohe Energiebarrieren für die Spin-Umkehr hin und mit Hilfe der Ferninfrarot-Spektroskopie konnten die axialen Anisotropie-Parameter zu $D = -115 \text{ cm}^{-1}$ für $(\text{HNEt}_3)_2\mathbf{2}$ und $D = -112.5 \text{ cm}^{-1}$ für $(\text{NMe}_4)_2\mathbf{2}$ bestimmt werden. Die zugehörigen Energiebarrieren gehören damit zu den höchsten bisher veröffentlichten Energiebarrieren für 3d-Metall-Komplexe^{11,24,28} und machen $(\text{HNEt}_3)_2\mathbf{2}$ und $(\text{NMe}_4)_2\mathbf{2}$ zu außerordentlich interessanten Systemen für die Erprobung von Einzelmolekülmagnet-Eigenschaften. Tatsächlich bestätigte die Untersuchung der dynamischen magnetischen Eigenschaften, dass es sich bei $(\text{HNEt}_3)_2\mathbf{2}$ und $(\text{NMe}_4)_2\mathbf{2}$ um Einzelmolekülmagneten handelt. Langsame Relaxation der Magnetisierung im magnetischen Wechselfeld konnte ohne Anlegen eines zusätzlichen statischen Magnetfelds nachgewiesen werden, was $(\text{HNEt}_3)_2\mathbf{2}$ und $(\text{NMe}_4)_2\mathbf{2}$ deutlich von vielen anderen Co(II)-basierten Einzelmolekülmagneten abhebt.^{11,24} Die einzigartigen magnetischen Eigenschaften konnten durch Auswertung spektroskopischer Daten erfolgreich erklärt werden. ESR-Spektren bei verschiedenen Frequenzen zeigten keinerlei Signale, was anhand der ESR-Auswahlregeln einerseits die hohen Werte und negativen Vorzeichen für D bestätigt und andererseits auf stark axiale, d.h. nahezu reine elektronische Grundzustände hindeutet. Die MCD-Spektren wiesen intensive Signale auf, welche spin-erlaubten d-d-Übergängen zugeordnet werden konnten. Die anschließende Kristallfeldanalyse unter Annahme von D_{2d} -Symmetrie verdeutlichte, dass das von den Liganden erzeugte starke axiale Kristallfeld zu einer starken Aufspaltung der elektronischen Terme führt, wodurch eine verhältnismäßig geringe Energiedifferenz zwischen dem elektronischem Grundzustand 4B_1 und dem ersten angeregten Zustand 4B_2 resultiert. Die dadurch bedingte verstärkte Spin-Bahn-Kopplung zweiter Ordnung erklärt die in $(\text{HNEt}_3)_2\mathbf{2}$ und $(\text{NMe}_4)_2\mathbf{2}$ beobachteten hohen Energiebarrieren. Die MCD-Signal-Intensitäten zeigten magnetische Hysterese mit Koerzitivfeldstärken von 0.24 T für $(\text{HNEt}_3)_2\mathbf{2}$ und 0.14 T für $(\text{NMe}_4)_2\mathbf{2}$, was das Vorliegen signifikanter magnetischer

Bistabilität beweist. Im Rahmen dieser Arbeit konnte demzufolge gezeigt werden, dass das Auftreten magnetischer Bistabilität in einkernigen Komplexen nicht zwangsläufig instabile lineare Koordinationssymmetrien erfordert, wie es in der aktuellen Literatur häufig vermittelt wird.²⁹⁻³¹ Als Schlüsselfaktoren für das Auftreten axialer Grundzustände konnten kleine N-Co-N-Winkel, d.h. axiale Verzerrung, sowie das Vorliegen von Symmetrie über die direkt koordinierten Donoratome hinaus identifiziert werden. **(HNEt₃)₂** und **(NMe₄)₂** bilden damit einen vielversprechenden Ausgangspunkt für die Synthese verbesserter Einzelmolekülmagnete.

Die zweite Klasse der in dieser Arbeit untersuchten Cobalt-Komplexe beinhaltete Dimere verzerrt oktaedrisch koordinierter Cobalt-Ionen, welche durch chinon-basierte Liganden verbrückt sind.³² In den Brückenliganden wurden jeweils ein oder zwei Sauerstoff-Donoren von 2,5-Dihydroxy-1,4-Benzochinon durch isoelektronische [NR]-Gruppen ersetzt, woraus im ersten Fall das asymmetrisch verbrückte Dimer **5[OTf]₂** und im zweiten Fall die symmetrisch verbrückten Dimere **3[BF₄]₂** und **4[BPh₄]₂** resultierten. Diese unterscheiden sich durch verschiedene Substituenten am Brückenliganden. Der Schwerpunkt der Untersuchungen lag hierbei auf dem Einfluss des Brückenliganden auf die magnetische Kopplung zwischen den Cobalt-Zentren, da in der Vergangenheit berichtet wurde, dass magnetische Kopplung das Auftreten unerwünschter Relaxationsmechanismen wie Quantentunneln der Magnetisierung einschränken kann.^{33,34} Aufgrund des potentiell nicht-unschuldigen Verhaltens der Brückenliganden betraf eine weitere Fragestellung das Auftreten von Valenz-Tautomerie in den zugehörigen einfach oxidierten Spezies, welche zu interessanten schaltbaren magnetischen Eigenschaften führen könnte.³⁵ Hinweise auf Valenztautomerie in den gemischt-valenten Spezies **3[BF₄]₃** und **5[OTf]₃** wurden allerdings nicht beobachtet. Die magnetischen Eigenschaften der Komplexe wurden mit Hilfe statischer Suszeptibilitäts- und Magnetisierungsmessungen untersucht und anhand verschiedener Modelle analysiert. Dabei zeigte sich, dass aufgrund der stark verzerrten oktaedrischen Umgebung der Co(II)-Ionen die Anwendung des gebräuchlichen Spin-Only-Formalismus gerechtfertigt ist. Für **5[OTf]₂** und **3[BF₄]₂** wurden schwach antiferromagnetische Austauschwechselwirkungen beobachtet und die zugehörigen Kopplungskonstanten wurden zu $J_{\text{ex}} = -0.47 \text{ cm}^{-1}$ für **3[BF₄]₂** und $J_{\text{ex}} = -0.52 \text{ cm}^{-1}$ für **5[OTf]₂** bestimmt. Trotz der unterschiedlichen Verbrückungs-Symmetrien sind die Kopplungen demzufolge sehr ähnlich. Im Gegensatz dazu wurde für **4[BPh₄]₂** eine ferromagnetische Austauschkopplung mit einer Kopplungskonstanten von $J_{\text{ex}} = +0.76 \text{ cm}^{-1}$ beobachtet. Die unterschiedlichen Vorzeichen der Austauschkopplung können durch unterschiedliche relative Beiträge möglicher

Austauschpfade, bedingt durch verschiedene Substituenten am Brückenliganden, bzw. leicht variierender Geometrien, erklärt werden. Die Ergebnisse deuten darauf hin, dass elektronenziehende Substituenten die im Bereich des molekularen Magnetismus bevorzugten ferromagnetischen Austauschwechselwirkungen begünstigen. Die magnetometrischen Untersuchungen wurden durch ESR-spektroskopische Messungen ergänzt. Zufriedenstellende Simulationen der erhaltenen Spektren erforderten die Annahme anisotroper Kopplungskonstanten, deren Mittelwerte allerdings sehr gute Übereinstimmung mit den magnetometrisch bestimmten Kopplungskonstanten aufwiesen.

Im Hinblick auf die Gesamtheit der hier vorgestellten Arbeit lässt sich abschließend zusammenfassen, dass diese einen signifikanten Beitrag zum besseren Verständnis der für Einzelmolekülmagneten relevanten Eigenschaften liefert. Die Ermittlung der elektronischen Strukturen ausgewählter Lanthanoid- und Cobalt-Komplexe anhand detaillierter magnetometrischer und spektroskopischer Untersuchungen führte nicht nur zum Verständnis von statischen und dynamischen magnetischen Eigenschaften, sondern ermöglichte auch die Entwicklung von Design-Kriterien sowie neuer Ansätze, die in naher Zukunft zu optimierten Einzelmolekülmagneten führen könnten.

1 Introduction

In 1993, the observation of magnetic hysteresis of purely molecular origin¹ in the famous manganese cluster $[\text{Mn}_{12}\text{O}_{12}(\text{OAc})_{16}(\text{H}_2\text{O})_4]$ (“ Mn_{12}ac ”) ¹³ resulted in great euphoria in the scientific community. Such magnetically bistable molecules are promising candidates for modern applications such as ultrahigh-density magnetic data storage devices^{1,36} and the vision that one day a single molecule could act as one bit attracted the interest of many research groups. Since then, the field of molecular magnetism^{2,3} has become a flourishing and versatile area of scientific research. A wealth of so-called single-molecule magnets (SMMs) has been reported,^{3-7,9-12,21-24,28,33,37} all of them showing an energy barrier for spin reversal, the essential condition for magnetic bistability and for slow relaxation of the magnetization. High spin-reversal barriers in metal complexes can be achieved by the combination of high ground state electron spins with large magnetic anisotropies. While early approaches for increasing the barriers mainly focused on increasing the total spins in clusters of exchange-coupled 3d-transition metal ions,¹⁰ more modern approaches are based on employing strongly anisotropic metal centers, i.e. metal ions with incompletely quenched orbital angular momenta. The development from large spins to large anisotropies led to the advent of single-molecule magnets containing e.g. lanthanide^{9,21,23,37} or cobalt ions^{11,22,28}, but also actinide based single-molecule magnets¹² are enjoying great interest.

However, in spite of the intense effort put into the design of new single-molecule magnets and the observation of record energy barriers up to several hundreds of wavenumbers, SMMs are still far away from practical application. One of the main reasons is the complex interplay of several magnetic relaxation pathways^{3,38}, including not only over-barrier relaxation, but also barrier-independent relaxation processes like quantum tunneling of the magnetization, Raman-like processes or direct relaxation. These processes prevent the observation of significant magnetic bistability and since they have not yet been fully understood, they are hard to predict and eliminate. A much deeper insight into the correlation between dynamic magnetic properties and the molecular as well as the electronic structure is therefore mandatory for the improvement of future molecular magnets.

In this context, the contribution of the work presented here lies in the comprehensive magnetometric and spectroscopic investigation of selected lanthanide- and cobalt-based molecular nanomagnets. The experimental results will serve to determine the electronic structures which in turn allow for an understanding of the magnetic behavior and for the derivation of new approaches towards improved materials.

2 Background

2.1 Basic Concepts in Molecular Magnetism

2.1.1 Characteristics of Single-Molecule Magnets

Typically, single-molecule magnets (SMMs)³⁻⁸ are clusters of exchange-coupled transition metal ions, with Mn_{12}ac ¹³ being the most prominent example.^{1,3-8,14} They show slow relaxation of the magnetization due to magnetic bistability, meaning that they remain magnetized for a certain time after having switched off an external magnetic field. Importantly, the characteristic magnetic properties are of purely molecular origin with negligible intermolecular interactions. The origin of magnetic bistability is the presence of an energy barrier for spin reversal which has to be overcome. For pure spin magnetism, i.e. for magnetic ions with completely quenched orbital angular momenta, this energy barrier is given by

$$\Delta E = |D| \cdot S^2 \quad (1)$$

for systems with integer electron spins S (non-Kramers systems) and by

$$\Delta E = |D| \cdot \left(S^2 - \frac{1}{4}\right) \quad (2)$$

for systems exhibiting half-integer spins S (Kramers systems).³ Thus, the energy barrier is determined by two factors: The spin S and the axial zero-field splitting (ZFS) parameter D . S is the ground state spin of the whole molecule and results from exchange coupling of the individual electron spins, usually via the bridging ligands (super-exchange). The strength of the exchange coupling is described by the coupling constant J_{ex} which can be isotropic or anisotropic. In the isotropic case the Hamiltonian describing the interaction between two paramagnetic ions can be formulated as

$$\mathcal{H}_{\text{ex}} = -J_{\text{ex}} \hat{S}_1 \cdot \hat{S}_2 \quad (3)$$

where \hat{S}_1 and \hat{S}_2 represent the spin operators for each of the two metal ions.³ According to equation (3), J_{ex} is positive for ferromagnetic coupling and negative for anti-ferromagnetic coupling but several sign conventions can be found in literature, some of them also including a factor of 2.³⁹ Thus, care has to be taken when comparing data. In Mn_{12}ac , ferrimagnetic

coupling between four Mn(IV) centers ($S = 3/2$) and eight Mn(III) centers ($S = 2$) results in a giant spin of $S = (8 \times 2) - (4 \times 3/2) = 10$ (Figure 1).¹ The sign and the magnitude of the exchange coupling not only depend on the metal centers themselves, but also on the nature of the bridging ligands and the relative orientation of the orbitals involved. Considering the extent of overlap of the spin-containing molecular orbitals based on the bridging geometry, the sign of the exchange coupling can be predicted by means of the so-called Goodenough-Kanamori rules.⁴⁰⁻⁴²

The ZFS parameter D is a measure for the axial anisotropy of the system and describes the separation of the M_S states within the spin ground state. M_S is the magnetic spin quantum number for the coupled system and adopts values from $-S$ to $+S$. In a completely isotropic system all M_S states are degenerate, but axial distortion and second-order spin-orbit coupling lift this degeneracy resulting in an energy level structure which is commonly described by a double-well potential.³⁻⁸ The value of D is expected to be high for systems with small energy gaps between the electronic ground term and admixing excited terms. The double-well potential for Mn₁₂ac is schematically illustrated in Figure 2a. Here D is negative, meaning that the states with $M_S = \pm S = \pm 10$ are lowest in energy. They remain twofold degenerate, but are separated by the energy barrier ΔE which was determined to 46 cm^{-1} .⁴³

In addition to axial zero-field splitting, low-symmetry molecules exhibit rhombic zero-field splitting which is accounted for by the transverse ZFS parameter E . Rhombic distortion causes mixing of different M_S states and in the case of non-Kramers systems all degeneracy can be lifted even in the absence of a magnetic field.

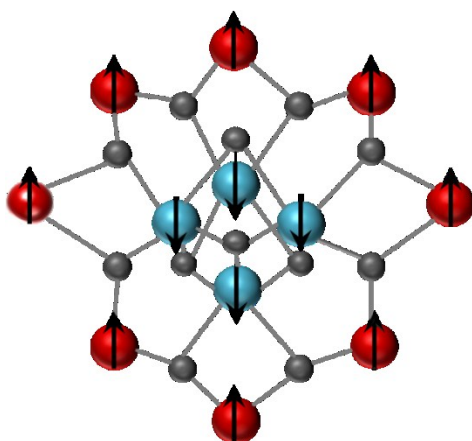


Figure 1: Spin structure in Mn₁₂ac.¹ Four Mn(IV) centers ($S = 3/2$; shown in blue) couple ferrimagnetically to eight Mn(III) centers ($S = 2$; shown in red), resulting in an $S = 10$ ground state. Grey circles represent oxygen bridges.

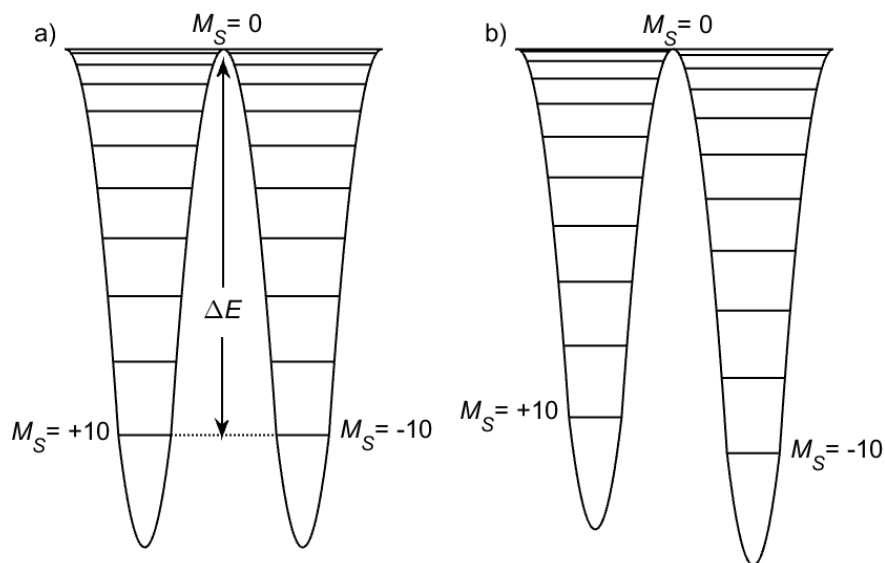


Figure 2: Schematic illustration of the double-well potential for Mn_{12}ac .⁶ a) In the absence of an external field the $\pm M_S$ states are degenerate. b) If an external magnetic field is applied, the twofold degeneracy is lifted, resulting in an asymmetric shape.

The corresponding ZFS Hamiltonian is given by

$$\mathcal{H}_{ZFS} = D(\hat{S}_z^2 - \frac{1}{3}(S(S+1))) + E(\hat{S}_x^2 - \hat{S}_y^2) \quad (4)$$

where x , y and z label the three principal axes and are conventionally chosen such that $0 \leq |E/D| \leq 1/3$.^{3,44} The distortion described by the E term mixes only states which differ by $\Delta M_S = \pm 2$ (second-rank operators). For 3d systems with $S \geq 2$ higher-rank terms are possible; however, they are often neglected in order to avoid over-parametrization.

When an external magnetic field B is applied, the states will be further split by the Zeeman interaction and the double-well potential will become asymmetric (Figure 2b). The well corresponding to negative values for M_S will be lowered in energy with respect to the other and will therefore be preferably populated: The molecule becomes magnetized and reaches its saturation magnetization at low temperatures and high fields when only the lowest-lying state is populated. The Zeeman splitting is described by the Hamiltonian

$$\mathcal{H}_{Zeeman} = \mu_B \sum_{k,q=x,y,z} g_{k,q} B_k \hat{S}_q \quad (5)$$

where μ_B denotes the Bohr magneton and g is the orientation-dependent Landé factor of the system.^{3,38}

When the external magnetic field is switched off, the system will relax, meaning that both wells will be populated equally again. This process requires overcoming the energy barrier by climbing up the ladder of M_S states (multi-step Orbach relaxation).³ Thus, for high energy barriers and at sufficiently low temperatures, slow relaxation of magnetization will be observed. In $Mn_{12}ac$ magnetic relaxation can take up to several months.¹

In an ideal SMM, such a thermally activated multi-step Orbach relaxation would be the only pathway for magnetic relaxation and the temperature dependence of the relaxation time τ could be solely described by an Arrhenius law

$$\tau_{Orbach} = \tau_0 \cdot e^{-\Delta E/k_B T} \quad (6)$$

with the attempt time τ_0 , the energy barrier ΔE , the Boltzmann constant k_B and the temperature T .^{3,38} In real systems however, not only the Orbach process contributes to the magnetic relaxation, but also the Raman process, the direct process and quantum tunneling of magnetization.^{3,38} These relaxation pathways give rise to effective energy barriers U_{eff} which are usually much smaller than the expected barrier ΔE . A more detailed description will be given in section 2.1.3.

The quadratic dependence of the energy barrier on the cluster spin S in equations (1) and (2) motivated chemists to synthesize metal ion complexes with rather large ground state spins. For instance, new records were obtained in 2006 in a ferromagnetically coupled Mn_{19} aggregate exhibiting a spin of $S = 83/2$ ¹⁵ and recently in a Fe_{42} cluster with $S = 45$ ¹⁸. However, in contrast to expectations the energy barriers were very small. Meanwhile it is well-known that the cluster anisotropy constant D is not independent of the ground state spin S and that large spins tend to come along with low anisotropies, preventing high anisotropy barriers.^{19,20} Attention therefore has turned to the design of metal ion complexes employing highly magnetically anisotropic metal centers.^{9,11,12,22-24,28,37} High anisotropy can be achieved by using metal centers with unquenched orbital angular momenta such as lanthanide(III) or octahedrally coordinated cobalt(II) ions (first-order spin-orbit interactions) or by ligand field design that leads to admixing of excited states with orbital angular momentum (second-order spin-orbit coupling).

2.1.2 Single-Ion Magnets

The term “single-ion magnets” (SIMs) denotes a newer generation of single-molecule magnets. Here each molecule contains only one single paramagnetic metal ion and the origin of the observed energy barriers therefore lies in the single ion anisotropy. The electron spins of such systems are limited to the individual spins of the metal centers, i.e. to a maximum of $S = 5/2$ for d-block ions and maximally $S = 7/2$ for f-block ions. However, strongly anisotropic metal centers such as Ln(III) ions are considered promising candidates.

In this context the major breakthrough was achieved in 2003 by Ishikawa *et al.* by the observation of SMM behavior in the dysprosium and terbium analogues of the lanthanide double-deckers (NBu₄)[Ln(Pc)₂].²⁵ In these molecules, the Ln(III) ions are complexed by two negatively charged phthalocyaninato ligands, resulting in a fairly axial complex geometry which can be described by D_{4d} symmetry (Figure 3). For the Tb(III) analogue, an experimentally determined effective energy barrier of 230 cm⁻¹ was reported,²⁵ a value that has never been achieved for any SMM of the first generation. In contrast to complexes of the d-block metal ions, the energy barriers in lanthanide complexes originate from the crystal field splitting which is a rather small effect compared to the spin-orbit interaction due to the effective shielding of the f-orbitals. In the context of lanthanides, the concept of zero-field splitting, i.e. the application of a spin Hamiltonian, is thus not appropriate anymore.

The high symmetry of the lanthanide double-deckers allowed the parametrization of the crystal field by analyzing magnetic susceptibility as well as NMR data and indeed a dependence of the energy barrier height on the energies of the crystal field states was found.^{25,45,46} The knowledge of these energies thus appears to be crucial to explain the magnetic properties of lanthanide SIMs.

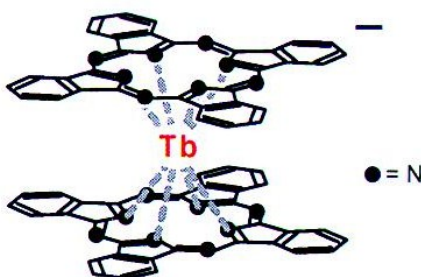


Figure 3: Chemical structure of the [Ln(Pc)₂]⁻ anion. Reprinted with permission from N. Ishikawa, M. Sugita, T. Ishikawa, S. Koshihara, Y. Kaizu, *J. Am. Chem. Soc.* **2003**, *125*, 8694.²⁵

However, most lanthanide complexes exhibit lower symmetries than D_{4d} and the determination of their electronic structures requires much more experimental effort. A detailed description of the electronic structure of lanthanide based SIMs and its determination will be given in chapter 2.2. Although the employment of lanthanide ions in single-ion magnets frequently leads to the observation of record effective energy barriers,^{9,21,23-25,37} real magnetic bistability is rarely observed. Out of hundreds of reported lanthanide based SIMs, only a few show magnetic hysteresis which is the ultimate proof for magnetic bistability. One reason is effective under-barrier relaxation like quantum tunneling of the magnetization (QTM) and a lot of research activity focusses on this issue. A possible way to suppress QTM is seen in the inclusion of exchange coupling, which is very hard to achieve between 4f ions and requires e.g. radical bridging ligands.^{23,33,34}

This finding suggests that it is worthwhile going back to 3d transition metal ions where exchange couplings are much easier obtained. Various examples of 3d single-ion magnets have already been reported^{11,24,28} and the challenge now is to find metal-ligand combinations that a) create a large uniaxial anisotropy resulting in a maximum zero-field splitting and b) allow the modification of the ligands making them potentially bridging ligands. Concerning the choice of the metal ions, metal centers with largely unquenched orbital angular momenta in a given coordination geometry are preferred: For metal complexes with quenched orbital momenta, the ZFS arises from second-order spin-orbit coupling which admixes excited states into the ground state. If orbital angular momentum is unquenched, however, spin-orbit coupling is a first-order effect and potentially leading to much higher energy barriers, as can be seen for the lanthanides. One of the most promising 3d ions is Co(II) due to its d^7 electronic configuration. As a representative of 3d SIMs and because Co(II) plays a major role in this work, the electronic structure of Co(II) complexes as well as suitable models for the description of their magnetic properties will be considered in section 2.2.

2.1.3 Magnetic Relaxation

Since single-molecule magnets are characterized by slow relaxation of the magnetization, the understanding of the contributing relaxation mechanisms is of crucial importance. In addition to the pure Orbach mechanism, Raman processes, direct relaxation and quantum tunneling of magnetization might occur.^{3,34,38} A schematic illustration is given in Figure 4.

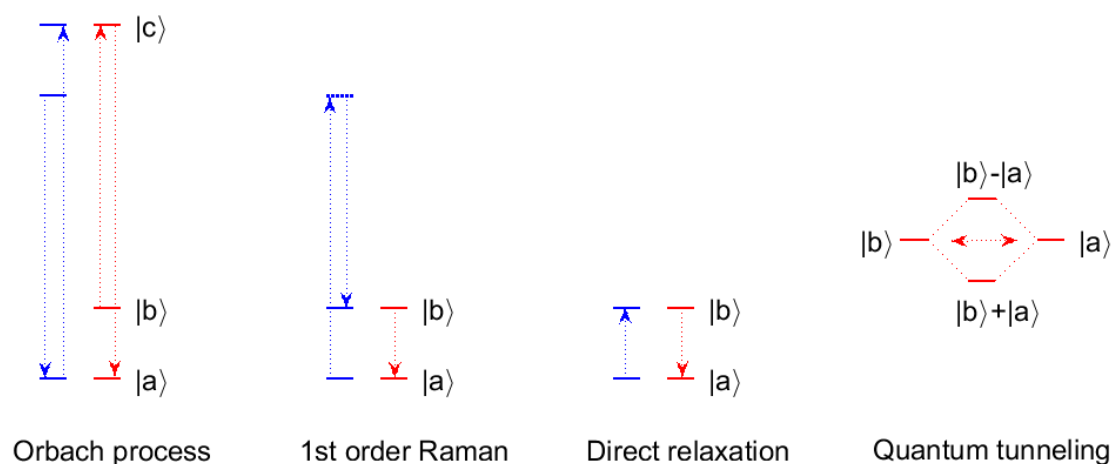


Figure 4: Schematic illustration of the mechanisms contributing to the magnetic relaxation in SMMs.³⁴ Blue horizontal lines correspond to energy levels of the lattice, whereas red lines represent levels (microstates) within the spin system. $|a\rangle$, $|b\rangle$ and $|c\rangle$ denote the microstates involved, i.e. $|S, M_S\rangle$ states for clusters of ions with quenched orbital momenta and $|J, m_J\rangle$ states for systems with largely unquenched orbital momenta, respectively. Arrows depict transitions between these levels.

The interplay of these processes hampers the progress towards practical application of SMMs since the Orbach mechanism (Figure 4, left) is the only process which directly depends on the energy gap between microstates.

Orbach relaxation^{3,34,38,47} is a type of spin-lattice relaxation, meaning that it requires energy exchange between the magnetic ion and the surrounding lattice: The absorption of phonons leads to temporary population of excited microstates from where the spin systems can either fall back to the initial states or relax to the other side of the energy barrier, in both cases under emission of phonons (2-phonon-process). Concerning the contributing microstates, three cases have to be distinguished: In the case of exchange-coupled 3d metal ions with quenched angular orbital momenta, the excited microstates are the higher lying M_S states within the total spin ground state and overcoming the energy barrier requires subsequent absorption of phonons (Figure 5a). In mononuclear 3d ion complexes however, the relevant microstates arise from the uncoupled ground state spin and are more commonly labeled by lower-case m_S . In lanthanide compounds, the excited states involved are low-lying crystal field levels, which in case of relatively pure states can be labeled by the magnetic total angular momentum quantum number m_J (Figure 5b). In all cases, the effectiveness of the Orbach mechanism is determined by the availability of phonons with the required energy.

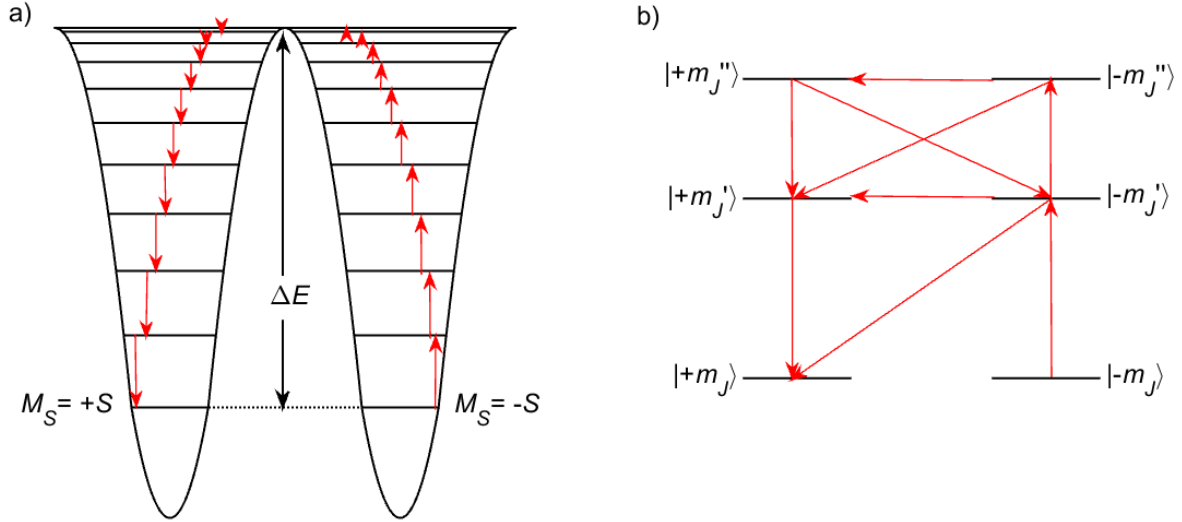


Figure 5: a) Schematic representation of the Orbach relaxation for clusters of exchange-coupled 3d transition metal ions. Overcoming the energy barrier requires subsequent absorption of phonons. b) Schematic illustration of thermally activated relaxation for lanthanide SIMs. Depending on the nature of the low-lying $|J, m_J\rangle$ states, various pathways are allowed, including not only Orbach relaxation but also thermally assisted QTM.

According to equation (6), the temperature dependence of the relaxation time for a pure Orbach mechanism is given by a simple Arrhenius law and the corresponding energy barrier can be determined by a linear fit of the $\ln \tau$ vs. $1/T$ plot. This is illustrated in Figure 6 for the exotic linear iron(I) SIM $[\text{K}(\text{crypt-222})][\text{Fe}(\text{C}(\text{SiMe}_3)_3)_2]$, where an effective energy barrier of $U_{\text{eff}} = 226 \text{ cm}^{-1}$ was obtained.²⁹ Figure 6 also shows that such a fit can be justified only at comparatively high temperatures whereas at low temperatures clear deviations from linearity occur. These deviations arise from the influence of the other relaxation pathways.

The Raman mechanism^{3,34,38,39,48,49} is depicted in Figure 4 as well. Similar to the Orbach process, it is a phonon-assisted mechanism, but in this case the relaxation occurs via virtual intermediate states. The energy released by the spin systems is then taken up by superpositions of lattice waves with frequency differences matching the released energy. The temperature dependence of the relaxation time for the Raman process is given in equation (7):

$$\tau_{\text{Raman}}^{-1} = C_{\text{Raman}} \cdot T^{n_{\text{Raman}}} \quad (7)$$

C_{Raman} is an empirically determined coefficient (Raman coefficient), T is the temperature and n_{Raman} is the Raman exponent which depends on the kind of system under study: For integer spin systems (non-Kramers systems) with isolated ground states an exponent of $n_{\text{Raman}} = 7$ was derived, whereas $n_{\text{Raman}} = 9$ was found for non-integer spin systems (Kramers ions). For systems with very low lying, i.e. thermally populated excited states, $n_{\text{Raman}} = 5$ is valid.

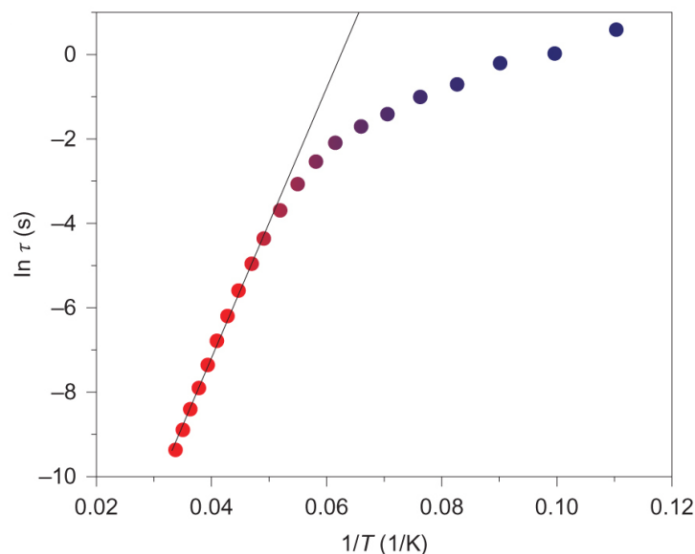


Figure 6: Arrhenius plot for the linear iron(I) single-ion magnet $[\text{K}(\text{crypt-222})][\text{Fe}(\text{C}(\text{SiMe}_3)_2)_2]$.²⁹ Gratefully adapted with permission from Macmillan Publishers Ltd: Nature Chemistry; J. M. Zadrozny, D. J. Xiao, M. Atanasov, G. J. Long, F. Grandjean, F. Neese, *Nat. Chem.* **2013**, *5*, 577; copyright (2013).

For temperatures above the Debye temperature of the studied compound, i.e. when all phonon states are occupied, the Raman exponent is $n_{\text{Raman}} = 2$. The contribution of the Raman process to the magnetic relaxation is manifested in a clear curvature in the Arrhenius plot.

The third spin-lattice relaxation mechanism is the direct relaxation (Figure 4).^{34,38,39} It is a one-phonon process, meaning that the energy released by flipping the spin is directly taken up by the lattice as a phonon. Since energy differences between spin up and spin down states are strongly affected by the magnetic field, the relaxation time for direct relaxation not only depends on the temperature but also on the magnetic field strength:

$$\tau_{\text{direct}}^{-1} = A_{\text{direct}} \cdot H^{n_{\text{direct}}} \cdot T \quad (8)$$

A_{direct} is an empirical coefficient again, H is the magnetic field strength, T is the temperature and n_{direct} is the exponent for direct relaxation. Obviously, this exponent has to be different for Kramers and non-Kramers systems, since Kramers systems always show twofold degeneracy in the absence of a magnetic field (Kramers theorem⁵⁰) while for non-Kramers systems this is not necessarily the case. Thus, for non-Kramers systems $n_{\text{direct}} = 2$ was derived and for Kramers systems $n_{\text{direct}} = 4$. However, in the presence of hyperfine coupling to nuclear spins, the microstates of Kramers systems cannot be considered degenerate anymore and $n_{\text{direct}} = 2$ as for non-Kramers systems becomes more appropriate.³⁸ Direct relaxation is especially important for so-called field-induced SMMs where slow relaxation of the magnetization can only be observed in the presence of an external magnetic field.

Besides the above-mentioned relaxation mechanisms quantum tunneling of the magnetization (QTM)^{3,34,51} might occur (Figure 4). This quantum mechanical phenomenon was predicted long ago, but first experimental evidence was found in the investigation of molecular magnets. Taking Mn₁₂ac as an example, characteristic steps in the magnetic hysteresis loop were observed, which were attributed to minima of the relaxation time due to QTM.⁵¹⁻⁵⁴ QTM means that the spins find a shortcut through the energy barrier, which leads to very fast relaxation even at low temperatures. Although it is a rather fascinating phenomenon, it is also a major problem concerning magnetic bistability. It occurs when the microstates on each side of the energy barrier are very close in energy, for example in zero field or at certain magnetic field strengths when the states are expected to cross. To make QTM possible, the states involved need to be coupled by transverse interactions, e.g. by rhombic ZFS, by transverse magnetic fields or by hyperfine coupling to nuclear spins. The resulting wave functions are then symmetric and antisymmetric linear combinations of the up and down states and are delocalized on both sides of the barrier.³⁴ The energy difference between them is termed tunnel splitting and corresponds to the rate τ_{QTM} with which the system can tunnel through the barrier. Successful avoiding of QTM requires highly axial systems, meaning that the rhombic ZFS parameter E as well as higher-order off-diagonal ZFS terms causing state mixing are close to zero. Furthermore, transverse magnetic fields, i.e. fields applied perpendicular to the preferred direction of magnetization (easy axis of magnetization) and the presence of nuclear spins in close proximity to the relaxing electron spins should be avoided. Since also magnetized neighboring molecules can cause transverse magnetic fields, SMMs are often diluted in diamagnetic host materials. However, reliable prediction and control of the extent of QTM for a given compound have not yet been achieved and remain a goal for the future. The tunneling rate is commonly described by equation (9)

$$\tau_{QTM}^{-1} = \frac{B_1}{1 + B_2 H^2} \quad (9)$$

where B_1 and B_2 are system dependent parameters and H is the magnetic field strength. In the Arrhenius plot QTM is manifested as a flattening of the curve in the low-temperature regime.

Real systems can show contributions of all of the above-mentioned relaxation mechanisms, leading to strongly curved Arrhenius plots. In such cases, linear fits are not justified at all and may yield unreasonable values for the energy barriers. The application of spectroscopic methods is then essential for the explanation of the magnetic properties.

2.2 Electronic Structure of Ln(III) Compounds

2.2.1 Free Ln(III) Ions

Understanding the magnetic properties of lanthanide-based single-molecule magnets requires the understanding of their electronic structures. A detailed description of the electronic structures of lanthanide compounds has been given e.g. by Wybourne and co-workers^{55,56}.

Free Ln(III) ions are characterized by electronic configurations $[\text{Xe}]4f^N$ with N being the number of electrons within the f-shell. Depending on the value of N , a number of different arrangements of the electrons within the f-shell is possible. The states arising from different electron arrangements, called terms, exhibit different energies due to electrostatic interactions. These terms are commonly labeled by term symbols of the general form ^{2S+1}L , where $2S+1$ denotes the spin multiplicity with S being the total electron spin of the respective Ln(III) ion and L corresponds to the total orbital angular momentum. According to Hund's rules^{57,58} and taking into account the Pauli exclusion principle⁵⁹, the ground state for a given $4f^N$ configuration is characterized by the maximum spin S and for a given spin S by the maximum value for L . Taking Dysprosium(III) as an example, the electrostatic interactions in its $4f^9$ electronic configuration lead to a ground state with $S = 5/2$ and $L = 5$, labeled by ${}^6\text{H}$. The first excited term is then given by ${}^6\text{F}$, corresponding to $S = 5/2$ and $L = 3$.

In addition to electronic repulsion, magnetic interactions have to be taken into account, including spin-orbit, spin-spin, spin-other-orbit and similar interactions. Spin-orbit coupling is by far the predominant one and arises from the coupling of the electron spin magnetic moment and the magnetic field originating in the orbital motion of the electron. In terms of a pure Russell-Saunders coupling scheme, coupling of the total spin S with the total orbital angular momentum L results in a total angular momentum, denoted by the quantum number J . J can adopt values ranging from $L + S$ to $|L - S|$, which means that each LS term is split into $(2S + 1)$ components. For $N > 7$, the ground state is given by $J = L + S$, whereas for $N \leq 7$ a ground state with $J = |L - S|$ is obtained. In many cases such a simple Russell-Saunders coupling scheme is not appropriate; however, the spin-orbit split states are commonly labeled by the corresponding term symbols $^{2S+1}L_J$. For Dysprosium(III) this is ${}^6\text{H}_{15/2}$.

A much more realistic description of the electronic states of Ln(III) ions is obtained by applying the so-called intermediate coupling scheme. Here, mixing of different LS states with the same J -value via second-order spin-orbit coupling is taken into account. Generally, the importance of these perturbations increases with decreasing separation of the levels and

neglecting them in energy calculations might lead to deviations of up to several hundreds of wavenumbers.

Taking into account not only the major electrostatic and spin-orbit interactions but also the remaining minor perturbations, the effective free-ion Hamiltonian⁶⁰ acting within the $4f^N$ configuration is given by

$$\begin{aligned} \mathcal{H}_{free\ ion} = & E_{AVE} + \sum_{k=2,4,6} F^k f_k + \zeta_{4f} A_{SO} + \alpha L(L+1) + \beta G(G_2) + \gamma G(R_7) \\ & + \sum_{i=2,3,4,6,7,8} t_i T^i + \sum_{k=0,2,4} m_k M^k + \sum_{k=2,4,6} p_k P^k \end{aligned} \quad (10)$$

E_{AVE} contains all the spherically symmetric perturbations and therefore only shifts the energy of the entire $4f^N$ configuration. Adjusting E_{AVE} allows setting the ground-state energy to zero. The above-mentioned electrostatic repulsion between the electrons of the $4f^N$ configuration is described parametrically by the second term. The radial electrostatic integrals F^k are taken as adjustable parameters while the f_k represent the angular parts of the matrix elements of the electrostatic interaction. The F^0 parameter is not included in this term since it is already incorporated in E_{AVE} . A complete tabulation of the electrostatic energy matrices for all the f^N configurations has been provided by Nielson and Koster.⁶¹

The term $\zeta_{4f} A_{SO}$ corresponds to the spin-orbit coupling, where ζ_{4f} is the spin-orbit coupling constant and A_{SO} represents the angular part of the spin-orbit interaction.

In order to obtain reasonable agreement between experimentally observed and calculated energy levels, higher-order terms also have to be included in the Hamiltonian. These are for example the two-electron Coulomb correlation contributions parametrized by α , β , γ and the three-electron correlation contributions parametrized by T^i with t_i being the three-particle operators. They account for spin-independent interactions between configurations of equal parity. Magnetically correlated corrections such as spin-spin and spin-other-orbit interactions are accounted for by the term $\sum_{k=0,2,4} m_k M^k$, where m_k are the operators and M^k the so-called Marvin integrals. Finally, the electrostatic correlated spin-orbit interactions are described by the last term in equation (10) with p_k as operators and P^k as parameters.

Praseodymium(III) with only two electrons in the f-shell serves as a comparatively simple example for demonstrating the calculation of the matrix elements for the major electrostatic and spin-orbit interactions:^{55,56} For two equivalent electrons, the matrix elements for Coulomb repulsion are of the form

$$\left\langle (nl)^2; SL \left| \frac{e^2}{r_{12}} \right| (nl)^2; SL \right\rangle = \sum_k f_k(l, l) F^k(nl, nl) \quad (11)$$

where n is the principal quantum number, e.g. $n = 4$ for 4f-electrons, l corresponds to the orbital angular momentum of a single electron ($l = 3$ for f-electrons), e is the electronic charge and r_{12} is the distance between the interacting electrons. The angular factors f_k can be evaluated by:

$$f_k(l, l) = (-1)^L \langle l \| C^{(k)} \| l \rangle^2 \begin{Bmatrix} l & l & k \\ l & l & L \end{Bmatrix} \quad (12)$$

$\langle l \| C^{(k)} \| l \rangle$ are reduced matrix elements of the spherical tensor operators $C_q^{(k)}$, which transform like the spherical harmonics Y_{kq} :

$$C_q^{(k)} = \sqrt{\frac{4\pi}{2k+1}} Y_{kq} \quad (13)$$

The part in curly brackets in equation (12) is a Wigner-6j-symbol. The reduced matrix elements can be calculated by

$$\langle l \| C^{(k)} \| l \rangle = (-1)^l [(2l+1)(2l+1)]^{0.5} \begin{pmatrix} l & k & l \\ 0 & 0 & 0 \end{pmatrix} \quad (14)$$

where the last factor is a Wigner-3j-symbol. For $k = 2$ and $l = 3$ for f-electrons we obtain

$$\langle f \| C^{(2)} \| f \rangle = (-7) \cdot \begin{pmatrix} 3 & 2 & 3 \\ 0 & 0 & 0 \end{pmatrix} = (-7) \cdot \frac{2}{\sqrt{105}} \quad (14a)$$

leading to the following expression for f_2 in the 3H term in Pr(III):

$$f_2(f, f) = (-1)^5 \cdot \left((-7) \cdot \frac{2}{\sqrt{105}} \right)^2 \begin{Bmatrix} 3 & 3 & 2 \\ 3 & 3 & 5 \end{Bmatrix} = -0.1111 \quad (12a)$$

The factors f_4 and f_6 can be calculated in the same way and for the 3H term of Pr(III), the Coulomb energy is then given by:

$$E(^3H) = -0.1111 \cdot F^2 - 0.0468 \cdot F^4 - 0.0018 \cdot F^6 \quad (15)$$

The corresponding energies of the other LS states of Pr(III) are given in Table A 1 in the appendix.

Within a two-electron configuration, the matrix elements for spin-orbit coupling can be written as:

$$\begin{aligned} & \langle (nl)^2 SLJM | \mathcal{H}_{SO} | (nl)^2 S' L' JM \rangle \\ &= \left\langle (nl)^2 SLJM \left| \sum_{i=1}^2 \zeta_{nl} (\hat{s}_i^{(1)} \cdot \hat{l}_i^{(1)}) \right| (nl)^2 S' L' JM \right\rangle \\ &= \zeta_{nl} (-1)^{S'+L+J} \begin{Bmatrix} S & S' & 1 \\ L' & L & J \end{Bmatrix} \sum_{i=1}^2 \langle s_1 s_2 S \| s_i^{(1)} \| s_1 s_2 S' \rangle \langle l_1 l_2 L \| l_i^{(1)} \| l_1 l_2 L' \rangle \\ &= (-1)^{S'+L+J+1} \cdot 2 \zeta_{nl} \\ &\cdot \sqrt{s(s+1)(2s+1)l(l+1)(2l+1)(2S+1)(2S'+1)(2L+1)(2L'+1)} \\ &\cdot \begin{Bmatrix} S & S' & 1 \\ L' & L & J \end{Bmatrix} \begin{Bmatrix} S & 1 & S' \\ s & s & s \end{Bmatrix} \begin{Bmatrix} L & 1 & L' \\ l & l & l \end{Bmatrix} \end{aligned} \quad (16)$$

Thus, for $l_1 = l_2 = 3$, $s_1 = s_2 = 1/2$, $L = L' = 5$, $S = S' = 1$ and $J = 4$ a diagonal matrix element of $-(3 \cdot \zeta_{4f})$ is obtained. In a pure Russell-Saunders coupling scheme, this would correspond to the 3H_4 term of Pr(III). The other matrix elements can be calculated in an analogous way.

In an intermediate coupling calculation, the obtained matrix elements of the electrostatic and spin-orbit interactions are arranged in energy matrices, one for each value of J . By choosing particular values for the parameters F^k and ζ_{4f} , the matrix elements are then expressed in numerical form. Finally, diagonalization of these matrices yields the sets of eigenvalues and eigenvectors. The energy matrix for $J=4$ in Pr(III) in the intermediate coupling scheme is obtained as

$$\begin{pmatrix} E(^3F) + \frac{3}{2}\zeta & \frac{\sqrt{33}}{3}\zeta & 0 \\ \frac{\sqrt{33}}{3}\zeta & E(^1G) & -\frac{\sqrt{30}}{3}\zeta \\ 0 & -\frac{\sqrt{30}}{3}\zeta & E(^3H) - 3\zeta \end{pmatrix} \quad (17)$$

where the terms $E(2S+1L)$ correspond to the Coulomb energies given in Table A 1. The matrix elements for $J = 0$ to $J = 6$ as well as the resulting eigenvalues and eigenvectors are tabulated in the appendix, Table A 2 and Table A 3. They clearly illustrate the differences between Russell-Saunders coupling and intermediate coupling calculations. While in the Russell-Saunders coupling scheme only diagonal matrix elements are obtained, the application of the intermediate coupling scheme yields mixed state compositions with different energies. The effect of the different coupling schemes on the energy level structure of Pr(III) is shown in Figure 7.

Since the f-shell is an inner shell, meaning that it is shielded by the closed s^2p^6 shells, the influence of the environment on the f-electronic structures of Ln(III) compounds is rather small compared to e.g. the d-electronic structures of 3d ions. Thus, for different compounds of a given lanthanide, the free-ion parameters will not differ to a large extent. The free-ion levels can be probed by spectroscopic techniques, especially optical spectroscopy. In this context a rather complete and very important analysis of the free-ion levels within the series of Ln(III) ions was provided by Dieke and coworkers.⁶² It led to the generation of so-called Dieke diagrams (Figure 8) which allow the estimation of the energetic positions of the respective terms and facilitate the interpretation of experimental spectra.

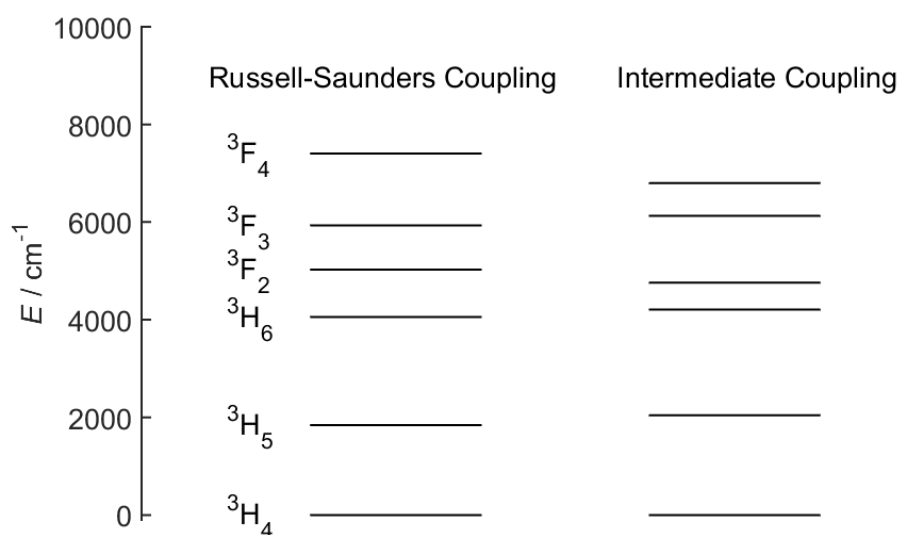


Figure 7: Comparison of the influence of Russell-Saunders coupling and intermediate coupling on the electronic level structure of Pr(III). For reasons of clarity, only the six lowest lying levels are shown. The corresponding energies are given in Table A 3. Only the electrostatic and the spin-orbit perturbations were considered. The free-ion parameters were set to $F^2 = 68995 \text{ cm}^{-1}$, $F^4 = 56119 \text{ cm}^{-1}$, $F^6 = 38864 \text{ cm}^{-1}$ and $\zeta_{4f} = 737 \text{ cm}^{-1}$. The ground state energies were set to zero.

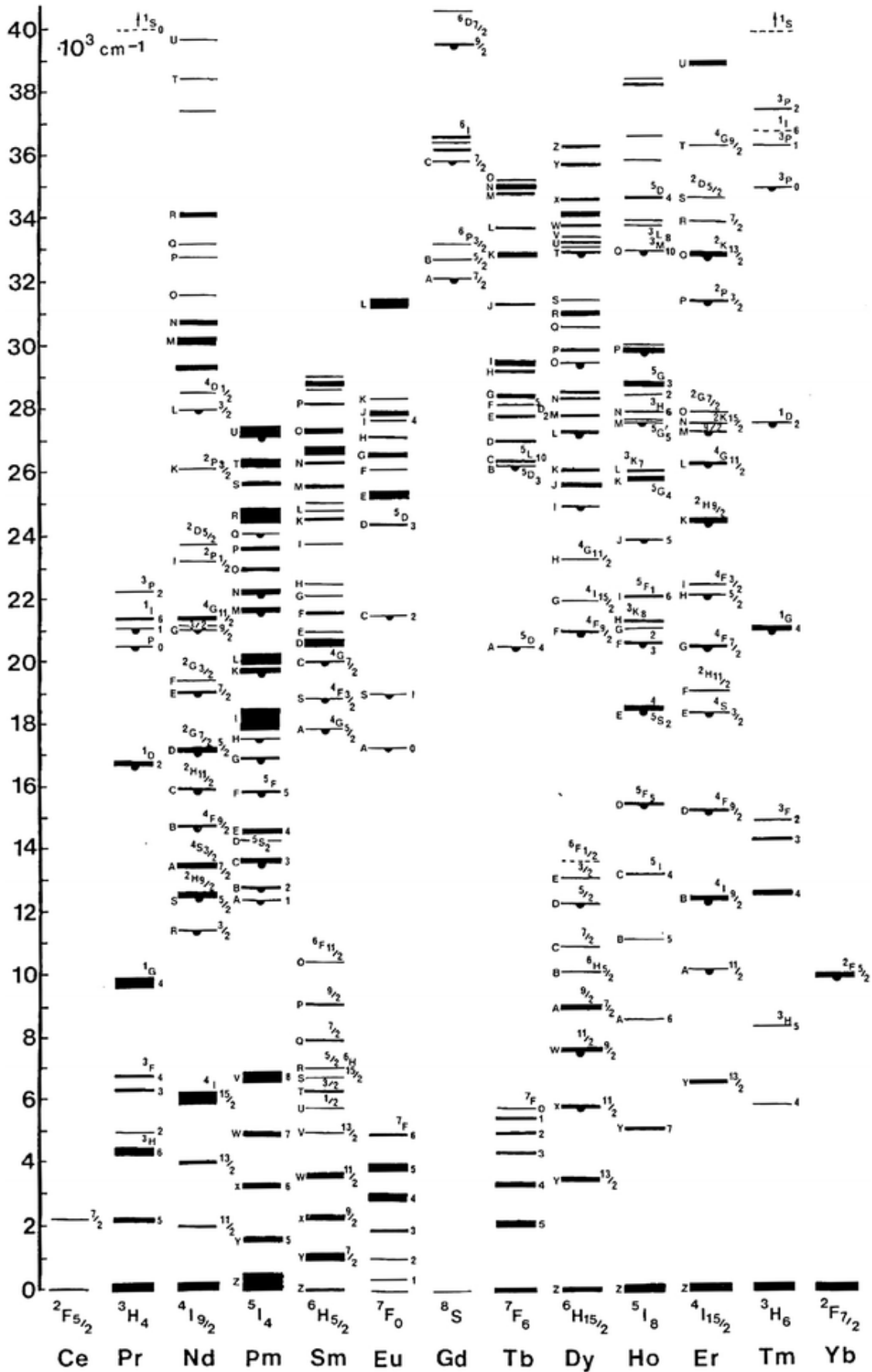


Figure 8: Dieke diagram illustrating the energy level structure of Ln(III) ions doped into host lattices. The thickness of a line indicates the magnitude of the respective crystal-field splitting.⁶³ Reprinted with permission from G. H. Dieke, H. M. Crosswhite, *Applied Optics* 1963, 2, 675.

2.2.2 Ln(III) Ions in a Crystal Field

In real systems, lanthanide ions are surrounded by ligands and the electric fields produced by the electrons of these ligands lead to a further splitting of the free ion states. This splitting is called crystal field splitting and strongly depends on the local symmetry around the Ln(III) ions. The $^{2S+1}L_J$ states are split into their m_J components, where m_J is the magnetic total angular momentum quantum number. For non-Kramers systems, where J is an integer, a maximum number of $2J + 1$ crystal field levels for each term may be observed, whereas for Kramers ions (non-integer values for J) according to Kramers' theorem⁵⁰ a twofold degeneracy of the $\pm m_J$ states has to be retained, leading to a maximum number of $J + \frac{1}{2}$ crystal field levels, respectively. For example, the ground state 3H_4 of Pr(III) might be split by a crystal field into nine microstates with different energies, whereas the $^6H_{15/2}$ ground state of Dy(III) can be maximally split into eight components.

Compared to electronic repulsion and spin-orbit coupling, the crystal field splitting is a rather small perturbation and the observed splittings are in the range of only hundreds of wavenumbers. Nevertheless, the crystal field splitting is responsible for the SIM behavior of many lanthanide complexes because the energy differences between the ground microstates and the first or second excited ones correspond to the energy barriers described in section 2.1.

Concerning the crystal field Hamiltonian, two different notations are commonly used: In the context of magnetism, the Hamiltonian is often expressed in terms of the so-called extended Stevens operators^{64,65}, whereas in optical lanthanide spectroscopy, only the so-called Wybourne notation^{55,56,60} is appropriate. In terms of the extended Stevens operators, the crystal field Hamiltonian is given by

$$\mathcal{H}_{CF}(ESO) = \sum_{k,q} B_k^q O_k^q = \sum_{k,q} A_k^q \langle r^k \rangle \theta_k O_k^q \quad (18)$$

The Stevens operators O_k^q are combinations of the cartesian components J_x , J_y and J_z of the total angular momentum operator \hat{J} and belong to the class of tesseral tensor operators. θ_k are the Stevens factors and depend not only on k , but also on the quantum number J and are therefore usually expressed as α_J , β_J and γ_J for $k = 2, 4, 6$, respectively. Explicit expressions for the Stevens operators and tabulated values for the Stevens factors can be found in literature.^{64,65} The coefficients B_k^q (A_k^q) are crystal field parameters that have to be empirically determined. Different possible definitions and symbols for the crystal parameters often cause confusion in literature and the comparison of literature values thus should be done very

carefully. As in the case for the free ion parameters F^k , the values for k are limited to $k \leq 2l$, i.e. $k \leq 6$ for f-electrons and they have to be even. Depending on the symmetry of the studied compound, q can adopt integer values ranging from $-k$ to k . An explanation will be given below. The dependence of the crystal field Hamiltonian (18) on the total angular momentum implicates the restriction of the crystal field parametrization to a given Russell-Saunders multiplet. This might be sufficient if one is only interested in the ground state crystal field splitting, but will inevitably lead to wrong descriptions of higher lying states. Furthermore, the different microstates do not all show the same sensitivity to the variation of a given crystal field parameter and the ground state crystal field levels thus might be insufficient to reliably determine all of them. Since the community of molecular magnetism has recently realized more and more the importance of spectroscopic techniques for the determination of crystal field parameters,^{66,67} the Wybourne notation of the Hamiltonian, which acts within the whole $4f^N$ configuration of a given Ln(III) compound should be preferred.

A description of the crystal field splittings of not only the ground terms but also of the energetically higher lying spectroscopically accessible terms requires a Hamiltonian including the free-ion part and the crystal field part:

$$\mathcal{H} = \mathcal{H}_{free\ ion} + \mathcal{H}_{CF} \quad (19)$$

$\mathcal{H}_{free\ ion}$ is the free-ion Hamiltonian defined in equation (10) and \mathcal{H}_{CF} is the crystal field Hamiltonian in Wybourne notation^{55,56,60} which is given by

$$\mathcal{H}_{CF}(Wyb) = -eV_{CF}(Wyb) \quad (20)$$

The crystal field potential $V_{CF}(Wyb)$ is defined as a linear combination of spherical tensor operators of various ranks:

$$V_{CF}(Wyb) = \sum_{k,q} B_{kq} C_q^{(k)} \quad (21)$$

The spherical tensor operators $C_q^{(k)}$ are related to the spherical harmonics Y_{kq} by equation (13) and the coefficients B_{kq} are the crystal field parameters that can contain a real and an imaginary part, which show the same symmetry properties as the corresponding tesseral harmonics. For f^N configurations, the matrix elements of the crystal field potential have the form

$$\begin{aligned}
& \langle f^N \alpha SLJm_J | V_{CF} | f^N \alpha' SL'J'm_{J'} \rangle \\
&= \sum_{k,q} B_{k,q} \langle f^N \alpha SLJm_J | U_q^{(k)} | f^N \alpha' SL'J'm_{J'} \rangle \langle f || C^{(k)} || f \rangle
\end{aligned} \quad (22)$$

where α is an additional quantum number for distinguishing terms with the same L and S values and $U_q^{(k)}$ is a unit tensor operator as defined by Racah^{68,69}. All the other symbols have their usual meaning. An expression for the reduced matrix elements $\langle f || C^{(k)} || f \rangle$ has already been given in equation (14). Due to the selection rules for non-vanishing 3j-symbols, non-zero values for these matrix elements are only obtained if $2l + k$ is even, meaning that k itself has to be even. Odd values for k become important if states of different parities are mixed, explaining the observed intensity of the actually forbidden f-f-transitions in optical spectra. Furthermore, the 3j-symbol is only different from zero if

$$|l - k| \leq l \leq |l + k| \quad (23a)$$

leading to

$$k \leq 2l \quad (23b)$$

Thus, for 4f ions k is restricted to the values $k = 0, 2, 4, 6$.

Taking into account the Wigner-Eckart theorem^{70,71}, evaluation of the matrix elements of the unit tensor operator $U_q^{(k)}$ yields

$$\begin{aligned}
& \langle f^N \alpha SLJm_J | U_q^{(k)} | f^N \alpha' SL'J'm_{J'} \rangle \\
&= (-1)^{J-m_J} \begin{pmatrix} J & k & J' \\ -m_J & q & m_{J'} \end{pmatrix} \cdot \langle f^N \alpha SLJ || U^{(k)} || f^N \alpha' SL'J' \rangle
\end{aligned} \quad (24)$$

where

$$\begin{aligned}
& \langle f^N \alpha SLJ || U^{(k)} || f^N \alpha' SL'J' \rangle \\
&= (-1)^{S+L+J'+k} [(2J+1)(2J'+1)]^{\frac{1}{2}} \\
& \cdot \begin{Bmatrix} J & J' & k \\ L' & L & S \end{Bmatrix} \langle f^N \alpha SL || U^{(k)} || f^N \alpha' SL' \rangle
\end{aligned} \quad (25)$$

The doubly reduced matrix elements of $U^{(k)}$ in equation (25) can be calculated by a recursion formula in terms of the so-called coefficients of fractional parentage. They are constants for a given lanthanide ion and tabulated in the work of Nielson and Koster.⁶¹

The selection rules for the Wigner-3j-symbol in equation (24) yields:

$$|q| \leq k \quad (26a)$$

and

$$q = m_j - m_{j'} \quad (26b)$$

This means that the values for q run from $-k$ to k and non-zero values for q are responsible for off-diagonal matrix elements, leading to a mixing of states with $\Delta m_J = q$. Thus, in an expanded form the crystal field potential can be expressed as

$$V_{CF}(Wyb) = \sum_{k=2,4,6} \left[B_{k0} C_0^{(k)} + \sum_{q=1} \left(B_{kq} \left(C_{-q}^{(k)} + (-1)^q C_q^{(k)} \right) + i B_{k-q} \left(C_{-q}^{(k)} - (-1)^q C_q^{(k)} \right) \right) \right] \quad (21b)$$

where the real and imaginary parts of B_{kq} are denoted as B_{kq} and B_{k-q} , respectively.⁶⁰ The term $B_{00}C_0^{(0)}$ is not included because it is spherically symmetric and is absorbed in the free ion parameter E_{AVE} . Further restrictions to the values of q appearing in (21b) are due to the local symmetry around the Ln(III) ion because the crystal field potential has to be invariant with respect to all the symmetry operations of the relevant point group. The non-zero (k, q) combinations can be determined by checking which tesseral harmonics show the same symmetry properties as the point group.⁶⁰

For instance, while the crystal field potential for the D_{4d} symmetric Ln(III) double-deckers described in section 2.1.2 includes only three crystal field parameters, nine parameters are needed for compounds exhibiting C_{2v} symmetry:

$$V_{CF}(D_{4d}) = B_{20}C_0^{(2)} + B_{40}C_0^{(4)} + B_{60}C_0^{(6)} \quad (21c)$$

$$\begin{aligned}
V_{CF}(C_{2v}) = & B_{20}C_0^{(2)} + B_{22}(C_{-2}^{(2)} + C_2^{(2)}) + B_{40}C_0^{(4)} + B_{42}(C_{-2}^{(4)} + C_2^{(4)}) \\
& + B_{44}(C_{-4}^{(4)} + C_4^{(4)}) + B_{60}C_0^{(6)} + B_{62}(C_{-2}^{(6)} + C_2^{(6)}) \\
& + B_{64}(C_{-4}^{(6)} + C_4^{(6)}) + B_{66}(C_{-6}^{(6)} + C_6^{(6)})
\end{aligned} \tag{21d}$$

As a simple example of a crystal field calculation, Pr(III) in D_{4d} symmetry might be chosen. The 3F_3 multiplet is the only $J = 3$ term and can be treated as a pure Russell-Saunders coupled term. According to the tables of Nielson and Koster⁶¹, the doubly reduced matrix elements are given by

$$\langle f^2 {}^3F \| U^{(2)} \| f^2 {}^3F \rangle = \langle f^2 {}^3F \| U^{(4)} \| f^2 {}^3F \rangle = \langle f^2 {}^3F \| U^{(6)} \| f^2 {}^3F \rangle = -1/3 \tag{27}$$

Subsequent application of equations (25), (24), (14) and (22) yields the matrix elements which allow the energy level calculation:

$$\langle f^2 {}^3F_{3,\pm 3} | V_{CF} | f^2 {}^3F_{3,\pm 3} \rangle = \frac{1}{12}B_{20} - \frac{1}{198}B_{40} - \frac{5}{1716}B_{60} \tag{28a}$$

$$\langle f^2 {}^3F_{3,\pm 2} | V_{CF} | f^2 {}^3F_{3,\pm 2} \rangle = \frac{7}{594}B_{40} + \frac{5}{286}B_{60} \tag{28b}$$

$$\langle f^2 {}^3F_{3,\pm 1} | V_{CF} | f^2 {}^3F_{3,\pm 1} \rangle = -\frac{1}{20}B_{20} - \frac{1}{594}B_{40} - \frac{25}{572}B_{60} \tag{28c}$$

$$\langle f^2 {}^3F_{3,0} | V_{CF} | f^2 {}^3F_{3,0} \rangle = -\frac{1}{15}B_{20} - \frac{1}{99}B_{40} + \frac{50}{858}B_{60} \tag{28d}$$

The influence of a D_{4d} symmetric crystal field on the level structure of Pr(III) calculated in an intermediate coupling scheme is illustrated in Figure 9.

In the context of molecular magnetism, crystal fields that lead to large separations between the ground microstates and the lowest excited microstates, i.e. large energy barriers, are desired. Furthermore, symmetries resulting in rather pure states ($q = 0$) with ground states exhibiting large m_J values are preferable in order to suppress under-barrier relaxation processes of the magnetization. One method for creating such strong axial crystal fields is e.g. the synthesis of linear complexes, as recently realized in $[(\text{Pr}_3\text{Si})_2\text{N}-\text{Sm}-\text{N}(\text{Si}'\text{Pr}_3)_2]$.⁷² However, the synthesis of such complexes is a demanding task and their low stability makes them unsuitable for practical applications.

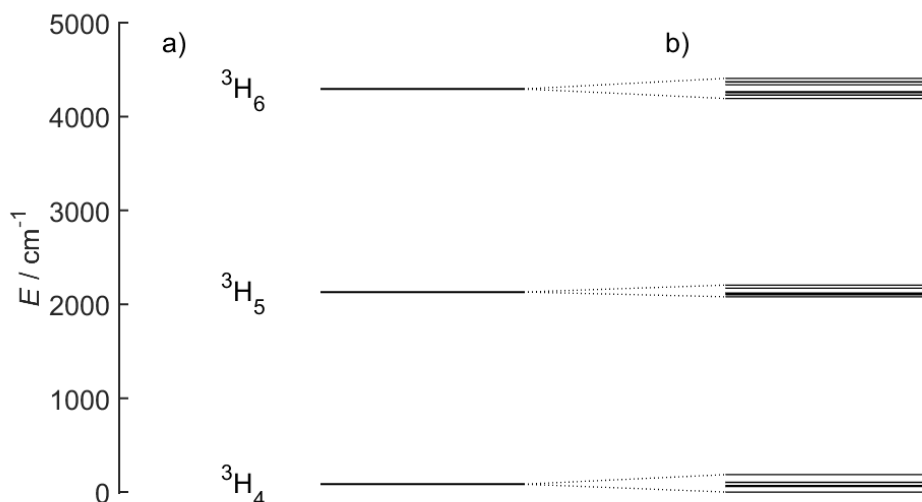


Figure 9: Influence of a D_{4d} symmetric crystal field on the level structure of Pr(III). a) Energies of the three lowest-lying free-ion terms calculated with $F^2 = 68995 \text{ cm}^{-1}$, $F^4 = 56119 \text{ cm}^{-1}$, $F^6 = 38864 \text{ cm}^{-1}$ and $\zeta = 737 \text{ cm}^{-1}$. b) Crystal field split energy levels with $B_{20} = 110 \text{ cm}^{-1}$, $B_{40} = -330 \text{ cm}^{-1}$ and $B_{60} = -650 \text{ cm}^{-1}$.

Fortunately, it has been shown that low-symmetry compounds might also possess axial crystal field eigenstates^{73,74} and in order to make progress towards the rational design of lanthanide based SIMs, the relations between electronic and molecular structure of such low-symmetry compounds need to be much better understood. This requires the accurate determination of the crystal field parameters, which can be a difficult task due to their high number (up to 27) for low symmetries. Thus, the combination of several magnetometric and spectroscopic methods is required and the obtained best-fit parameter sets should satisfactorily simulate all of the experimental data.

2.3 Electronic Structure and Magnetism of Co(II) Compounds

2.3.1 Octahedrally Coordinated Co(II)

Due to its incompletely quenched orbital angular momentum, octahedrally coordinated Co(II) has become a rising star in molecular magnetism.^{11,22,28} However, for the same reason the description of the electronic structure is comparatively complex and several cases have to be distinguished. The electronic configuration of Co(II) is [Ar]3d⁷, leading to a ⁴F free-ion ground term. Excited terms are ⁴P, ²G, ²H, ²P, ²D, ²F and ²D in order of ascending energy. The energies of these terms can be calculated in a similar way as shown for the free Ln(III) ions (compare section 2.2.1, equations (11), (12), (14)), but due to the presence of seven d-electrons, the calculation becomes more complicated compared to the example of Pr(III) with only two electrons. Since the values of k are restricted to $k \leq 2l$, only two radial electrostatic integrals, namely F^2 and F^4 , appear in the free-ion Hamiltonian of Co(II). However, for 3d-ions it is more convenient to express the energies of the LS states in terms of the so-called Racah parameters A , B and C , which are linear combinations of the parameters F^k .^{68,75,76}

$$A = F^0 - \frac{1}{9}F^4 \quad (29a)$$

$$B = \frac{1}{49}F^2 - \frac{5}{441}F^4 \quad (29b)$$

$$C = \frac{5}{63}F^4 \quad (29c)$$

The advantage of the Racah parameters consists in the sole dependence of the energies of terms with maximum spin S on the parameter B . Since F^0 is absorbed in the free ion parameter E_{AVE} , the Racah parameter A is usually set to zero. C can be roughly approximated as $C \approx 4.5 B$.⁷⁷ Explicit expressions for the diagonal electrostatic matrix elements of Co(II) are listed in Table A 4 in the appendix (section 8.1.2)^{75,78} while the left-hand side of the Tanabe-Sugano diagram⁷⁵ shown in Figure 10 provides a graphical illustration.

Since 3d-electrons are much more affected by the environment compared to 4f-electrons, the crystal field splitting is the next interaction to be considered.

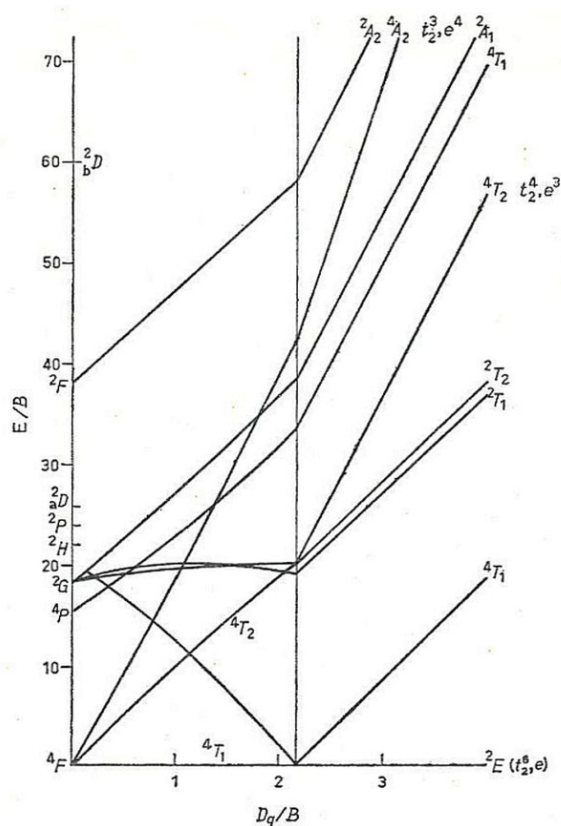


Figure 10: Tanabe-Sugano diagram for d^7 ions in an octahedral crystal field ($C = 4.633 B$). This image was published in Lever, A. B. P. *Inorganic Electronic Spectroscopy*, Copyright Elsevier (1968).⁷⁵

In perfect octahedral symmetry, the crystal field produced by the ligands splits the d-orbitals into two sets with energies of $-4 Dq$ (t_{2g} orbitals) and $+6 Dq$ (e_g orbitals), leading to an overall splitting of $\Delta_0 = 10 Dq$ with Dq being the cubic crystal field parameter as defined by Griffith.⁷⁸ The relations to the cubic crystal field parameters in Wybourne notation are given by.^{79,80}

$$B_{40} = 21 Dq \quad (30a)$$

$$B_{44} = 21 \cdot \sqrt{\frac{5}{14}} Dq \quad (30b)$$

e_g and t_{2g} are the group theoretical representations of the respective orbitals in the group O_h . e_g corresponds to the $d_{x^2-y^2}$ and d_{z^2} orbitals while t_{2g} represents the d_{xy} , d_{xz} and d_{yz} orbitals. As shown in Figure 11, population of these orbitals by seven electrons can lead to different configurations: Depending on the size of the splitting, either the high-spin (HS) or the low-spin (LS) configuration can be favored and the corresponding ground states are $^4T_{1g}$ and 2E_g , respectively. Excited HS states arising from the 4F free ion term are $^4T_{2g}$ and $^4A_{2g}$.

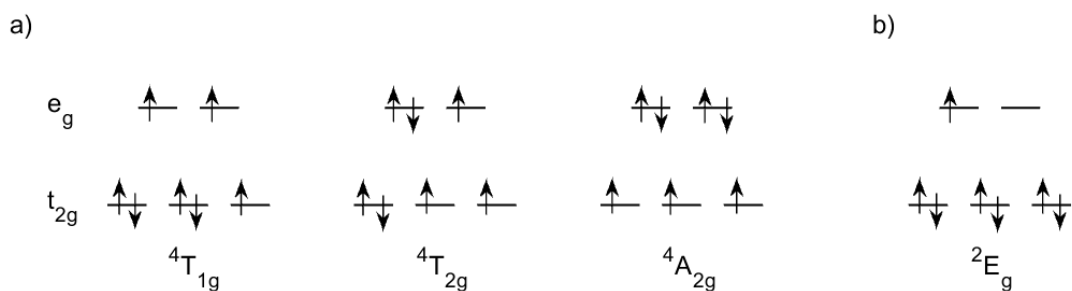


Figure 11: a) High-spin states arising from the 4F free ion state in octahedrally coordinated Co(II). ${}^4T_{1g}$ corresponds to the ground state, while ${}^4T_{2g}$ and ${}^4A_{2g}$ are excited states. b) Low-spin ground state for large crystal field splittings.

Approximations for the relative energies of these excited states can be derived by noting that ${}^4T_{2g}$ corresponds to a one-electron excitation and ${}^4A_{2g}$ to a two-electron excitation. Thus,

$$E({}^4T_{2g}) = E(e_g) + E(t_{2g}) = 6Dq - 4Dq = 2Dq \quad (31a)$$

$$E({}^4A_{2g}) = 2E(e_g) = 2 \cdot 6Dq = 12Dq \quad (31b)$$

Taking into account the degeneracy of the states and noting that the barycenter of the various terms obtained from a common free ion term lies at zero relative to that term, the energy of the ${}^4T_{1g}$ ground state can be derived as

$$E({}^4T_{1g}) = -E({}^4T_{2g}) - \frac{1}{3}E({}^4A_{2g}) = -6Dq \quad (31c)$$

resulting in relative energies of $E({}^4T_{1g}) = 0$, $E({}^4T_{2g}) = 8Dq$ and $E({}^4A_{2g}) = 18Dq$. However, equations (31a) to (31c) are only valid in very weak crystal fields. As the crystal field becomes stronger, configurational interaction can occur, meaning that terms of the same symmetry and same spin can mix. For example, ${}^4T_{1g}({}^4F)$ can mix with ${}^4T_{1g}({}^4P)$ and their energies become functions of both B and Dq .⁷⁵

The splitting patterns of the Co(II) free-ion terms in an octahedral crystal field and the relative energies depending on the ratio Dq/B are illustrated in the d^7 -Tanabe-Sugano diagram in Figure 10. Similar to the Dieke diagram for Ln(III) ions, it facilitates the interpretation of experimental spectra and allows the rough estimation of the parameters B and Dq .

Since the ${}^4T_{1g}$ ground state is an orbitally degenerate term, the magnetic properties of octahedrally coordinated Co(II) ions cannot be treated within the spin-only formalism where

any effects attributed to orbital magnetism are included only by allowing the g -factor to adopt values different from 2. More sophisticated models are needed and one of them was formulated by Lines⁸¹ more than 40 years ago. In its original version, the Lines model is a statistical description of paramagnetic Co(II) clusters in which unquenched orbital momentum plays an essential role, but for which Heisenberg coupling (i.e. isotropic exchange coupling) between real spins is qualitatively appropriate. Importantly, the ${}^4T_{1g}$ ground state is characterized by a spin $S = 3/2$ and an effective orbital quantum number $L = 1$, leading to a 12-fold degeneracy. The matrix elements of \hat{L} within the states of ${}^4T_{1g}$ are the same as those of $-\frac{3}{2}\hat{L}$ between the P functions (structural isomorphism of ${}^4T_{1g}$ and 4P).^{78,81} Thus, spin-orbit coupling can be accounted for by diagonalizing the operator $-\frac{3}{2}k_r\lambda_{SO}\hat{L}\hat{S}$ within the representation $|m_L, m_S\rangle$. λ_{SO} is the spin-orbit coupling coefficient related to ζ by $\lambda_{SO} = \frac{\pm\zeta}{2S}$, where a positive sign applies to electronic shells less than half-full and a negative sign for shells more than half-filled. k_r represents the reduction of the free-ion spin-orbit coupling due to the admixing of the 4P state into the ground state and due to distortions by the partial covalent bonding with the ligands. The diagonalization leads to a sixfold degenerate level with $E = -9/4 k_r \lambda_{SO}$, a fourfold degenerate level with $E = 3/2 k_r \lambda_{SO}$ and a ground Kramers doublet with $E = 15/4 k_r \lambda_{SO}$.⁸¹ Within this ground Kramers doublet, the real spin S can be replaced by $(5/3 s)$ with s being a fictitious spin $1/2$. For exchange-coupled clusters, this leads to the effective spin-1/2 Hamiltonian⁸¹

$$\mathcal{H} = -\frac{25}{9} \sum_{i,j} \frac{1}{2} J_{ex} \hat{S}_i \hat{S}_j - g_0 \mu_B H \sum_i \hat{S}_{i,z} \quad (32)$$

where $g_0 = (10/3 + k_r)$ is the effective g -value in the ground doublet. Diagonalizing yields the eigenvalues

$$E(S, M_S) = -\left(\frac{25}{18}\right) J_{ex} \left[S(S+1) - \left(\frac{3m}{4}\right) \right] - g_0 \mu_B H M_S \quad (33)$$

The magnetization of a system is defined as the energy change with an applied field. Taking into account the Boltzmann distribution, the cluster magnetization can be written as

$$M = g_0 \mu_B \frac{\sum_{S, M_S} M_S e^{-\frac{E(S, M_S)}{k_B T}}}{\sum_{S, M_S} e^{-\frac{E(S, M_S)}{k_B T}}} \quad (34)$$

In the limit of weak magnetic fields, the expansion of the exponentials leads to an expression for the molar magnetic susceptibility which is defined as the change of the magnetization with the magnetic field:

$$\chi_m = \frac{N_A}{k_B T} g_0^2 \mu_B^2 F_m(T) \quad (35)$$

N_A is Avogadro's constant and $F_m(T)$ depends on the number m of Co(II) centers within the cluster. For monomers and dimers it is derived as:

$$F_1 = \frac{1}{4} \quad (36a)$$

$$F_2 = \frac{2}{3 + e^{-\frac{25J_{ex}}{9k_B T}}} \quad (36b)$$

Please note that the original equations given by Lines⁸¹ have been modified in order to obtain negative coupling constants J for antiferromagnetic couplings.⁸²

However, so far only the ground Kramers doublet was taken into account, but the energy separation between the quartet and ground-state doublet is only ca. 300 cm⁻¹, which means that the upper levels cannot be neglected.⁸¹ In the Lines model they are now included in an effective field approximation, meaning that the exchange coupling within the ground Kramers doublet is treated exactly, while the excited levels are included as a molecular field.⁸¹ This is implemented by replacing g_0 by a temperature-dependent g factor $g(T)$ which also includes the effect of inter-cluster interactions. Equation (35) thus becomes

$$\chi_m = \frac{N_A}{k_B T} [g(T)]^2 \mu_B^2 F_m(T) \quad (37)$$

Explicit expressions for the evaluation of $g(T)$ are given in the appendix, section 8.1.3. The Lines model has been successfully applied to a range of Co(II) compounds,⁸²⁻⁸⁴ but reasonable agreement between experimental results and simulations can be only achieved for nearly perfect octahedral symmetries.

However, most compounds do not display perfect O_h symmetry and axial distortion of the octahedron causes symmetry lowering to D_{4h} . This is, of course, crucial for molecular magnets because in perfect cubic symmetry no magnetic anisotropy is observed. The terms split further and the description of these splittings requires further crystal field parameters in addition to Dq . For this purpose Ballhausen introduced the tetragonal radial parameters Ds and Dt .⁷⁶ With \hat{V}_{tet} signifying the tetragonal crystal field operator, they are defined by:

$$\langle d_{x^2-y^2} | \hat{V}_{tet} | d_{x^2-y^2} \rangle = 2Ds - Dt \quad (38a)$$

$$\langle d_{xy} | \hat{V}_{tet} | d_{xy} \rangle = 2Ds - Dt \quad (38b)$$

$$\langle d_{z^2} | \hat{V}_{tet} | d_{z^2} \rangle = -2Ds - 6Dt \quad (38c)$$

$$\langle d_{xz} | \hat{V}_{tet} | d_{xz} \rangle = \langle d_{yz} | \hat{V}_{tet} | d_{yz} \rangle = -Ds + 4Dt \quad (38d)$$

and the following relationships between Ballhausen's and Wybourne's crystal field parameters are obtained:^{79,80}

$$B_{20} = -7Ds \quad (39a)$$

$$B_{40} = 21Dq - 21Dt \quad (39b)$$

$$B_{44} = 21 \sqrt{\frac{5}{14}} Dq \quad (39c)$$

Thus, Ds contains the effects of B_{20} and Dt those of the difference between B_{40} and its value in an undistorted cubic symmetry. It is important to note that Dq in equation (39) has a different meaning than before: While Dq defined by Griffith denotes the crystal field parameter of the perfect cubic site, the Dq parameter in Ballhausen's notation also contains tetragonal components. It can be shown that⁷⁹

$$Dq(\text{Ballhausen}) = Dq(\text{Griffith}) + \frac{7}{12}Dt \quad (40)$$

Under the influence of an axial distortion, the ${}^4T_{1g}$ ground term of Co(II) splits into the two components ${}^4A_{2g}$ and 4E_g . Relative to the ${}^4T_{1g}$ term as zero, the energies of these terms can be calculated as:⁷⁵

$$E({}^4A_{2g}) = -2Ds + 8Dt \quad (41a)$$

$$E({}^4E_g) = Ds + 3Dt \quad (41b)$$

Thus, the energy difference Δ_{ax} between these terms is:

$$\Delta_{ax} = E({}^4E_g) - E({}^4A_{2g}) = 3Ds - 5Dt \quad (42)$$

Depending on the sign of Δ_{ax} , two cases can be distinguished: If $\Delta_{ax} > 0$, ${}^4A_{2g}$ becomes the ground state (compare Figure 12). Since this is an orbitally nondegenerate state, the magnetic properties of the system can be treated within the spin-only formalism and a typical spin Hamiltonian as described in equation (4) can be applied. If $\Delta_{ax} < 0$ however, 4E_g becomes the ground state and neither the Lines model nor the spin-only formalism is appropriate to describe the magnetic properties.

An empirical model dealing with this latter situation and based on a perturbational approach has recently been developed by Lloret *et al.*⁸⁵ Following Lines' idea, the ground doublet is described through an effective spin $S_{\text{eff}} = 1/2$ with a Landé factor g_0 . In order to simulate the magnetic susceptibility over the whole temperature range, g_0 is then replaced by a temperature dependent function $G(T)$, which takes into account the population of excited states in an empirical way:

$$G(T) = \frac{\sum_{k=0}^4 [\prod_{j=1}^3 (\sum_{i=0}^2 A_{i,j,k} x_j^i) T^k]}{\sum_{k=0}^4 [\prod_{j=1}^3 (\sum_{i=0}^2 B_{i,j,k} x_j^i) T^k]} \quad (43)$$

with $x_1 = \alpha_r$, $x_2 = \Delta_{ax}$ and $x_3 = \lambda$. The parameter α_r has a similar meaning as the parameter k_r appearing in the Lines model accounting for the orbital reduction. The empirical coefficients $A_{i,j,k}$ and $B_{i,j,k}$ depend on the sign of Δ_{ax} and are listed in the appendix, section 8.1.4.

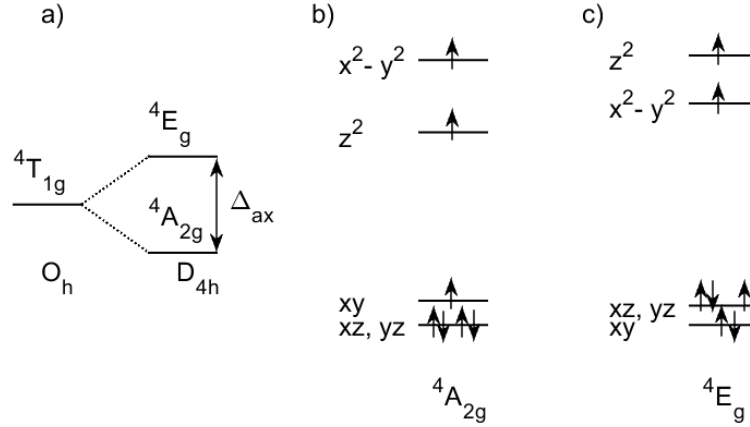


Figure 12: a) Splitting of the ${}^4T_{1g}$ ground term under an axial distortion. b) For $\Delta_{ax} > 0$, ${}^4A_{2g}$ becomes the ground state. c) For $\Delta_{ax} < 0$, 4E_g becomes the ground state.

Comparable to equations (36a) and (37), the product of molar magnetic susceptibility and temperature for mononuclear axially distorted octahedral Co(II) complexes can be modeled by

$$\chi_m T = \frac{N_A \mu_B^2}{4k_B} [G(T)]^2 \quad (44)$$

In polynuclear compounds the situation is complicated by the presence of exchange interaction. The corresponding Hamiltonian has to contain at least the terms indicated in equation (45)⁸⁵

$$\begin{aligned} \mathcal{H} = & - \sum_{i=1}^n J_{ex,i} \hat{S}_i \hat{S}_{i+1} - \sum_{i=1}^n \alpha_{ri} \lambda_i \hat{L}_i \hat{S}_i + \sum_{i=1}^n \Delta_{ax,i} \left[\hat{L}_{zi}^2 - \frac{2}{3} \right] \\ & + \mu_B H \sum_{i=1}^n (-\alpha_{ri} \hat{L}_i + g_e \hat{S}_i) \end{aligned} \quad (45)$$

in which the first term represents the isotropic exchange between the different Co(II) sites, the second term is the spin-orbit coupling, the third term treats the deviation from the ideal octahedron and the last term describes the Zeeman interaction in the presence of a magnetic field. A relevant point in the approximations by Lloret is the application of the magnetic coupling described by J_{ex} solely to the ground Kramers doublet of each interacting ion. The magnetic interaction in the excited doublets is ruled out and the magnetic properties are those of magnetically isolated ions, described by the $G(T)$ function. Furthermore, the contributions

from the excited levels on the magnetic properties of the ground doublet are accounted for by using a perturbational approach.

It can be shown that the Landé factor of the ground doublet is strongly anisotropic as expected in non-cubic symmetries and it depends both on the magnetic properties of the single Co(II) ions and on the strength of the exchange coupling. Thus, for polynuclear complexes, the $G(T)$ function has to be replaced by a function $G(T, J_{ex})$:⁸⁵

$$G(T, J_{ex}) = G(T) + \frac{n}{2} \Delta g P_0 \quad (46)$$

where n is the average number of Co(II)-Co(II) interactions of each Co(II) ion, e.g. $n = 1$ for dimers. Δg is the difference between the g -values parallel and perpendicular to the molecular z axis

$$\Delta g = -\frac{100J_{ex}}{81\alpha_r\lambda} (\alpha_r + 2) \quad (47)$$

and P_0 is a population factor given by

$$P_0 = \frac{e^{\left(\frac{-4\alpha\lambda}{k_B T}\right)}}{3 + 2e^{\left(\frac{-5\alpha\lambda}{2k_B T}\right)} + e^{\left(\frac{-4\alpha\lambda}{k_B T}\right)}} \quad (48)$$

The molar susceptibility is then calculated by using equation (37) where $g(T)$ is replaced by $G(T, J_{ex})$. The advantage of this model lies in the fact that it is not restricted to a given sign of Δ_{ax} and reasonable agreement between experiment and simulation can be achieved for both cases.⁸⁵

2.3.2 Tetrahedrally Coordinated Co(II)

The basic concepts for the description of the electronic structure of octahedral Co(II) compounds introduced in section 2.3.1 can now be adapted to tetrahedral systems. In tetrahedral symmetry, the splitting of the d-orbitals is reversed compared to octahedral symmetry, i.e. the e orbitals are lower in energy than the t_2 orbitals. Since they do not point exactly towards the ligating atoms, the energy separation $10 Dq$ is generally smaller than for octahedral symmetry with $|Dq(\text{tetrahedron})| \approx |-4/9 Dq(\text{octahedron})|$.⁷⁶ According to the

different possibilities of orbital populations, the 4F free ion ground term splits up into the terms $^4A_2(F)$, $^4T_2(F)$ and $^4T_1(F)$ in order of ascending energy.

Because of the orbitally non-degenerate 4A_2 ground term, tetrahedrally coordinated Co(II) is a typical ZFS system, where orbital contributions to the magnetic properties due to admixing of excited states manifest themselves in large g -values.⁴⁴ Neglecting configurational interactions, the energies of the terms arising from the 4F free ion term can be estimated by equations (31a) – (31c) taking negative signs.⁷⁵ Thus, the resulting relative energies are given by $E(^4A_2) = 0$, $E(^4T_2) = 10 Dq$ and $E(^4T_1) = 18 Dq$. A graphical illustration is provided by the Tanabe-Sugano diagram in Figure 13, noting that the diagram for d^7 configuration in tetrahedral environment is the same as for d^3 in octahedral symmetry due to the reversed splitting patterns in tetrahedral and octahedral crystal fields.

Symmetry reduction to D_{2d} leads to further splittings of the degenerate terms, e.g. the excited terms $^4T_2(F)$ and $^4T_1(F)$ split into $^4B_2 + ^4E$ and $^4A_2 + ^4E$, respectively, whereas the ground state transforms as 4B_1 . The corresponding relative energies can be expressed in terms of the crystal field parameters defined by Ballhausen and are listed in Table A 7 in the appendix.⁷⁵

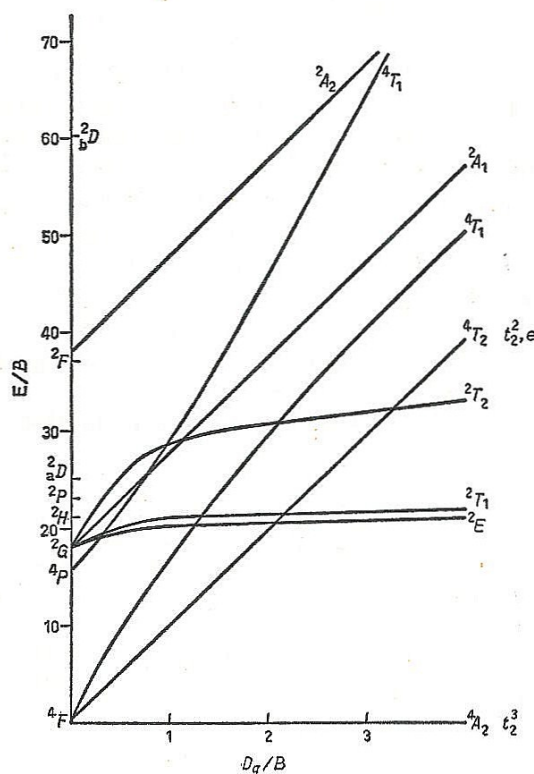


Figure 13: Tanabe-Sugano diagram for d^3 ions in an octahedral field ($C = 4.5 B$). This image was published in Lever, A. B. P. *Inorganic Electronic Spectroscopy*, Copyright Elsevier (1968).⁷⁵

In addition to these symmetry-related energy level splittings, second-order spin-orbit coupling will split the states, leading to a zero-field-splitting of the 4B_1 ground state given by $2D$, with D being the axial ZFS parameter introduced in section 2.1.1. The value of D strongly depends on the energy separation between the ground state and the lowest excited states and can be estimated by equation (49) which is based on perturbation theory.⁴⁴

$$D = 4\lambda^2 \left[\frac{1}{E({}^4E)} - \frac{1}{E({}^4B_2)} \right] \quad (49)$$

Equation (49) clearly shows that large negative ZFS parameters are only obtained if 4B_2 lies lower in energy than 4E and if there is a large energy separation between them. In other words, designing pseudo-tetrahedral Co(II) based single-ion magnets with large energy barriers requires axial crystal fields with high values of the crystal field parameter Dt . Indeed, fourfold coordinated Co(II) complexes with rather high energy barriers have been reported.^{28,86-92}

2.4 Experimental Methods for Studying SMMs

2.4.1 Magnetometry

SQUID magnetometry (SQUID: Superconducting Quantum Interference Device) is by far the most common method for studying single-molecule magnets.^{3,65} A direct current (dc) SQUID experiment allows the investigation of the static magnetic properties: The sample is magnetized by an external static magnetic field while being moved up and down in a system of superconducting coils. The thereby induced current is proportional to the magnetization of the sample and with the help of the SQUID element this current is converted to a voltage. Calibration is usually performed using a palladium reference sample and allows the direct output of the sample magnetization.

The magnetization is defined as the change of energy with respect to the magnetic field²

$$M = -\frac{\partial E}{\partial H} \quad (50)$$

whereas the magnetic susceptibility is the change of the magnetization with respect to the field, i.e. the second derivative of the energy. At weak fields, a linear dependence is observed and the susceptibility is in good approximation given by the ratio of the magnetization and the magnetic field.²

$$\chi = \frac{\partial M}{\partial H} \approx \frac{M}{H} \quad (51)$$

The susceptibility contains a positive paramagnetic part due to the presence of unpaired electrons and a negative diamagnetic part, which is due to the movement of paired electrons:²

$$\chi_{total} = \chi_{dia} + \chi_{para} \quad (52)$$

Since they cannot be measured independently, the molar diamagnetic susceptibility $\chi_{m,dia}$ is commonly estimated with the help of the empirically determined Pascal's constants⁹³ or simply by $\chi_{m,dia} = -\frac{MM}{2} \cdot 10^{-6} \text{ cm}^3 \text{ mol}^{-1}$, where MM is the molar weight of the sample. According to Curie's law, the molar paramagnetic susceptibility is given by^{2,3,65}

$$\chi_m = \frac{g^2 \mu_B^2}{3k_B T} S(S+1) \quad (53a)$$

resulting in a horizontal line in the χT vs. T plot, as demonstrated in Figure 14 for an $S = 1/2$ system. In the case of lanthanides, S has to be replaced by J and g denotes the theoretical g -value g_J .⁶⁵

$$g_J = 1 + \frac{J(J+1) + S(S+1) - L(L+1)}{2J(J+1)} \quad (53b)$$

However, equation (53) is only valid for isotropic, thermally isolated electronic ground states. If zero-field splitting or crystal field splitting contribute to the magnetic properties, the depopulation of excited M_S , m_S or m_J states will cause a decrease in χT at low temperatures. In the presence of exchange coupling, minima or maxima will be observed and the positions of these extrema depend on the coupling strengths and the ground state spins (Figure 14).

In addition to the temperature dependent measurements yielding information about the microstate level structure, field dependent measurements at low temperatures are of great interest, since they provide information about the composition of the ground state. At low temperatures and high fields only the lowest lying Zeeman level will become populated and the magnetization will saturate.

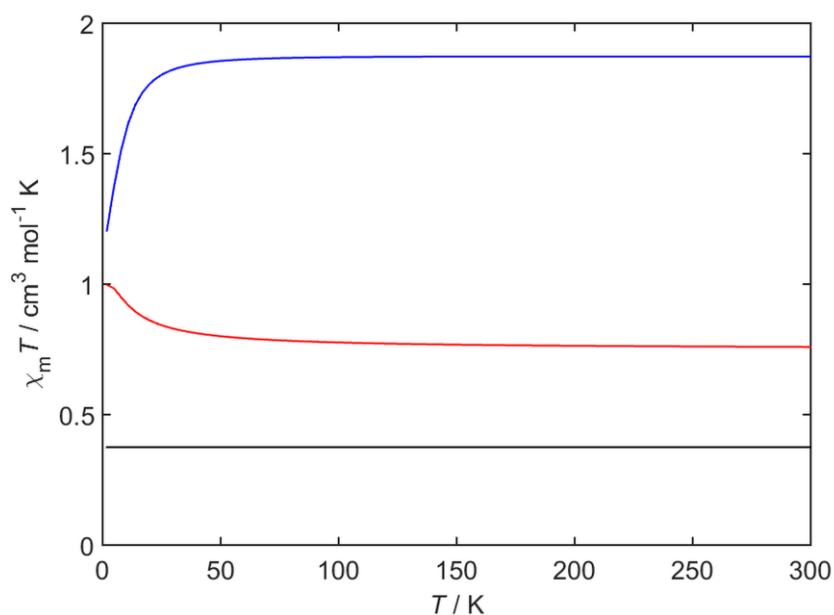


Figure 14: Examples of the temperature-dependence of the molar paramagnetic susceptibility. Black: Simulation for $S = 1/2$ and $g = 2$. Red: Simulation for an exchange-coupled system of two $S = 1/2$ ions with $g = 2$ and $J_{\text{ex}} = 10 \text{ cm}^{-1}$. Blue: Simulation for $S = 3/2$ with $g = 2$ and a negative ZFS parameter $D = -10 \text{ cm}^{-1}$.

The saturation behavior strongly depends on the ground state spin as well as on the zero-field splitting parameters or the crystal field parameters. Furthermore, the observation of hysteresis in a field dependent magnetization loop is of course proof of magnetic bistability.

The dynamic magnetic properties of SMMs are usually probed by alternating current (ac) SQUID magnetometric measurements, where the sample is exposed to an oscillating magnetic field.³ In the presence of an energy barrier, the sample magnetization is not able to follow the fast field oscillations and an out-of-phase component of the magnetic susceptibility will be observed:

$$\chi_{ac} = \chi' - i\chi'' \quad (54)$$

where χ' and χ'' denote the in-phase and the out-of-phase components, respectively. A temperature dependent maximum in χ'' is observed when the relaxation time corresponds to the angular frequency ω of the oscillating magnetic field, i.e.

$$\omega\tau = 1 \quad (55)$$

Thus, relaxation times can be determined by temperature and frequency dependent ac magnetometric measurements. A very convenient way is the generation of so-called Argand diagrams³, where χ'' is plotted against χ' resulting in semi-circularly shaped plots. The experimental data can then be fitted to modified Debye functions of the form^{3,94}

$$\chi' = \frac{(\chi_0 - \chi_\infty)[1 + (\omega\tau)^{1-\alpha} \sin \frac{\alpha\pi}{2}]}{1 + 2(\omega\tau)^{1-\alpha} \sin \frac{\alpha\pi}{2} + (\omega\tau)^{2(1-\alpha)}} + \chi_\infty \quad (56a)$$

$$\chi'' = \frac{(\chi_0 - \chi_\infty)[(\omega\tau)^{1-\alpha} \cos \frac{\alpha\pi}{2}]}{1 + 2(\omega\tau)^{1-\alpha} \sin \frac{\alpha\pi}{2} + (\omega\tau)^{2(1-\alpha)}} \quad (56b)$$

where χ_0 and χ_∞ are the isothermal and adiabatic susceptibilities, i.e. the x-intercepts in the Argand plots and α describes the distribution of relaxation times, i.e. the widths of the semi-circles. Based on the relaxation times, the contributing relaxation mechanisms and the effective energy barrier can be determined by analyzing the resulting Arrhenius plot.

However, although SQUID magnetometry is definitely a very useful method, it is usually not sufficient for the complete electronic structure analysis of low-symmetry

compounds since the high number of parameters required for their description inevitably leads to over-parametrization. Thus, magnetometry needs to be complemented by spectroscopic techniques, e.g. EPR, FIR or optical spectroscopy.

2.4.2 EPR Spectroscopy

In the presence of an external magnetic field, the remaining degeneracies of the microstates will be lifted due to the Zeeman interaction. The corresponding Hamiltonian has been already introduced in section 2.1.1. In an EPR experiment (EPR: Electron Paramagnetic Resonance)^{38,95} transitions between these Zeeman sublevels are induced by the irradiation of microwaves. Commonly, spectra are recorded at a constant microwave frequency by sweeping the magnetic field (continuous wave EPR) and the signals are obtained as the first derivative of the absorption bands. Other experimental techniques include for example frequency domain magnetic resonance (FDMR) where the magnetic field is kept constant and the frequency is varied, or pulsed methods. A signal is obtained when the resonance condition

$$\Delta E = h\nu = g\mu_B\Delta m_S B \quad (57)$$

is fulfilled, where Δm_S has to be replaced by Δm_J for lanthanides or by ΔM_S for exchange-coupled spin-only systems. Since EPR transitions are magnetic dipole transitions, the selection rule is given by $\Delta m_S = \pm 1$. This selection rule is relaxed for low-symmetry compounds where state-mixing occurs and as a result, m_S (m_J , M_S) is no good quantum number anymore. Due to magnetic anisotropy the g -value shows an orientation dependence, which gives rise to up to three lines in the spectra. However, not only g -value anisotropy leads to the observation of more than one line, also hyperfine coupling to nuclear spins, weak exchange coupling or zero-field splitting can cause additional signals. For instance, if the zero-field splitting lies in the range accessible by the applied microwave frequency, transitions between the Zeeman sublevels of different Kramers doublets might be observed. In order to distinguish between the signals of different nature, it is useful to compare spectra recorded at different microwave frequencies. g -value anisotropy will be resolved much better at higher frequencies while signals due to zero-field splitting will result in a non-zero y -intercept in a plot of microwave frequency vs. resonance field. Thus, multi-frequency EPR is a powerful tool not only for the accurate determination of the g -values of the ground Kramers doublet, but it might also give information about low lying excited states.

2.4.3 FIR Spectroscopy

The far-infrared (FIR) region of the electromagnetic spectrum ranges from about 10 to 700 cm^{-1} , making FIR spectroscopy a powerful tool for the investigation of zero-field splittings (3d single-ion magnets) or crystal field splittings (lanthanide-based single-ion magnets) within the electronic ground term.^{44,96,97} The selection rule is the same as for EPR spectroscopy and similarly it is relaxed by the mixing of states in low-symmetry compounds. An important aspect concerning FIR spectroscopy is the occurrence of low-energy vibrations in the same range as the studied zero-field splittings or crystal field splittings, which complicates the recorded spectra. In order to distinguish between these vibrational transitions and the transitions of interest, it is thus useful to record the spectra in the presence of magnetic fields with different field strengths. While transitions due to vibrations will not be strongly affected by the magnetic field, the transitions due to zero-field splitting or crystal field splitting will shift depending on the magnetic field strength. Normalizing the spectra by dividing them by the spectrum at highest magnetic field then allows their assignment. Although vibronic coupling can still lead to a splitting pattern of the ZFS or crystal field based signals, normalized FIR spectra allow a much more accurate determination of the zero-field splitting or the energies of the crystal field states compared to e.g. SQUID magnetometry. Whenever it is possible, FIR spectroscopy should thus be applied to complement magnetometry or EPR spectroscopy.

2.4.4 Optical Spectroscopy

The term optical spectroscopy usually includes spectroscopic methods operating with excitation wavelengths in the near-infrared, visible and ultra-violet regions of the electromagnetic spectrum, i.e. ranging from about 5000 to 50000 cm^{-1} . Absorption of optical photons induces transitions to states arising from excited free-ion terms, called d-d- or f-f-transitions. If the spectra are recorded at low temperatures with sufficient resolution, they provide important information about the electronic level structure. Transitions may occur through magnetic dipole, electric dipole or electric quadrupole mechanisms.^{75,98} The majority of optical transitions are electric dipole transitions, but magnetic dipole transitions are also frequently observed in the optical spectra of lanthanide compounds. For magnetic dipole transitions, the selection rules are given by $\Delta J = 0, \pm 1$; $\Delta L = 0$; $\Delta S = 0$ and $\Delta m_S (\Delta m_J) = \pm 1$ (compare EPR and FIR spectroscopy).⁹⁸ Generally, the selection rules follow from the transition dipole moment, which has to be non-zero:

$$\langle \psi_a | \hat{\mu} | \psi_b \rangle \neq 0 \quad (58)$$

ψ_a and ψ_b are the wave functions of the initial and final states and $\hat{\mu}$ denotes the dipole moment operator. Non-zero values of the transition dipole moment are only possible if the direct product of the group theoretical representations of the initial and final wave functions with the particular dipole moment operator contains the totally symmetric representation, e.g. A_{1g} .⁷⁵ Concerning electric dipole transitions, the components $\hat{\mu}_x$, $\hat{\mu}_y$ and $\hat{\mu}_z$ of the electric dipole moment operator transform as translations, therefore having an ungerade parity. Allowed transitions thus require that the direct product of the representations of the wave functions involved is odd, which is only possible if $\Delta l = \pm 1$. It immediately follows that d-d- and f-f-transitions are parity forbidden. A similar argumentation taking into account the orthogonality of spin states leads to the spin selection rule $\Delta S = 0$.⁷⁵

However, in spite of the forbidden character of d-d and f-f-transitions, non-zero intensities are observed in experimental spectra. This phenomenon can be explained by any mechanism which permanently or temporarily removes inversion symmetry.⁷⁵ One of the most important mechanisms is the temporary removal of the symmetry center by vibronic coupling, meaning that electronic transitions occur with simultaneous excitation of ungerade vibrational modes.^{60,75,98} Vibronic coupling manifests itself in the observation of vibrational fine structures in the observed signals, thus complicating the interpretation of experimental spectra.⁶⁰ Besides vibronic coupling, permanent symmetry reductions by the coordination of the ligands can lead to relaxation of the parity selection rule. If the molecule does not show a center of symmetry, it is not appropriate to talk about orbitals being even or odd to inversion.⁷⁵ Taking D_{2d} symmetry as an example, a transition from B_2 to E will be allowed in x- and y-direction.

A very important theory explaining the observed intensities in optical spectra of lanthanide compounds was independently derived by both Judd and Ofelt.⁹⁸⁻¹⁰⁰ The basic idea is that the intensity of so-called induced electric dipole transitions arises from the admixing of states of opposite parity (e.g. $4f^{N-1}n'd^1$) into the $4f^N$ ground state. This is only possible in non-centrosymmetric compounds where odd crystal field parameters B_{kq} appear ($k = 1, 3, 5, 7$) and can be explained by the integer perimeter rule concerning the 3j-symbol given in equation (14), i.e. $l + k + l'$ with $l' = l \pm 1$ has to be an integer. According to the Judd-Ofelt theory, the following relaxed selection rules for induced electric dipole transitions are obtained: $\Delta S = 0$, $\Delta L \leq 6$, $\Delta J \leq 6$ and $\Delta m_J = -(\rho + q)$, where ρ represents the light

polarization, i.e. $\rho = +1$ for right circularly polarized light and $\rho = -1$ for left circularly polarized light.⁹⁸

Having mentioned the mechanisms accounting for the intensity of d-d- or f-f-transitions, which are the same for the different optical techniques, it is now important to distinguish between luminescence, electronic absorption and magnetic circular dichroism spectroscopy.

Luminescence spectroscopy can be seen as complementary to FIR spectroscopy, since it allows the determination of the level structure within the electronic ground term. In a luminescence experiment the irradiation of light leads to the population of an excited state which can be either a state within the $3d^N$ or $4f^N$ configuration or an excited state of the ligand. If electrons of the ligands are excited, one can make use of the so-called antenna effect, meaning that the excitation is followed by an energy transfer from the ligand to the metal ion.^{101,102} After successful excitation, the system will return to the ground state by emission of radiation which can be detected perpendicular to the excitation light beam. According to Kasha's rule¹⁰³, considerable emission takes only place from the lowest microstate of an excited term and experimentally observed splitting patterns of the signals thus correspond to the level structure (e.g. crystal field levels) of the ground term. Of course vibronic coupling might lead to additional signals, shoulders or line-broadening and complicates the interpretation of the experimental spectra. Another issue is the existence of efficient quenching mechanism, e.g. energy can be taken up very efficiently by OH-vibrations leading to non-radiative deactivation.^{101,102}

The counterpart to luminescence is electronic absorption spectroscopy. If the spectra are recorded at very low temperatures, only the lowest lying state will be populated and from there the absorption of radiation will lead to population of the microstates within the excited electronic terms. Thus, the observed splitting patterns of the detected absorption bands correspond to the crystal field splittings of the excited terms. The excited term crystal field splittings can then serve to determine the corresponding crystal field parameters, which in turn provide information about the electronic ground state.⁶⁰

In addition to luminescence and electronic absorption spectroscopy, magnetic circular dichroism (MCD) spectroscopy^{104,105} is a very powerful optical method for the investigation of single-molecule magnets. In an MCD-spectrum, the absorption difference of left and right circularly polarized light (abbreviated as lcp and rcp) is recorded, but in contrast to conventional circular dichroism (CD) spectroscopy, MCD-measurements are performed in the presence of a magnetic field applied parallel to the excitation light beam. Due to the Faraday

effect¹⁰⁶, which states that all substances in a longitudinal magnetic field show optical activity caused by circular birefringence, MCD-spectroscopy is not restricted to chiral compounds. The different absorption of lcp and rcp by the magnetized sample leads to elliptical polarization and the MCD signal is defined by

$$MCD \equiv \Delta A = A(lcp) - A(rcp) - \text{natural } CD \quad (59)$$

with ΔA being the differential absorption, $A(lcp)$ and $A(rcp)$ being the absorption of lcp and rcp and *natural CD* designating the zero-field dichroism of chiral samples. The differential absorption is related to the ellipticity θ by a simple conversion factor:

$$\theta = \Delta A \cdot 32980 \quad (60)$$

One of the great advantages of MCD-spectroscopy immediately follows from equation (59): Since ΔA is a signed quantity, MCD-spectra often provide a much better resolution compared to conventional electronic absorption spectroscopy. Another advantage lies in the enhanced intensity of intra-configurational d-d- and f-f-transitions compared to e.g. intra-ligand or charge-transfer transitions, allowing their identification. Similarly to electronic absorption, MCD-spectroscopy at low temperatures allows the determination of excited term crystal field splittings, but dependent on the nature of the states involved, different signal shapes can be observed.¹⁰⁷ The general MCD-expression^{104,105} is provided in equation (61)

$$\frac{\Delta A}{E} = \gamma \mu_B B \left[A_1 \left(-\frac{\partial f(E)}{\partial E} \right) + \left(B_0 + \frac{C_0}{k_B T} \right) f(E) \right] \quad (61)$$

where γ is a collection of spectroscopic constants and $f(E)$ is a line-shape function, e.g. a Gaussian. A_1 , B_0 and C_0 represent the so-called MCD terms: An A-term is observed if degenerate states are involved in the transition. If a magnetic field is applied, the degeneracy is lifted and lcp and rcp will be absorbed at different energies, as illustrated in Figure 15 for the simple example of a transition from a non-degenerate ¹S state to an orbitally threefold degenerate ¹P term. A-terms manifest themselves as temperature-independent derivative shaped signals. B-terms arise from the field-induced mixing of the zero-field eigenfunctions. Since this is a second-order effect, B-terms usually show rather weak absorption-like signals (Figure 15). C-terms are the greatest source of information concerning MCD spectroscopy on single-molecule magnets.

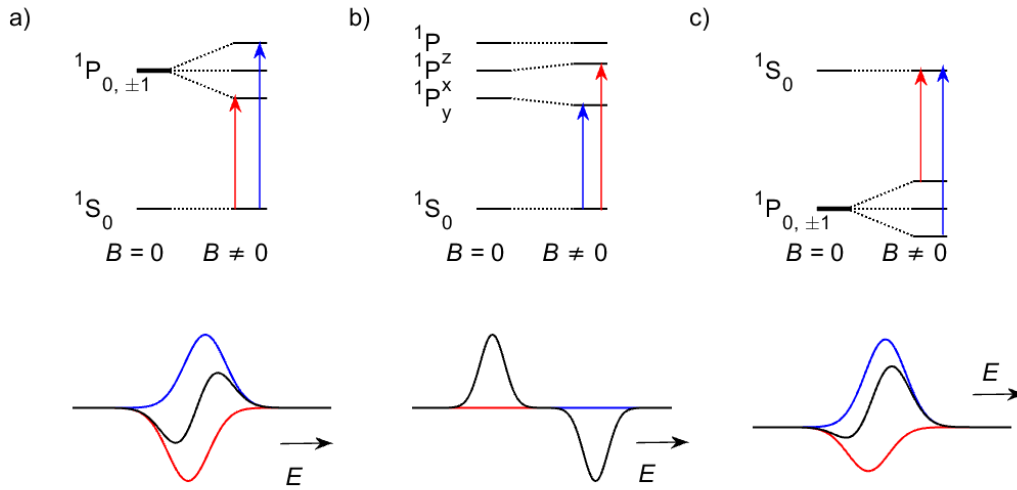


Figure 15: Schematic illustration of different MCD terms. a) Faraday A-term due to a degenerate excited state. b) Faraday B-term due to field-induced mixing of states. c) Faraday C-term due to a degenerate ground state. Blue lines represent the absorption of lcp and red lines represent the absorption of rcp.^{104,105}

They occur due to the Zeeman splitting of degenerate ground states and according to the Boltzmann equilibrium among the Zeeman sublevels, they show pronounced temperature dependence (Figure 15). The shape of C-terms is asymmetric absorption-like.

At low temperatures, C-terms dominate the MCD-spectra of paramagnetic metal complexes and their temperature and field dependence provide information about the electronic ground state. Thus, MCD-spectroscopy links the benefits of electronic absorption and EPR-spectroscopy since it allows the simultaneous investigation of electronic ground and excited states. Ground state properties are usually investigated by variable temperature and variable field experiments on C-terms (VTVH-MCD spectroscopy), where the wavelength of the excitation light is kept constant at the signal maximum while the field and the temperature are varied. The recorded VTVH isotherms are comparable to SQUID magnetometric magnetization curves: At low fields, the intensity increases linearly with the field. At intermediate fields, the intensity starts to level off and at high fields, saturation is observed. The saturation behavior depends on the ground state properties, e.g. the g -values and the ZFS parameters. A general expression for the analysis of VTVH curves for typical ZFS systems has been derived by Solomon and Neese¹⁰⁸:

$$\frac{\Delta\epsilon_{av}}{E} = \frac{\gamma}{4\pi S} \int_0^\pi \int_0^{2\pi} \sum_i N_i (l_x \langle S_x \rangle_i M_{yz} + l_y \langle S_y \rangle_i M_{xz} + l_z \langle S_z \rangle_i M_{xy}) \sin\theta d\theta d\phi \quad (62)$$

where the summation is performed over all levels i of the ground state. $\Delta\epsilon_{av}$ is the orientation-averaged difference of the extinction coefficients for lcp and rcp, N_i is the Boltzmann population of the i^{th} sublevel, $\langle S_p \rangle$ with $p = x, y, z$ are the spin expectation values, l_p are direction cosines and M_{pp} are effective polarization products.

It has been shown that the MCD saturation behavior is a weak function of the ratio E/D but a strong function of the sign of D and moderately sensitive to the value of D . Furthermore, it strongly depends on the polarization of the transition under study. In case of systems with large axial zero-field splittings, the ground state can be treated within the effective spin-1/2 approximation and equation (62) simplifies to¹⁰⁸

$$\frac{\Delta\epsilon_{av}}{E} = -\frac{\gamma}{4\pi} \int_{\theta} \int_{\phi} \tanh\left(\frac{g\mu_B B}{2k_B T}\right) \frac{\sin\theta}{g} (l_x^2 g_x M_{yz}^{eff} + l_y^2 g_y M_{xz}^{eff} + l_z^2 g_z M_{xy}^{eff}) d\theta d\phi \quad (63)$$

where the g_p are effective g -values and g is given by $g = (G_x + G_y + G_z)$ with $G_p = l_p g_p$. Due to the strong dependence of the MCD C-term intensity on the polarization of a given transition, one more advantage of MCD is the possibility to obtain orientation-dependent information even by studying frozen solutions or mulls with randomly oriented molecules. For instance, magnetic bistability might be probed by recording MCD-detected magnetic hysteresis curves of only a subset of excited molecules, e.g. those with their molecular z -axis oriented parallel to the magnetic field.

3 Aim of this Work

Lanthanide and cobalt complexes belong to the most promising candidates for improved single-molecule magnets and a lot of research activity is focused on the synthesis of new compounds.^{9,11,22,23,28,37,66} However, SMMs are still far from practical application. The reasons are for example the lack of rational design criteria and the interplay of several relaxation mechanisms, which have not yet been fully understood. The general aim of this work is therefore the comprehensive magnetic and spectroscopic investigation of molecular lanthanide and cobalt compounds in order to gain deeper insight into the correlation between the molecular as well as the electronic structure and the magnetic properties. Besides magnetometry, which is often the only tool employed for studying SMMs, a range of spectroscopic techniques including electron paramagnetic resonance, far-infrared spectroscopy and optical methods will serve to determine the electronic structures.

Since magnetic circular dichroism spectroscopy has been shown to be an outstanding tool for studying ground state as well as excited state properties,^{104,105,108-116} the first part of this work is concerned with the setup and characterization of a modern MCD-spectrometer allowing measurements at wavelengths ranging from the ultra-violet to the near-infrared region of the electromagnetic spectrum (200 – 2000 nm). This comparatively wide wavelength range allows gaining as much information as possible and to the best of my knowledge has rarely been realized up to now. The setup of the MCD-spectrometer not only involves choosing the main parts, i.e. the CD-spectrometer and the magnet, but also connecting these parts by appropriate optics and optomechanics. After successful installation, the spectrometer needs to be characterized, e.g. concerning the baseline, the signal calibration and the sensitivity. Especially the sensitivity is an interesting aspect because if it is high enough, MCD-spectroscopy could provide a possibility for studying orientation-dependent properties of SMM monolayers, which usually requires more sophisticated and less available methods. Once the MCD-spectrometer is operative, it will serve together with the other above-mentioned methods to study the chosen lanthanide and cobalt compounds.

Regarding the study of lanthanide compounds, isostructural molecular tetra-carbonates of dysprosium and erbium with the general formula $[C(NH_2)_3]_5[Ln(CO_3)_4] \cdot 11 H_2O$ ($Ln = Er, Dy$; **1-Er** and **1-Dy**)^{26,27} were chosen. In addition to the potential SIM behavior, this choice is mainly based on the colorlessness of the carbonate ligands, which allows for the detection of optical f-f-transitions without disturbing intra-ligand transitions. Another criterion is the facile

and literature-known synthesis as well as the stability of the compounds. After successful synthesis and structural characterization, this subproject aims for probing and understanding the SIM behavior by performing detailed magnetometric and spectroscopic studies. Although optical spectroscopy is a well-established and extremely useful tool for the electronic structure determination of lanthanide compounds,^{60,117} it is not yet a standard method for studying single-ion magnets. Instead, it is still quite common to perform only magnetometric measurements, frequently combined with ab initio calculations. Magnetometry is definitely essential while ab initio calculations might be suitable to obtain a first idea about the electronic ground state but they are not sufficient for a full understanding. The community has realized more and more this fact and spectroscopic methods have been called for in recent SMM-related literature.^{66,67} Thus, the detailed spectroscopic studies in this work are aimed to progress clearly beyond what has ever been done before regarding the electronic structure determination of lanthanide based SIMs. Furthermore, this work is intended to provide a recipe for the reliable determination of crystal field parameters for low-symmetry compounds and to show which difficulties may arise.

Another subproject of this work is concerned with the investigation of Co(II) complexes. The studied Co(II) complexes can be divided into two groups. The first group involves the distorted tetrahedrally coordinated complexes $(\text{HNet}_3)_2[\text{Co}^{\text{II}}(\text{L}^1)_2]$ (**(HNet₃)₂2**) and $(\text{NMe}_4)_2[\text{Co}^{\text{II}}(\text{L}^1)_2]$ (**(NMe₄)₂2**) with $\text{H}_2\text{L}^1 = 1,2\text{-bis(methanesulfonamido)benzene}$. The strong axial distortion compared to regular tetrahedrons displayed by these complexes makes them interesting candidates for SIMs. Thus, the performance as SIMs will be probed by magnetometric measurements and the observations will be explained by the analysis of spectroscopic results. Based on these results, design criteria for improved Co(II)-based SIMs will be confirmed and complemented. In this regard, special attention is focused on the development of realistic design criteria, meaning that they can be applied without too much synthetic effort and that stable complexes are obtained, which can be handled in air. Only such design criteria can lead to practically applicable compounds and this work is intended to provide an important contribution towards this objective.

The second group of cobalt compounds investigated in this work are dimers of octahedrally coordinated cobalt centers bridged by quinone-based bridging ligands, where one or more oxygen donors of 2,5-dihydroxy-1,4-benzoquinone are substituted by isoelectronic [NR] groups. Substitution of two oxygen donors leads to symmetric bridges while the substitution of only one oxygen donor results in an unsymmetrical bridging situation. Two symmetrically bridged dimers, namely $[\{(\text{tmpa})\text{Co}^{\text{II}}\}_2(\mu\text{-L}^2)][\text{BF}_4]_2$ (**3[BF₄]₂**) and

[{(tmpa)Co^{II}}₂(μ-L³)] [BPh₄]₂ (**4**[BPh₄]₂) as well as the unsymmetrically bridged dimer [(tmpa)Co^{II}}₂(μ-L⁴)] [OTf]₂ (**5**[OTf]₂) are studied with H₂L² = 2,5-di-[2-(methoxy)-anilino]-1,4-benzoquinone, H₂L³ = 2,5-di-[2-(trifluoromethyl)-anilino]-1,4-benzoquinone and H₂L⁴ = 2-[4-(isopropyl)-anilino]-5-hydroxy-1,4-benzoquinone. Tris(2-pyridylmethyl)amine (tmpa) serves as a co-ligand. Concerning these dimers, the focus lies on the study of the nature of the exchange coupling, especially by means of SQUID magnetometry and EPR spectroscopy. Depending on the variation of the bridging ligand or the substituting groups, ferromagnetic or antiferromagnetic coupling might be observed. For single-molecule magnets ferromagnetic coupling combined with a large anisotropy is preferred and finding magnetostructural correlations is a prevailing goal concerning Co(II) based SMMs.¹¹⁸ Another very interesting property of quinonoid-bridged dicobalt complexes is the possible observation of valence tautomerism due to the potential non-innocent behavior of the bridging ligands.³⁵ This means that oxidation of one of the Co(II) centers may lead to a redox-induced electron transfer from the second Co(II) center to the bridging ligand, resulting in a radical bridge between two diamagnetic Co(III) centers. Valence tautomeric equilibria have been shown for several dicobalt complexes and provide a possibility for switching the magnetic properties by external stimuli like temperature, light irradiation or pressure.^{35,119,120} Therefore, the study of quinonoid-bridged cobalt complexes in this project not only involves the determination of the exchange coupling but also probing the presence of valence tautomeric phenomena.

4 Results and Discussion

4.1 Design and Setup of the MCD-Spectrometer

4.1.1 General Considerations

Typically, a MCD-spectrometer operating in the visible region of the electromagnetic spectrum consists of a conventional CD-spectrometer equipped with a magnet.^{105,121} A principle scheme of the experimental single-beam setup is presented in Figure 16. The CD-spectrometer contains the light source, the monochromator, the polarizer for generating linearly polarized light, the photoelastic modulator (PEM) for the generation of circularly polarized light and the detector. The detector compartment needs to be detachable since the magnet has to be placed in front of it. The magnet provides a magnetic field parallel to the direction of light propagation and the studied sample is positioned in the center of this magnetic field. Preventing disturbing interactions between the electronics or the magnetic parts of the spectrometer and the magnetic field requires a sufficient distance depending on the stray field of the magnet. With the help of appropriate optics and optomechanics, the circularly polarized light produced by the spectrometer is focused onto the optically transparent sample, where differential absorption of lcp and rcp takes place. The resulting elliptically polarized light then needs to be refocused onto the detector, e.g. a photomultiplier (PMT) for the visible range.

In the following sections, the different parts of the MCD-spectrometer built up in this work will be described, followed by its characterization concerning the baseline, the signal calibration and the sensitivity.

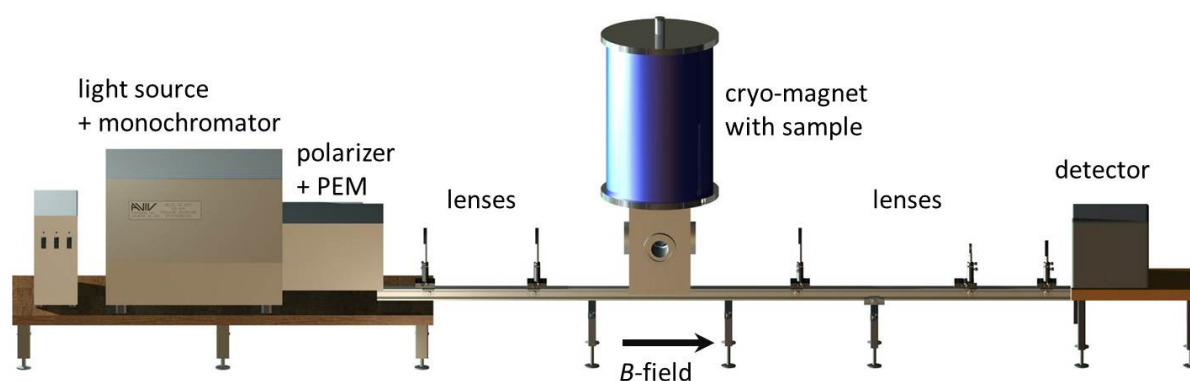


Figure 16: Schematic representation of the experimental single-beam MCD-setup. Drawn with the help of Jan Vaverka (ERASMUS student, February – August 2015), using the Autodesk 3D-CAD-Software Inventor®.

4.1.2 The CD-Spectrometer

The CD-spectrometer utilized in this work is an Aviv Model 42 Spectrometer manufactured by Aviv® biomedical, inc. It allows time- and wavelength dependent CD-measurements in a wide wavelength range (200 – 2000 nm) with an excellent resolution of up to 0.1 nm.

The light source is a commercially available tungsten halogen low-voltage lamp (OSRAM HLX 64663) with a nominal voltage of 36 V and a nominal wattage of 400 W. The luminous flux is 16200 lm and the color temperature is 3250 K. According to Planck's law for black body radiation^{122,123}, this color temperature corresponds to a maximum in spectral energy density $u(\lambda, T)$ at approximately 900 nm, as shown in Figure 17. At higher wavelengths, the spectral energy density slowly decreases while at lower wavelengths this decrease is much steeper. The light source is placed in a ventilated box at the backside of the spectrometer and a screw allows the adjustment of the height in order to optimize the light intensity reaching the sample (Figure 17).

The polychromatic light provided by the light source is guided to a Cary 14 double monochromator, which disperses the light into its individual wavelengths. It consists of a Czerny-Turner fused silica prism monochromator in series with a 600 lines/mm echelette grating. Figure 18 illustrates the arrangement of the optical elements: The radiation from the lamp enters the monochromator through the entrance slit, gets dispersed by the prism and the grating and the resulting monochromatic radiation leaves through the variable exit slit.¹²⁴ The prism-grating design not only improves wavelength resolution compared to single monochromators but also reduces stray light.

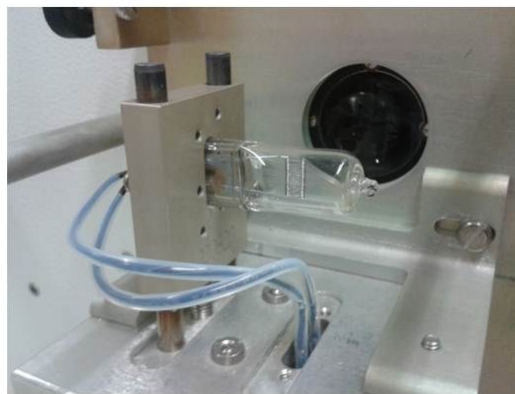
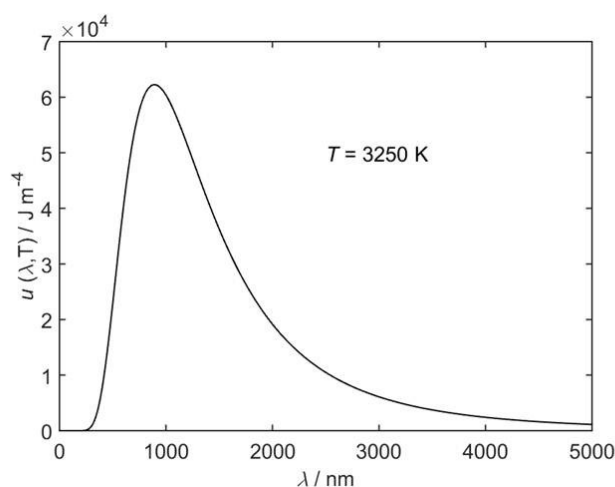


Figure 17: Left: Black body radiation spectrum at 3250 K. Around 200 nm, the energy density gets close to zero and determines the high energy limit of the spectrometer. Right: Photograph of the halogen low-voltage lamp used in the CD-spectrometer.

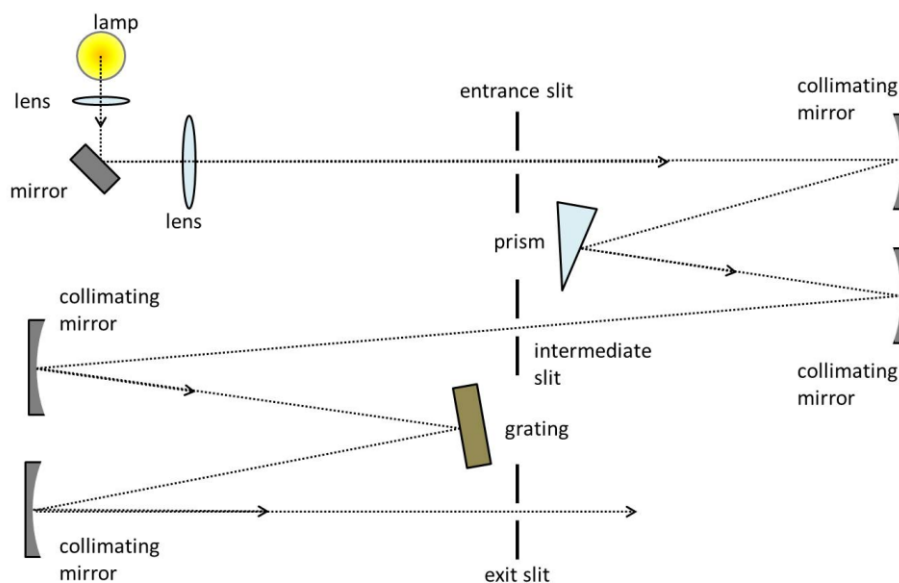


Figure 18: Arrangement of the optical elements in the prism-grating double monochromator.¹²⁴

While prisms suffer from light absorption of the glass leading to poor dispersion curves in the NIR, gratings exhibit more uniform dispersion curves. However, gratings show different orders of reflection besides the used first order. Due to second-order stray light at a given angle, multiples of the prime wavelengths may be reflected. One way to solve these issues is the combination of prisms and gratings: At long wavelengths, a prism does not separate the wavelengths efficiently anymore, but it eliminates second order stray light. The grating then provides the necessary spectral resolution.¹²¹

The dispersive elements are connected to a wavelength cam, which converts the non-linear dispersion into the linear motion of an external gear drive mechanism moved by a stepper motor. Each motor step corresponds to a wavelength change of 0.01 nm and thus sets the limit for wavelength specification. The wavelength repeatability is better than 0.05 nm in the entire wavelength range (typically 0.02 nm) and the spectral resolution is ca. 0.1 nm in most of the UV-Vis range. Due to the linear wavelength scale, only one point needs to be specified for wavelength calibration. The calibration wavelength corresponds to the position of an optical beam switch linked to the motion of the wavelength cam. More details about wavelength calibration will be given below. The monochromator slit widths contributing to the spectral bandwidth are controlled by a stepper motor, and a potentiometer on the drive senses the slit positions. The bandwidth can be chosen between 0.005 nm and 10 nm and in the constant bandwidth mode the spectrometer software converts the desired bandwidth to the corresponding slit width using a stored version of the monochromator dispersion function.

The slit height can be manually regulated using a knob adjusting a mask. This option allows optimizing the light intensity and the beam position on the sample.

After the monochromator, an achromatic lens and a Rochon polarizer generating linearly polarized light are placed. In the Aviv Model 42 CD Spectrometer, the Rochon polarizer consists of two optically connected prisms of single crystal magnesium fluoride. Magnesium fluoride was chosen because of its high and rather uniform transparency in the spectral range from 200 to 6000 nm,¹²⁵ making it an ideal material for the application in the desired MCD-spectrometer. It exhibits a tetragonal, i.e. uniaxial crystal system resulting in optical anisotropy. Due to different refractive indices along different axes, birefringence is observed whenever the light path is not parallel to the principal axis.^{121,126} A schematic illustration of the utilized Rochon polarizer is given in Figure 19.¹²⁷ The optical axes of the MgF₂ prisms are oriented perpendicular to each other, with one of them being parallel to the direction of light propagation. At the interface, double refraction occurs and the incident ray splits up into two separate beams with vertical and horizontal polarizations, i.e. the ordinary and extraordinary ray. While the ordinary beam passes straight through the polarizer, the extraordinary ray is refracted. The angular separation between the ordinary and the extraordinary ray is 5.1 degrees at 200 nm and 4.6 degrees at 546 nm.¹²⁷ For the CD- or MCD-measurements in this work, the extraordinary ray is discarded by a mask after the photoelastic modulator and only the ordinary ray is forwarded to the sample (single-beam setup).

As shown in Figure 20, the photoelastic modulator (PEM)¹²¹ is positioned after the Rochon polarizer and converts the linearly polarized light into circularly polarized light. The PEM consists of a metal plated crystalline quartz block, which acts as a large piezoelectric oscillator with a resonance frequency of 50 kHz.

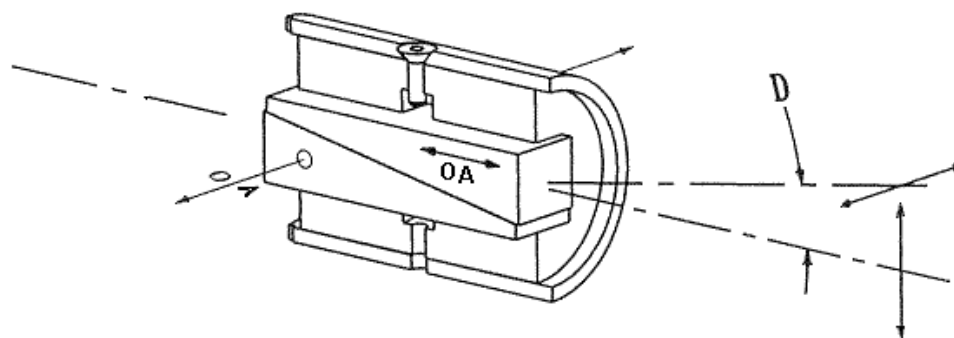


Figure 19: Schematic illustration of the MgF₂ Rochon polarizer utilized in the Aviv Model 42 CD Spectrometer. OA denotes the optical axes of the MgF₂ prisms and D denotes the angular separation between the ordinary and the extraordinary ray. Reprinted with permission from Karl Lambrecht Corporation, Chicago.¹²⁷

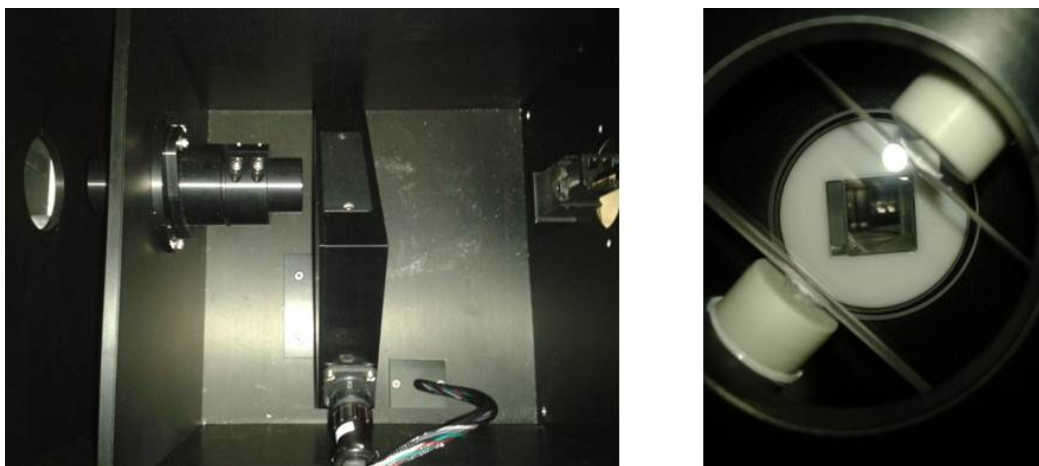


Figure 20: Left: Polarizer compartment containing an achromat, the Rochon polarizer and the photoelastic modulator. A cuvette holder behind the PEM allows conventional CD-measurements at room temperature. Right: View through the fused silica block of the PEM towards the polarizer.

At one end it is attached to a clear fused silica block where the light passes through. By applying a varying voltage to the metal plated part (1 V per 400 nm), a mechanical strain is induced, which is transferred as pressure waves to the fused silica block. The pressure waves cause birefringence in the usually optically isotropic fused silica, resulting in different refractive indices for light with vertical and horizontal polarizations. The PEM is mounted at a 45 degree angle relative to the linear polarization of the incident rays, i.e. relative to the PEM the incident light exhibits equal portions of vertical and horizontal polarization in phase with each other. Due to the strain-induced birefringence, the vertical and horizontal components traverse the glass at different rates, leading to a phase shift when the light emerges the PEM. Since the pressure waves are continuously passing back and forth through the fused silica block, the phase shifts periodically between +90 and -90 degrees resulting in alternatingly left and right circularly polarized light. Different conventions regarding the definition of lcp and rcp exist. The convention used throughout this work is demonstrated in Figure 21: Lcp corresponds to the case where the electric field vector rotates counter-clockwise when propagating towards the observer, while rcp corresponds to a clockwise rotation.¹²⁸ The periodically alternatingly left and right circularly polarized radiation passes the sample, which is either placed inside a cuvette behind the PEM (see Figure 20) for conventional CD-measurements at room temperature or inside a magnet for MCD-measurements.

Detection is carried out using a photomultiplier (PMT) for the UV and visible range and an indium gallium arsenide (InGaAs) photodiode for the NIR range. As shown in Figure 22, both detectors are placed in the detector compartment, which is detachable from the polarizer compartment in order to allow MCD measurements. A software controlled detector motor allows automatic detector crossover at a user specified wavelength.

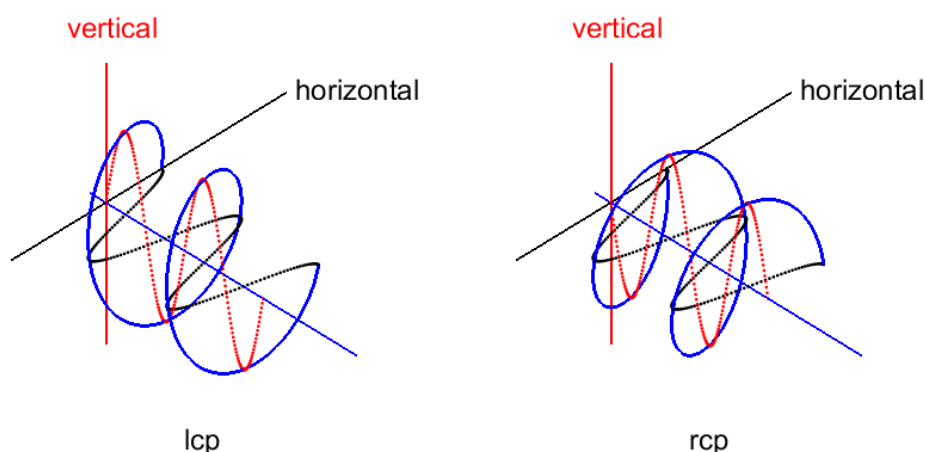


Figure 21: Definition of left and right circularly polarized light used throughout this work.

The PMT is a custom-built end window photomultiplier tube manufactured by Hamamatsu Photonics K.K. with an S20 response range from 190 to 870 nm. S20 is the spectral number and refers to multialkali photocathodes. During the CD-measurements an adjustable voltage is applied to the dynodes while the DC current induced by the photoelectric effect is held constant. This leads to increased sensitivity. The applied voltage is thus a measure for the light intensity reaching the detector, e.g. low light intensity due to absorption by a sample leads to a positive peak in the dynode voltage. The typical dynode voltage profile between 200 and 900 nm for the model 42 MCD spectrometer is shown on the right hand side in Figure 22. It was recorded without any sample and with the detector compartment being directly attached to the polarizer compartment. The DC level was fixed to the default value of 1 V and the bandwidth was set to 1 nm.

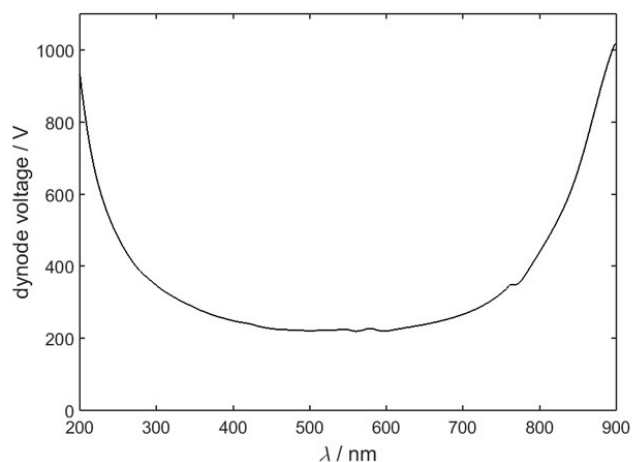
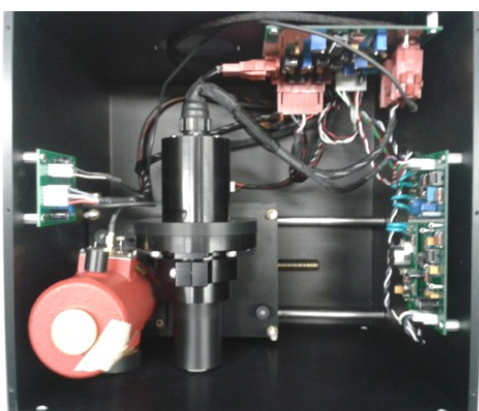


Figure 22: Left: Detector compartment containing the InGaAs NIR detector and the photomultiplier tube. Right: Characteristic dynode voltage profile of the photomultiplier recorded at a fixed bandwidth of 1 nm and a DC level of 1 V.

The increase of the dynode voltage at low wavelengths ($\lambda < 300$ nm) is attributed to the emission limit of the light source (Figure 17) and the limited transmission of the optics. At high wavelengths ($\lambda > 800$ nm), a second increase is observed because the lower energy of the incoming photons leads to less emission of electrons from the metal. Very high dynode voltages result in increased noise in the CD-spectrum and if the dynode voltage reaches a plateau above ca. 800 V, the CD-measurement is not reliable at all anymore. When measuring an absorbing sample, the bandwidth should be chosen in a way that finds a compromise between the spectral resolution and the light intensity reaching the detector.

The peaks arising in the PMT voltage due to light absorption by a standard sample were employed for the wavelength calibration of the spectrometer. The wavelength calibration was performed in factory by using a solution of 40 g L⁻¹ holmium oxide in 10 % (volume fraction) perchloric acid and repeated during the installation of the instrument. The solvated Ho³⁺ cation has a very stable coordination and shows characteristic narrow f-f-transitions. Most of the observed bands in the visible range are thus NIST-certified (NIST: National Institute of Standards and Technology) as intrinsic traceable wavelength standards.¹²⁹ Especially the most intense peak attributed to the transition to the ⁵F₄ free ion state and located at 536.4 nm for a spectral bandwidth of 0.1 nm¹²⁹ was employed for assigning the calibration wavelength (the so-called “home wavelength”). The calibration wavelength corresponds to the starting position of the optical beam switch linked to the motion of the wavelength cam.

The InGaAs NIR detector was manufactured by Teledyne Judson Technologies (model J23D-M204-R02M-60-2.6-CSW) and operates over the spectral range from about 800 nm to 2200 nm. In order to reduce the dark current, the detector is surrounded by a metal dewar (model M204) enabling cooling with liquid nitrogen. Suprasil quartz glass was chosen for the windows. Since the detector’s active area is only 2 mm, special care has to be taken when focusing and adjusting the incoming light beam. Details about the utilized optics and optomechanics will be given in section 4.1.4.

If a CD active sample is placed in the light path, lcp and rcp will be absorbed to a different extent and the light intensity after the sample will oscillate with the resonance frequency of the PEM. Compared with the overall light intensity, this oscillation is very small and as a result a signal with a small AC component superimposed on the DC component is obtained. The signal path is schematically shown in Figure 23: The components of the detected mixed signal are separated with the help of a band-pass filter and after amplification the AC signal reaches a sample-and-hold circuit, which also receives square wave time

signals from the PEM. The sample-and-hold circuit samples the signal at a given time and stores the information for a given time interval. The time signals arriving at the sample-and-hold circuit correspond to the phase shifts of +90 and -90 degrees and are thus used to trigger the measurement of the lcp and rcp amplitudes. The difference is the amplitude of the AC signal and is sent to the computer, where an A/D card samples the AC amplitude as well as the amplified DC signal. The software builds the AC/DC ratio, which is scaled to become the CD signal. CD signal intensity calibration is performed by adjusting the gain on the amplifier in the AC signal circuit.

Also the CD signal intensity calibration was performed in factory and repeated during the installation of the instrument. As a reference sample, a solution of 1.0 mg mL⁻¹ (1S)-(+)-10-camphor sulfonic acid (CSA) in water was used that shows an intense positive CD signal at 290.5 nm. However, after adding the additional optics for the MCD-setup, some slight recalibration was required and the corresponding data will be discussed in section 4.1.5.

Both detectors use the same circuit but for the InGaAs detector the data need to be corrected for the dark current. The dark signal is measured with the help of a (closed) chopper, which is located between the light source and the monochromator entrance slit (not shown in Figure 18). The CD signal is then calculated as

$$CD_{NIR} = 100 \cdot \Delta Gain \cdot \frac{\Delta I - \Delta I_{Offset}}{I - I_{Dark} - I_{Offset}} \quad (64)$$

where I and ΔI are the measured total intensity and intensity difference and I_{Dark} accounts for the dark signal. ΔI_{Offset} is a correction for electrical offsets and I_{Offset} is an optional additional correction besides the dark correction. The factor 100 is a scaling factor for converting voltage to millidegrees and $\Delta Gain$ is included to correct for differences between the PMT and the InGaAs detector outputs. Signal calibration in the NIR range thus includes the appropriate adjustment of the offset parameters.

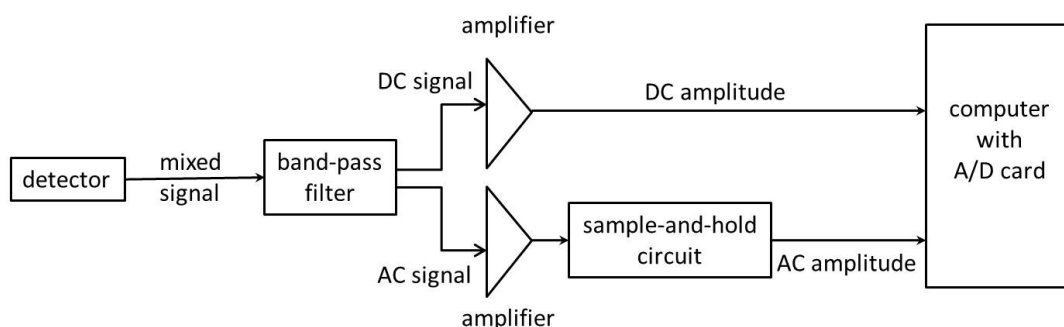


Figure 23: Schematic illustration of the electronic circuit used to extract the CD signal (according to a draft by Dr. Glen Ramsay, Chief Scientist at Aviv Biomedical, Inc.).

4.1.3 Magnet and Sample Holder

For MCD-measurements, basically three types of magnets are available: Permanent magnets, electromagnets and superconducting magnets. Although superconducting magnets are usually the most expensive and require cooling with liquid helium, they are preferred in modern MCD-spectrometers since they allow VTVH MCD measurements up to much higher fields. Furthermore, the liquid helium from the helium reservoir can be used for cooling the sample. A superconducting magnet was therefore chosen for the MCD-spectrometer built up in this work. The magnet employed is an Oxford Instruments SM-4000-10 optical split-coil cryomagnet providing horizontal magnetic fields up to ± 10 T. The magnetic field is controlled by a Mercury iPS power supply, which also monitors the cryogen levels. A schematic illustration of the magnet system is given in Figure 24. The helium reservoir (20 l) is shielded from thermal radiation by a liquid nitrogen bath (24 l) and both are thermally insulated from the environment by an outer vacuum chamber (OVC). The Nb₃Sn superconducting coils are thermally linked to the liquid helium bath. Four outer windows out of Spectrosil B allow optical access to the sample.

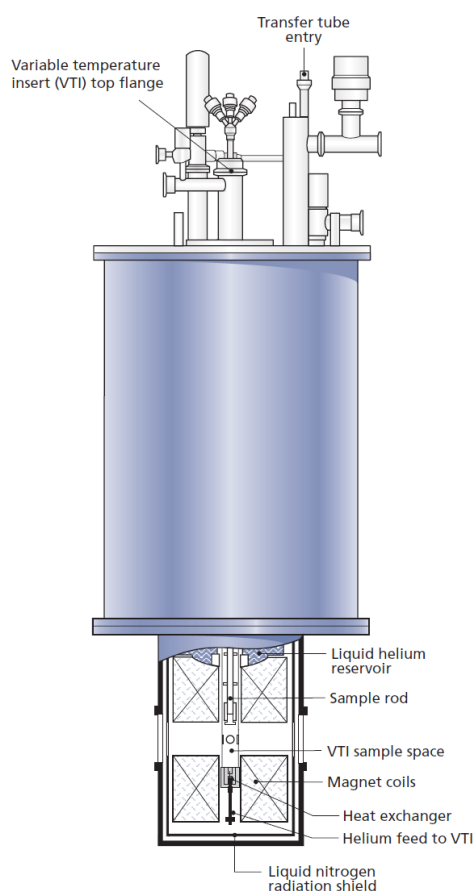


Figure 24: Schematic illustration of the Oxford Instruments SM-4000-10 optical cryomagnet containing the VTI and the sample rod. Reprinted with permission from Oxford Instruments GmbH.¹³⁰

The choice of Spectrosil B as the window material is based on its excellent transmission in the desired spectral range and the absence of birefringence which would affect the polarized light. A variable temperature insert (VTI) with a sample space diameter of 25 mm allows temperature stabilization between 1.5 and 300 K. A stepper motor controlled needle valve regulates the helium flow from the helium reservoir to the sample. However, before the helium arrives at the sample, it passes a heat exchanger at the base of the sample tube. The heat exchanger is fitted with a heater and a calibrated CernoxTM thin film resistance temperature sensor allowing temperature measurement and control. The temperature regulation system is controlled by a Mercury iTC temperature controller. Four inner Spectrosil B windows, each having a diameter of 10 mm, provide optical access to the VTI.

An appropriate sample rod was supplied together with the magnet system. It is equipped with an additional heater and a CernoxTM temperature sensor allowing an accurate determination of the sample temperature. As shown in Figure 25, the sample cell containing the sample is attached to the bottom of the sample rod. The sample cell is home-built and designed for studying samples as mulls, polymer films or frozen solutions. It consists of a copper middle part, which can be screwed to the sample rod and contains a 12 mm diameter bore for the light passing through. When studying mulls or polymer films, the sample is pressed between two fused silica disks (15 mm diameter) which are screwed to one side of the middle part with the help of an appropriate copper counterpart. For studying frozen solutions, each side of the middle part is covered with a fused silica disk and a copper counterpart and O-rings serve for sealing. The solution can be injected via a small hole in the middle part. In order to avoid losing the sample by evaporation or leaking, the solution is frozen in liquid nitrogen before inserting it into the VTI.



Figure 25: Home-built sample cell screwed to the sample rod. Fused silica disks are attached to both sides of the middle part. Left: Top view. Right: Side view.

The cryomagnet is placed on a home-built non-magnetic table which enables horizontal and vertical fine positioning with the help of a crank and a micrometer screw. This fine positioning allows finding the optimum spot of the light beam passing the sample. Due to the comparatively high stray fields of superconducting magnets, the magnet has to be placed at adequate distances from the CD-spectrometer and the detector compartment. This precaution not only prevents the photomultiplier or the PEM control circuit from being affected by the magnetic field but also poor homogeneity of the magnetic field by interaction with static steel. According to the stray field of the magnet, distances of about 1 m between the polarizer compartment and the outer magnet window and 1.5 m between the opposite magnet window and the detector compartment were chosen. For practical reasons, e.g. the location of the helium recovery line in the laboratory, the magnet was oriented with the magnetic field anti-parallel to the light path. This means that the observed MCD signals show reversed signs and the spectra have to be corrected by multiplication with a factor of -1 .

4.1.4 Optics and Optomechanics

The design and construction of the optical layout were one of the main tasks in the design of the MCD-spectrometer. The material of the employed lenses should show a high transmission over the entire wavelength range and no birefringence affecting the light polarization should occur. Thus, UV-grade fused silica lenses (Thorlabs) suitable for wavelengths between 185 and 2100 nm were chosen. Uncoated lenses were chosen since anti-reflection coatings are available only for limited wavelength ranges.

Focusing the light first onto the sample within the magnet and afterwards onto the detector requires at least four lenses. Depending on the nature of these lenses, two possible basic layouts illustrated in Figure 26 and their combinations have been considered: Option 1 involves two pairs of biconvex lenses while option 2 employs two pairs of plano-convex lenses with the first lens of each pair collimating the light and the second one focusing it. In order to find out which option performs better, simulations using the ZEMAX 8.0 optical design software¹³¹ were carried out. The required data of the optical layout within the polarizer compartment were provided by Aviv and the corresponding light path is shown in Figure 27. Simulations based on these data showed that smaller spot sizes as well as lower wavelength dependencies can be achieved by implementation of option 2. Best results were obtained with four plano-convex lenses having diameters of 50.8 mm and focal lengths of 250 mm for lenses 1, 3 and 4 and a focal length of 200 mm for lens 2. The corresponding data and drawings are shown in the appendix, section 8.2.1.

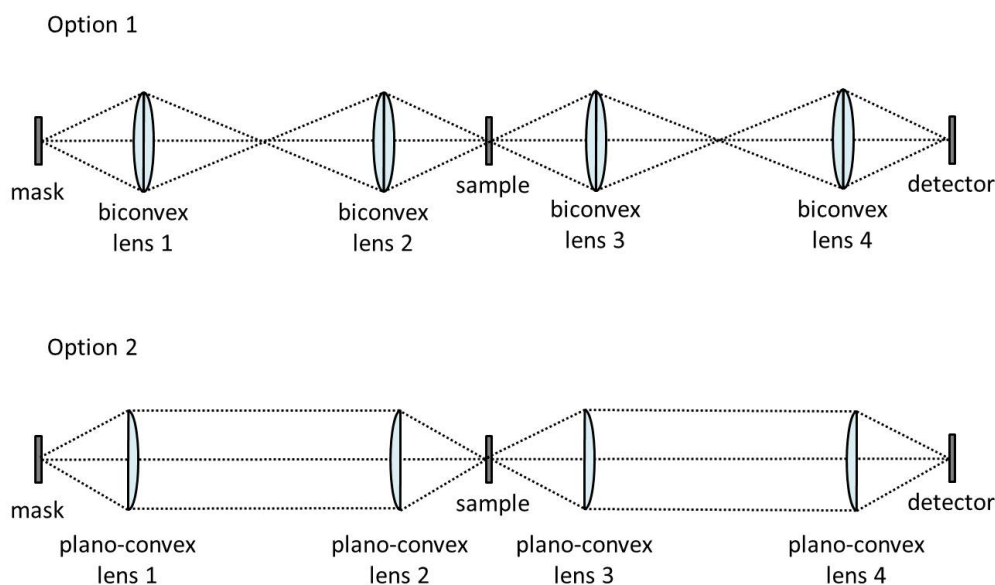


Figure 26: Schematic illustration of the basic optical layouts considered for focusing the light onto the sample and the detector.

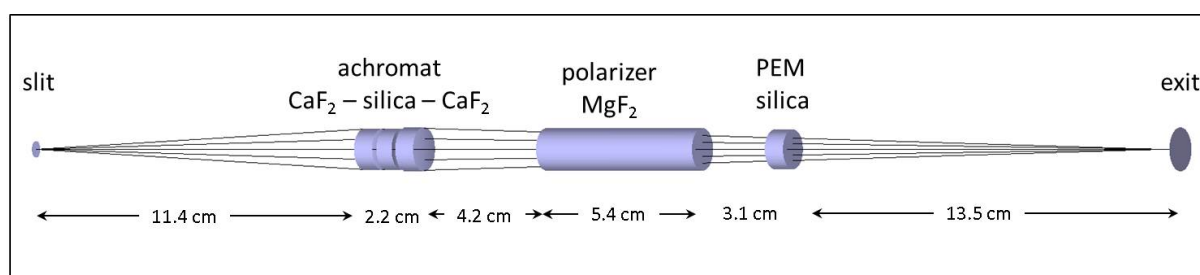


Figure 27: Optical layout within the polarizer compartment according to the data provided by Aviv biomedical, Inc. For reasons of clarity, only five rays belonging to one field point (center) and one wavelength (1000 nm) are shown.

This version of the optical layout sufficed for CD- and MCD-measurements in the visible range. However, due to the comparatively small active area of the InGaAs detector, satisfactory spectra in the NIR range required an improved focusing of the light beam onto the detector, i.e. a smaller spot size. According to equation (64), insufficient light intensity leads to high baseline offsets and unphysically large CD signals. Thus, simulations were revised by adding an additional small lens in front of the detector. Although the light beam is rectangularly shaped, which suggests that the integration of a cylindrical lens would be beneficial, better performance was simulated by adding another plano-convex lens with a diameter of 25.4 mm and a focal length of 75 mm. The simulated light path beginning from the polarizer compartment is shown in Figure 28, while Figure 29 shows the full field spot diagrams at the sample surface and at the detector position. The selected field points for the

simulations correspond to the maximum monochromator slit width of about 3 mm and a rather small slit height of 4 mm. The full field spot diagrams show that a sample diameter of at least 6 mm and a detector surface diameter of at least 3 mm are necessary in order to catch the full light intensity of the given field points. Since the clear sample cell diameter is 12 mm, no intensity is cut off when the light passes the cell, even if the experimental slit height is larger than in the simulation. However, care has to be taken when preparing the sample, i.e. it has to be rather homogeneous. When single crystals are going to be studied, either the implementation of an additional lens or an aperture is required.

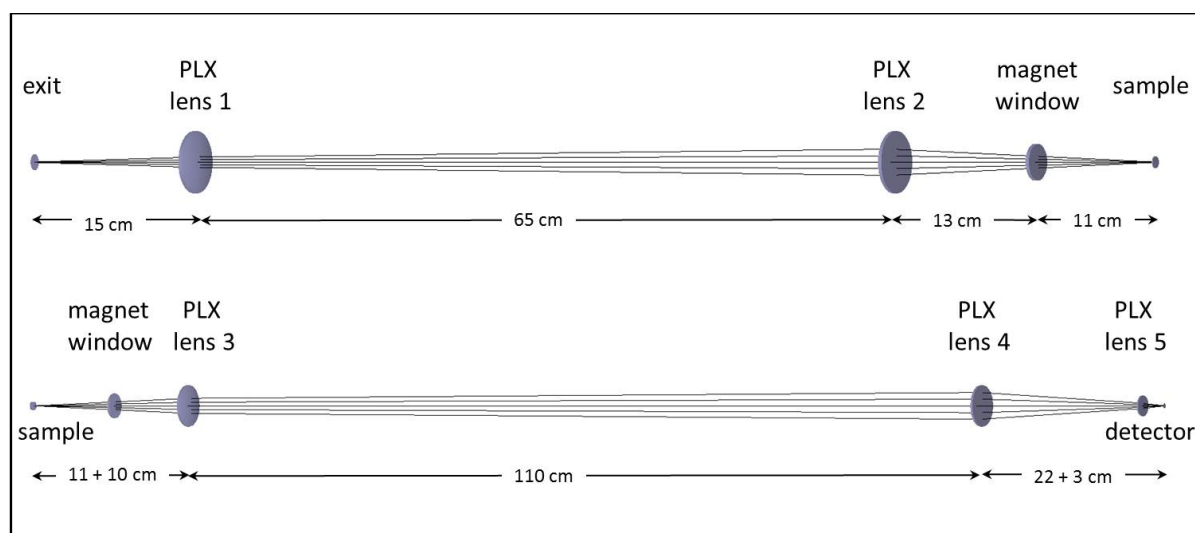


Figure 28: Simulated optical layout for the MCD-spectrometer using five plano-convex (PLX) lenses. Top: Light path from the spectrometer exit to the sample. Bottom: Light path from the sample to the detector. For reasons of clarity, only five rays corresponding to one field point (center) and one wavelength (1000 nm) are shown.

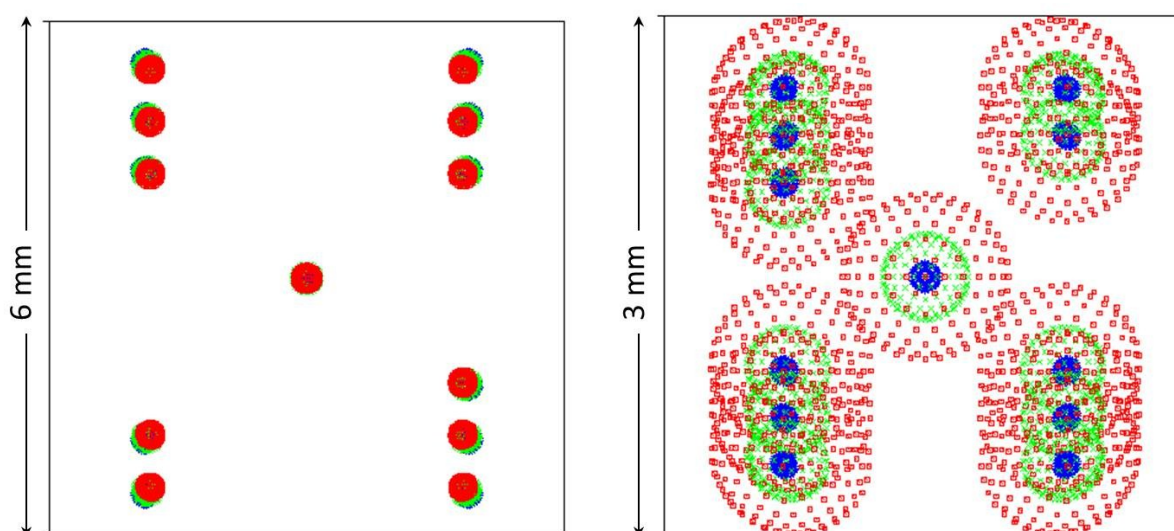


Figure 29: Simulated full field spot diagrams corresponding to the optical layout shown in figure 28. Left: Sample surface. Right: Detector position. Different colors represent different wavelengths: 1000 nm (blue), 1500 nm (green) and 2000 nm (red).

With a diameter of only 3 mm, the illuminated area at the detector position is much smaller than at the sample surface because lens number 5 is positioned directly in front of the detector. Although the required area is still larger than the active area of the InGaAs detector, the spot size corresponds to a reduction of about 40 % compared to the first version of the MCD-spectrometer with only four lenses (compare Figure A 2 in the appendix). Figure 29 also shows a clear wavelength dependency of the focal spots, which is more pronounced at the detector site. The spot size is smallest for wavelengths around 1000 nm since the distances given in Figure 28 were optimized for 1000 nm. The utilization of achromatic lenses could reduce the wavelength dependency and has to be considered for future versions of the spectrometer.

The experimental realization of the simulated optical layout involved mounting the lenses onto aluminum rails, which were fixed to the tables where the CD-spectrometer, the magnet and the detector compartment are placed on (Figure 16). Appropriate rail carriers allow the fine positioning of the lenses parallel to the light path, which was performed by monitoring the detector signal while carefully moving the lenses. The experimentally determined optimum distances agree rather well with the simulated ones and only slight changes were necessary. Fine-positioning of the lenses perpendicularly to the light beam was performed with the help of linear translation stages placed on top of the rail carriers while vertical adjustment was possible by height adjustable optical post holders.

The light path had to be shielded from ambient light since ambient light reaching the detector leads to artificial CD signal lowering (compare equation 64). In the first version of the MCD-spectrometer, light shielding was achieved by a combination of rigid PVC pipes and flexible rubber hoses. However, although ambient light was efficiently shielded, this setup turned out to be rather cumbersome concerning maintenance work, e.g. readjusting the lenses or checking the magnet windows for impurities. Thus, for the second version of the MCD-setup a more user-friendly alternative was chosen by designing a wooden box that perfectly fits to the dimensions of the tables and the optomechanics. This wooden box was designed and assembled with the help of Michal Kern and Jan Vaverka as part of their Erasmus projects at the University of Stuttgart and with the help of Dr.-Ing. Petr Neugebauer (Institute of Physical Chemistry, University of Stuttgart). The top and the side covers of the box can be removed separately whenever it is necessary, e.g. for lens readjustment. For efficient light shielding, the fixed parts of the box are sealed with polyethylene sealant while black foam serves for sealing the flexible parts. Figure 30 shows the current state of the complete MCD-setup including the wooden box.

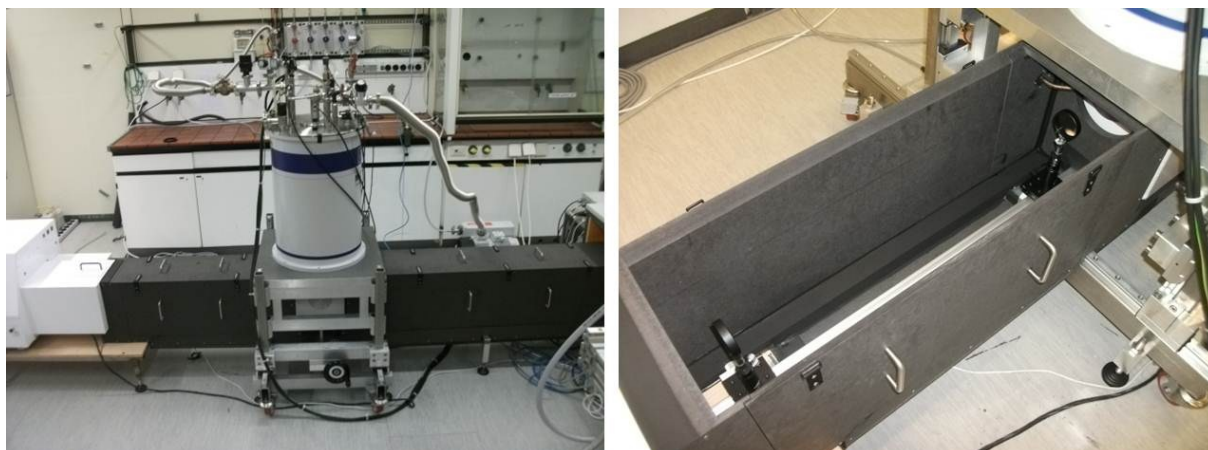


Figure 30: Photographs showing the current state of the MCD-setup. Left: Front view onto the completed MCD-setup. Right: View into the opened box containing the lenses.

However, work is ongoing concerning the user-friendly change of the magnet between several applications, e.g. MCD-, torque-detected EPR- or FDMR-spectroscopy.

4.1.5 Characterization of the MCD-Spectrometer

Figure 31 shows the PMT dynode voltage profile and the corresponding CD baseline recorded with the completed MCD-setup (shown in red) in comparison to the baseline measurements for the CD-spectrometer with the detector box directly attached to the spectrometer (shown in blue). The measurements were performed using bandwidths and step sizes of 1.0 nm, default DC levels of 1.0 V and averaging times of 1 s. The baselines corresponding to the completed MCD-setup were recorded with the magnet cooled down but the VTI temperature set to 300 K and no magnetic field applied, in order to provide similar experimental conditions. Compared to the dynode voltage of the CD-spectrometer, the dynode voltage of the MCD-spectrometer shows a similar shape, i.e. reaching high values at the wavelength limits due to low source emission at low wavelengths and lower detector sensitivity at higher wavelengths. However, higher voltages have to be applied for keeping the DC level constant, which might be attributed to the longer distance between the light source and the detector and the additional lenses and windows the light passes through. Close to the wavelength limits, the dynode voltage recorded with the MCD-setup shows a flattening which was not observed before. This flattening might hint to an imperfect shielding of ambient light resulting in a higher overall light intensity on the detector. Although the laboratory lamps were switched off during the measurement, a remaining source for ambient light is the spectrometer light source itself with its light shining through the lamp compartment at the back of the spectrometer.

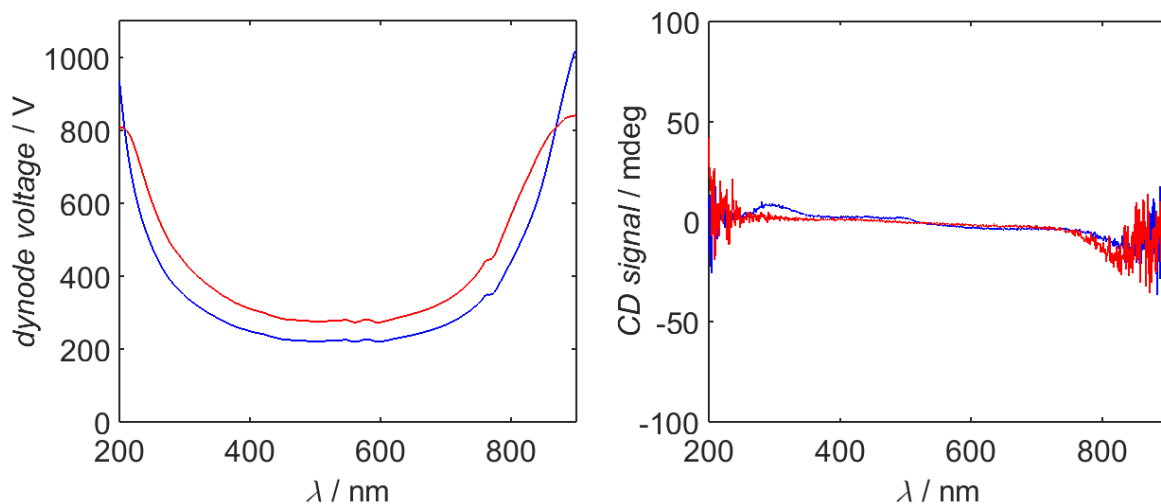


Figure 31: Left: Dynode voltage profiles recorded without any samples, using bandwidths and step sizes of 1.0 nm. Right: Corresponding CD baselines. Spectra recorded with the detector box directly attached to the CD-spectrometer are shown in blue while red lines correspond to measurements with the completed MCD-setup.

This effect is negligible in wavelength regions where light intensity is high enough but leaves room for improvement close to the wavelength limits, e.g. by designing an additional light shielding for the lamp compartment.

At about 765, 580, 545 and 420 nm the dynode voltage profiles show weak artefacts, which can be attributed to the optics within the CD-spectrometer since they are not enhanced by the additional optics in the MCD-setup. However, these artefacts do not affect the CD baselines shown on the right of Figure 31. As expected, the CD baselines show a higher noise level in regions where the dynode voltage is high but are essentially flat in between. Interestingly, the CD baseline recorded with the MCD-setup is smoother than the one recorded with the CD-spectrometer, indicating that the light reaches the detector more uniformly due to the additional lenses.

Figure 32 shows the NIR baseline recorded at room temperature using the InGaAs NIR detector. The bandwidth was set to 5.0 nm and the step size was 1.0 nm. The offset parameters defined in equation (64) were fixed to $\Delta I_{\text{Gain}} = 2.00$, $\Delta I_{\text{Offset}} = 0.04$ and $I_{\text{Offset}} = 0$. As will be shown below, these offset parameters were determined with the help of an aqueous Ni(II) tartrate solution. However, the optimum values, especially ΔI_{Offset} , strongly depend on the light intensity reaching the detector and thus in turn on the bandwidth and the sample properties. While the energies at which CD signals appear are reliable, absolute CD signal intensities in the NIR region should therefore be regarded critically. The NIR baseline shows some artefacts with signs and intensities depending on the offset parameters. The presence of the artefacts can be partially attributed to the fused silica optics and for comparison, the

transmission spectrum of fused silica¹³² is given in Figure 32 as well. Clear transmission minima around 940, 1250 and 1380 nm and a rather broad feature around 1900 nm occur, which can be assigned to overtone and combination vibrations from OH groups within the silica.^{133,134} Water molecules might also play a role, especially concerning the broad absorption around 1900 nm.¹³⁵ One possibility to improve the situation is the employment of fused silica with a lower OH content. However, not only the lenses for the MCD-setup consist of fused silica but also parts within the CD-spectrometer itself. In addition to the fused silica based signals, rather strong artefacts appear at wavelengths around 1000 nm, but their origin remains unclear so far. Since they do not correspond to the transmission spectrum shown in Figure 32 and since they have already been observed in factory, they cannot be solely attributed to the additional optics of the MCD-setup. However, future improvements could be achieved by employing a red-enhanced PMT allowing for covering the range from 800 to 1200 nm with this detector.

Although baseline effects are undesirable, they are less problematic in MCD-spectroscopy than in CD-spectroscopy, since they can be easily eliminated by recording spectra at opposite magnetic fields and subtracting the data. By doing so, all the field-independent artefacts will be eliminated while the MCD signal intensity is doubled.

The signal intensity calibration of the CD-spectrometer in the visible range was already performed in the factory and during the installation of the instrument by using a reference solution of CSA in water.

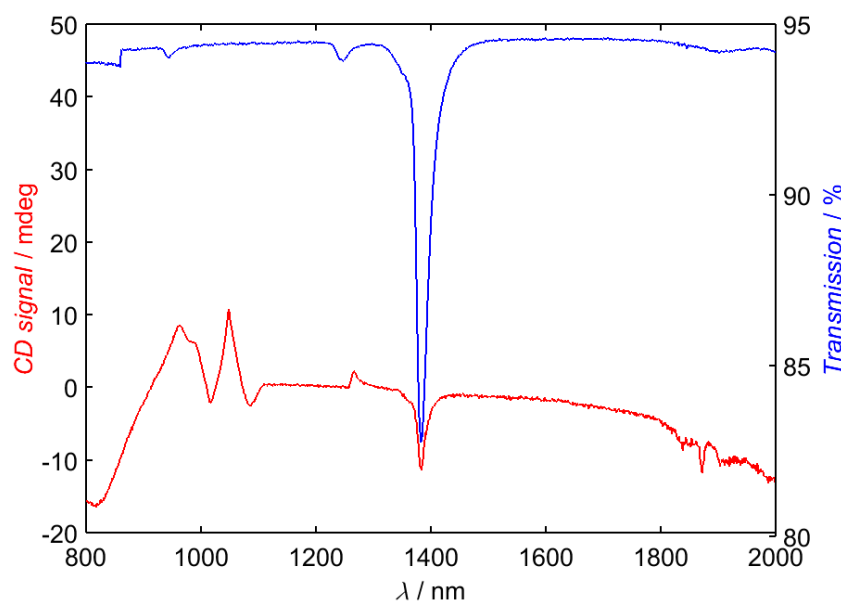


Figure 32: CD baseline in the NIR range using the InGaAs NIR detector (shown in red) compared to the transmission spectrum of UV-grade fused silica¹³² (shown in blue). The CD-spectrum was recorded at room temperature with a bandwidth of 5.0 nm and a step size of 1.0 nm. The transmission data were provided by Thorlabs, Inc.

However, additional optics might lead to depolarization effects and therefore slight recalibration was performed after setting up the MCD-spectrometer. CSA shows an intense positive CD signal at 290.5 nm with a molar ellipticity of $[\theta]_M = 7.78 \cdot 10^3 \text{ deg cm}^2 \text{ dmol}^{-1}$.¹³⁶ Thus, CD-spectra of a solution of dried CSA in doubly distilled water (1.006 g L^{-1}) in a 1 cm cuvette were recorded and the AC gain was adjusted until the observed baseline-corrected CD signal was satisfactorily close to the expected value. The final spectrum is shown in the appendix, section 8.2.2.

Since it is known from literature that CD signal calibration at only one wavelength might not be sufficient,¹³⁶ calibration was additionally checked by recording CD-spectra of an aqueous solution of Ni(II) tartrate, which shows a wealth of literature-reported CD signals¹³⁷ in the entire visible range. The Ni(II) tartrate solution was prepared by mixing aqueous solutions of nickel(II) chloride hexahydrate (0.5682 g in 10 ml H₂O) and sodium L-(+)-tartrate dihydrate (0.8285 g in 10 ml H₂O), leading to a Ni(II) concentration of 7.043 g L^{-1} . For final CD calibration, the AC gain was adjusted in such a way that both the CSA and the Ni(II) tartrate solution spectra showed excellent agreement with literature data¹³⁷. The observed signal maxima compared to literature values¹³⁷ are summarized in Table 1 while Figure 33 shows the baseline-corrected CD spectrum of the Ni(II) solution recorded in the visible range with a bandwidth of 1.0 nm, increments of 0.3 nm and an averaging time of 1.5 s. It should be mentioned that the calibration measurements using CSA and Ni(II) tartrate were performed using the first version of the MCD-setup, i.e. with only four plano-convex lenses and PVC pipes for light shielding. In order to make sure that the fifth lens and the wooden box for light shielding do not affect the calibration, the measurements were repeated using the current version of the MCD-setup. The obtained spectra (see Figure 33) in the visible range showed no significant differences to the previous measurements. Generally, wavelength and CD signal intensity calibration should be checked regularly, especially when the instrument has been out of use for some longer time period.

In addition to the CD signals in the visible range, Ni(II) tartrate shows a strong negative band around 1100 - 1200 nm and this compound was thus also used for checking the performance of the InGaAs NIR detector. For a solution having a Ni(II) concentration of 7.043 g L^{-1} and a pathlength of 1 cm, an absorption difference of $\Delta A = -0.0023$ corresponding to a molar ellipticity of $[\theta]_M = -632 \text{ deg cm}^2 \text{ dmol}^{-1}$ was reported¹³⁸ and this value was used in order to determine the optimum offset parameters appearing in equation (64).

Table 1: Comparison of experimentally observed CD signals for aqueous solutions of CSA and Ni(II) tartrate with literature values.

Observed CD maxima		Literature data ^{136,137}	
λ / nm	$[\theta]_M / \text{deg cm}^2 \text{ dmol}^{-1}$	λ / nm	$[\theta]_M / \text{deg cm}^2 \text{ dmol}^{-1}$
(1S)-(+)-10-camphor sulfonic acid (CSA)			
290.5	$(+7.71 \pm 0.06) \cdot 10^3$	290	$+7.78 \cdot 10^3$
nickel(II) tartrate			
371.2	$+50.4 \pm 0.6$	371	+50.3
399.1	-49.9 ± 1.9	399	-46.7
427.9	$+35.9 \pm 0.5$	428	+35.8
471.7	$+8.6 \pm 0.2$	470	+8.3
718.3	-104.3 ± 0.8	718	-101.2
778.3	-112.4 ± 1.6	777	-110.7

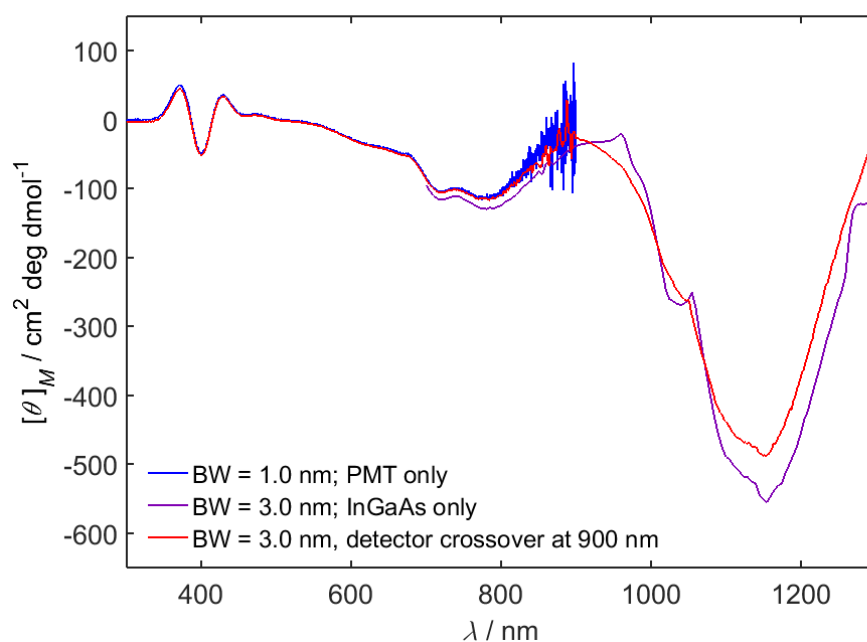


Figure 33: Room temperature CD-spectra of aqueous Ni(II) tartrate solutions. The spectra shown in blue and purple were recorded using the first version of the MCD-setup (four plano-convex lenses). The NIR and the visible range were studied separately. The spectrum shown in red corresponds to the current MCD-setup (five lenses) and was recorded with an automatic detector change at 900 nm. Intensity differences in the NIR range are attributed to the different light intensities reaching the InGaAs detector as well as different offset parameters during the measurements. In the NIR spectrum recorded with the first version of the spectrometer, baseline effects are more pronounced.

The offset parameters were adjusted until the CD signal intensity was close to the reported value and the overlap with the PMT detected CD-spectrum and the quality of the baseline were also taken into account. For a bandwidth of 3.0 nm, the following optimized offset parameters were obtained: $\Delta\text{Gain} = 2.00$, $\Delta I_{\text{Offset}} = 0.0505$ and $I_{\text{Offset}} = 0.0005$. The corresponding spectrum (recorded with the first version of the MCD-setup) is shown in Figure 33. However, for the NIR CD-spectrum recorded with the current MCD-setup and the same bandwidth (see also Figure 33), the offset parameters were set to $\Delta\text{Gain} = 2.00$, $\Delta I_{\text{Offset}} = 0.04$ and $I_{\text{Offset}} = 0$. This clearly demonstrates the dependence of the offset parameters on the light intensity reaching the detector and, as already mentioned above, absolute CD signal intensities in the NIR range are not reliable yet. However, this effect might play a lesser role in MCD- than in CD-spectroscopy, since in MCD-spectroscopy baseline effects can be eliminated by subtracting spectra for opposite magnetic fields and because typically normalized intensities are considered.

The very first MCD-measurements in this work were performed on a poly(vinyl alcohol) film of $\text{K}_3[\text{Fe}(\text{CN})_6]$. $\text{K}_3[\text{Fe}(\text{CN})_6]$ has been subjected to a range of MCD studies¹³⁹⁻¹⁴² in the past and therefore is a suitable sample for comparison purposes. The $[\text{Fe}(\text{CN})_6]^{3-}$ anion shows three very intense ligand-to-metal charge transfer (LMCT) transitions, which are due to excitations from the occupied ligand orbitals to the t_{2g} orbitals of the octahedrally coordinated low-spin (LS) Fe(III) central ions.¹⁰⁴ The electronic ground state of LS Fe(III) is $^2T_{2g}$ and the LMCT transitions can be identified as $^2T_{2g} \rightarrow ^2T_{1u}(\pi)$ (LMCT1), $^2T_{2g} \rightarrow ^2T_{2u}(\pi)$ (LMCT2) and $^2T_{2g} \rightarrow ^2T_{1u}(\sigma)$ (LMCT3) at approximately 24500, 32700 and 40500 cm^{-1} , respectively.¹⁴¹ The spectra are dominated by Faraday C-terms and group theoretical considerations predict a positive sign for the signals arising from LMCT1 and LMCT3 and a negative sign for the signal due to LMCT2.¹⁰⁴

Films of $\text{K}_3[\text{Fe}(\text{CN})_6]$ in PVA were prepared according to a procedure described in literature.¹⁴² Aqueous solutions of $\text{K}_3[\text{Fe}(\text{CN})_6]$ and PVA were mixed and the resulting mixture was put onto glass slides. After drying in the dark for several days, the films were removed with the help of a razor blade and the clearest and most homogeneous film was used for the MCD measurements. MCD-spectra were recorded at several temperatures and magnetic fields and the baseline corrected spectra obtained at 2 K are shown in Figure 34. The three LMCT bands showing the expected signs and relative intensities are observed around 24000, 33000 and 38500 cm^{-1} , in good agreement with literature.^{140,141} Comparable to the spectra reported in literature, splittings of the bands are observed, which might be attributed to vibrational overtones or excited-state vibronic, crystal-field or spin-orbit effects.¹⁴²

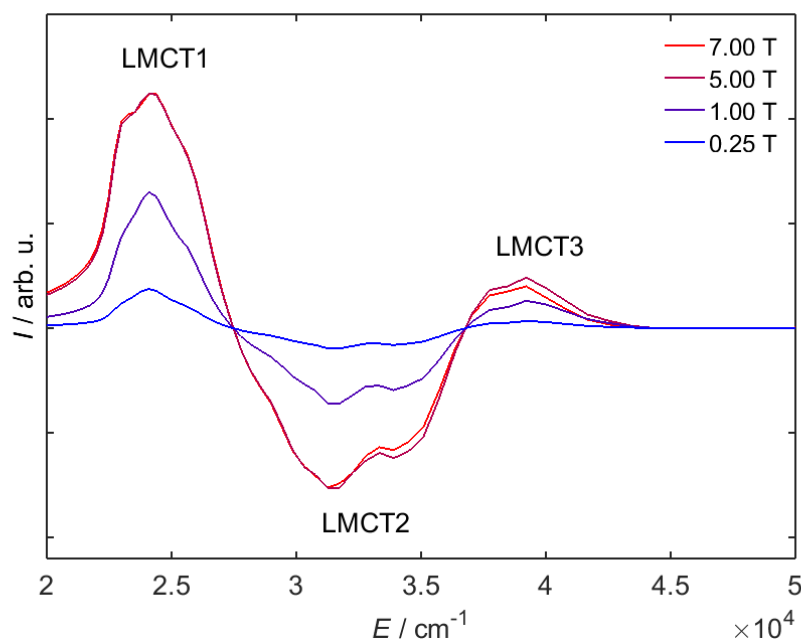


Figure 34: MCD-spectra of a film of $K_3[Fe(CN)_6]$ in poly(vinyl alcohol) recorded at 2 K and different magnetic fields, as indicated. The bandwidth was set to 3.0 nm and the step size was 5.0 nm.

All in all, the rather satisfactory agreement between the experimental spectra and literature data shows that the MCD-spectrometer provides reliable results and can thus also be used for studying new compounds.

Another very interesting aspect concerning the MCD-spectrometer is its sensitivity. If the sensitivity is high enough, MCD-spectroscopy could provide a possibility to study monolayers of single-molecule magnets, which currently requires much more sophisticated and less available techniques, e.g. synchrotron based methods. Since lanthanide bis(phthalocyanines) are not only relevant in molecular magnetism but also show strong absorptions in the visible range, they are promising candidates for sensitivity studies. The strong absorptions are based on intra-ligand electronic transitions and depending on the participating orbitals, they are classified into the B-band and the Q-band.¹⁴³⁻¹⁴⁵ Especially the Q-band leading to characteristic derivate-shaped MCD signals around 16000 cm^{-1} is extremely useful, since it is very sensitive to structural changes. For this reason, polystyrene films with varying concentrations of the famous SIM $(NBu_4)[Dy(Pc)_2]$ ²⁵ were studied by MCD-spectroscopy. The films were prepared by mixing various amounts of solutions of polystyrene in toluene and $(NBu_4)[Dy(Pc)_2]$ in ethanol and spreading the mixture onto glass slides for drying. The effective thickness, i.e. the number of molecules along the direction of light propagation for the MCD measurements was estimated with the help of the mass and the physical thickness of the dried film. A more detailed description is given in the experimental

part. The $[\text{Dy}(\text{Pc})_2]^-$ species oxidized during the film drying process and nearly quantitative oxidation was confirmed by comparing the room temperature electronic absorption spectrum of the most highly concentrated film with reported spectral data¹⁴⁶ of the $[\text{Dy}(\text{Pc})_2]$ complex in different redox states. The corresponding absorption spectrum is provided in the appendix, section 8.2.3. It was thus not the MCD signal of the anionic form but the signal of the neutral form of the compound that was observed during the sensitivity studies. However, since the neutral form is also expected to show SIM behavior¹⁴⁷ and since the main interest was to probe the possibility of monolayer detection, the oxidation was not a concern.

The obtained baseline-corrected MCD-spectra of the most highly concentrated film with an estimated effective thickness of 3.2 molecules are shown in Figure 35a. The spectra were recorded at 2 K and various magnetic fields, as indicated. The main feature is a strong negative peak at 15198 cm^{-1} , which is attributed to the Q-band and serves as the reference peak for comparison with the spectra of the lower concentrated films. The magnetic field dependence of this peak shows that at 2 T, the intensity is close to saturation and further increasing the magnetic field would not result in a significant intensity gain. Thus, the spectra of the lower concentrated films were recorded at 2 K and 2 T only. A comparison of the spectra for the different concentrations is shown in Figure 35b: Down to an effective thickness of 0.06 molecules, a clear MCD signal was observed. This number is extremely small and it has to be emphasized that the estimation of the films' effective molecular thicknesses (see experimental section) was not very accurate.

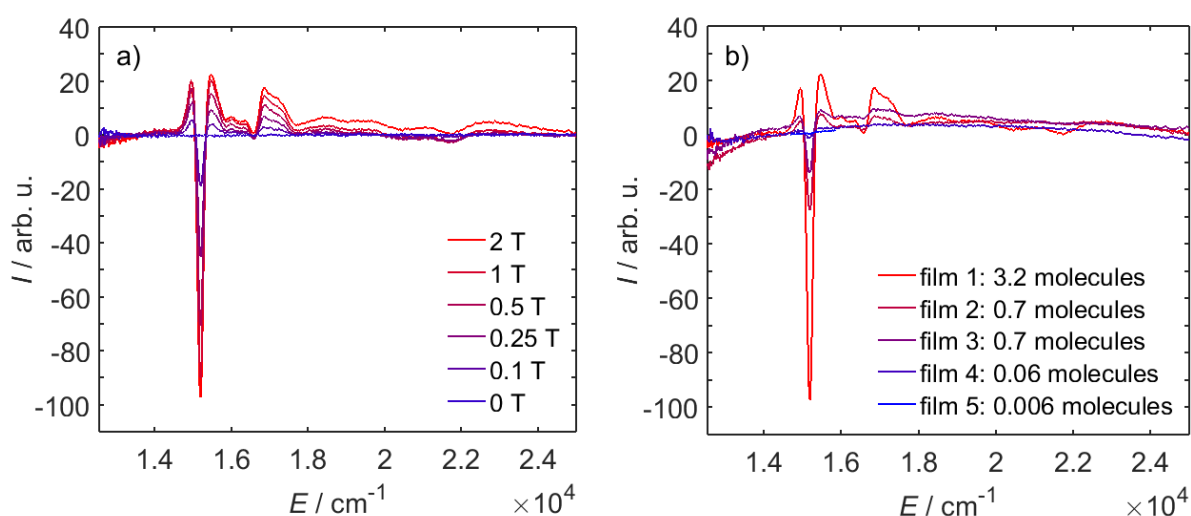


Figure 35: MCD spectra of films of the oxidized dysprosium bis(phthalocyanine) complex. a) Spectra of the most highly concentrated film with an estimated effective thickness of 3.2 molecules, recorded at 2 K and various magnetic fields. b) MCD spectra for different concentrations recorded at 2 K and ± 2 T. The estimated effective thicknesses of the films are shown online.

This is clearly demonstrated in the spectra of films 2 and 3, since for both of them an effective thickness of 0.7 molecules was calculated but different MCD intensities are observed. The intensity difference indicates large error bars. However, these preliminary results are very promising and strongly hint at the possibility of monolayer detection.

Monolayer detection was probed by studying samples of dysprosium bis(phthalocyanine) deposited on fused quartz coverslips. The samples were fabricated by Dr. Jiří Novák, Dr. Chennan Wang and Jakub Rozbořil at the Central European Institute of Technology at the Masaryk University, Brno by Langmuir-Blodgett deposition of a 1.78 mg ml^{-1} solution of $(\text{NBu}_4)[\text{Dy}(\text{Pc})_2]$ in chloroform. Preliminary characterization by XRD measurements indicated effective thicknesses of 1-2 molecules. An example for a baseline-corrected MCD-spectrum at 1.5 K and ± 2 T is shown in Figure 36a. It is gratifying to see that the spectrum clearly shows the expected negative MCD peak even though it is weaker than expected from the results on the polystyrene films. The spectrum thus confirms the previously assumed possibility of monolayer detection for lanthanide bis(phthalocyanines).

Figure 36b shows the MCD detected hysteresis curve for the Langmuir-Blodgett deposited sample recorded at 1.5 K. The wavelength was kept fixed at 656 nm and the intensity data were recorded while sweeping the magnetic field between -2 and $+2$ T with a sweep rate of 0.5 T min^{-1} . The hysteresis curve shows a clear and promising opening, possibly due to slow relaxation of magnetization. Work in this direction is still ongoing and measurements on more and better characterized samples will be performed in the near future. Interesting aspects are for example the orientation dependence or the behavior of multilayers.

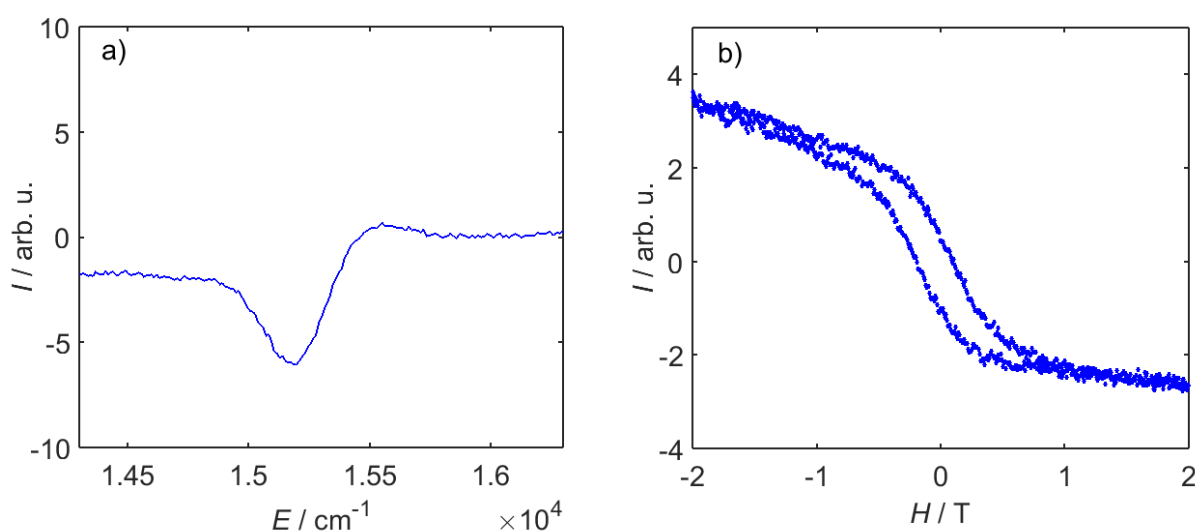


Figure 36: MCD spectra of a dysprosium bis(phthalocyanine) layer deposited on fused quartz. a) Baseline corrected MCD spectrum recorded at 1.5 K and ± 2 T. b) MCD detected hysteresis curve at 1.5 K, 656 nm and a magnetic field sweep rate of 0.5 T min^{-1} .

4.2 Molecular Lanthanide Tetra-Carbonates

Preliminary work regarding this subproject was performed by Claudio Eisele during his six week student's research internship (February/March 2012) and by Julia E. Fischer as part of her diploma thesis (April – October 2012).¹⁴⁸ Both projects were carried out under my supervision. Work done by others is indicated in the text at the position where it appears for the first time.

Part of the results presented below has already been published in: *Journal of the American Chemical Society*, **2015**, *137*, 13114 – 13120.¹⁴⁹

4.2.1 Synthesis and Structural Characterization

The molecular tetra-carbonates **1-Er** and **1-Dy** with the general formula $[\text{C}(\text{NH}_2)_3]_5[\text{Ln}(\text{CO}_3)_4] \cdot 11 \text{H}_2\text{O}$ (Ln = Er, Dy) were synthesized according to a slightly modified literature method²⁶ by mixing aqueous solutions of guanidine carbonate and the respective Ln(III) nitrate. Filtering off the resulting precipitates led to clear solutions out of which the products were crystallized. Pale pink (**1-Er**) and colorless (**1-Dy**) crystals were obtained that were characterized by elemental analysis and conventional infrared spectroscopy.

Elemental analyses were performed by Barbara Förtsch (Institute of Inorganic Chemistry, University of Stuttgart) and the analyses of freshly prepared samples showed excellent agreement between experimental and calculated values. However, the compounds tend to lose lattice water molecules, as shown by repetition of the elemental analyses after the crystals had been exposed to air for six days. The corresponding data are given in section 6.2.1.

Conventional infrared spectra at room temperature were recorded as part of the diploma thesis by Julia E. Fischer.¹⁴⁸ The observed peaks agree well with the reported literature data²⁷ and can be assigned to the internal modes of the coordinated bidentate carbonate anions^{27,150} (appendix, section 8.3.1).

X-Ray crystallographic analyses at 100 K, performed by Dr. Wolfgang Frey (Institute of Organic Chemistry, University of Stuttgart), revealed that both **1-Er** and **1-Dy** crystallize as hendecahydrates in the monoclinic space group $P2_1/n$. The respective cell parameters are listed in Table 2 and for **1-Er** they are in good agreement with the data published by Goff *et*

*al.*²⁶ For the dysprosium tetra-carbonate, Goff *et al.* reported the chemical formula $[\text{C}(\text{NH}_2)_3]_4[\text{Dy}(\text{CO}_3)_4(\text{H}_2\text{O})](\text{H}_3\text{O}^+) \cdot 13 \text{H}_2\text{O}$, including a ninefold coordinated Dy(III) central ion, in contrast to our results. They reported a rather atypical Dy-H₂O bond and a hydronium ion in the lattice for charge balance.²⁶ However, since the accurate determination of hydrogen positions solely by X-Ray diffraction studies is rather difficult, their assignments are not beyond doubt. Janicky *et al.* reported the structures of a series of molecular lanthanide tetra-carbonates with the chemical formulae $[\text{C}(\text{NH}_2)_3]_5[\text{Ln}(\text{CO}_3)_4(\text{H}_2\text{O})] \cdot 2 \text{H}_2\text{O}$ (for Ln = Pr(III), Nd(III), Sm(III), Eu(III), Gd(III), Tb(III)) and $[\text{C}(\text{NH}_2)_3]_5[\text{Ln}(\text{CO}_3)_4] \cdot 2 \text{H}_2\text{O}$ (for Ln = Y(III), Dy(III), Ho(III), Er(III), Tm(III), Yb(III), Lu(III)), showing a change in the coordination number from nine for Tb(III) to eight for Dy(III) due to the decreasing ionic radii of the Ln(III) central ions.²⁷ Although they obtained dihydrates instead of hendecahydrates, which might be attributed to their different synthetic procedure²⁷, their finding supports the eight-fold coordination of Dy(III) in **1-Dy** found in this work.

Table 2: Crystallographic data for **1-Er** and **1-Dy** at 100 K.

	$[\text{C}(\text{NH}_2)_3]_5[\text{Er}(\text{CO}_3)_4] \cdot 11 \text{H}_2\text{O}$ (1-Er)	$[\text{C}(\text{NH}_2)_3]_5[\text{Dy}(\text{CO}_3)_4] \cdot 11 \text{H}_2\text{O}$ (1-Dy)
formula weight / g mol ⁻¹	905.92	901.10
<i>a</i> / Å	8.8284(6)	8.7616(6)
<i>b</i> / Å	20.9625(14)	21.1384(16)
<i>c</i> / Å	19.6598(13)	19.7207(13)
<i>α</i> / deg	90.00	90.00
<i>β</i> / deg	94.266(2)	94.254(2)
<i>γ</i> / deg	90.00	90.00
volume / Å ³	3628.3(4)	3642.3(4)
<i>Z</i>	4	4
R-factor / %	4.73	7.42
space group	<i>P</i> 2 ₁ / <i>n</i>	<i>P</i> 2 ₁ / <i>n</i>
system	monoclinic	monoclinic

The crystal structures of **1-Er** and **1-Dy** were reproducible for several batches and the obtained data can be considered reliable. Experimental details about the structure determination and refinement are provided in the experimental part, section 6.2.2.

The unit cells of **1-Er** and **1-Dy** contain discrete $[\text{Ln}(\text{CO}_3)_4]^{5-}$ anionic units, where the Ln(III) centers are coordinated by eight oxygen atoms of the bidentate carbonate ligands. For molecular symmetry considerations, it is helpful to map the distances between the carbonate carbon atoms of the $[\text{Ln}(\text{CO}_3)_4]^{5-}$ anions, as shown in Figure 37. Three sets of distances are found, showing that the site symmetry is far from perfectly tetrahedral (all distances in Å): 3.970/4.030, 4.318/4.352, 5.043/5.069 for **1-Er** and 4.046/4.101, 4.297/4.384, 5.138/5.139 for **1-Dy**. The highest approximate symmetry is thus C_{2v} , which was used for the analysis of the spectroscopic data. The real symmetry is C_1 since the rest of the ligands has to be taken into account as well. The average Ln-O bond lengths are 2.336 Å for **1-Er** and 2.363 Å for **1-Dy**, which is somewhat shorter than in reported extended three-dimensional Ln(III) carbonate structures¹⁵¹⁻¹⁵⁴ and thus further confirms the molecular nature of the systems.

As shown in Figure 38, the $[\text{LnO}_8]$ polyhedra and the guanidine counter ions $[\text{C}(\text{NH}_2)_3]^+$ are stacked in columns along the crystallographic a axis and are separated by ribbons of guanidine cations stacked along b in the bc plane. Within the ab plane, the $[\text{LnO}_8]$ units are separated by guanidine counter ions and lattice water molecules. Although the water molecules are part of an extended network of hydrogen bonds, they also act as additional spacers between the Ln(III) centers. Indeed, the shortest Er-Er and Dy-Dy distances in **1-Er** and **1-Dy** are 8.828 Å and 8.762 Å, respectively, justifying neglecting of intermolecular interactions.¹⁵⁵

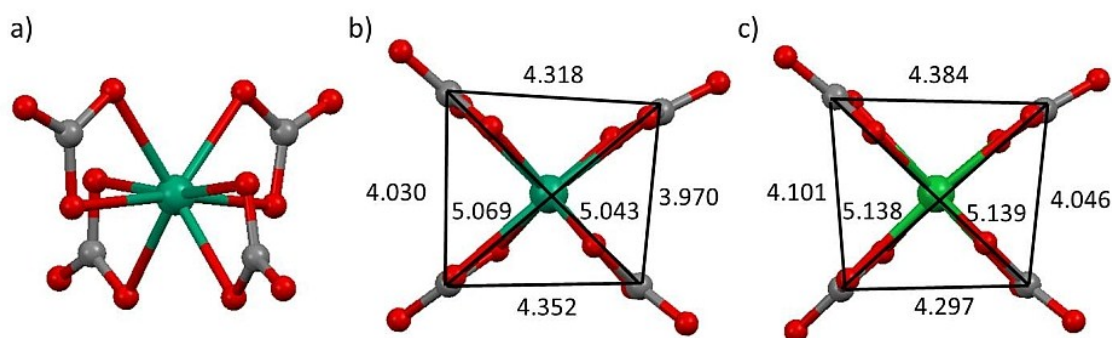


Figure 37: a) Crystallographically determined molecular structure of the $[\text{Er}(\text{CO}_3)_4]^{5-}$ anion in **1-Er** viewed perpendicular to the pseudo C_2 -axis. b) Molecular structure of the $[\text{Er}(\text{CO}_3)_4]^{5-}$ anion in **1-Er** viewed along the pseudo C_2 -axis, with distances between carbonate carbon atoms (in Å) indicated. c) Molecular structure of the $[\text{Dy}(\text{CO}_3)_4]^{5-}$ anion in **1-Dy** viewed along the pseudo C_2 -axis, with distances between carbonate carbon atoms (in Å) indicated.

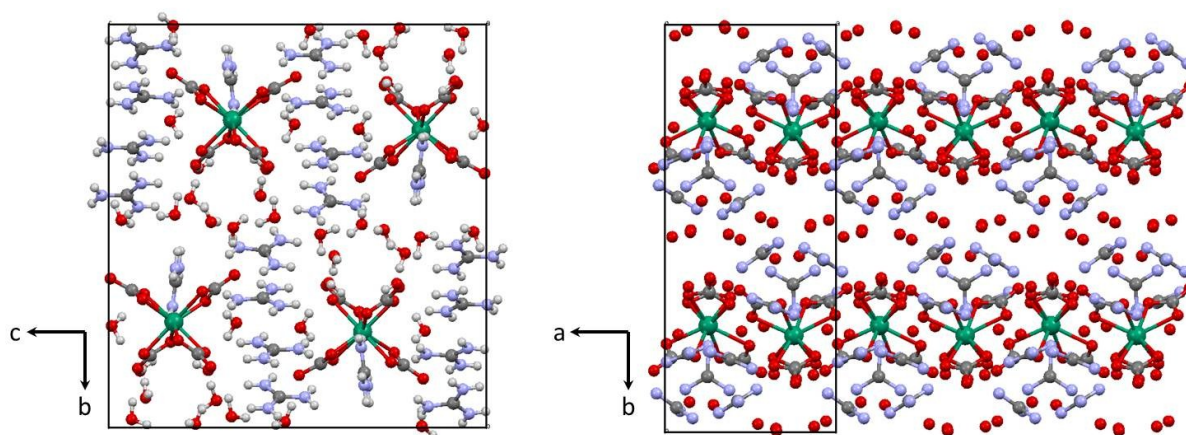


Figure 38: Packing diagrams of **1-Er**. Left: Unit cell viewed along the crystallographic *a* axis. Right: View along the crystallographic *c* axis. Erbium: green, oxygen: red, nitrogen: violet, carbon: grey, hydrogen: light grey.

The identity and phase purity of the compounds were further confirmed by room temperature X-ray powder diffraction studies performed by Dr. Pierre Eckold at the Institute of Inorganic Chemistry at the University of Stuttgart. Figure 39 shows the experimentally obtained X-ray diffraction data of **1-Er** and **1-Dy** together with the calculated diffraction patterns. The peak positions agree rather well, only some slight signal intensity differences were observed. These intensity differences are probably due to the fact that the powders were measured in their respective mother liqueurs while the calculated patterns are based on the single crystal X-ray analysis.

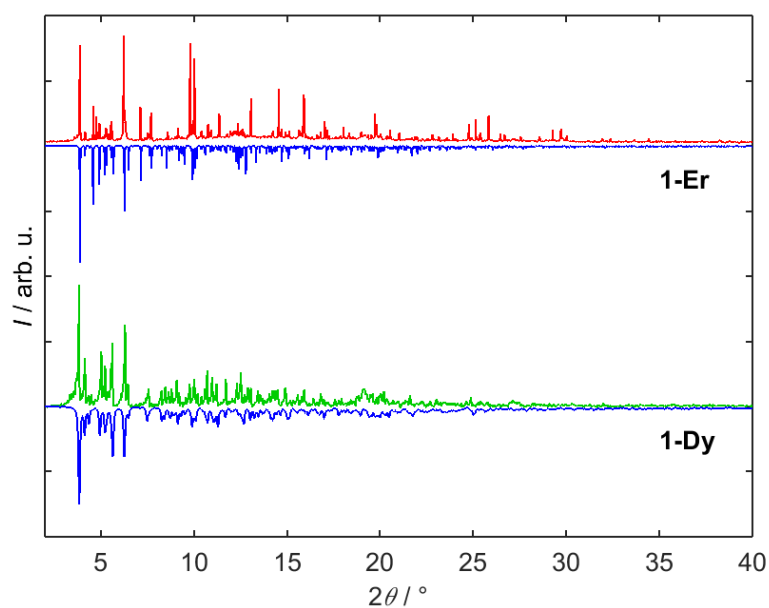


Figure 39: Powder X-ray diffraction patterns of **1-Er** and **1-Dy** at room temperature. Red and green color refers to experimentally observed data while simulated diffraction patterns are displayed in blue. The measurements were performed by Dr. Pierre Eckold.

4.2.2 Magnetic Properties

The magnetic characterization of **1-Er** and **1-Dy** was carried out by means of detailed direct current (dc) and alternating current (ac) susceptibility and magnetization measurements. Figure 40 shows the temperature dependence of the products of the molar magnetic susceptibility χ and the temperature T for **1-Er** and **1-Dy**, studied as mixtures with silicone grease. The dc χT value of **1-Er** at room temperature is $\chi T = 10.82 \text{ cm}^3 \text{ K mol}^{-1}$ while for **1-Dy** a room temperature value of $\chi T = 13.12 \text{ cm}^3 \text{ K mol}^{-1}$ is observed. These numbers are somewhat smaller than the free ion values of $11.48 \text{ cm}^3 \text{ K mol}^{-1}$ for the $^4I_{15/2}$ ground term of **1-Er** and $14.17 \text{ cm}^3 \text{ K mol}^{-1}$ for the $^6H_{15/2}$ ground state of **1-Dy** expected from Curie's law in equation (53). Such deviations can be indicative for large crystal field splittings, meaning that not all of the crystal field states are occupied at 300 K. With decreasing temperature, χT decreases until at 1.8 K values of $\chi T = 3.75 \text{ cm}^3 \text{ K mol}^{-1}$ (**1-Er**) and $8.57 \text{ cm}^3 \text{ K mol}^{-1}$ (**1-Dy**) are reached. This decrease is attributed to the influence of the crystal field splittings of the electronic ground multiplets and the resulting depopulation of higher lying crystal field states at low temperatures. As shown in Figure 40, the molar magnetization reaches values of $4.59 \mu_B$ (**1-Er**) and $5.28 \mu_B$ (**1-Dy**) at 1.8 K and 7 T.

Extracting the nine crystal field parameters required for C_{2v} symmetry solely from the magnetic data would lead to rather meaningless results because of the problem of over-parametrization. However, with the help of comprehensive spectroscopic studies it was possible to determine reliable sets of crystal field parameters that allowed reasonable simulation of not only the spectroscopic but also the magnetic data (solid lines in Figure 40). The crystal field analysis will be subject of section 4.2.4.

The magnetization dynamics of **1-Er** and **1-Dy** was investigated by temperature and frequency dependent ac susceptibility measurements. Figure 41 shows the temperature dependence of the real and imaginary components χ' and χ'' at various ac frequencies and an applied dc field of $H_{dc} = 1000 \text{ Oe}$. Applying a dc field in addition to the ac field permanently lifts the degeneracy of the microstates and therefore reduces the probability for quantum tunneling of the magnetization.¹⁵⁶ Clear frequency dependent maxima of the out-of-phase susceptibilities χ'' are observed, indicating slow relaxation of the magnetization due to the presence of effective energy barriers and the inability of the magnetization to follow the oscillating magnetic field. However, without an applied dc field no such maxima were observed, meaning that **1-Er** and **1-Dy** are so-called field-induced single-ion magnets.

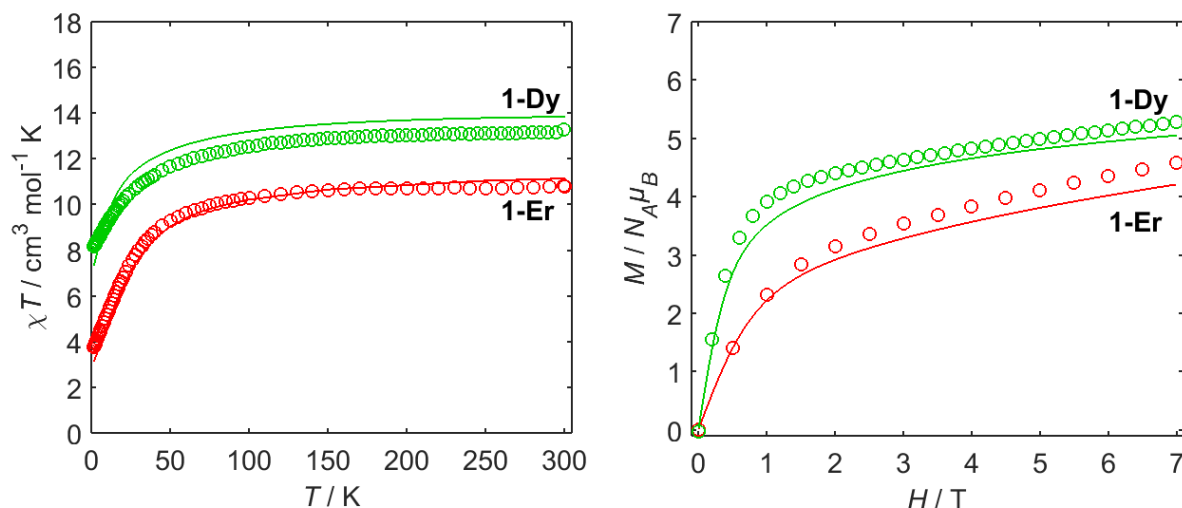


Figure 40: Left: Temperature dependence of the product of the magnetic susceptibility χ and the temperature T for **1-Er** (red) and **1-Dy** (green). The measurements were performed at an applied dc field of 0.1 T. Right: Magnetic field dependence of the magnetization of **1-Er** (red) and **1-Dy** (green) at 1.8 K. Solid lines correspond to the simulations based on the crystal field analysis (see text).

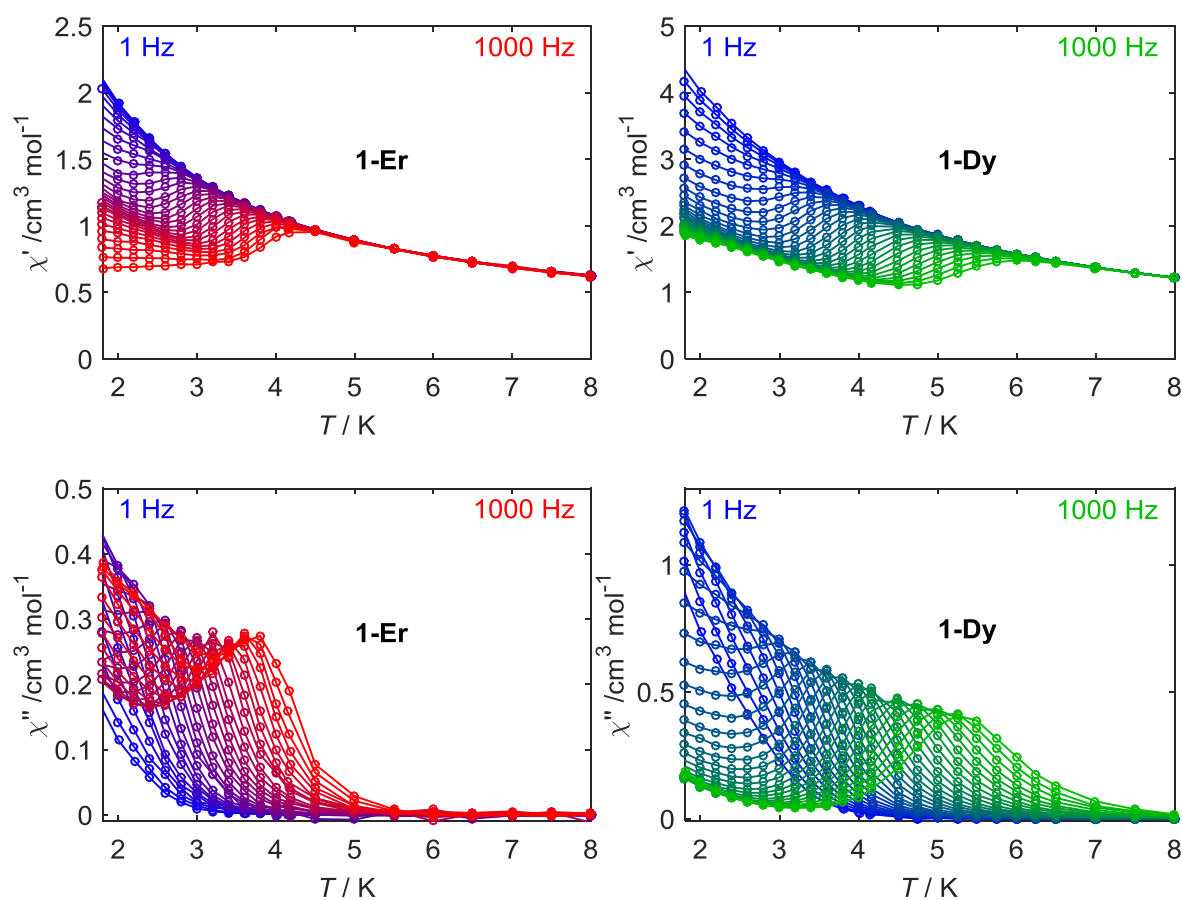


Figure 41: Temperature dependence of the ac susceptibilities for **1-Er** (left) and **1-Dy** (right) at an applied dc field of $H_{dc} = 1000$ Oe and at various ac frequencies. Top: In-Phase component χ' ; bottom: Out-of-phase component χ'' . Solid lines are guides for the eyes.

The generation of Argand plots of the out-of-phase (χ'') as functions of the in-phase components (χ') of the ac susceptibilities allowed the extraction of relaxation times and their distributions by fitting with generalized Debye functions^{3,94} (equation 56). The Argand plots for **1-Er** and **1-Dy** are shown in Figure 42. For **1-Er**, the Argand diagram clearly shows two overlapping semicircles revealing the presence of two well separated relaxation domains. Satisfactory fits were therefore only possible with the help of the sum of two modified Debye functions¹⁵⁷, yielding best-fit parameters for a fast and a slow relaxation process. Lanthanide-based SIMs with multiple relaxation processes are well-known in literature and the appearance of more than one relaxation domain is often attributed to different environments of the individual lanthanide ions or to intermolecular interaction.^{155,157-162} Since the Er(III) centers in **1-Er** are all symmetry-equivalent, the second relaxation process in **1-Er** appearing at very low temperatures (the fast process) might be attributed to the influence of distorted water molecules or the partial loss of lattice water. Partial loss of water molecules may result in increased dipolar interactions between the Er(III) centers, creating additional relaxation pathways. Indeed, no clear maximum of χ'' but only a shoulder is observed for longer dried samples of **1-Er** and **1-Dy**. The corresponding data are shown in the appendix, section 8.3.2. However, distinct relaxation phases with significantly different time constants were also reported for single spin systems and attributed to the temperature- and field-dependent contribution of distinct relaxations paths.^{163,164}

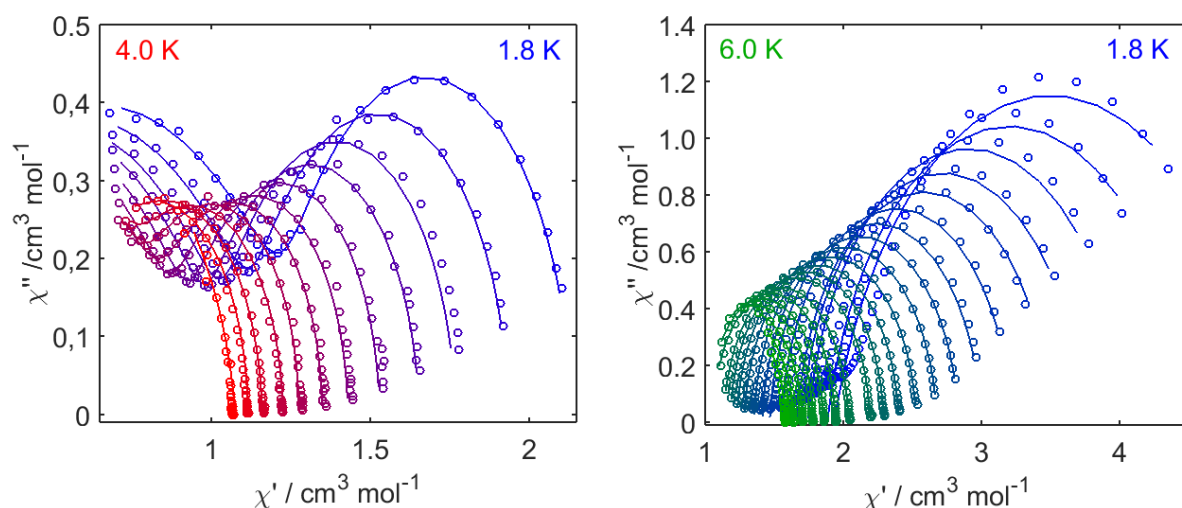


Figure 42: Argand plots for **1-Er** (left) and **1-Dy** (right) at different temperatures and an applied dc field of $H_{dc} = 1000$ Oe. Solid lines correspond to the best fits using generalized Debye equations.

For **1-Dy**, the presence of two distinct relaxation processes is much less pronounced and the Argand plots were thus satisfactorily simulated by assuming only one relaxation domain. The respective best-fit parameters are listed in Table A 10 in the appendix (section 8.3.3). The quality of the fits is further demonstrated in Figure 43, where the obtained parameters are used for the simulation of the frequency dependence of the ac susceptibilities of **1-Er** and **1-Dy**. For **1-Er**, reliable parameters were only obtained for temperatures up to 3.2 K (fast process) and 4.0 K (slow process), where the corresponding semi-circles in the Argand plots are sufficiently pronounced. The fast process not only shows significantly smaller relaxation times than the slow process but also much weaker temperature dependence. The fast process is therefore not attributed to a thermally activated 2-phonon mechanism, for which strong temperature dependence would be expected. However, clear temperature dependence was observed for the relaxation times of the slow process, indicating significant contributions of thermally activated relaxation mechanisms.

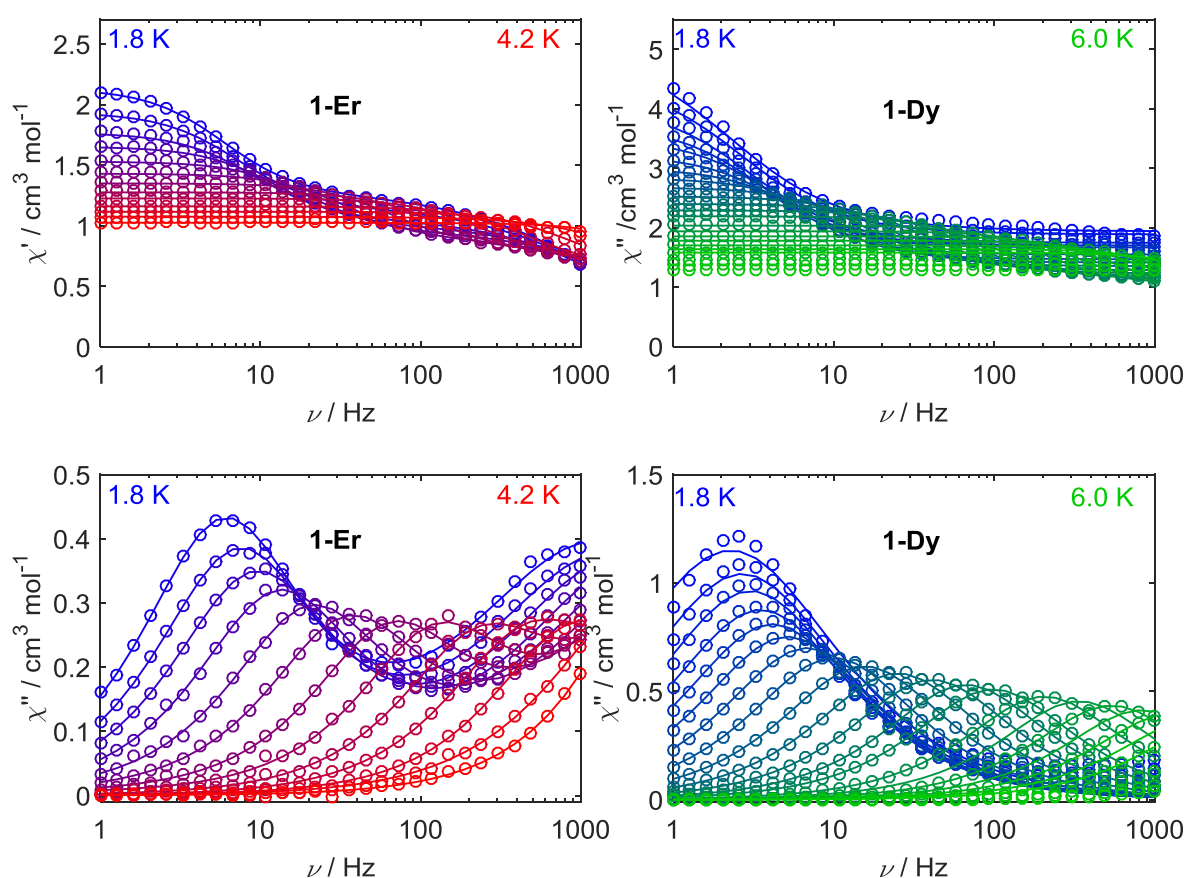


Figure 43: Frequency dependence of the ac susceptibilities of **1-Er** (left) and **1-Dy** (right) at an applied dc field of $H_{dc} = 1000$ Oe and various temperatures. Top: In-phase component χ' ; bottom: Out-of-phase component χ'' . Solid lines correspond to simulations using the parameters obtained by fitting the Argand plots.

While the distribution of relaxation times of the slow process is quite narrow ($\alpha \leq 0.04$), that of the fast process is rather broad ($\alpha = 0.1$ to $\alpha = 0.3$), supporting the assumption of structural distortions being the reason for the observation of two distinct relaxation domains.

For **1-Dy**, the Argand plots provided reliable parameters for temperatures up to 6.0 K and the obtained parameter for the distribution of relaxation times is in the range of $\alpha = 0.01$ (for 6.0 K) to $\alpha = 0.19$ (for 1.8 K).

In Figure 44, the relaxation times τ extracted for **1-Er** and **1-Dy** are displayed as Arrhenius plots ($\ln \tau$ as functions of the inverse temperature T^{-1}), showing a strongly curved dependence for the slow process and a rather temperature independent fast process in **1-Er**. Since a linear Arrhenius plot is expected for a pure Orbach mechanism, further relaxation mechanisms like quantum tunneling of the magnetization, direct relaxation and Raman processes have to be taken into account. The temperature dependence of these four relaxation mechanisms is given by the combination of equations (6), (7), (8) and (9):

$$\tau^{-1} = \frac{B_1}{1 + B_2 H^2} + A_{direct} \cdot H^{n_{direct}} \cdot T + C_{Raman} \cdot T^{n_{Raman}} + \tau_0^{-1} \exp\left(-\frac{\Delta E}{k_B T}\right) \quad (65)$$

In contrast, the Arrhenius plot obtained for **1-Dy** shows a pronounced linear regime at higher temperatures ($T \geq 3.6$ K), hinting at a rather pure Orbach mechanism. A linear fit using equation (6) seems to be reasonable and yields an effective energy barrier of $U_{eff} = 30 \text{ cm}^{-1}$ (appendix, section 8.3.4). However, at low temperatures ($T \leq 3.6$ K), clear deviation from linearity is observed and simulating the data in the entire temperature range requires application of equation (65) as well. Interestingly, reasonable fits can be obtained even without including the Orbach mechanism at all, demonstrating that equation (65) represents a severely over-parametrized problem (appendix, section 8.3.4). For getting deeper insight into the nature of the relaxation mechanisms involved, more detailed magnetometric and spectroscopic studies are required.

At very low temperatures (in practice at 1.8 K), it can be assumed that the contributions of the two-phonon mechanisms (Raman, Orbach) are negligible and only the field dependent direct relaxation and quantum tunneling processes have to be taken into account. Thus, further ac susceptibility measurements were performed at 1.8 K and various applied dc bias fields.

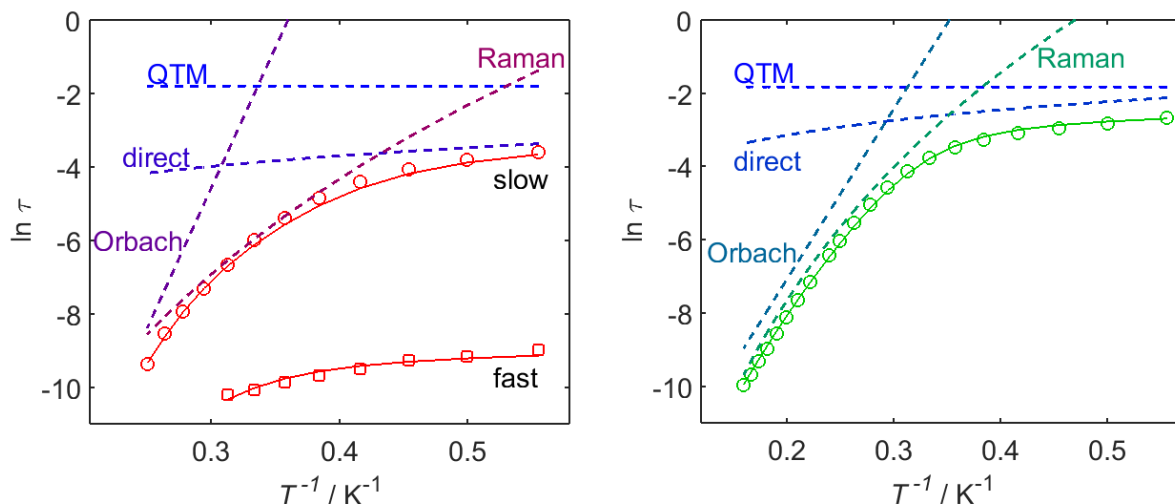


Figure 44: Arrhenius plots for **1-Er** (left) and **1-Dy** (right) obtained at applied dc fields of 1000 Oe. Open symbols correspond to the experimentally observed data. Dashed lines illustrate the different contributions to the relaxation while solid lines represent the sums of these contributions. For reasons of clarity, only the contributions to the slow process are shown for **1-Er**.

The resulting frequency dependence of χ' and χ'' as well as the simulations based on the parameters obtained by fitting the corresponding Argand plots are shown in the appendix, section 8.3.5. The field dependence of the relaxation times for **1-Er** and **1-Dy** is illustrated in Figure 45 and can be explained by equation (65): At low dc fields, quantum tunneling dominates and relatively fast relaxation is observed. With increasing field, the relaxation times increase due to suppressing of quantum tunneling until a maximum is reached at intermediate fields. Higher fields favor direct relaxation processes and the relaxation times decrease again. This behavior was modeled by using the combination of equations (8) and (9), i.e. the first two terms in equation (65) and least-squares fitting yielded the best-fit parameters given in Table 3. n_{direct} was fixed to the theoretical value of $n_{\text{direct}} = 2$ for a Kramers doublet in the presence of hyperfine interactions.³⁸

Table 3: Best-fit parameters describing the magnetic field-dependence of the relaxation times for **1-Er** and **1-Dy** at 1.8 K.

	1-Er		1-Dy
	fast process	slow process	
$A_{\text{direct}} / \text{T}^{-2} \text{K}^{-1} \text{s}^{-1}$	$19 \cdot 10^4$	1621	466
B_1 / s^{-1}	$50 \cdot 10^{15}$	25.2	9.82
B_2 / T^{-2}	$3 \cdot 10^{14}$	318	58.3

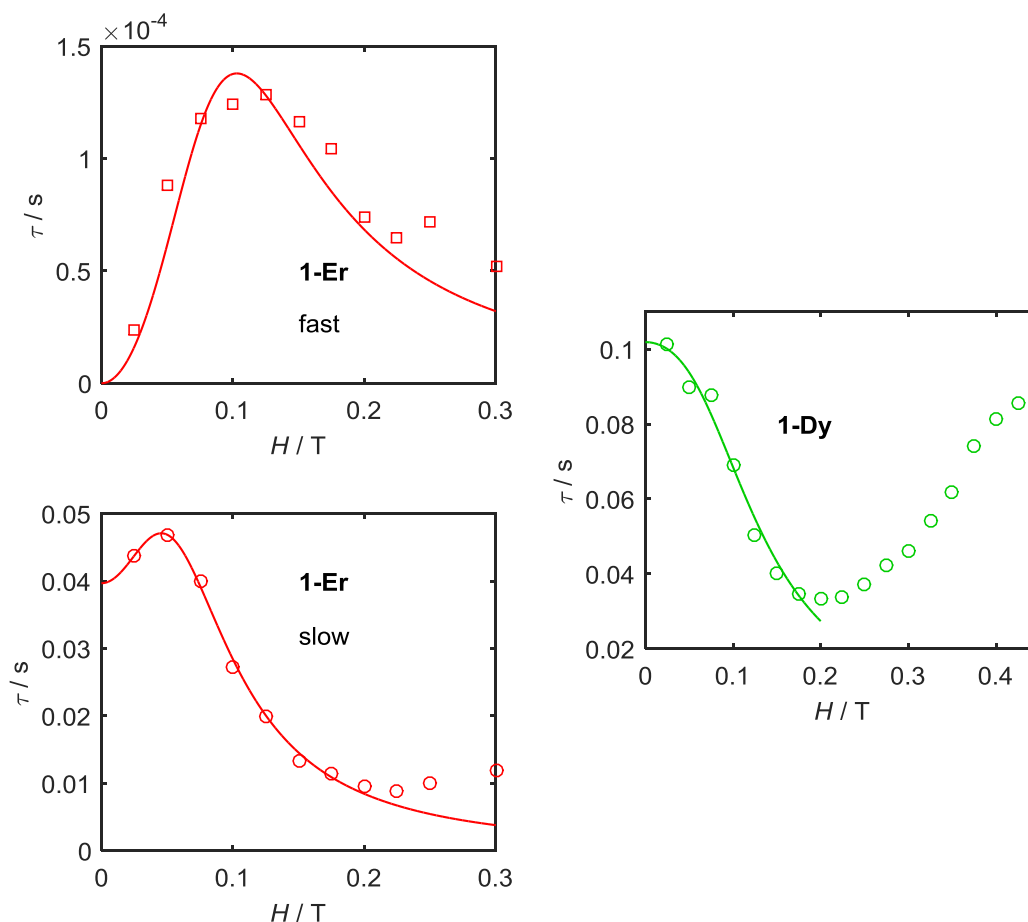


Figure 45: Magnetic field dependence of the relaxation times of **1-Er** and **1-Dy** at 1.8 K. Solid lines correspond to the best fits (see text).

At dc fields higher than 0.2 T, the relaxation times for **1-Dy** increase again, which cannot be simulated by equations (8) and (9). Such a behavior has been observed by others as well³⁰ but has not yet been fully understood. Possible explanations might lie for example in the presence of nuclear spins or small intermolecular interactions that lead to minima in the relaxation times at given fields.^{165,166}

Table 3 reveals that the values derived for the fast process in **1-Er** are extremely larger than those for the slow process, supporting the previously made assumption that the fast process in **1-Er** does not arise from a thermally driven two-phonon relaxation mechanism. Comparing **1-Er** and **1-Dy**, lower values are found for **1-Dy**, consistent with the overall higher relaxation times in **1-Dy**.

Fixing the parameters for direct relaxation and quantum tunneling of the magnetization to the values given in Table 3 reduces the number of free parameters in equation (65). Furthermore, the Raman exponent n_{Raman} can be fixed to the value derived for Kramers ions in the low temperature limit, i.e. to $n_{\text{Raman}} = 9$.³⁸ At this stage, the remaining

unknown parameters are the Raman coefficients C_{Raman} , the attempt times τ_0 and the energy barriers ΔE , which correspond to the energies of real intermediate crystal field states. Due to the strong curvature in the Arrhenius plot for the slow process in **1-Er**, the magnetic data are not sufficient to unequivocally determine the energy of the crystal field state involved in the Orbach process. For **1-Dy**, a preliminary linear fit yielded an effective energy barrier of $U_{\text{eff}} = 30 \text{ cm}^{-1}$ but since a reasonable fit can also be obtained by not including the Orbach process at all, this value might be wrong. Spectroscopic measurements are thus mandatory for determining the crystal field states of **1-Er** and **1-Dy**. As will be shown below, the first crystal field excited doublets are located at 52 cm^{-1} (**1-Er**) and 29 cm^{-1} (**1-Dy**). Using them as fixed values for ΔE , the best-fit parameter values given in Table 4 were obtained. The corresponding simulations are shown in Figure 44.

Altogether, the derived parameter values indicate the dominance of the Raman mechanism and the direct relaxation for the slow process in **1-Er** in the studied temperature range. In contrast, the contribution of the Orbach mechanism for **1-Dy** is much more pronounced although the energy barrier, i.e. the energy of the first excited Kramers doublet, seems to be lower. These results clearly demonstrate that SIM behavior cannot be solely explained by large crystal field splittings.

Table 4: Best-fit parameters describing the thermally assisted magnetic relaxation in **1-Er** and **1-Dy**.

	1-Er		1-Dy
	fast process	slow process	
$\Delta E / \text{cm}^{-1}$	-	52	29
τ_0 / s^{-1}	-	$1.2 \cdot 10^{-12}$	$1.8 \cdot 10^{-7}$
$C_{\text{Raman}} / \text{K}^{-9} \text{ s}^{-1}$	0.57	0.02	0.001

4.2.3 Spectroscopic Results

To determine the energies of the crystal field levels and to obtain more information about the composition of the eigenstates that are responsible for the static and dynamic magnetic properties, extensive spectroscopic studies on **1-Er** and **1-Dy** were carried out.

With the help of Raphael Marx and Dr. María Dörfel (Institute of Physical Chemistry, University of Stuttgart), far-infrared (FIR) spectra at 9 and 10 K and at magnetic fields

between 0 T and 6 T were recorded. Figure 46 shows the obtained transmission spectra as well as the normalized spectra obtained by dividing by the spectra at 6 T. For **1-Er**, three crystal field excitations were observed, namely at 52, 84 and 105 cm^{-1} . The splitting of the middle feature is attributed to the coupling of crystal field and vibrational transitions. Similar splittings were observed in the far-infrared spectra of the four-coordinate Co(II) complexes studied in the further course of this work (section 4.3.3), for which theoretical calculations confirmed the presence of spin-phonon couplings.¹⁶⁷ Crystal field analysis for **1-Er** (see below) confirmed that the level at 52 cm^{-1} corresponds to the first excited Kramers doublet and this value was therefore used as ΔE for the simulation of the Arrhenius plot (Figure 44). The normalized FIR-spectrum of **1-Dy** shows an intense feature at around 100 cm^{-1} that can be attributed to a crystal field excitation. Interestingly, there is no clear signal close to 30 cm^{-1} as expected from the magnetic data. Further spectroscopic data are required to find out the reason for this discrepancy as well as the correct energetic position of the first excited crystal field state.

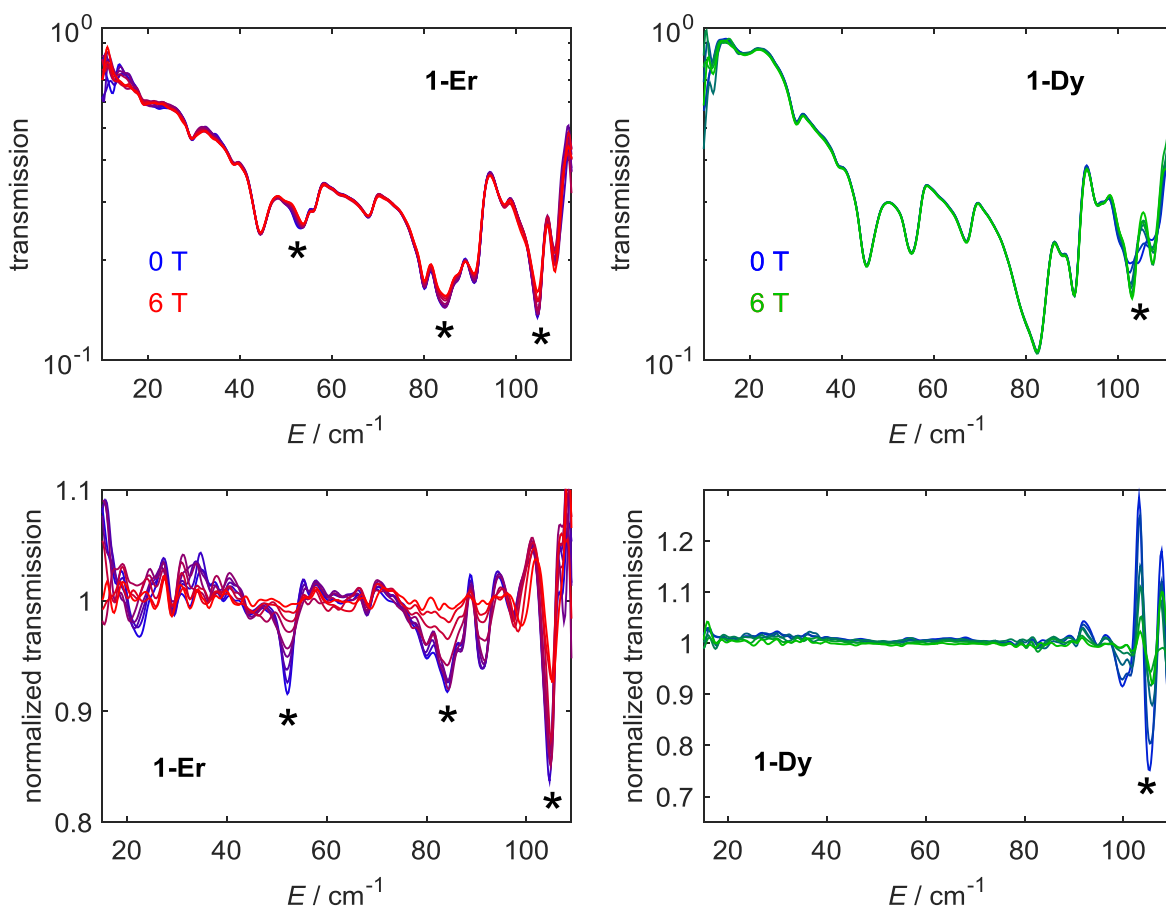


Figure 46: Far-infrared spectra of **1-Er** (left) and **1-Dy** (right) recorded at 9 K and 10 K, respectively. Asterisks indicate signals that arise from crystal field excitations. The spectra were recorded with the help of Raphael Marx and Dr. María Dörfel.

Another useful method for gaining information about the Kramers doublets within the electronic ground term is luminescence spectroscopy. Thus, solid state luminescence spectra of **1-Er** and **1-Dy** at low temperatures were recorded at the University of Copenhagen with the help of Maren Gysler (Institute of Physical Chemistry, University of Stuttgart), Dr. Stergios Piligkos and Theis Brock-Nannestad (both Department of Chemistry, University of Copenhagen).

Er(III) is mainly known for its NIR emission^{102,168} but some Er(III) compounds display luminescence in the visible range as well.¹⁶⁹⁻¹⁷¹ Especially the transition from the excited $^4S_{3/2}$ multiplet to the $^4I_{15/2}$ ground state has been shown to be very useful for the determination of the crystal field level structure of the electronic ground term.¹⁷⁰ However, no Er(III) emission was observed in the luminescence spectra of **1-Er**, neither in the visible nor in the NIR range. Instead of the expected Er(III)-based sharp luminescence signals a very broad feature was observed, exhibiting negative dips located at 355, 364, 379, 403, 442, 449, 485, 520 and 541 nm. An example of a spectrum recorded at 20 K using an excitation wavelength of 290 nm is shown in the appendix, section 8.3.6. The energies of the negative dips match the optical absorption bands (see below) and therefore might be attributed to resonant reabsorption of the ligand emission by the Er(III) center. Similar reabsorption phenomena have been already observed by others.¹⁷²⁻¹⁷⁴ According to the Dieke diagram⁶², the observed dips can be assigned to the following f-f-transitions of the Er(III) ion: $^4I_{15/2} \rightarrow ^2G_{7/2}$, $^2K_{15/2}$, $^4G_{9/2}$ (335 and 364 nm), $^4I_{15/2} \rightarrow ^4G_{11/2}$ (379 nm), $^4I_{15/2} \rightarrow ^2H_{9/2}$ (403 nm), $^4I_{15/2} \rightarrow ^4F_{3/2}$ (442 nm), $^4I_{15/2} \rightarrow ^4F_{5/2}$ (449 nm), $^4I_{15/2} \rightarrow ^4F_{7/2}$ (485 nm), $^4I_{15/2} \rightarrow ^2H_{11/2}$ (520 nm) and $^4I_{15/2} \rightarrow ^4S_{3/2}$ (541 nm). Increasing the excitation wavelengths in order to avoid ligand excitation led to a weakening of the negative dips, but still no Er(III) luminescence was observed, indicating efficient quenching mechanisms, e.g. due to the surrounding water molecules. Luminescence spectroscopy thus turned out to be unsuitable for determining the ground state crystal field splittings of **1-Er**. Instead, excited state splittings probed by electronic absorption and MCD-spectroscopy had to be used for indirectly obtaining more information about the ground state levels.

In contrast, usable luminescence data were obtained for **1-Dy** and signals arising from the transitions $^4F_{9/2} \rightarrow ^6H_{15/2}$ and $^4F_{9/2} \rightarrow ^6H_{13/2}$ were observed in the recorded low temperature luminescence spectra. As shown in Figure 47, the emission bands show splitting patterns due to the crystal field splitting of the respective final states and the $^4F_{9/2} \rightarrow ^6H_{15/2}$ emission thus yields information about the ground state level structure while the $^4F_{9/2} \rightarrow ^6H_{13/2}$ transition complements the absorption and MCD data. However, Figure 47 clearly shows that

the resolution is not sufficient to unequivocally determine the energies of all the crystal field levels involved and the observed patterns thus only allow their rough estimation. The low resolution might be due to overlapping vibronic transitions, which is a common problem in optical lanthanide spectra, or due to distributions in the crystal field parameters.⁶⁰ Only the better resolved emission lines were thus initially included in the crystal field analysis for **1-Dy** (section 4.2.4). Interestingly, the high-energy peak in the ${}^4F_{9/2} \rightarrow {}^6H_{15/2}$ emission spectrum shows a shoulder, for which Gaussian deconvolution yielded an energy separation of 29 cm^{-1} . It is not fully clear at this stage if this energy separation corresponds to the energy of an excited Kramers doublet or if it is due to a vibronic transition. Strikingly, the value of 29 cm^{-1} coincides well with the effective energy barrier derived from the ac susceptibility measurements and should thus be considered at least as an option for the energy of the first excited doublet in the crystal field analysis. If so, the luminescence spectrum hints at the second excited doublet lying at 94 cm^{-1} , in reasonably good agreement with the observed signal in the FIR-spectrum.

All in all, FIR and luminescence spectroscopy provided information about the energies of some single Kramers doublets but they did not allow the full determination of the ground state level structures, neither for **1-Er** nor for **1-Dy**. Even the observation of all eight expected transitions would not be sufficient for the unambiguous determination of the nine crystal field parameters required in C_{2v} symmetry.

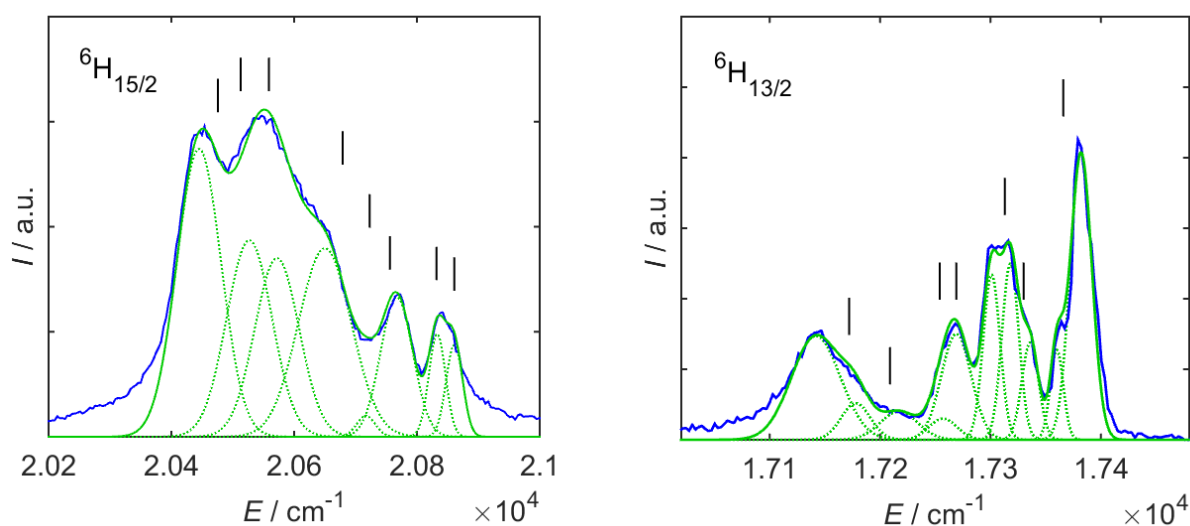


Figure 47: Low temperature luminescence spectra of **1-Dy** for the transitions from ${}^4F_{9/2}$ to the ground multiplet ${}^6H_{15/2}$ (left) and to the first excited multiplet ${}^6H_{13/2}$ (right). Blue solid lines show the experimentally obtained spectra while green lines show the deconvolution into individual Gaussian bands (dashed lines) and their sums (solid lines). Black bars show the calculated transition energies based on the crystal field analysis. The spectra were recorded with the help of Maren Gysler, Dr. Stergios Piligkos and Theis Brock-Nannestad.

That means that spectroscopic methods which solely probe the ground multiplet of low-symmetry compounds at best allow the determination of energies but not the determination of crystal field parameters that correctly describe the nature of the states. However, it is mainly the nature of the states that determines the dynamic magnetic properties.

Electronic absorption and MCD-spectroscopy at low temperatures were thus used for determining as many energy levels as possible, including those that are most sensitive to the variation of certain crystal field parameters B_{kq} . For Er(III), these are the levels arising from the free ion terms $^4S_{3/2}$, $^4F_{3/2}$ ($k=2$), $^4F_{5/2}$, ($k=4$) and $^4I_{9/2}$ ($k=6$) while for Dy(III) the levels arising from $^6F_{3/2}$ ($k=2$), $^6F_{5/2}$ ($k=4$) and $^6F_{7/2}$, $^4F_{9/2}$ ($k=6$) are most sensitive to changes of the parameters with the k -values given in brackets.⁶⁰ A wealth of high resolution UV/Vis/NIR-absorption and MCD-spectra of **1-Er** and **1-Dy** dispersed in transparent silicone grease were recorded and the observed signals were assigned to the corresponding free ion terms according to the Dieke diagram⁶². Some selected examples are shown in Figure 48 and Figure 49 while further spectra are shown in the appendix, section 8.3.7.

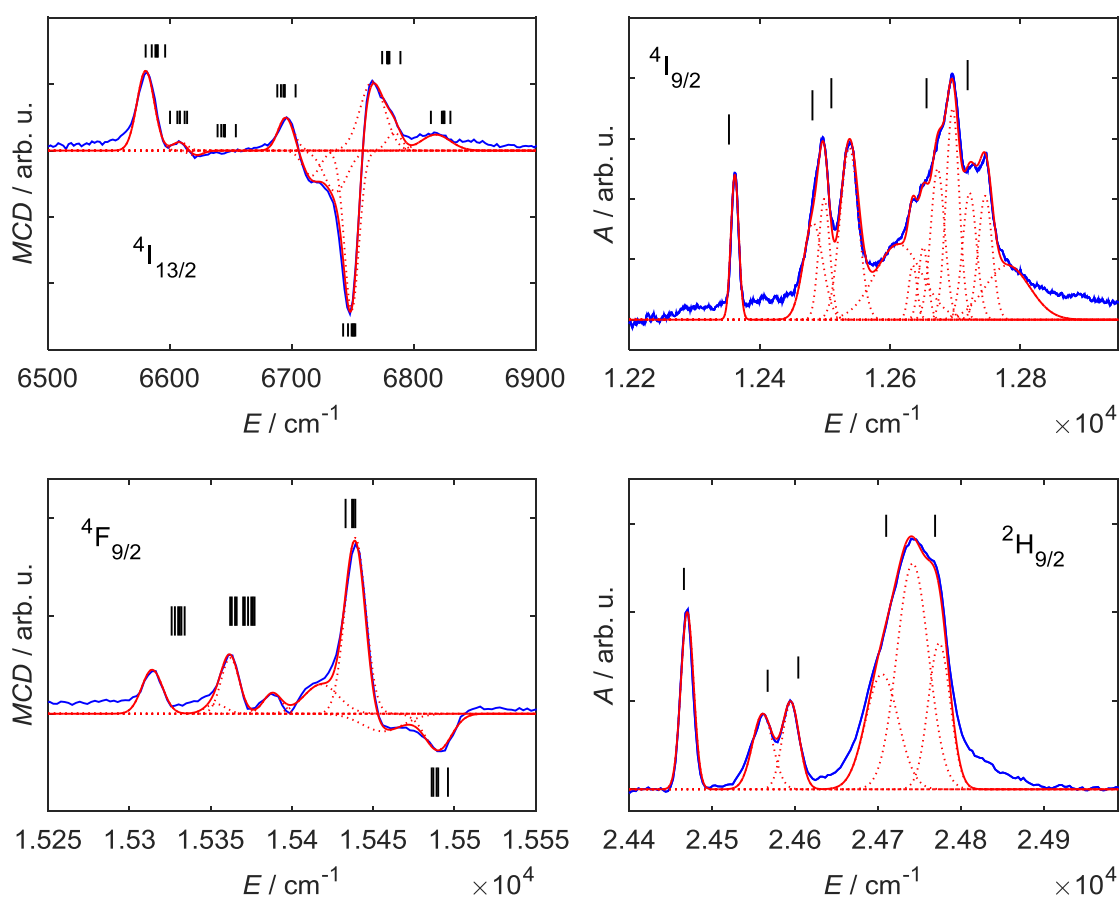


Figure 48: Selected examples of electronic absorption and MCD-spectra of **1-Er** recorded at 2 K and 3 T. Experimentally observed spectra are shown in blue while red lines show the deconvolution into individual Gaussian lines (dotted) and their sums (solid). Black bars depict the calculated transition energies based on the parameters obtained from crystal field analysis.

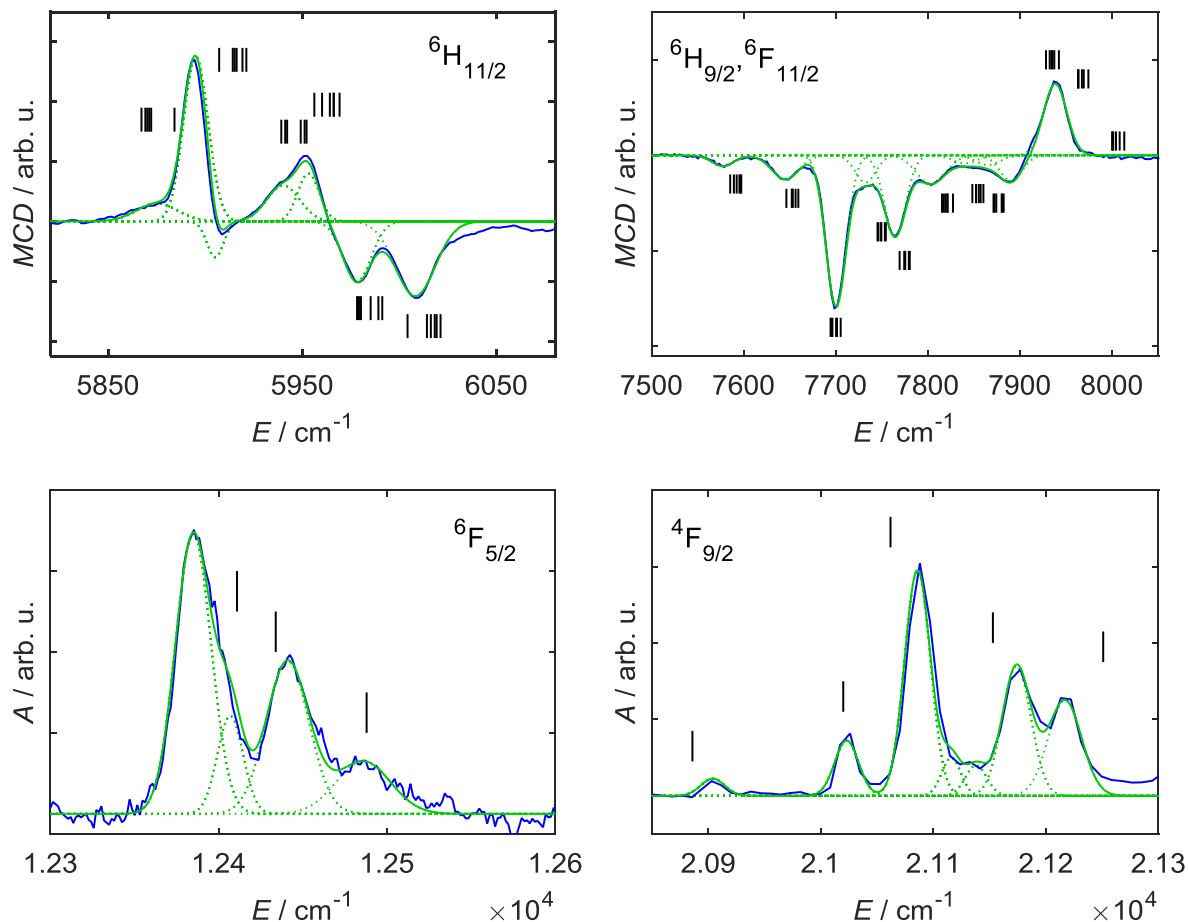


Figure 49: Selected examples of electronic absorption and MCD-spectra of **1-Dy** recorded at 2 K and 3 T. Experimentally observed spectra are shown in blue while green lines show the deconvolution into individual Gaussian lines (dotted) and their sums (solid). Black bars depict the calculated transition energies based on the parameters obtained from crystal field analysis.

The signals are clearly split due to the excited state crystal field splittings and the individual energetic positions were determined by careful deconvolution into sums of Gaussian lines. In some cases, the signal shapes were better reproduced by adding more Gaussian lines than expected according to the multiplicity of the final states. Similarly to the luminescence spectra, the additional peaks can be attributed to vibronic excitations since most f-f transitions are induced electric dipole transitions and might gain intensity by vibronic coupling to ungerade vibrational modes.⁶⁰ The FIR-spectra already confirmed the existence of vibrational transitions in the same energy range as the crystal field splittings. This aspect was kept in mind during the subsequent crystal field analysis and in most cases the lower-energy component was used. However, structural imperfections, e.g. caused by the lattice water molecules in **1-Er** and **1-Dy**, might also have led to the observed satellite bands. From the FIR and optical spectra together, the energetic positions of no fewer than 48 crystal field levels of **1-Er** and 55 levels of **1-Dy** were determined, with the main contribution provided by

electronic absorption and MCD-spectroscopy. These energy levels provided the foundation for the subsequent crystal field analysis.

The above-mentioned spectroscopic measurements were complemented by EPR-spectroscopy since this method is exquisitely sensitive to the composition of the lowest Kramers doublet and can therefore be applied as a tool for verifying the correct description of the ground state by a set of empirically determined crystal field parameters. Low-temperature EPR-spectra of mulls of **1-Er** and **1-Dy** in fluorolube® were recorded at conventional X-band frequency (9.5 GHz) and at higher frequencies (90 – 400 GHz). The high-frequency EPR (HF-EPR) spectra were recorded with the help of Raphael Marx and Dr.-Ing. Petr Neugebauer (both Institute of Physical Chemistry, University of Stuttgart). As shown in Figure 50, two clear and one weaker resonance line with effective g -values of $g_1 = 7.64$, $g_2 = 4.85$ and $g_3 = 1.94$ are observed in the HF-EPR-spectra of **1-Er**.

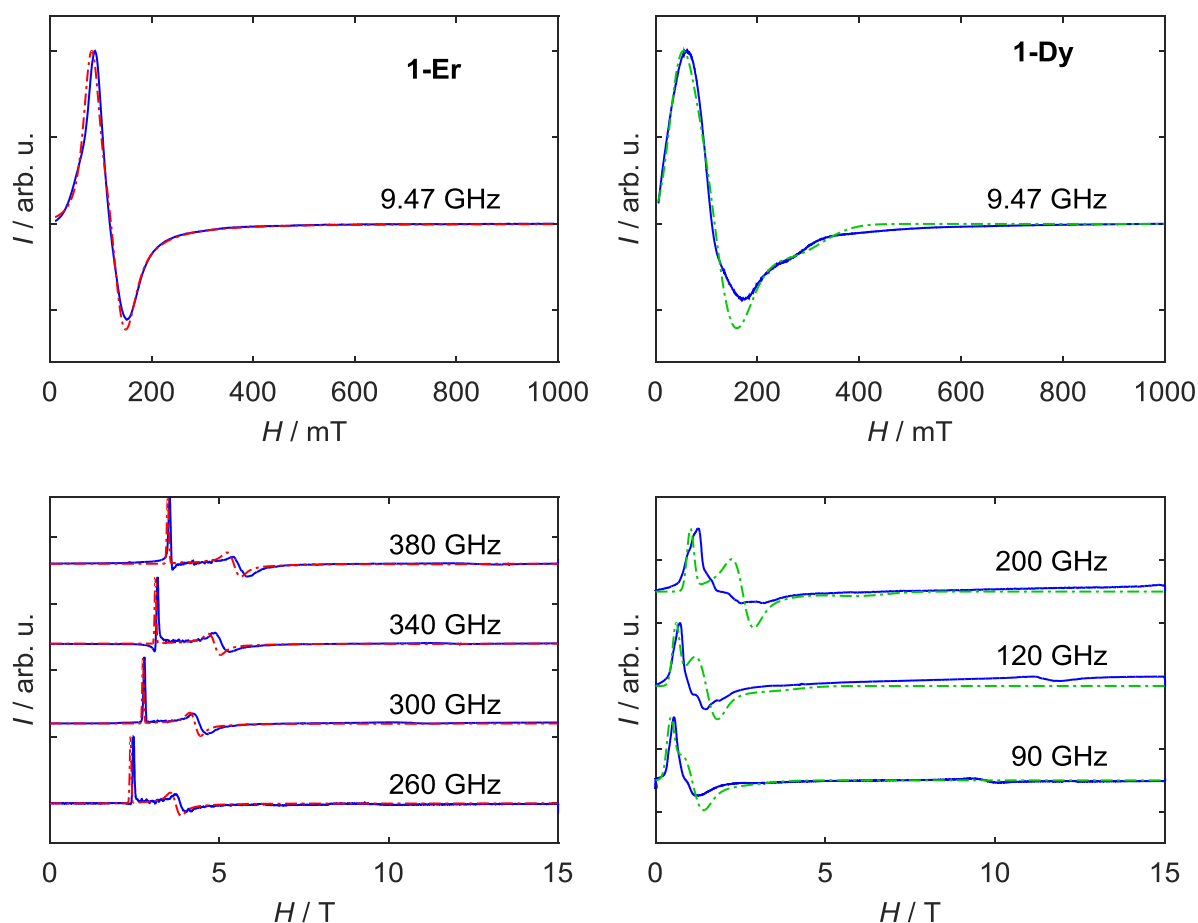


Figure 50: Low temperature multi-frequency EPR-spectra of **1-Er** (left) and **1-Dy** (right). Blue lines correspond to experimental spectra while dashed red (**1-Er**) or green (**1-Dy**) lines show the simulations based on the effective g -tensors obtained from the crystal field analysis. The HF-EPR-spectra were recorded with the help of Raphael Marx and Dr.-Ing. Petr Neugebauer.

For **1-Dy**, the situation looks more complicated: The EPR signals show complex structures and the determination of the principal g -values from the experimental spectra is not straightforward. Within the $S_{\text{eff}} = \frac{1}{2}$ model and neglecting the structure observed in the spectra, the best simulation is obtained using $g_1 = 12.5$, $g_2 = 6.0$ and $g_3 = 2.5$ but the uncertainties are rather high. The reason for the observed structure is not fully clear. One possible explanation is the presence of very low-lying excited Kramers doublets that are populated at low temperatures and contribute to the observed signals. However, according to the results of the crystal field analysis (see below), this explanation can almost certainly be ruled out. Another, more probable explanation is the effect of structural distortions like impurities or disordered water molecules that lead to slight variations of the environment of the individual Dy(III) centers.³⁸ Indeed, as evidenced by the crystallographic R -indices of 4.73 % for **1-Er** and 7.42 % for **1-Dy**, the crystal quality of **1-Dy** was worse compared to that of **1-Er**, which further supports this explanation.

4.2.4 Crystal Field Analysis and Electronic Structure

Based on the combined results from FIR, optical and EPR-spectroscopy, crystal field parametrization was performed for complexes **1-Er** and **1-Dy** in order to find out the composition of their eigenfunctions. The employed Hamiltonian was introduced in section 2.2 and consists of a free-ion part and a crystal field part:^{55,56,60}

$$\begin{aligned} \mathcal{H}_{\text{free ion}} = & E_{\text{AVE}} + \sum_{k=2,4,6} F^k f_k + \zeta_{4f} A_{SO} + \alpha L(L+1) + \beta G(G_2) + \gamma G(G_7) \\ & + \sum_{i=2,3,4,6,7,8} t_i T^i + \sum_{k=0,2,4} m_k M^k + \sum_{k=2,4,6} p_k P^k \end{aligned} \quad (10)$$

$$\begin{aligned} V_{CF}(C_{2\nu}) = & B_{20} C_0^{(2)} + B_{22} (C_{-2}^{(2)} + C_2^{(2)}) + B_{40} C_0^{(4)} + B_{42} (C_{-2}^{(4)} + C_2^{(4)}) \\ & + B_{44} (C_{-4}^{(4)} + C_4^{(4)}) + B_{60} C_0^{(6)} + B_{62} (C_{-2}^{(6)} + C_2^{(6)}) \\ & + B_{64} (C_{-4}^{(6)} + C_4^{(6)}) + B_{66} (C_{-6}^{(6)} + C_6^{(6)}) \end{aligned} \quad (21d)$$

The free-ion parameters and the crystal field parameters were determined by least-squares fitting of calculated against experimental energy levels using the software package “f-shell empirical programs” developed by Prof. Dr. Michael F. Reid (Department of Physics and Astronomy, University of Canterbury)¹⁷⁵. The calculations were performed in the full basis of

states arising from the respective $4f^N$ configuration, i.e. 364 states for **1-Er** and 2002 states for **1-Dy**. Of the free ion parameters only E_{AVE} , F^2 , F^4 , F^6 and ζ_{4f} were varied. The remaining parameters have no significant influence on the crystal field splittings and were thus kept fixed to mean literature values.⁶⁰

The main difficulty during the fitting process arose from the presence of overlapping bands in the optical spectra and their assignment to crystal field or vibronic transitions. Thus, the following procedure was chosen: The spectroscopically determined energies were first ordered in ascending energy and preliminarily assigned. These preliminary assignments to crystal field or vibronic transitions were mainly based on the signal intensities and linewidths. After the actual least-squares fitting had taken place, some signals were reassigned and the fitting was repeated. Different sets of starting parameters were tried and once a reasonable agreement between experimental and calculated energy levels had been achieved, the quality of the obtained parameter set was checked by simulating the corresponding EPR-spectra and the static magnetic data. The effective g -tensors required for simulating the EPR-spectra were calculated with the help of the program `pycf`¹⁷⁶, written by Sebastian Horvath (Department of Physics and Astronomy, University of Canterbury). The parameter set that described the spectroscopic and magnetic data in the most satisfactory way was finally fine-tuned by manually adjusting the crystal field parameters. The final parameter sets obtained for **1-Er** and **1-Dy** are listed in Table 5 while Table A 13 and Table A 14 in the appendix provide a comparison between experimental and calculated energy levels. The root mean squares (rms) deviations for **1-Er** and **1-Dy** are ca. 17 cm^{-1} and ca. 18 cm^{-1} , respectively, confirming the quality of the fits. As a rule of thumb, parameter sets leading to rms values below 20 cm^{-1} are considered as reasonably describing the electronic structure.⁶⁰

The crystal field parameters were transformed to lie in the standard range defined by $0 \leq B_{22}/B_{20} \leq (1/6)^{1/2}$. Standardization of crystal field parameters corresponds to 90 degree rotations of the coordinate frame and was proposed by Rudowicz *et al.* in order to facilitate the comparison of crystal field parameters for different compounds.^{177,178} Most of the parameters obtained for **1-Er** and **1-Dy** are reasonably similar but B_{40} and B_{60} differ significantly. However, Burdick *et al.* pointed out that crystal field standardization based exclusively upon rank 2 terms might be insufficient and they proposed to utilize crystal field strength parameters instead of standardized crystal field parameters for comparing the influence of the crystal field in different compounds.¹⁷⁹

Table 5: Free-ion and crystal field parameters determined for **1-Er** and **1-Dy**.

	free-ion parameters / cm^{-1}		crystal field parameters / cm^{-1}		
	1-Er	1-Dy	1-Er	1-Dy	
E_{AVE}	35469 ± 10	55944 ± 60	B_{20}	145 ± 50	189 ± 30
F^2	95991 ± 100	91778 ± 240	B_{22}	40 ± 25	10 ± 40
F^4	69046 ± 105	64782 ± 260	B_{40}	0 ± 50	-460 ± 100
F^6	51686 ± 170	50920 ± 210	B_{42}	930 ± 30	828 ± 40
ζ_{4f}	2355 ± 2	1883 ± 3	B_{44}	-386 ± 30	-510 ± 90
α (fixed)	15.86	17.86	B_{60}	350 ± 30	613 ± 50
β (fixed)	-541	-628	B_{62}	440 ± 20	293 ± 100
γ (fixed)	1572	1170	B_{64}	620 ± 15	540 ± 70
T^2 (fixed)	286	326	B_{66}	330 ± 50	400 ± 30
T^3 (fixed)	48	23	crystal field strength parameters / cm^{-1}		
T^4 (fixed)	14	83			
T^6 (fixed)	-319	-294	1-Er 1-Dy		
T^7 (fixed)	203	403	S^2	70 ± 32	85 ± 31
T^8 (fixed)	333	340	S^4	475 ± 37	483 ± 94
M^0 (fixed)	5.58	4.46	S^6	339 ± 36	334 ± 87
M^2 (fixed)	3.12	2.50			
M^4 (fixed)	2.12	1.69			
P^2 (fixed)	730	610			
P^4 (fixed)	548	458			
P^6 (fixed)	365	305			

The crystal field strength parameters are defined by⁶⁰

$$S_{cf}^k = \sqrt{\frac{1}{2k+1} \left[(B_{k0})^2 + 2 \sum_{q>0} |B_{kq}|^2 \right]} \quad (66)$$

and are invariant under rotation of the coordinate frame. Indeed, the crystal field strength parameters obtained for **1-Er** and **1-Dy** are very similar (Table 5), as expected for isostructural compounds. Only the rank 2 parameters show some deviation, which might be ascribed to the parameter uncertainties. The parameter uncertainties given in Table 5 were estimated by taking the standard deviations given in the f-shell output and modifying them by considering the effect of parameter change on the EPR simulations.

The simulations of the magnetic data and the EPR-spectra based on the final parameter sets are shown in Figure 40 and Figure 50 while black bars in Figure 48, Figure 49, Figure A 11 and Figure A 12 indicate the calculated transition energies in the electronic absorption and MCD-spectra. Excellent agreement between experimental data and simulations was achieved for **1-Er**, confirming the reliability of the obtained set of crystal field parameters. The energy of the first excited Kramers doublet was calculated to be 44 cm^{-1} , showing that the signal in the FIR-spectra at 52 cm^{-1} corresponds to a transition to this state.

An interesting point and important to mention is the fact that a rather different parameter set with a lower rms deviation (about 13 cm^{-1}) was obtained for **1-Er** when only the optically and FIR-spectroscopically determined energy levels were taken into account during the fitting procedure.¹⁴⁹ However, this parameter set did not allow for satisfying simulations of the EPR-spectra and the magnetization curve, e.g. it does not correctly describe the composition of the lowest Kramers doublet. Thus, the important conclusion can be drawn that crystal field analyses exclusively based on optical data in some cases might be insufficient to find crystal field parameters that allow the explanation of the magnetic properties.

For **1-Dy**, the agreement between experiment and simulation is still reasonably good, but worse than for **1-Er**. This can be explained by partially less defined signals in the optical spectra of **1-Dy** and the obtained structure in the EPR-spectra, which complicated the accurate determination of the experimental g -values. The worse agreement is also reflected in higher parameter uncertainties (Table 5). Interestingly, the crystal field analysis for **1-Dy** strongly hints at the first excited Kramers doublet lying at about 30 cm^{-1} , in agreement with the energy barrier derived by a linear fit to the Arrhenius plot but in contrast to the FIR-spectrum. Attempts to find parameter sets which describe very low lying first excited Kramers doublets

or very high lying ones, explaining the absence of a signal at 30 cm^{-1} in the FIR-spectrum, were not successful. For such parameter sets either the simulation of the magnetization curve or the simulated EPR-spectra were unacceptable.

This gives rise to the following questions: a) Is the best-fit parameter set obtained for **1-Dy** able to explain the missing signal in the FIR-spectrum and b) Do the crystal field parameters for both **1-Dy** and **1-Er** allow for the understanding of the dynamic properties, which is one of the main purposes of crystal field analysis in the field of molecular magnetism? To answer these questions, it is useful to look at the compositions of the eigenfunctions, which are provided in Table 6 and Table 7. For **1-Er**, a strongly mixed ground doublet is obtained, containing not only contributions from low m_J values but also from both positive and negative m_J components within the same microstate. For instance, the first microstate of the ground doublet is described by: $|\text{KD1}\rangle = \sum c_i |m_J\rangle_i = 0.50 \left| -\frac{13}{2} \right\rangle - 0.50 \left| -\frac{5}{2} \right\rangle + 0.42 \left| \frac{11}{2} \right\rangle - 0.36 \left| \frac{3}{2} \right\rangle - 0.27 \left| \frac{15}{2} \right\rangle - 0.27 \left| -\frac{1}{2} \right\rangle - 0.20 \left| -\frac{9}{2} \right\rangle$. In a qualitative way, this already explains the observation of efficient under-barrier relaxation of the magnetization, making **1-Er** a relatively poor single-ion magnet. The ground state in **1-Dy** also shows a mixed character but less than for **1-Er** and with main contributions from $m_J = 13/2$ (68 %) and $m_J = 9/2$ (20 %), e.g. relatively high m_J values.

Table 6: Calculated energy levels and composition of the wave functions for the ground multiplet $^4\text{I}_{15/2}$ in **1-Er**.

KD	E / cm^{-1}	composition of the wave functions / %							
		$\pm 1/2$	$\pm 3/2$	$\pm 5/2$	$\pm 7/2$	$\pm 9/2$	$\pm 11/2$	$\pm 13/2$	$\pm 15/2$
1	0	7	13	25	2	4	17	25	7
2	44	< 1	< 1	5	3	8	35	21	27
3	91	29	18	< 1	31	8	< 1	5	8
4	112	28	36	14	4	10	4	3	2
5	280	31	3	13	29	5	10	9	< 1
6	325	< 1	1	4	< 1	59	< 1	34	< 1
7	437	3	28	36	12	6	10	2	3
8	462	< 1	< 1	3	21	< 1	24	< 1	51

Table 7: Calculated energy levels and composition of the wave functions for the ground multiplet ${}^6\text{H}_{15/2}$ in **1-Dy**.

KD	E / cm^{-1}	composition of the wave functions / %							
		$\pm 1/2$	$\pm 3/2$	$\pm 5/2$	$\pm 7/2$	$\pm 9/2$	$\pm 11/2$	$\pm 13/2$	$\pm 15/2$
1	0	3	< 1	2	2	20	4	68	< 1
2	29	< 1	10	< 1	11	< 1	69	6	3
3	105	38	4	30	< 1	21	< 1	6	< 1
4	138	12	23	9	30	10	< 1	< 1	16
5	182	6	20	2	9	9	3	1	50
6	302	1	< 1	24	13	28	6	13	15
7	348	2	11	12	29	10	17	4	15
8	385	38	30	20	7	1	1	1	< 1

Under-barrier relaxation is therefore expected to be less operative in **1-Dy** than in **1-Er**, consistent with the lower coefficients for quantum tunneling of magnetization, direct relaxation and the Raman process for **1-Dy** than for **1-Er** (compare section 4.2.2).

A more quantitative consideration is possible by calculating the magnetic dipole strengths for the transitions between the microstates within the ground multiplets. The magnetic dipole strengths D_{MD} are given by the squared magnetic dipole matrix elements⁹⁸

$$D_{MD} = \left| \left\langle l^N \alpha S L J M \left| -\frac{eh}{4\pi m_e c} (\hat{L} + 2\hat{S})_{\rho}^{(1)} \right| l^N \alpha' S' L' J' M' \right\rangle \right|^2 \quad (67)$$

where h is the Planck constant, m_e is the electron mass, c is the speed of light and all the other symbols have their usual meaning. The matrix elements can be easily evaluated by making use of the Wigner-Eckart theorem as described in ref⁹⁸ and they are also part of the output of the f-shell program¹⁷⁵.

Figure 51 illustrates the magnetic dipole strengths calculated for transitions within and between the three lowest Kramers doublets for **1-Er** and **1-Dy**, respectively. For **1-Er**, the highest value is obtained for the transition to the first excited Kramers doublet, which was observed as a well-defined signal at 52 cm^{-1} in the FIR-spectrum. The direct transition to the second lowest Kramers doublet at 84 cm^{-1} is much less allowed and might gain its intensity by

coupling to vibrations, consistent with the observed splitting of the corresponding signal. Rather high matrix elements, e.g. in the same range as for the transition to the first excited doublet were calculated for the intra-Kramers doublet transition within the ground doublet, confirming the efficiency of under-barrier relaxation processes for the relaxation of the magnetization. In contrast, the matrix elements for the diagonal transitions between the ground doublet and the first excited doublet are rather low, indicating that the Orbach process via the first excited state is not dominant. Instead, quantum tunneling via the first excited doublet is much more probable. As indicated by the rather high dipole strengths for the diagonal transition to the second excited Kramers doublet, an Orbach process via this doublet would be possible. However, the observation of this process would require higher temperatures where the competing Raman process with its much more pronounced temperature dependence becomes extremely efficient.

Similarly to **1-Er**, the matrix elements for the transitions to the first excited doublet in **1-Dy** are relatively large, meaning that their values cannot explain the missing signal in the FIR-spectrum around 30 cm^{-1} . However, the matrix elements for the diagonal transitions are considerably higher, indicating a large contribution of the Orbach relaxation via the first excited state. According to the Heisenberg uncertainty principle¹⁸⁰, fast relaxation leads to less defined energies and the corresponding signals can become rather broad. Signal-broadening due to fast relaxation might therefore be the explanation for the experimental observations.

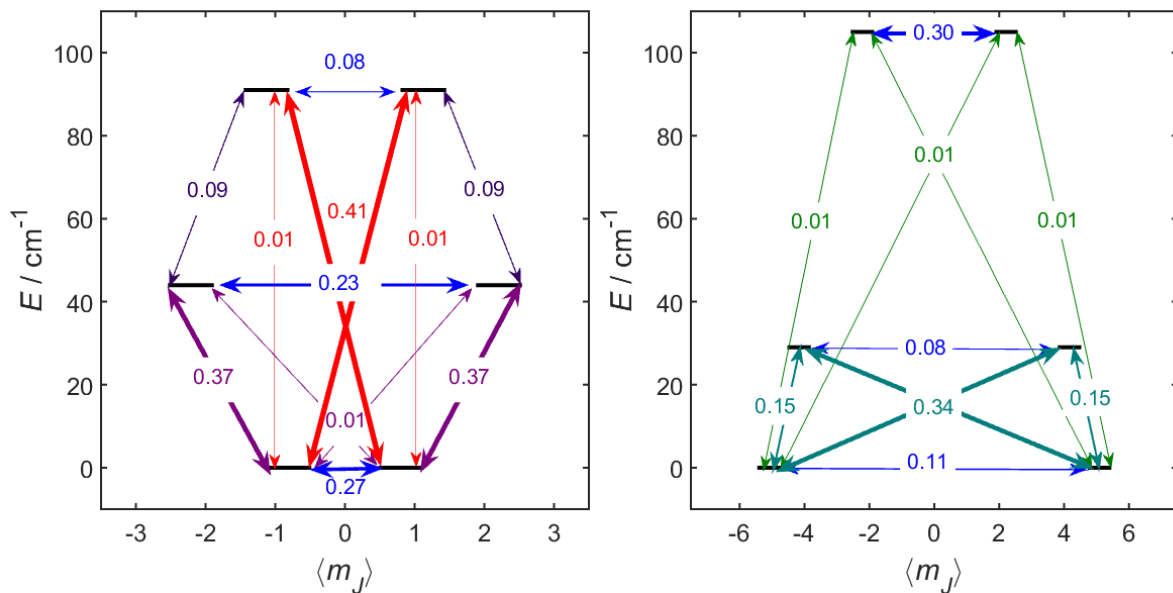


Figure 51: Magnetic dipole strengths for the transitions between the microstates of the lowest three Kramers doublets in **1-Er** (left) and **1-Dy** (right). Black lines represent the Kramers doublets as a function of their m_J expectation value and arrows depict possible transitions between states. The numbers at the arrows correspond to the isotropic average of the dipole strengths, given in units of $e^2 10^{-20} \text{ cm}^2$.

For the lowest intra-doublet transition, slightly lower matrix elements are found than for the inter-doublet transitions between the lowest two Kramers doublets, further confirming the dominance of the Orbach process. However, the intra-doublet matrix elements are still non-zero and thus explain why no slow relaxation of the magnetization is observed at zero bias field and **1-Dy** is only a field-induced single ion magnet.

Summarizing this chapter, the in-depth investigation of the magnetic and spectroscopic properties of two novel lanthanide based single-ion magnets was presented. The combination of magnetometry and multiple spectroscopic techniques allowed the determination of their electronic structures and the analysis was progressing clearly beyond what is commonly done in the field of molecular magnetism. However, it was shown that it is exactly this combination of techniques that is required for obtaining reliable crystal field parameters for low-symmetry compounds. With the help of the experimentally determined sets of crystal field parameters, it was possible to determine the compositions of the ground states, which in turn allowed for a detailed understanding of the dynamic magnetic properties, e.g. the relaxation behavior. Thus, this work provides a substantial contribution to the understanding of the electronic structures of lanthanide single-ion magnets, which is essential for their rational design in the future.

However, one important aspect to be considered is the general applicability of the recipe for electronic structure determination presented in this chapter. Since the presented method not only involves a rather large experimental effort but also a lengthy fitting procedure, it is not likely to become a standard method for the quick characterization of lanthanide-based single-molecule magnets in the future. Furthermore, the studied lanthanide tetra-carbonates represented an ideal case regarding the applicability of a range of experimental techniques, i.e. useful information were obtained by applying magnetometry, optical spectroscopy, far-infrared and EPR-spectroscopy. For the characterization of other lanthanide single-ion magnets not all of these methods will be useful. For instance, optical detection of f-f transitions is only possible if the compounds do not exhibit strongly colored ligands where ligand-based transitions govern the spectra in the visible range. EPR-spectroscopy is only useful for compounds with ground states showing partial $m_J = \pm \frac{1}{2}$ character. For purely axial ground states EPR transitions are forbidden; however, axial ground states are one of the main conditions for the good performance of single-molecule magnets. Actually, only magnetometry and far-infrared spectroscopy are always applicable. While magnetometry already belongs to the standard methods for studying SIMs, this is not true for far-infrared spectroscopy. Since the information obtained by far-infrared spectroscopy is of crucial importance, this spectroscopic method should be employed whenever possible. At this point,

also the method of inelastic neutron scattering should be mentioned, which can complement far-infrared spectroscopy.⁹⁷

Another aspect concerns the complexity of the investigated systems. With only one lanthanide center per molecule, the studied lanthanide tetra-carbonates exhibit rather simple structures. For compounds exhibiting more lanthanide ions with different low-symmetry environments, even the combined application of all the experimental techniques presented above might not be sufficient for a complete electronic structure determination. In such cases simplified models for describing the electronic structure have to be taken into account and also the results of ab initio calculations might be useful for obtaining rough ideas about the energy level structures. However, the full determination of the electronic structures for simple model complexes like the lanthanide tetra-carbonates can serve for the development of databases containing crystal field parameters for given ligands in given symmetries. Such databases could then be useful for the estimation of crystal field parameters of new and more complicated compounds.

4.3 Mononuclear Cobalt Complexes

This section was part of a collaboration with the group of Prof. Dr. Biprajit Sarkar (Institute for Chemistry and Biochemistry, Freie Universität Berlin) who provided the compounds and the structural data. The syntheses were performed by Dr. Margarethe van der Meer. Part of the magnetic characterization of the samples was carried out as part of the MSc thesis of Frauke D. Breitgoff (September 2014 – March 2015) under my supervision.¹⁸¹ Work done by others is indicated in the text at the position where it appears for the first time.

Part of the results presented below has already been published in *Nature Communications*, **2016**, 7, 10467.¹⁶⁷

4.3.1 Structures of the Mononuclear Co(II) Complexes

The air-stable mononuclear cobalt complexes $(\text{HNEt}_3)_2[\text{Co}^{\text{II}}(\text{L}^1)_2]$ (**(HNEt₃)₂2**) and $(\text{NMe}_4)_2[\text{Co}^{\text{II}}(\text{L}^1)_2]$ (**(NMe₄)₂2**) were synthesized and structurally characterized by Dr. Margarethe van der Meer (Institute for Chemistry and Biochemistry, Freie Universität Berlin).

As shown in Figure 52, both compounds consist of a central Co(II) ion ligated by the nitrogen donors of two doubly deprotonated 1,2-bis(methanesulfonamido)benzene ligands (H_2L^1), leading to fourfold coordination. The net charge of the complexes is thus -2 and charge balance is provided by two $(\text{HNEt}_3)^+$ counter ions in **(HNEt₃)₂2** and two $(\text{NMe}_4)^+$ cations in **(NMe₄)₂2**. The angles between the planes defined by the Co-NCCN metallacycles are 84.83° for **(HNEt₃)₂2** and 83.91° for **(NMe₄)₂2**, i.e. the ligands are oriented almost perpendicular to each other. Strong axial distortion is revealed by the N-Co-N angles, which are 80.59° and 80.70° for **(HNEt₃)₂2** and 81.18° and 81.52° for **(NMe₄)₂2**, i.e. significantly smaller than the 109.5° for regular tetrahedrons. As outlined in section 2.3.2, this high axiality makes **(HNEt₃)₂2** and **(NMe₄)₂2** extraordinarily interesting systems for studying SIM behavior. The actual site symmetry is C_1 but can be idealized to D_{2d} with the S_4 axis being the bisecting line of the N-Co-N angles. D_{2d} point symmetry was used later on for the analysis of the spectroscopic data.

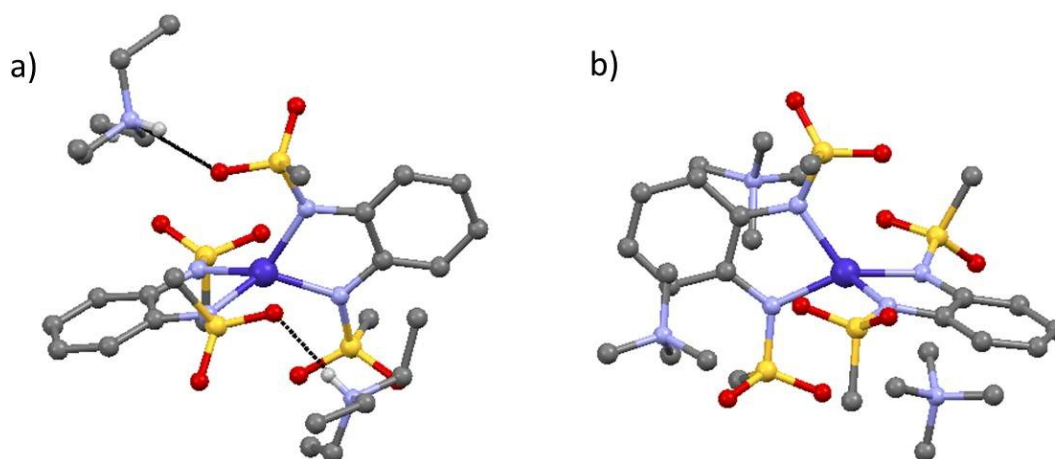


Figure 52: a) Molecular structure of $(\text{HNEt}_3)_2\mathbf{2}$. b) Molecular structure of $(\text{NMe}_4)_2\mathbf{2}$. Cobalt is shown in blue, oxygen in red, sulfur in yellow, nitrogen in violet, carbon in grey and hydrogen in light grey. For reasons of clarity, most of the hydrogens are omitted, except the ones forming hydrogen bonds. Hydrogen bonds are shown as black lines. The crystallographic data were provided by Dr. Margarethe van der Meer.

Although the chemical formulae of $(\text{HNEt}_3)_2\mathbf{2}$ and $(\text{NMe}_4)_2\mathbf{2}$ differ only in their counter ions, different crystal systems are found: $(\text{HNEt}_3)_2\mathbf{2}$ crystallizes in the orthorhombic $P 2_1 2_1 2_1$ space group containing four symmetry-related molecules in the unit cell. H-bonds are formed between the ligands and the counter ions. $(\text{NMe}_4)_2\mathbf{2}$ crystallizes in the monoclinic space group $P 2_1/n$ with eight symmetry-related molecules in its unit cell. No hydrogen bonds are found. Thus, not only the magnetic and spectroscopic properties of the individual complexes are interesting to study but also the comparison of both compounds might lead to a better understanding of the influence of small structural variations on the electronic structure and the magnetic behavior.

4.3.2 Magnetic Properties

The static and dynamic magnetic properties of $(\text{HNEt}_3)_2\mathbf{2}$ and $(\text{NMe}_4)_2\mathbf{2}$ were studied by means of dc and ac susceptibility and magnetization measurements.¹⁸¹ Figure 53 shows the observed temperature dependence of the product χT of the dc magnetic susceptibility χ and the temperature T . At 300 K, χT adopts values of $3.14 \text{ cm}^3 \text{ mol}^{-1} \text{ K}$ ($(\text{HNEt}_3)_2\mathbf{2}$) and $3.10 \text{ cm}^3 \text{ mol}^{-1} \text{ K}$ ($(\text{NMe}_4)_2\mathbf{2}$). These values are higher than the spin-only value of $\chi T = 1.88 \text{ cm}^3 \text{ mol}^{-1} \text{ K}$ expected from Curie's law for $S = 3/2$ systems with $g = 2$ but they lie in the typical range for fourfold coordinated Co(II) complexes with second-order spin-orbit coupling^{86,87}.

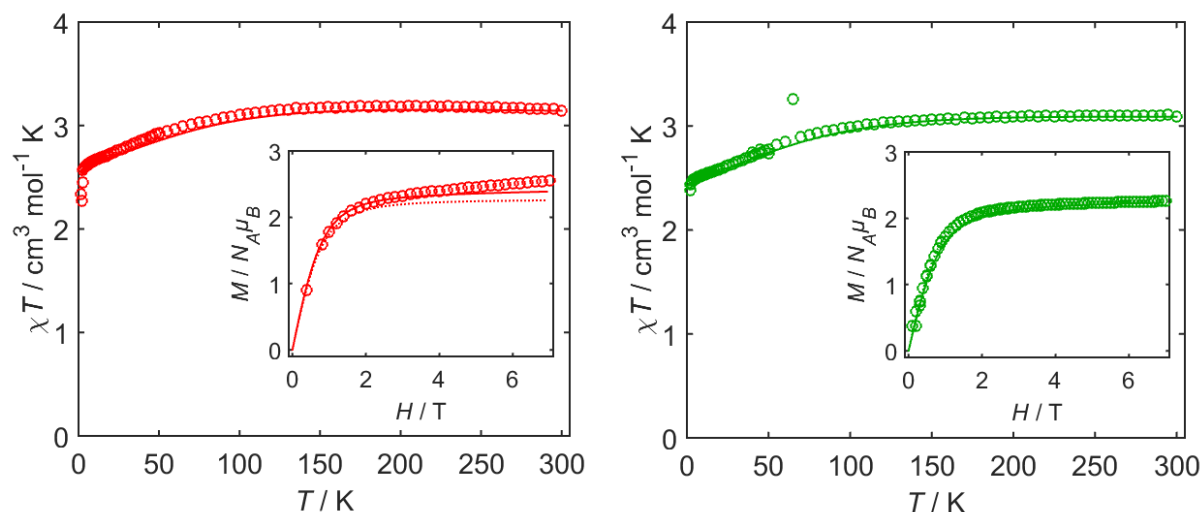


Figure 53: Temperature dependence of the product of the magnetic susceptibility χ and the temperature T for **(HNEt₃)₂** (left) and **(NMe₄)₂** (right). The insets show the magnetic field dependence of the magnetization recorded at 1.8 K. Solid lines correspond to the simulations using a spin Hamiltonian with the parameters given in the text. Dotted lines correspond to simulations assuming a completely axial system with an effective spin of $S_{\text{eff}} = 1/2$ (see section 4.3.3).

As outlined in sections 2.1.1 and 2.3.2, second-order spin-orbit coupling denotes the interaction of an orbitally non-degenerate ground state with orbitally degenerate excited states, leading to zero-field splitting. Below 150 K, χT gradually decreases with decreasing temperature until at 1.8 K values of $\chi T = 2.34 \text{ cm}^3 \text{ mol}^{-1} \text{ K}$ (**(HNEt₃)₂**) and $\chi T = 2.44 \text{ cm}^3 \text{ mol}^{-1} \text{ K}$ (**(NMe₄)₂**) are reached. The decrease is attributed to zero-field splitting and the depopulation of the corresponding excited microstates at low temperatures. The magnetic field dependence of the magnetization is shown as insets in Figure 53. At 1.8 K and 7 T, magnetization values of $2.56 \mu_B$ for **(HNEt₃)₂** and $2.26 \mu_B$ for **(NMe₄)₂** are obtained. Preliminary fits using a typical spin Hamiltonian as described by the combination of equations (4) and (5) and without taking into account any spectroscopic data yielded axial ZFS parameters of $D = -95 \pm 20 \text{ cm}^{-1}$ for **(HNEt₃)₂** and $D = -90 \pm 20 \text{ cm}^{-1}$ for **(NMe₄)₂** (with E fixed to zero).¹⁸¹ However, as will be shown in section 4.3.3, spectroscopy revealed that the actual zero-field splittings are even higher, namely $D = -115 \text{ cm}^{-1}$ for **(HNEt₃)₂** and $D = -112.5 \text{ cm}^{-1}$ for **(NMe₄)₂**. The static magnetic data were therefore simulated with the spectroscopically determined D -values and $g_x = g_y = 2.20$ and $g_z = 3.03$ for **(HNEt₃)₂** and $g_x = g_y = 2.25$ and $g_z = 2.95$ for **(NMe₄)₂**. In both cases satisfactory simulations were obtained without including a rhombic ZFS parameter E , consistent with high axiality. The corresponding simulations are shown as solid lines in Figure 53. Compared to other pseudo-tetrahedral Co(II) compounds, the obtained D values are extraordinarily large (Table 8) and in

combination with high axiality, they strongly hint at possible SIM properties of **(HNEt₃)₂2** and **(NMe₄)₂2**.

Magnetization dynamics was therefore investigated by temperature and frequency dependent ac susceptibility measurements. The temperature dependence of the in-phase and out-of-phase components of the ac susceptibilities without applying a dc bias field are shown in Figure 54. The out-of-phase components χ'' show frequency dependent maxima, making **(HNEt₃)₂2** and **(NMe₄)₂2** two of the rare examples of pseudo-tetrahedral Co(II) complexes showing SIM properties in zero dc field.^{11,28} However, towards very low temperatures, an additional increase in χ'' is observed, indicating an additional process for magnetic relaxation, which is often attributed to quantum tunneling. Since applying a dc field permanently lifts the twofold degeneracy of the Kramers doublets and therefore limits the efficiency of QTM processes, the ac susceptibility measurements were repeated in the presence of a 1000 Oe dc field. Indeed, no increase of χ'' towards low temperatures is visible any longer (Figure 55).

The relaxation times τ for **(HNEt₃)₂2** and **(NMe₄)₂2** with and without an applied dc field were extracted by the generation of Argand diagrams and fitting to generalized Debye functions, as described by equation 56. Reliable fits were obtained for temperatures between ca. 6 K and 20 K, where a characteristic semi-circle shape is observed. The Argand diagrams together with the best fits are shown in Figure 56 while Table A 15 and Table A 16 in the appendix provide the corresponding best-fit parameters.

Table 8: Fourfold coordinated Co(II) complexes exhibiting negative axial ZFS parameters with $|D| > 50 \text{ cm}^{-1}$ and their effective energy barriers derived by linear fits to the corresponding Arrhenius plots.

Compound	D / cm^{-1}	$U_{\text{eff}} / \text{cm}^{-1}$	Literature
(Ph ₄ P) ₂ [Co(C ₃ S ₅) ₂]	-161	33.9	Fataftah <i>et al.</i> ⁸⁶
(HNEt ₃) ₂ [Co(L ¹) ₂]	-115	118	this work
(NMe ₄) ₂ [Co(L ¹) ₂]	-112.5	67	this work
(Ph ₄ P) ₂ [Co(SePh) ₄]	-83	19.1	Zadrozny <i>et al.</i> ⁸⁷
[Co(AsPh ₃) ₂ (I) ₂]	-74.7	32.6	Saber <i>et al.</i> ⁸⁸
(Ph ₄ P) ₂ [Co(SPh) ₄]	-62	21.1	Zadrozny <i>et al.</i> ⁸⁷
[Co{(NtBu) ₃ SMe} ₂]	-58	75	Carl <i>et al.</i> ⁸⁹

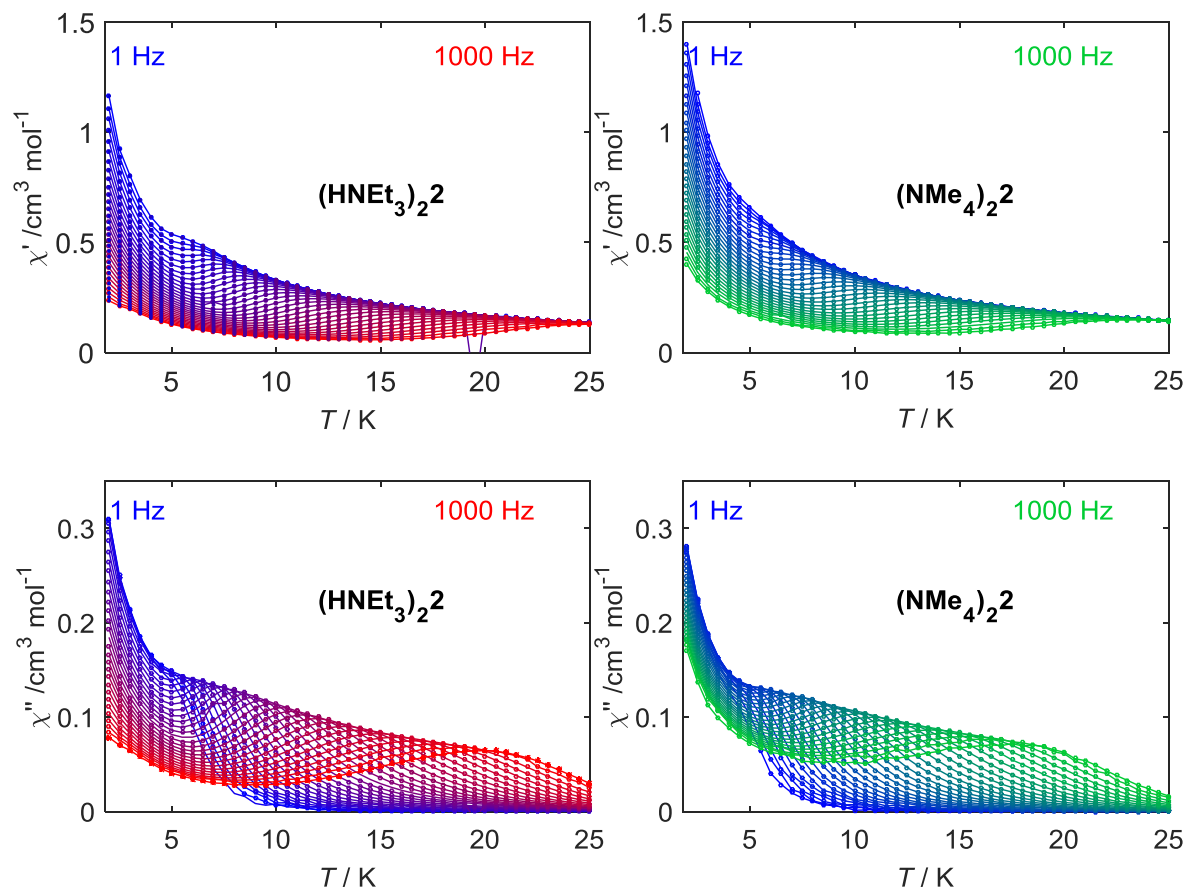


Figure 54: Temperature dependence of the ac susceptibilities for $(\text{HNEt}_3)_2$ (left) and $(\text{NMe}_4)_2$ (right) at various frequencies. No dc bias field was applied. Top: In-phase components; bottom: Out-of-phase components. Solid lines are guides for the eye.

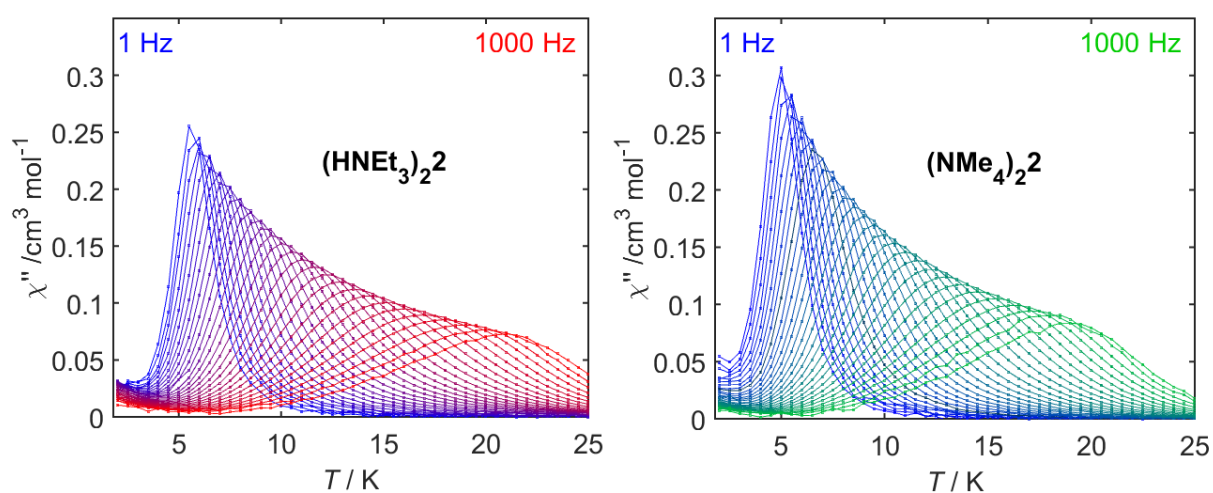


Figure 55: Temperature dependence of the out-of-phase ac susceptibilities for $(\text{HNEt}_3)_2$ (left) and $(\text{NMe}_4)_2$ (right) at various frequencies and with an applied dc bias field of $H_{\text{dc}} = 1000$ Oe. Solid lines are guides for the eye.

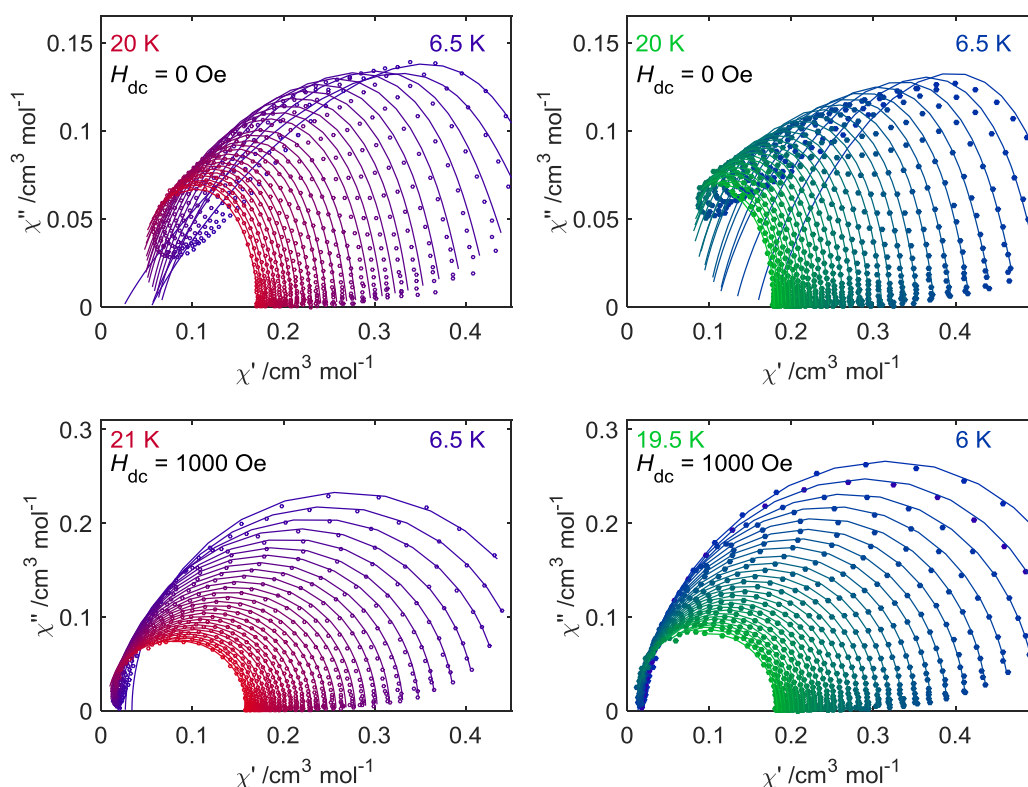


Figure 56: Argand diagrams for **(HNEt₃)₂2** (left) and **(NMe₄)₂2** (right) at different temperatures. Top: Data obtained without an external dc bias field. Bottom: Data obtained with an external dc field of $H_{dc} = 1000$ Oe. Solid lines correspond to the best fits using generalized Debye equations.

For both compounds, the distribution parameters of relaxation times α are smaller when an external dc field is applied, which is also reflected by the less distorted semi-circle shape of the Argand plots when applying a dc field. Under the assumption that the distribution of relaxation times is strongly influenced by the contribution of quantum tunneling, these observations confirm the suppressing of quantum tunneling of the magnetization by applying a dc field.

Figure 57 shows the resulting Arrhenius plots, i.e. $\ln \tau$ as functions of the inverse temperature T^{-1} . In all cases, a more or less pronounced linear regime at higher temperatures is observed, suggesting a dominant contribution of Orbach relaxation in this temperature range. Preliminary linear fits yielded the effective energy barriers given in Table 9. These energy barriers are amongst the highest values reported for d-block ion based SIMs (Table 8).^{11,24,28} However, according to the previously mentioned spectroscopically determined ZFS parameters (see below), even much higher energy barriers, namely $\Delta E = |2D| = 230$ cm⁻¹ for **(HNEt₃)₂2** and $\Delta E = |2D| = 225$ cm⁻¹ for **(NMe₄)₂2** would be expected.

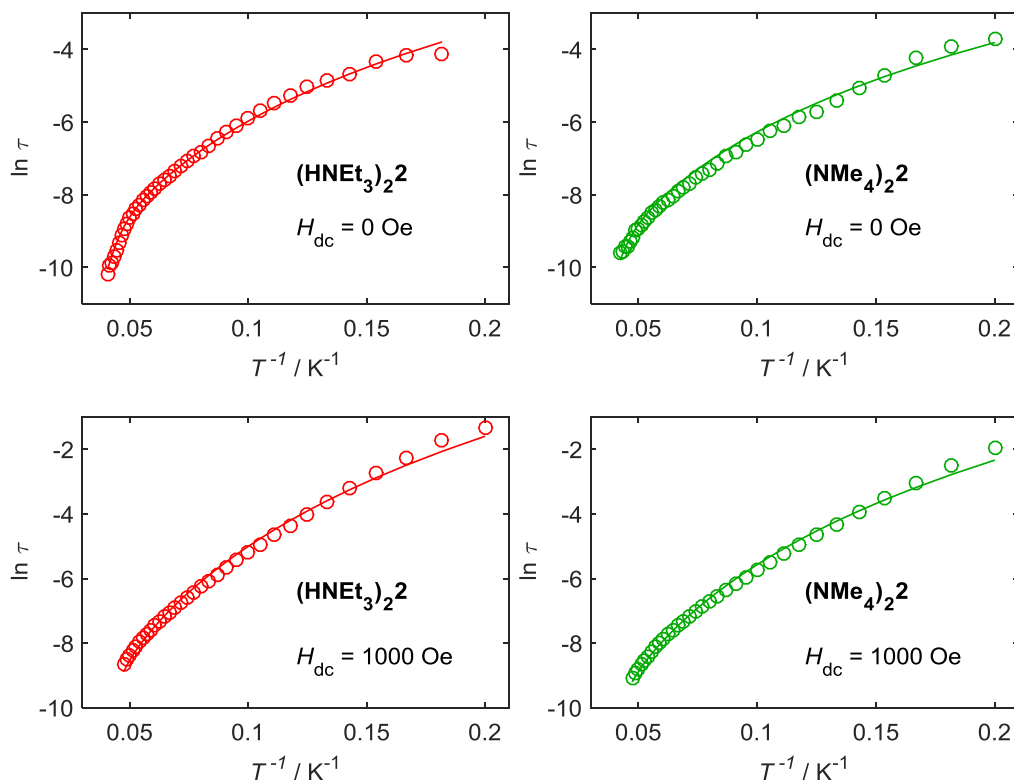


Figure 57: Arrhenius plots for $(\text{HNEt}_3)_2\mathbf{2}$ (left) and $(\text{NMe}_4)_2\mathbf{2}$ (right) with and without an applied dc field. Solid lines correspond to the best fits (see text).

This finding indicates that in spite of the linear regimes not only the Orbach relaxation process dominates at high temperatures, but also the Raman process plays a significant role. The presence of quantum tunneling of the magnetization at low temperatures was already indicated by the increase of the out-of-phase ac susceptibilities towards low temperatures and the absence of this increase with an applied external dc field. However, when applying an external dc field, the direct process for spin reversal might play a role as well. Strictly speaking, the correct elucidation of the contributing relaxation mechanism from the shape of the Arrhenius plots requires taking into account all of the above-mentioned relaxation mechanisms, as described by equation (65) in section 4.2.2 for the lanthanide carbonates. However, in order to avoid over-parametrization, the simplest model was assumed for fitting the Arrhenius plots for $(\text{HNEt}_3)_2\mathbf{2}$ and $(\text{NMe}_4)_2\mathbf{2}$. Since QTM and direct relaxation are much more important at very low temperatures but reliable fits to the Argand diagrams were obtained only for temperatures above 6 K (see above), these two low-temperature relaxation mechanisms were not included in the fit of the Arrhenius plots. Indeed, preliminary fitting attempts revealed that the inclusion of QTM and direct relaxation does not lead to improved fits. Equation (65) then reduces to

$$\tau^{-1} = C_{Raman} \cdot T^{n_{Raman}} + \tau_0^{-1} \exp\left(-\frac{\Delta E}{k_B T}\right) \quad (68)$$

Here, the energy barrier ΔE was fixed to the spectroscopically determined ZFS, i.e. $\Delta E = |2D| = 230 \text{ cm}^{-1}$ for **(HNEt₃)₂2** and $\Delta E = |2D| = 225 \text{ cm}^{-1}$ for **(NMe₄)₂2**. However, although a Raman exponent of $n_{Raman} = 9$ was derived for Kramers ions with isolated ground states,³⁸ n_{Raman} was treated here as a free fit parameter since fitting attempts with $n_{Raman} = 9$ did not lead to satisfactory results. Thus, three parameters were varied during the fits, namely C_{Raman} , n_{Raman} and τ_0 . The attempt times τ_0 were determined only from the data obtained without an applied dc field since relaxation times up to higher temperatures were accessible here and therefore more pronounced linear regimes are observed. The determined attempt times τ_0 were subsequently kept fixed for fitting the Arrhenius plots constructed from the data obtained in the presence of a dc bias field. The best fits are shown as solid lines in Figure 57 while Table 9 provides the respective best-fit parameters.

As expected for structurally similar compounds, the determined Raman coefficients for **(HNEt₃)₂2** and **(NMe₄)₂2** in the absence of a dc field lie in the same range, with $C_{Raman} = 0.088 \text{ K}^{-3.65} \text{ s}^{-1}$ for **(HNEt₃)₂2** and $C_{Raman} = 0.103 \text{ K}^{-3.76} \text{ s}^{-1}$ for **(NMe₄)₂2**. Significantly smaller coefficients are found in the presence of a 1000 Oe dc field, namely $C_{Raman} = 0.0018 \text{ K}^{-4.97} \text{ s}^{-1}$ (**(HNEt₃)₂2**) and $C_{Raman} = 0.0056 \text{ K}^{-4.70} \text{ s}^{-1}$ (**(NMe₄)₂2**). However, the Raman exponents n_{Raman} found for the data obtained with applied dc fields are higher, hinting at a magnetic field dependence of the Raman exponents due to the field-induced change of the electronic energy level structure. In all cases, the Raman exponents are significantly lower than $n_{Raman} = 9$ derived for Kramers ions with isolated ground states. Similarly low values, i.e. $n_{Raman} = 2.8 - 5.0$ have already been reported for several other Co(II) compounds^{90,182-186} and are commonly attributed to the contribution of the so-called optical/acoustic Raman relaxation mechanism⁴⁹. While for the conventional Raman process only acoustic phonons are assumed to interact with the spin system, the optical/acoustic Raman mechanism also includes optical phonons. For example, absorption of an acoustic phonon can induce a transition to a virtual intermediate state and an optical phonon can subsequently be emitted or vice versa. It was shown that the combined participation of acoustic and optical phonons might lead to a lowering of the exponent appearing in the temperature dependence of the relaxation time with $n = 1 - 6$, depending on the electronic energy level structure of the system.^{48,49} It would be interesting to study the level structure and field-dependence of the Raman exponent in more detail; however, this is beyond the scope of this work.

Table 9: Best-fit parameters obtained for the Arrhenius plots for **(HNEt₃)₂2** and **(NMe₄)₂2** with and without an external dc field, respectively.

	(HNEt₃)₂2		(NMe₄)₂2	
	$H_{dc} = 0$ Oe	$H_{dc} = 1000$ Oe	$H_{dc} = 0$ Oe	$H_{dc} = 1000$ Oe
	linear fit ¹⁸¹			
U_{eff} / cm^{-1}	117.8	74.5	66.6	65.3
τ_0 / s	$3.89 \cdot 10^{-8}$	$1.08 \cdot 10^{-8}$	$4.03 \cdot 10^{-7}$	$4.78 \cdot 10^{-7}$
	Raman + Orbach			
$\Delta E / \text{cm}^{-1}$	230	230	225	225
τ_0 / s	$1.099 \cdot 10^{-10}$	$1.099 \cdot 10^{-10}$	$1.585 \cdot 10^{-10}$	$1.585 \cdot 10^{-10}$
$C_{\text{Raman}} / \text{T}^{-n} \text{s}^{-1}$	0.088	0.0018	0.103	0.0056
n_{Raman}	3.65	4.93	3.55	4.67

Summarizing the conclusions drawn from analyzing the ac susceptibility data and the corresponding Arrhenius plots, magnetic relaxation in **(HNEt₃)₂2** and **(NMe₄)₂2** is governed by a combination of quantum tunneling of the magnetization (low temperatures), optical/acoustic Raman mechanisms (intermediate temperatures) and Orbach processes (high temperatures). The direct process was shown to be negligible in the entire temperature range, hinting at high axiality of the systems. High axiality means that the rhombic ZFS parameters E are close to zero and therefore vanishingly small magnetic dipole transition matrix elements are obtained for direct transitions within the ground doublets. Due to the rather high zero-field splittings found for **(HNEt₃)₂2** and **(NMe₄)₂2**, the Orbach relaxation is almost negligible at low temperatures, being one of the reasons for the observation of slow relaxation of the magnetization.

The observation of slow relaxation of the magnetization even in the absence of an external dc field gives rise to the question whether **(HNEt₃)₂2** and **(NMe₄)₂2** show real magnetic bistability, one of the necessary conditions for progress towards practical application. The ultimate proof of magnetic bistability is coercivity. The coercive field is defined as the field required for complete demagnetization of the sample, i.e. the half width of the opening of the magnetic hysteresis loop at zero magnetization. SQUID magnetometric hysteresis loops at 1.8 K were therefore recorded for a sample of **(HNEt₃)₂2** dispersed in

fluorolube®. Figure 58 shows the observed hysteresis loops for field sweeping rates of 100 Oe s^{-1} , 200 Oe s^{-1} and 500 Oe s^{-1} . For all of these scan rates, more or less butterfly-shaped hysteresis curves were observed, meaning that magnetic hysteresis occurs at low magnetic fields where saturation is not yet achieved, but without significant coercivity. At the highest applied scan rate of 500 Oe s^{-1} , a small opening of the hysteresis curve with a coercive field of 0.055 T is visible. However, due to the intrinsic hysteresis of superconducting magnets used in SQUID magnetometers and due to the comparatively long measurement time (1 s per data point) compared to the scan rate, this small coercive field should be regarded critically. Thus, it can be assumed that no significant magnetic bistability is observed, explained by efficient quantum tunneling of the magnetization around zero field.

Since QTM is favored by the presence of transverse magnetic fields and since magnetized neighboring molecules can be a source of such transverse magnetic fields, further hysteresis measurements were carried out on a diluted sample of $(\text{HNEt}_3)_2\mathbf{2}$. For this purpose, a diluted powder sample was prepared by dissolving $(\text{HNEt}_3)_2\mathbf{2}$ and the isostructural diamagnetic Zn complex $(\text{HNEt}_3)_2\text{Zn}$ with a molar ratio of 1 : 9 in acetonitrile and subsequently removing the solvent by evaporation. The required Zn complex $(\text{HNEt}_3)_2\text{Zn}$ was synthesized and structurally characterized by Dr. Margarethe van der Meer (Institute for Chemistry and Biochemistry, Freie Universität Berlin). The observed hysteresis curves for a pellet of the doped powder are shown on the right hand side of Figure 58.

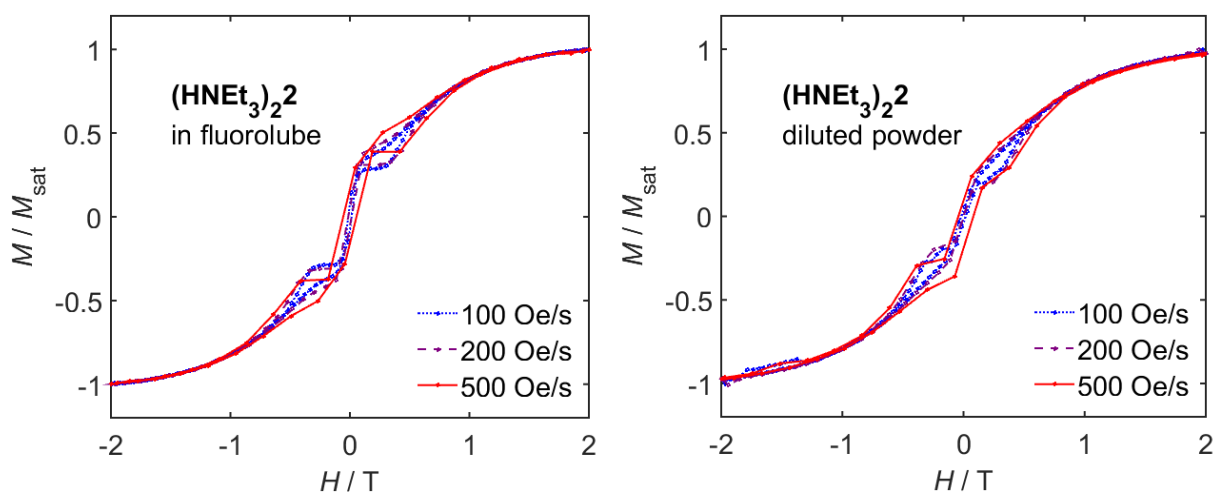


Figure 58: Magnetic hysteresis curves for $(\text{HNEt}_3)_2\mathbf{2}$ at 1.8 K and different scan rates, as indicated. Left: Data obtained for a sample of $(\text{HNEt}_3)_2\mathbf{2}$ dispersed in fluorolube®. Right: Data obtained for $(\text{HNEt}_3)_2\mathbf{2}$ doped into the analogous Zn(II) complex.

Although the hysteresis behavior at small fields is slightly different than for the sample dispersed in fluorolube®, no significant coercivity is observed as well. The coercive field at a scan rate of 500 Oe s⁻¹ is 0.070 T, i.e. comparable to that obtained for the sample dispersed in fluorolube®. This finding indicates that magnetized neighboring molecules are not the only source for QTM in **(HNEt₃)₂2** and the responsible transverse interactions have a different origin. One aspect to be considered is for example the presence of nuclear spins with $I_{\text{nuc}}(^{59}\text{Co}) = 7/2$. However, since ⁵⁹Co is the only stable Co isotope, this is an unavoidable situation in cobalt based SIMs.

Another important point to mention is the fact that the hysteresis curves were recorded on unoriented samples, although only the very few molecules with their easy axes of magnetization oriented parallel to the external magnetic field are expected to show magnetic bistability. One useful method for observing coercivity is therefore single crystal SQUID magnetometry using carefully oriented single crystals. However, the crystallographic unit cell of **(HNEt₃)₂2** does not allow the orientation of the crystals in a way that leads to parallel orientation of all the individual easy axes with respect to the magnetic field. Single crystal measurements were therefore not performed. As outlined in section 2.4.4, MCD detected hysteresis studies provide an alternative to single crystal measurements. The MCD detected hysteresis curves for **(HNEt₃)₂2** and **(NMe₄)₂2** will be presented as part of the spectroscopic results in section 4.3.3.

4.3.3 Spectroscopic Results and Electronic Structure

The magnetic studies performed on **(HNEt₃)₂2** and **(NMe₄)₂2** already hinted at highly axial ground states, i.e. largely negative axial ZFS parameters D and vanishingly small rhombic ZFS parameters E . However, magnetometry neither allows the unequivocal determination of the signs and exact magnitudes of D and E , nor explains the observations in terms of the electronic structures. Spectroscopic techniques including EPR-, FIR- and MCD-spectroscopy were thus applied to obtain deeper insight.

Low-temperature EPR-spectra were recorded at conventional X-band (9.47 GHz) and at higher frequencies between 100 and 720 GHz but no transitions were observed, neither for **(HNEt₃)₂2** nor for **(NMe₄)₂2**. The absence of EPR lines matches the expectations since negative signs of D lead to ground states characterized by the highest m_S values. In Co(II) complexes, a negative ZFS parameter D results in ground doublets with $m_S = \pm 3/2$ and EPR transitions within these ground doublets would correspond to magnetic dipole transitions with

$\Delta m_S = \pm 3$, which are not allowed. In the presence of significant rhombicity, i.e. a non-zero ZFS parameter E , state-mixing would occur, leading to relaxed selection rules and non-vanishing EPR intensities. The EPR results for **(HNEt₃)₂2** and **(NMe₄)₂2** thus support the assumption of negative D parameters and negligibly small E parameters. Furthermore, D has to be rather large. Otherwise, inter-doublet transitions between the $m_S = \pm 3/2$ and $m_S = \pm 1/2$ states would be expected to occur, but they were not observed. Since the highest applied frequency was 720 GHz, the EPR results suggest ZFS splittings of at least 24 cm^{-1} , corresponding to minimum D values of -12 cm^{-1} .

On the one hand, it is gratifying to see that the EPR results support the conclusions drawn from the analysis of the magnetic data, but on the other hand, the absence of EPR lines precludes the accurate determination of g -values for **(HNEt₃)₂2** and **(NMe₄)₂2**. The g -values derived from fitting the dc susceptibility curves should be considered only as estimates. One possibility for the accurate determination of the g -values of such large ZFS systems is the measurement of EPR-spectra at very high fields, e.g. up to 70 T and frequencies in the THz range, e.g. by using free-electron lasers. However, beam time for such experiments is rarely available and these measurements have therefore not yet been performed on **(HNEt₃)₂2** and **(NMe₄)₂2**. They are planned for the near future.

In order to obtain a better idea about the actual size of the ZFS in **(HNEt₃)₂2** and **(NMe₄)₂2**, FIR-spectroscopy was applied. FIR-spectra at 4 K and magnetic fields between 0 and 11 T were recorded by Dr. Milan Orlita and Michael Hakl (Laboratoire National des Champs Magnétiques Intenses, Grenoble). Figure 59 and Figure 60 show the obtained transmission spectra as well as the normalized spectra obtained by dividing the spectra by the spectrum at highest field. Clear field-dependent features are observed in the regions around 230 cm^{-1} (**(HNEt₃)₂2**) and 225 cm^{-1} (**(NMe₄)₂2**). These features are attributed to allowed magnetic dipole transitions between the $m_S = \pm 3/2$ ground states and the $m_S = \pm 1/2$ excited states and therefore directly correspond to the zero field gaps given by $|2D|$. FIR-spectroscopy thus allowed the unequivocal experimental determination of very large axial ZFS parameters, namely $D = -115 \text{ cm}^{-1}$ for **(HNEt₃)₂2** and $D = -112.5 \text{ cm}^{-1}$ for **(NMe₄)₂2**. As previously mentioned, these values were used for the final simulations of the dc susceptibility and magnetization data (Figure 53) as well as for analyzing the Arrhenius plots derived from the ac susceptibility data (Figure 57).

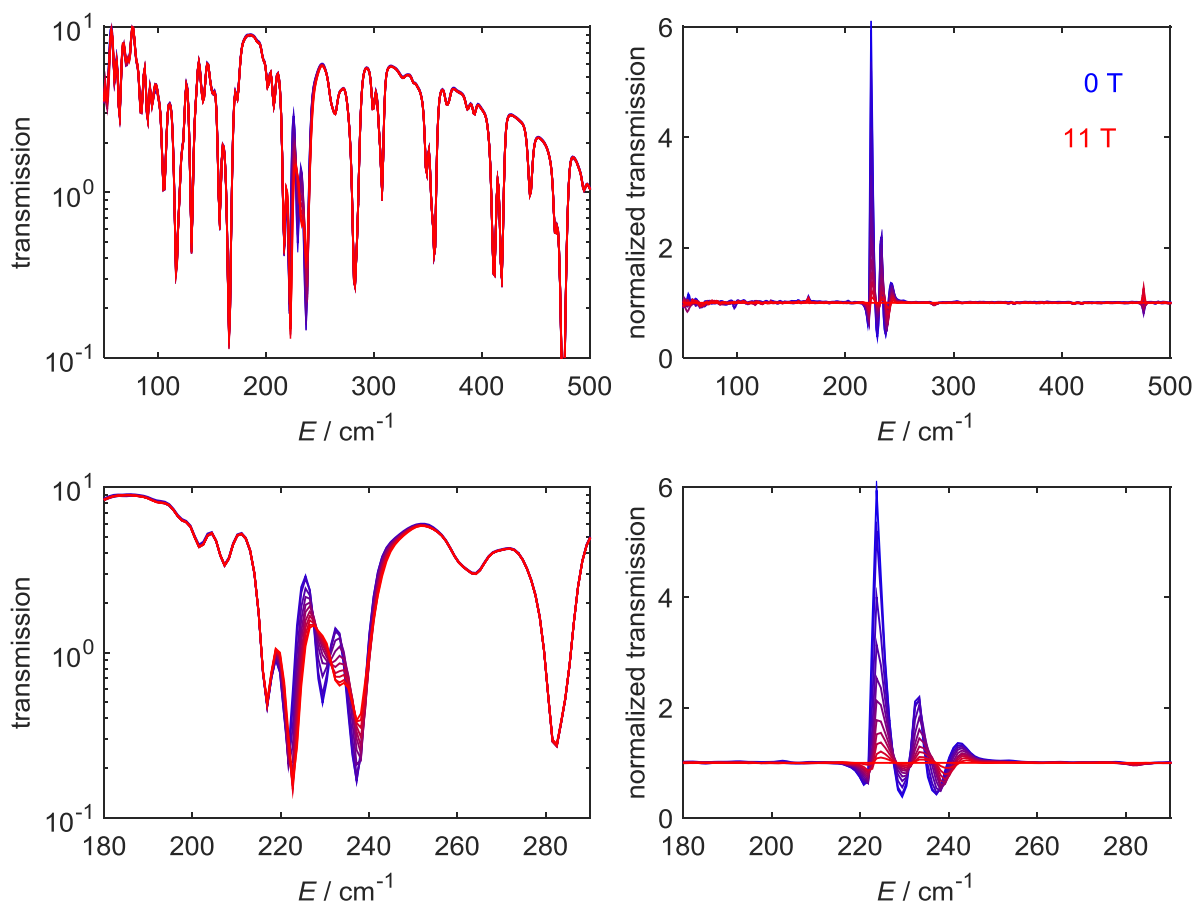


Figure 59: Left: FIR transmission spectra of $(\text{HNEt}_3)_2\mathbf{2}$ recorded at 4 K and various magnetic fields. Right: Normalized transmission spectra obtained by dividing by the spectrum at highest field. The image details at the bottom show zooms of the field-dependent features. The spectra were recorded by Dr. Milan Orlita and Michael Hakl.

The field-dependent features in the FIR-spectra show splittings that cannot be explained by g -value anisotropy or rhombic distortion and therefore must be due to spin-vibrational couplings. Theoretical calculations on $(\text{HNEt}_3)_2\mathbf{2}$ performed by Dr. Mihail Atanasov (Max Planck Institute for Chemical Energy Conversion, Mülheim a. d. R.) strongly support this assumption.¹⁶⁷ Correlated calculations performed at the CASSCF/NEVPT2 level (CASSCF: Complete active space self-consistent field; NEVPT2: Second-order n -electron valence state perturbation theory) provided a calculated D value of -112 cm^{-1} , in very good agreement with the experimental results. Furthermore, a very small E value of -1.1 cm^{-1} was calculated, confirming the axial nature of the electronic ground state. The effective g -values of the lowest $m_S = \pm 3/2$ Kramers doublet were calculated as $g_x = g_y = 0.056$ and $g_z = 9.43$. Calculation of the vibrational far infrared spectrum based on a DFT optimized geometry (DFT: Density functional theory) showed that there are at least three vibrational excitations in the region of 230 cm^{-1} that have some metal-ligand stretching character. Such vibrations can

induce modulations of the crystal field and thus lead to spin-phonon coupling. Indeed, the eigenfunctions obtained by applying a simplified spin-vibronic Hamiltonian showed mixed spin/vibrational character, thus explaining the observed splitting in the experimental FIR-spectra.¹⁶⁷ The presence of spin-phonon coupling is consistent with the dominance of the optical/acoustic Raman mechanism for magnetic relaxation in the intermediate temperature range.

The combination of magnetometry, EPR- and FIR-spectroscopy allowed for a relatively precise determination of the ZFS in $(\text{HNEt}_3)_2\mathbf{2}$ and $(\text{NMe}_4)_2\mathbf{2}$, but these methods do not provide any explanation for the origin of the very high values in terms of the electronic structures. Since MCD-spectroscopy is an outstanding tool for linking ground state with excited state properties, this method was applied for probing the electronic structures of $(\text{HNEt}_3)_2\mathbf{2}$ and $(\text{NMe}_4)_2\mathbf{2}$ beyond the electronic ground state.

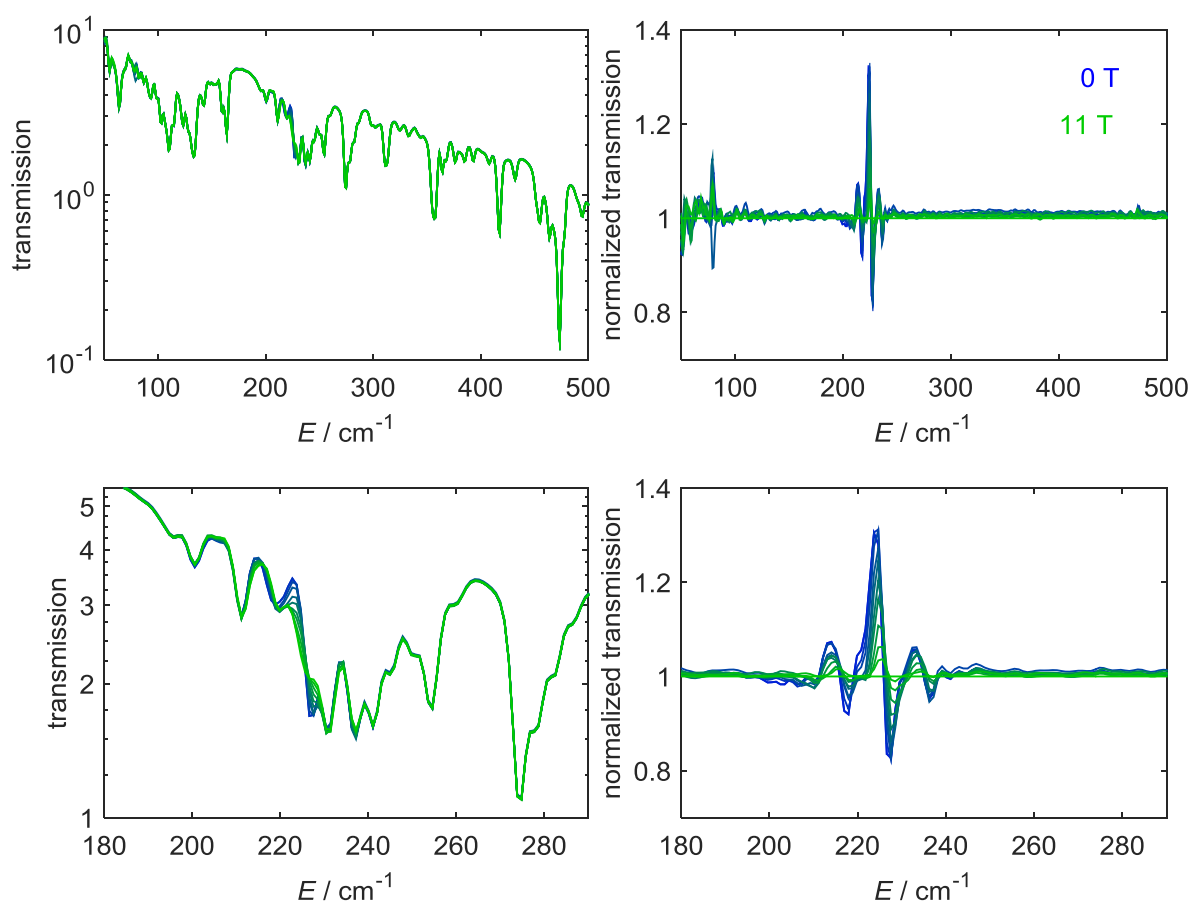


Figure 60: Left: FIR transmission spectra of $(\text{NMe}_4)_2\mathbf{2}$ recorded at 4 K and various magnetic fields. Right: Normalized transmission spectra obtained by dividing by the spectrum at highest field. The image details at the bottom show zooms of the field-dependent features. The spectra were recorded by Dr. Milan Orlita and Michael Haki.

Figure 61 shows the low-temperature MCD-spectra recorded on mulls of **(HNEt₃)₂2** and **(NMe₄)₂2** in fluorolube®. Two sets of intense bands, namely around 7000 cm⁻¹ and around 18000 cm⁻¹ are observed, which are typical for (pseudo-)tetrahedral Co(II) compounds.^{75,187} Within the *T_d* symmetry notation, they are attributed to spin-allowed transitions from the ⁴A₂(⁴F) electronic ground state to the excited states ⁴T₁(F) (7000 cm⁻¹) and ⁴T₁(P) (18000 cm⁻¹). One more spin-allowed transition, namely the transition to the ⁴T₂(F) state, is expected around 3500 cm⁻¹ but is out of the spectral range accessible by our MCD-spectrometer. In addition to the intense bands, several sharp but very weak signals are observed, which are attributed to spin-forbidden transitions.

With the help of the corresponding Tanabe-Sugano diagram (Figure 13), the positions of the spin-allowed transitions were used to roughly estimate the respective cubic crystal field parameters *Dq* and the Racah parameters *B*. For **(HNEt₃)₂2**, parameter values of *Dq* = 430 cm⁻¹ and *B* = 880 cm⁻¹ were obtained, while for **(NMe₄)₂2**, values of *Dq* = 455 cm⁻¹ and *B* = 855 cm⁻¹ were derived. Due to the relatively high energies of the ⁴A₂(⁴F) → ⁴T₁(⁴P) transition (18000 cm⁻¹) compared to other tetrahedrally coordinated Co(II) compounds, the obtained parameter values lie in the upper part of the typical range⁷⁵ and indicate rather large crystal field splittings. However, the cubic crystal field parameter values are not sufficient to explain the unique magnetic properties of **(HNEt₃)₂2** and **(NMe₄)₂2** since for cubic symmetry no ZFS is expected.

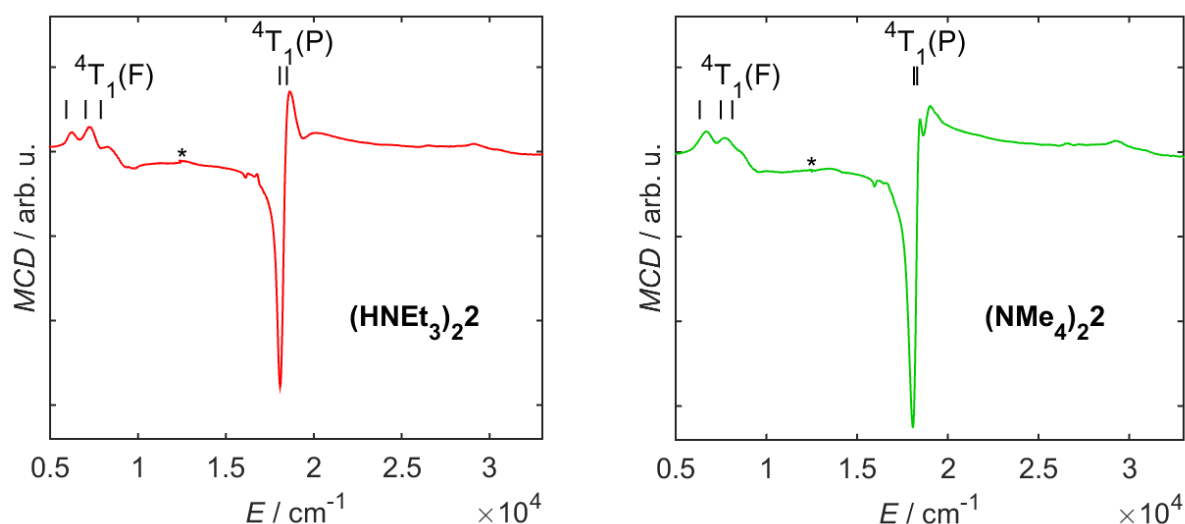


Figure 61: MCD-spectra of **(HNEt₃)₂2** (left) and **(NMe₄)₂2** (right) recorded at 1.5 K and magnetic fields of 2 T and 1 T. Black bars illustrate calculated transition energies based on the derived crystal field parameters (see main text). Asterisks indicate artefacts due to detector change.

As described in section 2.3.2, symmetry-lowering from T_d to D_{2d} symmetry causes splitting of the 4T states into two components each, which is reflected by splittings in the experimentally observed MCD bands. However, the low-energy bands around 7000 cm^{-1} appear to be split into three components rather than two and the size of the splittings seems to be too large to be explained by spin-orbit coupling or by further symmetry lowering to C_{2v} . In fact, crystal field analysis (see below) revealed that the additional signals, i.e. the low-energy peaks at 6211 cm^{-1} (**(HNEt₃)₂2**) and at 6671 cm^{-1} (**(NMe₄)₂2**) do not arise from the ${}^4A_2({}^4F) \rightarrow {}^4T_1({}^4F)$ transitions but belong to the 4E components of the largely split lower lying ${}^4T_2(F)$ states, indicating extraordinarily large axial distortions produced by the crystal field of the ligands.

The influence of the D_{2d} crystal field on the electronic structures of **(HNEt₃)₂2** and **(NMe₄)₂2** was estimated in terms of the crystal field parameters Dq , Dt and Ds defined by Ballhausen.⁷⁶ The corresponding energy calculations were performed in the $\alpha S_m S L m$ basis of states with the help of the Crystal Field Computer Package by Yeung and Rudowicz⁸⁰ as well as with a self-written Matlab script. The previously estimated values for Dq and B (see above) were used as starting parameters and the tetragonal parameters Dt and Ds were introduced to reproduce the splittings observed in the MCD spectra. As nicely illustrated in a publication by Wildner,⁷⁷ the splitting of the ${}^4T_1({}^4F)$ state is mainly affected by Dt and the corresponding MCD detected energies were therefore used for adjusting this parameter. Increasing the value of Dt not only results in an increased splitting of the ${}^4T_1({}^4F)$ state but also in an overall shift of its components to higher energies. Thus, increasing Dt required decreasing the value for Dq , consistent with the fact that Dq defined by Ballhausen contains tetragonal components.⁷⁹ The sign of Dt was set negative because this corresponds to a splitting of the ${}^4T_2({}^4F)$ term with the resulting 4B_2 component lower in energy than the 4E component, in agreement with a negative axial ZFS parameter D according to equation (49). Once the experimentally observed energies and splittings of the ${}^4T_1({}^4F)$ levels were reasonably well reproduced, the parameters Dq and Dt were kept fixed and the remaining tetragonal crystal field parameters Ds as well as the Racah parameters B were adjusted to reproduce the energies and the splittings of the higher lying ${}^4T_1({}^4P)$ terms. The Racah parameters C were fixed to $C = 4.5 B$. The final parameter sets derived for **(HNEt₃)₂2** and **(NMe₄)₂2** are listed in Table 10 while black bars in Figure 61 illustrate the calculated transition energies based on these parameters. Table A 17 in the appendix provides a comparison between experimental and calculated energies. Rather high values for Dt and Ds are required for reproducing the experimentally observed energies and the high value of Dt explains the observed structure in the NIR region of the MCD-spectra:

Since the splitting of the lowest excited cubic term ${}^4T_2({}^4F)$ is even more affected by Dt than the ${}^4T_1({}^4F)$ state, the higher lying 4E component arising from ${}^4T_2({}^4F)$ is raised in energy to such an extent that the corresponding transition moves from the mid-infrared to the near-infrared. In the MCD-spectra, the transitions ${}^4B_1 \rightarrow {}^4E({}^4T_2)$ are therefore observed close to the transitions ${}^4B_1 \rightarrow {}^4E({}^4T_1)$ and ${}^4B_1 \rightarrow {}^4A_2({}^4T_1)$. A graphical illustration is provided in Figure 62. The derived values for Dq seem to be rather low, but taking into account the relation between Dq defined by Griffith and Dq defined by Ballhausen (equation (40)), they agree well with the values obtained preliminarily with the help of the Tanabe-Sugano diagram (see Table 10).

It is important to mention that the derived parameters for **(HNEt₃)₂2** and **(NMe₄)₂2** should be considered as estimates rather than best-fit parameters since they were manually adjusted without applying a software-based fitting routine. The existence of better solutions cannot be excluded. The uncertainties given in Table 10 were estimated by checking the influence of parameter changes on the calculated transition energies. Furthermore, the calculations are based on a strongly simplified model, i.e. crystal field theory assuming ideal D_{2d} symmetry and without including spin-orbit coupling. However, the parameter sets not only explain the observed structures in the MCD-spectra but they also provide a plausible explanation for the large zero-field splittings observed in **(HNEt₃)₂2** and **(NMe₄)₂2**: Due to the low values for Dq (Dq in Ballhausen notation), the energy separations between the ground states ${}^4B_1({}^4A_2)$ and the first excited states ${}^4B_2({}^4T_2)$ are rather low, i.e. $10 Dq = 1300 \text{ cm}^{-1}$ for **(HNEt₃)₂2** and $10 Dq = 1400 \text{ cm}^{-1}$ for **(NMe₄)₂2**, leading to increased second-order interactions between these states.

Table 10: Crystal field and Racah parameters derived for **(HNEt₃)₂2** and **(NMe₄)₂2** assuming D_{2d} symmetry.

	(HNEt₃)₂2	(NMe₄)₂2
Dq (Ballhausen) / cm^{-1}	130 ± 30	140 ± 30
Dq (Griffith) / cm^{-1}	440 ± 60	470 ± 60
Dt / cm^{-1}	-530 ± 50	-565 ± 50
Ds / cm^{-1}	500 ± 100	550 ± 100
B / cm^{-1}	830 ± 30	790 ± 30
C / cm^{-1} (fixed to $4.5 B$)	3735	3555

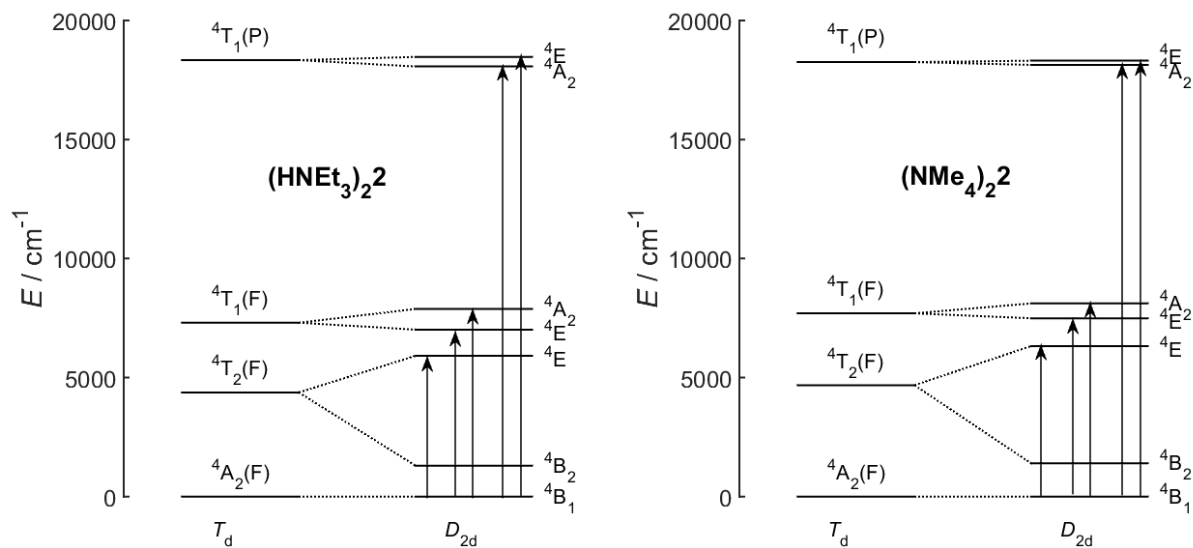


Figure 62: Energy level diagrams derived for **(HNEt₃)₂2** (left) and **(NMe₄)₂2** (right) showing the splitting of the cubic quartet states under the influence of a strong axial distortion. For D_{2d} symmetry, the shown energy levels are based on the calculations using the derived sets of crystal field and Racah parameters (see main text). Arrows depict the experimentally observed transitions.

In contrast, the energy separation between the states ${}^4B_2({}^4T_2)$ and ${}^4E({}^4T_2)$ is high and applying equation (49)

$$D = 4\lambda^2 \left[\frac{1}{E({}^4E)} - \frac{1}{E({}^4B_2)} \right] \quad (49)$$

with the spin-orbit coupling constant set to the free-ion value⁷⁸ of $\lambda = -180 \text{ cm}^{-1}$ gives $D = -78 \text{ cm}^{-1}$ for **(HNEt₃)₂2** and $D = -72 \text{ cm}^{-1}$ for **(NMe₄)₂2**, in qualitative agreement with the D values determined by FIR-spectroscopy and magnetometry. Please note that equation (49) was derived by means of perturbation theory. Strictly speaking, equation (49) is thus only valid for small perturbations, i.e. large energy gaps between the ground state and the first excited state compared to spin-orbit coupling.

Since the ground state 4B_1 is a spin-degenerate state, the observed MCD transitions are expected to show C-term character, which makes MCD-spectroscopy not only a tool for probing excited state energy levels, but also for probing the ground state itself. VTVH-MCD experiments were thus carried out on **(HNEt₃)₂2**, i.e. the MCD intensities at 18083 cm^{-1} and 18657 cm^{-1} were recorded as functions of the field at temperatures between 1.5 and 20 K. In Figure 63, the normalized intensities are plotted against $\mu_B H / 2kT$. For both wavelengths, the recorded isotherms coincide well, which is indicative for large zero-field splittings, i.e. no excited m_S states of the electronic ground state but only the ground Kramers doublet is

involved in the transitions. The system can thus be treated within the effective spin-1/2 approximation and equation (63) can be used for fitting the curves. For purely axial Co(II) systems, the effective g -values are given by $g_{z,\text{eff}} = 3 g_z$ and $g_{x,\text{eff}} = g_{y,\text{eff}} = 0$. Rather good fits are obtained using an effective polarization product of $M_{xy} = 1$ and effective g -values of $g_{z,\text{eff}} = 3 \cdot 3.03 \cong 9.1$ and $g_{x,\text{eff}} = g_{y,\text{eff}} = 0$, in good agreement with the magnetic data and the theoretical calculations. Consistently, the magnetic field dependence of the molar magnetizations for **(HNEt₃)₂2** and **(NMe₄)₂2** can also be simulated using the respective effective g -values (dotted lines in Figure 53).

The VTVH-MCD experiments thus provided a further confirmation of the axial nature of the ground state in **(HNEt₃)₂2**. However, a much more important observation is related to the polarization of the studied transition: The VTVH-MCD curves were fitted with an effective polarization product of $M_{xy} = 1$ and perpendicular g -values equal to zero. According to equation (63), this means that only the molecules with their quantization axis oriented parallel to the magnetic field contribute to the intensity, making the studied transitions extraordinarily interesting for MCD detected hysteresis curves.

MCD detected hysteresis studies on **(HNEt₃)₂2** and **(NMe₄)₂2** were performed by recording the field-dependence of the MCD intensities at 18083 cm⁻¹. Figure 64 shows the hysteresis loops obtained at 1.5 K and magnetic field sweep rates of 0.5 T min⁻¹, i.e. 83 Oe s⁻¹. For both **(HNEt₃)₂2** and **(NMe₄)₂2**, clear hysteresis with coercive fields of ca. 0.24 and 0.14 T is observed and to the best of my knowledge this is the first example of the observation of sizeable coercivity in Co(II) based single-ion magnets.

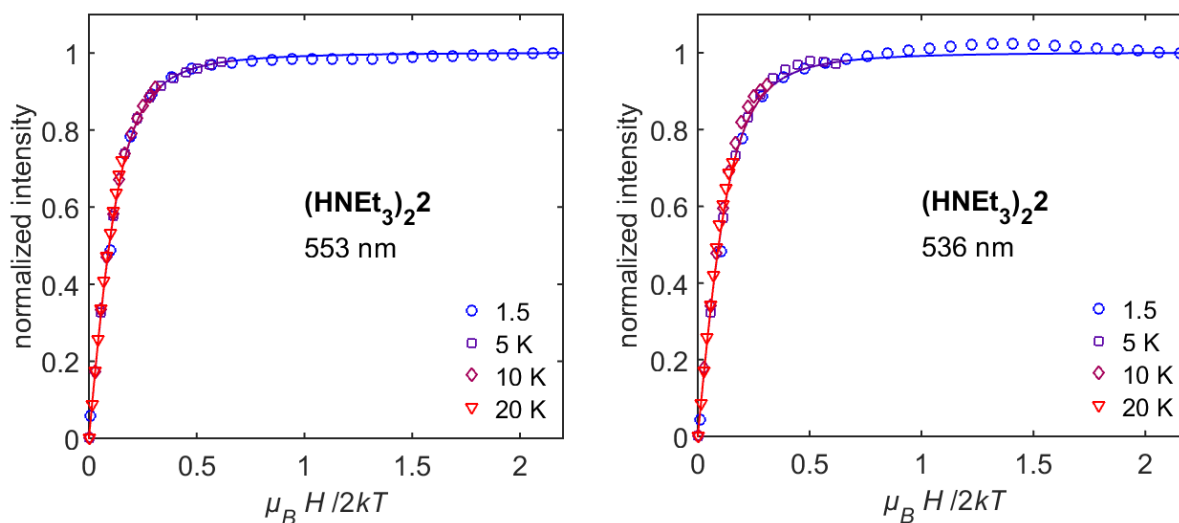


Figure 63: VTVH-MCD data recorded on a mull of **(HNEt₃)₂2** at 553 nm (left) and at 536 nm (right). Data were obtained at 1.5, 5, 10 and 20 K with magnetic fields up to 10 T. Open symbols correspond to experimental data points while solid lines correspond to best fits within the $S_{\text{eff}} = \frac{1}{2}$ approximation (see main text).

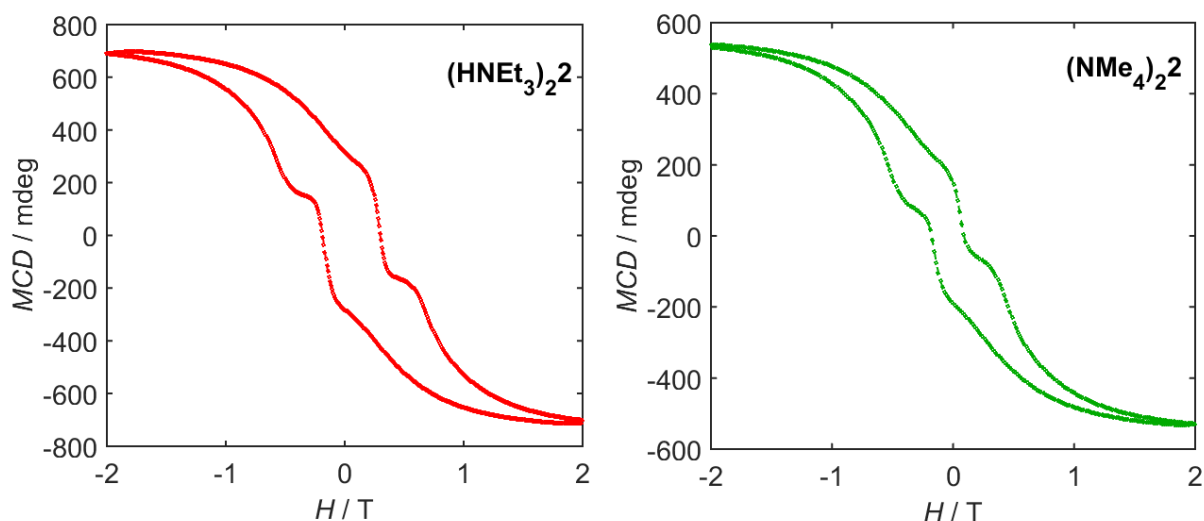


Figure 64: MCD detected hysteresis curves recorded on mulls of **(HNEt₃)₂2** (left) and **(NMe₄)₂2** (right) by measuring the field-dependence of the MCD signals at 18083 cm⁻¹. The measurements were performed at 1.5 K and a magnetic field scan rate of 0.5 T min⁻¹.

The previous highest coercive field was reported by Ruamps *et al.* for diluted single crystals of a pentacoordinate trigonal bipyramidal Co(II) complex, showing a coercive field of 5 mT at 30 mK.¹⁸⁸ As outlined above, the observation of MCD detected coercivity is attributed to the polarization of the transition, making MCD-spectroscopy an orientation selective method, in contrast to SQUID magnetometry on powder samples. It would be interesting to study further Co(II) complexes exhibiting similar molecular structures compared to **(HNEt₃)₂2** and **(NMe₄)₂2**. If they exhibit crystallographic unit cells that allow for crystal orientations with all molecular quantization axes oriented parallel to an applied field, single crystal SQUID measurements could provide a nice complementation to MCD-spectroscopy. Further variations of the counter ions could provide the possibility to obtain suitable crystal structures.

Comparing **(HNEt₃)₂2** and **(NMe₄)₂2**, a lower coercive field is found for the latter, consistent with the lower zero-field splitting. However, the difference in the coercive fields seems to be too high to be explained solely by the only slightly smaller zero-field splitting in **(NMe₄)₂2** compared to **(HNEt₃)₂2**. Further explanations might be the presence of small (and thus not measurable) rhombic ZFS, which is higher in **(NMe₄)₂2** than in **(HNEt₃)₂2**, or different relative orientations of the molecules in the unit cells, leading to different dipolar interaction strengths. Of course also the measurement accuracy has to be taken into account. Slight field delays during the field sweeps result in small errors in the determined coercive fields.

Summarizing this chapter, the magnetic and spectroscopic investigation of the two novel Co(II) based single-ion magnets (**(HNEt₃)₂2** and **(NMe₄)₂2**) was presented. In contrast to most other cobalt complexes, they show slow magnetic relaxation in zero bias dc field, which is attributed to the highly axial nature of their ground states. By analyzing MCD-spectroscopic data, it was possible to relate the high axial zero-field splittings to the electronic structures. It was shown that strong crystal fields combined with enormous axial distortion lead to relatively small energy gaps between the ⁴B₁ ground states and the ⁴B₂ first excited states, resulting in enhanced second-order interactions and thus large ZFS parameters *D*. The unique electronic structures are thus correlated to the molecular structures: The strong crystal fields can be explained by the ability of the bis(sulfonamide) ligand to act as both a σ - and π -donor while the axial distortion results from the geometric arrangement, i.e. the very acute N-Co-N angles and the almost perpendicular orientations of the aromatic rings. The N-Co-N angles for **(NMe₄)₂2** are slightly larger than for **(HNEt₃)₂2**, reflected by a slightly smaller zero-field gap.

The conclusion that axial geometries lead to axial ground states has been reported before and a current trend in the field of single-ion magnets is therefore the design of rather exotic linear complexes,^{29-31,72} e.g. the linear iron(I) compound [K(crypt-222)][Fe(C(SiMe₃)₃)₂]²⁹ mentioned in section 2.1.3. However, they are usually highly air- and moisture sensitive, precluding practical application. Furthermore, their performance as single-ion magnets is not necessarily better, e.g. quantum tunneling of magnetization in zero field still precludes the observation of sizeable coercivity. Thus, the presented pseudo-tetrahedral Co(II) complexes **(HNEt₃)₂2** and **(NMe₄)₂2** represent a good alternative for obtaining axial systems without too much synthetic effort. Regarding the design criteria of such complexes, it can be concluded that bidentate ligands leading to metallacycles with acute bite angles should be preferred. The donor atoms should be strong σ - and π -donors. Furthermore, the ligand backbone should be rather rigid and symmetric, leading to perpendicular orientation of the ligands with respect to each other and thus symmetry beyond the directly coordinated donor atoms.

However, although the ligand employed in **(HNEt₃)₂2** and **(NMe₄)₂2** fulfills these conditions and axial ground states are observed, the performance of the complexes as single-ion magnets is still far from being suitable for practical application. Reasons are the presence of tunneling processes at low temperatures and Raman-like relaxation processes at higher temperatures. One possibility to achieve better performance could be the modification of the ligand, e.g. converting it into a tetradentate bridging ligand, leading to exchange-coupled

systems for which quantum tunneling is further suppressed. Since such ligands are also redox-active, very strong exchange couplings could be achieved by employing the ligand in a radical form.³³

4.4 Binuclear Cobalt Complexes

This subproject was part of a collaboration with the group of Prof. Dr. Biprajit Sarkar (Institute for Chemistry and Biochemistry, Freie Universität Berlin), who provided the compounds and the structural data. Magnetic measurements and preliminary EPR studies on the symmetric compounds were carried out as part of the teacher thesis of Irina Peremykin (January – July 2013) under my supervision.¹⁸⁹ Preliminary analyses of the magnetic data of the asymmetric compounds were carried out as part of the MSc thesis of Frauke D. Breitgoff (September 2014 – March 2015), also under my supervision.¹⁸¹ Work done by others is indicated in the text at the position where it appears for the first time.

Part of the results presented below has already been published in: *Chemistry – A European Journal*, **2014**, *20*, 3475 – 3486.³²

4.4.1 Structures of the Cobalt Dimers

The symmetrically bridged Co(II)-Co(II) dimers [$\{(t\text{mpa})\text{Co}^{\text{II}}\}_2(\mu\text{-L}^2)\text{][BF}_4\text{]}_2$ (**3[BF₄]₂**) and [$\{(t\text{mpa})\text{Co}^{\text{II}}\}_2(\mu\text{-L}^3)\text{][BPh}_4\text{]}_2$ (**4[BPh₄]₂**) (with $\text{H}_2\text{L}^2 = 2,5\text{-di-[2-(methoxy)-anilino]-1,4-benzoquinone}$, $\text{H}_2\text{L}^3 = 2,5\text{-di-[2-(trifluoromethyl)-anilino]-1,4-benzoquinone}$ and $t\text{mpa} = \text{tris(2-pyridylmethyl)amine}$) were synthesized and structurally characterized by Dr. David Schweinfurth (Institute for Chemistry and Biochemistry, Freie Universität Berlin).³² In both complexes, the Co(II) centers are bridged by quinone-based bridging ligands, where two oxygen donors of 2,5-dihydroxy-1,4-benzoquinone are substituted by isoelectronic [NR] groups, leading to symmetrical bridging situations. In **3[BF₄]₂**, R refers to 2-(methoxy)-phenyl (R^2 in Figure 65) while in **4[BPh₄]₂**, R stands for 2-(trifluoromethyl)-phenyl (R^3 in Figure 65). In both cases, $t\text{mpa}$ serves as a co-ligand and the Co(II) centers are distorted octahedrally coordinated. For **4[BPh₄]₂**, crystallographic data were available and the obtained molecular structure is illustrated in Figure 65.

4[BPh₄]₂ crystallizes in the triclinic $P\bar{1}$ space group with one molecule in the unit cell. The Co-O and Co-N bond lengths from Co to the donors of the bridging ligand are 1.980 and 2.162 Å, respectively, and thus in the same range as reported for related high-spin Co(II) complexes.¹⁹⁰ The bond lengths within the bridging ligand, especially the C-O bond lengths (1.289 Å) being longer than those in the free ligand and the C-N bond lengths (1.301 Å) being

shorter than those in the free ligand, hint to negatively charged O donors and neutral imine-type N donors.³² The O-Co-N bite angles are 78.14°, i.e. significantly smaller than the 90° expected for regular octahedrons. The Co-Co intra-dimer distance is 7.954 Å and the shortest inter-dimer Co-Co distance is 9.478 Å.

$3[\text{BF}_4]_2$ was chemically oxidized and the one- and two-electron oxidized species $3[\text{BF}_4]_3$ and $3[\text{BF}_4]_4$ were isolated in their pure forms.³² Single crystals were obtained for $3[\text{BF}_4]_4$ and X-ray crystallographic analysis revealed that it crystallizes in the tetragonal space group $I4_1/a$ with 8 molecules per unit cell. The molecular structure is shown on the right hand side of Figure 65. The Co-O and Co-N bond lengths to the bridging ligand are 1.877 and 1.946 Å, respectively, and thus shorter than the corresponding bond lengths in $4[\text{BPh}_4]_2$. This indicates that the two-electron oxidation led to the formation of octahedrally coordinated low-spin Co(III) centers. In octahedral LS-Co(III), the e_g orbitals pointing towards the ligands are empty and due to reduced electrostatic repulsion the ligand donors can approach more closely. A more regular octahedron than in $4[\text{BPh}_4]_2$ is formed, reflected by the O-Co-N bite angle of 85.5°. The intra-ligand bond lengths are almost the same for both complexes, indicating the same bonding situation, i.e. negatively charged oxygen donors and imine-type nitrogen donors. The Co-Co intra-dimer distance in $3[\text{BF}_4]_4$ is 7.638 Å.

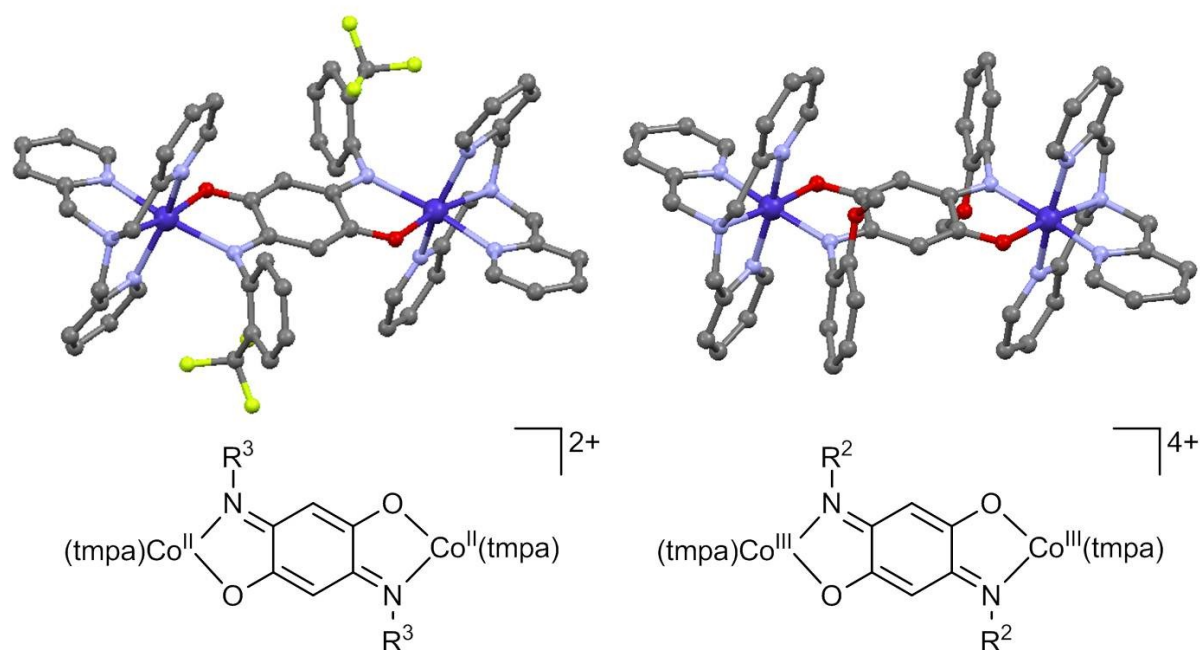


Figure 65: Molecular structures of 4^{2+} (left) and 3^{4+} (right). Cobalt is shown in blue, oxygen in red, fluorine in yellow, nitrogen in violet and carbon in grey. Hydrogens and counter ions are omitted for clarity. The samples as well as the crystallographic data were provided by Dr. David Schweinfurth.

An asymmetrically bridged Co(II)-Co(II) dimer, namely $[\{(t\text{mpa})\text{Co}^{\text{II}}\}_2(\mu\text{-L}^4)][\text{OTf}]_2$ (**5**[OTf]₂) with $\text{H}_2\text{L}^4 = 2\text{-}[4\text{-}(\text{isopropyl})\text{-anilino}]\text{-5-hydroxy-1,4-benzoquinone}$ as well as the corresponding oxidized species **5**[OTf]₃ and **5**[OTf]₂[BF₄]₂ were synthesized and characterized by Dr. Margarethe van der Meer (Institute for Chemistry and Biochemistry, Freie Universität Berlin). In these complexes, only one of the oxygen donors of 2,5-dihydroxy-1,4-benzoquinone is substituted by a [NR] group, resulting in an asymmetric bridging situation with the cobalt centers in different surroundings. Here R refers to 4-(isopropyl)-phenyl (R⁴ in Figure 66). The molecular structures of **5**[OTf]₂ and **5**[OTf]₃, obtained by X-ray crystallography, are shown in Figure 66. Both **5**[OTf]₂ and the one-electron oxidized species **5**[OTf]₃ crystallize as dichloromethane solvates in the triclinic *P*-1 space group with two formula units per unit cell. Except for the asymmetry, the coordination geometry of the bridging ligand is similar to those obtained for **4**[BPh₄]₂ and **3**[BF₄]₄, i.e. the negative charges are localized on the oxygen donors. One of the cobalt centers (Co1) is coordinated by a negatively charged oxygen donor (O3) and by the neutral imine-type nitrogen donor (N1) of the bridge. The other cobalt center (Co2) is coordinated by a negatively charged oxygen donor (O1) and a neutral keto-type oxygen donor (O2) of the bridge. In **5**[OTf]₂, the Co1-N1 and Co1-O3 distances are 2.192 and 2.006 Å, respectively, while the Co2-O1 and Co2-O2 distances are 1.987 and 2.212 Å. The N1-Co1-O3 and O1-Co2-O2 bite angles are 76.49° and 77.35°, both showing large deviations from ideal octahedral symmetry.

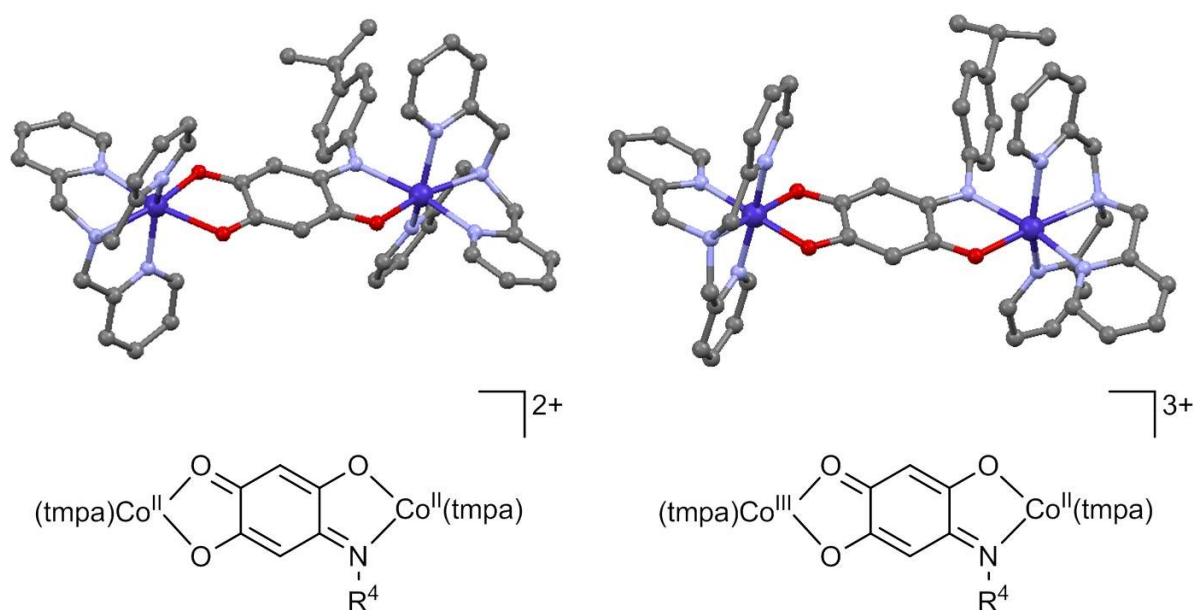


Figure 66: Molecular structures of **5**²⁺ (left) and **5**³⁺ (right). Cobalt is shown in blue, oxygen in red, nitrogen in violet and carbon in grey. Hydrogens and counter ions are omitted for clarity. The samples as well as the crystallographic data were provided by Dr. Margarethe van der Meer.

In **5[OTf]₃**, the Co1-N1 and Co1-O3 bond lengths are 2.187 and 2.039 Å, respectively, and thus comparable to those in **5[OTf]₂**. However, with 1.888 and 1.913 Å, the Co2-O1 and Co2-O2 distances are significantly shorter, indicating that one-electron oxidation preferentially takes place at Co2, yielding a low-spin Co(III) center. Consistently, the bite angles are 76.36° (N1-Co1-O3) and 85.96° (O1-Co2-O2). **5[OTf]₂** is thus best described as a cobalt dimer containing two six-coordinate high-spin Co(II) centers, while **5[OTf]₃** contains one high-spin Co(II) (Co1) and one low-spin Co(III) center (Co2). The Co1-Co2 intra-dimer distances are 8.025 Å (**5[OTf]₂**) and 7.765 Å (**5[OTf]₃**) and the shortest inter-dimer Co-Co distances (Co2-Co2) are 6.576 and 8.130 Å, respectively.

4.4.2 Magnetic Properties

The magnetic properties of complexes **3[BF₄]₂**, **3[BF₄]₃**, **3[BF₄]₄**, **4[BPh₄]₂**, **5[OTf]₂**, **5[OTf]₃** and **5[OTf]₂[BF₄]₂** were investigated by means of dc susceptibility and magnetization measurements and the obtained data were analyzed by means of different models. Due to the lack of unpaired electrons in LS-Co(III), complexes **3[BF₄]₄** and **5[OTf]₂[BF₄]₂** are diamagnetic and therefore not particularly interesting in the context of molecular magnetism. However, measuring their diamagnetic susceptibility allowed for the experimental determination of the diamagnetic corrections to the susceptibilities of the other complexes instead of estimating them by using Pascal's constants. The measured field-dependence of the magnetization of **3[BF₄]₄** is shown in Figure 67. Since there is no temperature dependence for diamagnetic susceptibilities while the effects of possible para- or ferromagnetic impurities are minimized at high temperatures, the measurement was performed at 300 K. The data points describe a straight line whose slope yields a diamagnetic susceptibility of $\chi_{\text{dia}} = -1820 \cdot 10^{-6} \text{ cm}^3 \text{ mol}^{-1}$. This value is much larger than the value estimated by using Pascal's constants⁹³ ($\chi_{\text{dia}} = -768 \cdot 10^{-6} \text{ cm}^3 \text{ mol}^{-1}$), showing that the direct determination of diamagnetic corrections should be preferred whenever a diamagnetic analogue of a paramagnetic compound is available. The experimentally determined diamagnetic correction also includes sample holder effects (ca. $-6.9 \cdot 10^{-9} \text{ cm}^3$).

The diamagnetic corrections to the susceptibilities of complexes **3[BF₄]₂**, **3[BF₄]₃**, **4[BPh₄]₂**, and **5[OTf]₃** were subsequently calculated by correcting the molar susceptibility of **3[BF₄]₄** for the differing structural elements, i.e. the substituents R, the oxidation state of Co and the counter ions with the help of Pascal's constants⁹³. The obtained values are listed in Table 11.

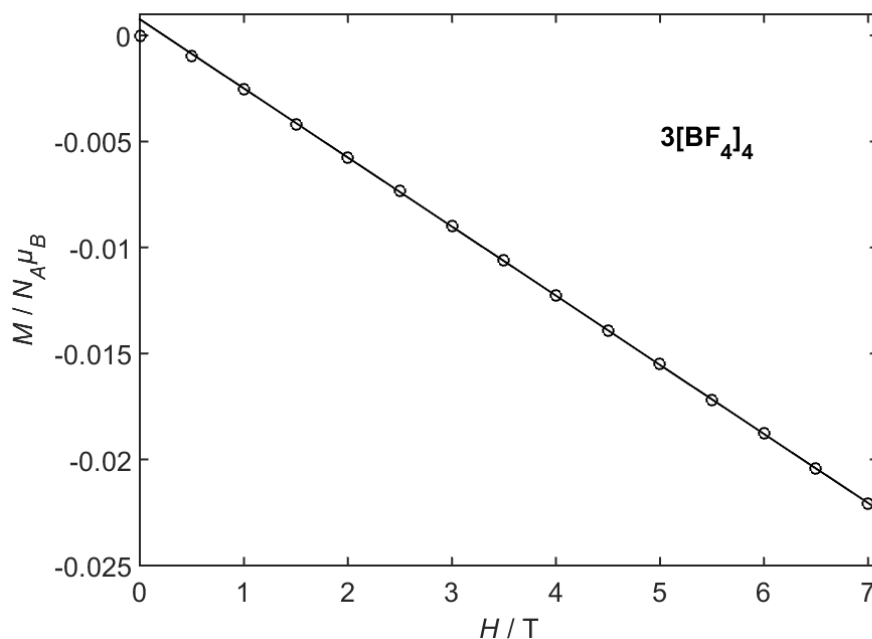


Figure 67: Magnetic field dependence of the molar magnetization of $3[\text{BF}_4]_4$ measured at 300 K. Open circles depict experimental data points while the solid line corresponds to the linear fit.

Table 11: Diamagnetic corrections to the susceptibilities of the studied Co dimers.

Compound	$\chi_{\text{dia}} / 10^{-6} \text{ cm}^3 \text{ mol}^{-1}$
$3[\text{BF}_4]_2$	-1750
$3[\text{BF}_4]_3$	-1785
$3[\text{BF}_4]_4$	-1820
$4[\text{BPh}_4]_2$	-2118
$5[\text{OTf}]_2$	-672.6
$5[\text{OTf}]_3$	-1775

In contrast, the diamagnetic correction for $5[\text{OTf}]_2$ was solely estimated using Pascal's constants since its magnetic properties were investigated using another instrument. The magnetometer used for studying $5[\text{OTf}]_2$ had a negligible sample holder contribution, as shown by field-dependent magnetization measurements on the corresponding diamagnetic species $5[\text{OTf}]_2[\text{BF}_4]_2$ (data shown in the appendix, section 8.5.1).

Figure 68 shows the temperature dependence of the products of the paramagnetic susceptibilities χ and the temperature T for complexes $3[\text{BF}_4]_2$, $3[\text{BF}_4]_3$, $4[\text{BPh}_4]_2$, $5[\text{OTf}]_2$

and $5[\text{OTf}]_3$. The mixed valent dimers $3[\text{BF}_4]_3$ and $5[\text{OTf}]_3$ show rather similar curves with room-temperature χT values of 2.25 and 1.88 $\text{cm}^3 \text{mol}^{-1} \text{K}$, respectively. The value for $3[\text{BF}_4]_3$ is larger than the spin-only value expected for an $S = 3/2$ system according to Curie's law (1.88 $\text{cm}^3 \text{mol}^{-1} \text{K}$) but lies in the typical range for sixfold coordinated Co(II) ions with incompletely quenched orbital angular momenta.⁶⁵ No plateau is reached at high temperatures, indicative of temperature independent paramagnetism (TIP)² arising from second-order Zeeman effects. The slope at high temperatures yields $\chi_{\text{TIP}} = 985 \cdot 10^{-6} \text{cm}^3 \text{mol}^{-1}$. For $5[\text{OTf}]_3$, no TIP is observed. Below 50 K, a rapid decrease of the χT products is observed for both $3[\text{BF}_4]_3$ and $5[\text{OTf}]_3$, which is attributed to the thermal depopulation of excited states. Depending on the degree of symmetry and the accordingly assumed model, these excited states result either from spin-orbit coupling induced splittings of the electronic ${}^4\text{T}_{1g}$ ground states (O_h symmetry) or from zero-field splittings of the ${}^4\text{A}_{2g}$ ground states in the presence of axial distortion (see section 2.3.1). At 1.8 K, χT reaches values of 1.33 $\text{cm}^3 \text{mol}^{-1} \text{K}$ ($3[\text{BF}_4]_3$) and 1.36 $\text{cm}^3 \text{mol}^{-1} \text{K}$ ($5[\text{OTf}]_3$).

Interestingly, no valence tautomerism is observed. Valence tautomerism in the mixed-valent compounds $3[\text{BF}_4]_3$ and $5[\text{OTf}]_3$ would correspond to a temperature-dependent change from an $S = 3/2$ system with three unpaired electrons at the Co(II) center to an $S = 1/2$ system with one unpaired electron at the bridge, leading to steps in the χT versus T curves.¹⁹¹⁻¹⁹³ In the studied temperature range no steps were observed, showing that the redox-active and potentially non-innocent ligand essentially acts as innocent in the studied compounds.

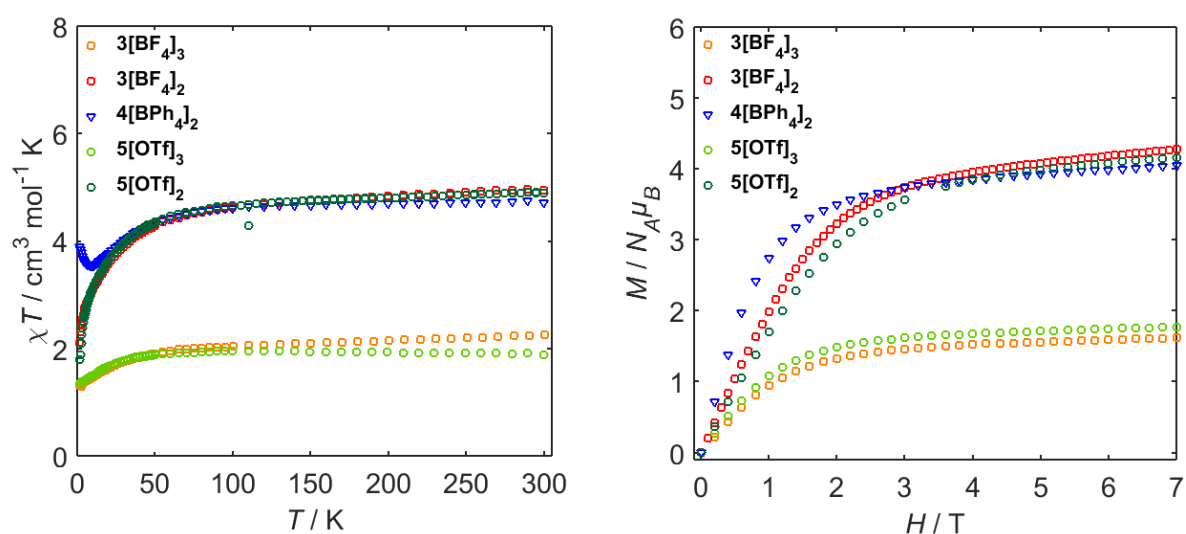


Figure 68: Temperature dependence of χT (left) and magnetic field dependence of the magnetization at 1.8 K (right) for the compounds $3[\text{BF}_4]_3$, $3[\text{BF}_4]_2$, $4[\text{BPh}_4]_2$, $5[\text{OTf}]_3$ and $5[\text{OTf}]_2$, as indicated.

Despite the different bridging situations, the χT versus T plots for the Co(II)-Co(II) dimers **3[BF₄]₂** and **5[OTf]₂** are also rather similar, showing room-temperature χT values of 4.97 cm³ mol⁻¹ K and 4.89 cm³ mol⁻¹ K, respectively. Positive slopes at high temperatures indicate temperature-independent paramagnetism with $\chi_{\text{TIP}} = 1570 \cdot 10^{-6}$ cm³ mol⁻¹ for **3[BF₄]₂** and $\chi_{\text{TIP}} = 1350 \cdot 10^{-6}$ cm³ mol⁻¹ for **5[OTf]₂**. With decreasing temperature, χT gradually decreases until at 50 K values of 4.28 and 4.34 cm³ mol⁻¹ K are observed. Due to thermal depopulation of excited states, a rapid decrease of χT is observed below 50 K, reaching values of 2.11 and 1.78 cm³ mol⁻¹ K at 1.8 K. At high temperatures, the χT values of the Co(II) dimers **3[BF₄]₂** and **5[OTf]₂** are slightly higher than twice the values of the corresponding mixed-valent species **3[BF₄]₃** and **5[OTf]₃**, respectively, whereas at low temperatures ($T \leq 6$ K), the χT values are lower than twice the values of the mixed-valent forms. This behavior hints at weak antiferromagnetic couplings, resulting in effective coupled spins of $S_{\text{eff}} = 0$ at low temperatures.

Interestingly, a rather different temperature dependence of χT is observed for the symmetrically bridged dimer **4[BPh₄]₂**. With a room-temperature value of $\chi T = 4.74$ cm³ mol⁻¹ K, the behavior at high temperatures is still similar to that of **3[BF₄]₂** and **5[OTf]₂**. However, with decreasing temperature, χT decreases until at 8 K a minimum with $\chi T = 3.54$ cm³ mol⁻¹ K is reached. At lower temperatures, χT increases again, reaching a value of 3.90 cm³ mol⁻¹ K at 1.8 K. The increase at low temperatures hints at weak ferromagnetic coupling between the Co(II) centers, in contrast to the observations for **3[BF₄]₂** and **5[OTf]₂**.

The magnetic field dependence of the molar magnetization at 1.8 K for compounds **3[BF₄]₂**, **3[BF₄]₃**, **4[BPh₄]₂**, **5[OTf]₂** and **5[OTf]₃** is shown on the right hand side of Figure 68. The curves show the same tendency as observed for the temperature dependence, i.e. the plots for the mixed-valent forms **3[BF₄]₃** and **5[OTf]₃** as well as those for the Co(II) dimers **3[BF₄]₂** and **5[OTf]₂** are relatively similar while more pronounced deviations are observed for **4[BPh₄]₂**. The higher slope observed for **4[BPh₄]₂** is consistent with the ferromagnetic coupling found in the temperature dependent susceptibility measurements. At 7 T, the molar magnetization reaches values of 4.28 μ_{B} (**3[BF₄]₂**), 1.62 μ_{B} (**3[BF₄]₃**), 4.04 μ_{B} (**4[BPh₄]₂**), 4.16 μ_{B} (**5[OTf]₂**) and 1.77 μ_{B} (**5[OTf]₃**).

As described in section 2.3.1, incompletely quenched orbital angular momenta in octahedral Co(II) complexes might complicate the analysis of the magnetic data and a conventional spin Hamiltonian is only suitable for highly distorted octahedral environments, which lead to orbitally non-degenerate ground states. The magnetic data presented above were thus first analyzed by applying the Lines approach⁸¹, i.e. in terms of the parameters k_{r} , λ_{SO} , J_{ex}

and $z'J'$. λ_{SO} is the spin-orbit coupling coefficient while k_r is the orbital reduction factor describing the reduction of the free-ion spin-orbit interaction in the complex. J_{ex} is the exchange coupling constant between the Co(II) centers and $z'J'$ is an inter-dimer interaction parameter with z' being the number of relevant neighbors. The obtained best fits to the susceptibility data of **3**[BF₄]₂, **3**[BF₄]₃, **4**[BPh₄]₂, **5**[OTf]₂ and **5**[OTf]₃ are illustrated in Figure 69 while Table 12 lists the corresponding parameter values. Visually, more or less acceptable agreement between experimental and calculated values seems to be observed; however, most of the agreement factors R defined by

$$R = \frac{\sum[(\chi T)_{\text{exp}} - (\chi T)_{\text{calc}}]^2}{\sum[(\chi T)_{\text{exp}}]^2} \quad (69)$$

are rather high. As a rule of thumb, good fits to susceptibility data are characterized by agreement factors in the order of 10^{-4} or lower.⁸²

The signs of the exchange coupling constants J_{ex} indicate antiferromagnetic couplings for the dimers **3**[BF₄]₂ and **5**[OTf]₂ and ferromagnetic coupling for **4**[BPh₄]₂, as already concluded from the shape of the curves and the comparison with those of the one-electron oxidized species (see above). The small magnitudes of J_{ex} hint at rather weak exchange couplings, a situation which is not uncommon in Co(II) species,⁴⁴ also in view of the long bridge.

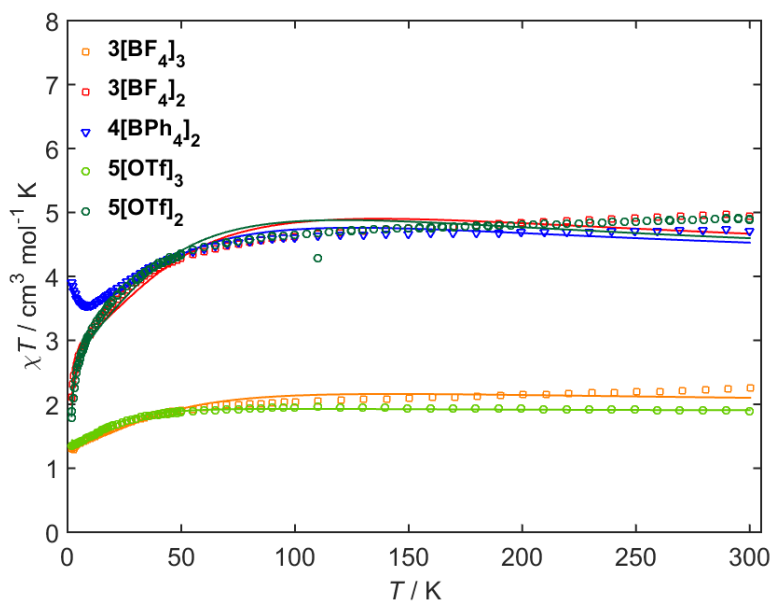


Figure 69: Experimentally observed temperature-dependence of χT for **3**[BF₄]₂, **3**[BF₄]₃, **4**[BPh₄]₂, **5**[OTf]₂ and **5**[OTf]₃ (open symbols) and best fits obtained by applying the Lines approach (solid lines).

Table 12: Best-fit parameters obtained for the dc susceptibility data of **3[BF₄]₂**, **3[BF₄]₃**, **4[BPh₄]₂**, **5[OTf]₂** and **5[OTf]₃** by applying the Lines model.

	3[BF₄]₂	3[BF₄]₃	4[BPh₄]₂	5[OTf]₂	5[OTf]₃
k_r	0.49	0.31	0.46	0.48	0.10
$\lambda_{SO} / \text{cm}^{-1}$	-119	-164	-118	-110	-203
$J_{\text{ex}} / \text{cm}^{-1}$	-0.62	-	2.90	-0.76	-
$z'J' / \text{cm}^{-1}$	-0.30	-0.14	-0.06	-0.34	-0.36
$R / 10^{-4}$	9.6	11	3.37	11	1.62

However, most of the other best-fit parameter values are out of the expected range. One discrepancy concerns the values of the spin-orbit coupling coefficients λ_{SO} . Compared to the free-ion value of -180 cm^{-1} , the values determined for the Co(II) dimers **3[BF₄]₂**, **4[BPh₄]₂** and **5[OTf]₂** are very low while those for the oxidized species **3[BF₄]₃** and **5[OTf]₃** are higher. An opposite trend is observed for the orbital reduction parameters k_r , i.e. lower values were obtained for the oxidized complexes than for the Co(II) dimers. Furthermore, all of the values for k_r are significantly lower than usually expected for octahedrally coordinated Co(II) complexes ($0.70 \leq k_r \leq 0.95$)^{81,85}. Since it has been shown that strong deviations from octahedral symmetry lead to artificial (i.e. physically meaningless) lowering of the spin-orbit coupling constants,⁸² these findings indicate that the Lines model is not appropriate for analyzing the magnetic properties of the compounds studied here.

As outlined in section 2.3.1, an empirical model taking into account axial distortion was developed by Lloret *et al.*⁸⁵ and this model was subsequently applied for analyzing the susceptibility data of compounds **3[BF₄]₂**, **3[BF₄]₃**, **4[BPh₄]₂**, **5[OTf]₂** and **5[OTf]₃**. Here, the fit parameters are the exchange coupling J_{ex} , the orbital reduction factor α_r , the spin-orbit coupling constant λ_{SO} and the axial distortion parameter Δ_{ax} , describing the splitting of the Co(II) $^4T_{1g}$ ground state due to axial distortion. The orbital reduction factor α_r has a similar meaning as the parameter k_r in the Lines model, but due to its slightly different definition, α_r typically adopts higher values ($0.75 \leq \alpha_r \leq 1.5$)⁸⁵. The obtained best fits applying this model are shown in Figure 70 while Table 13 lists the corresponding best-fit parameter values.

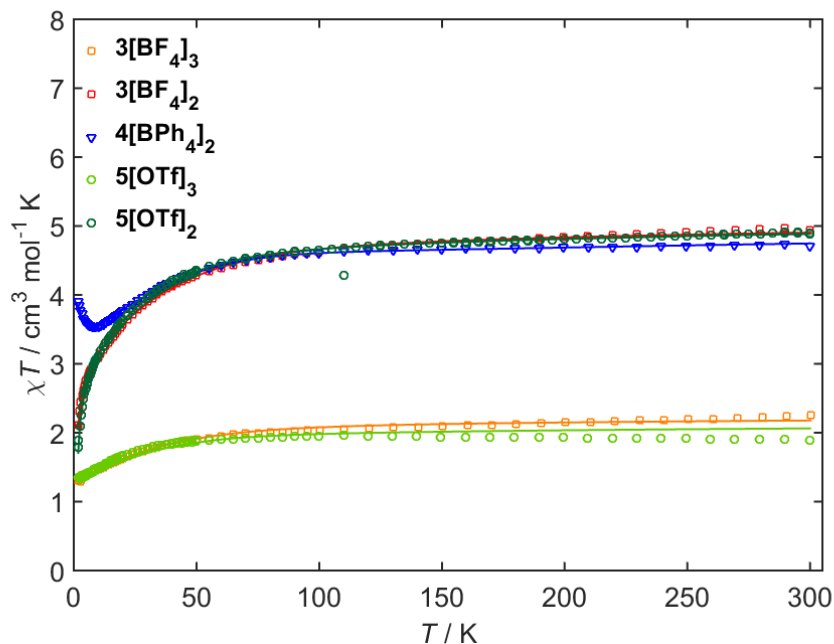


Figure 70: Experimentally observed temperature-dependence of χT for **3[BF₄]₂**, **3[BF₄]₃**, **4[BPh₄]₂**, **5[OTf]₂** and **5[OTf]₃** (open symbols) and best fits obtained by applying the empirical model developed by Lloret *et al.*⁸⁵ (solid lines).

Table 13: Best-fit parameters obtained for the dc susceptibility data of **3[BF₄]₂**, **3[BF₄]₃**, **4[BPh₄]₂**, **5[OTf]₂** and **5[OTf]₃** by applying the empirical model developed by Lloret *et al.*⁸⁵. The listed D values were estimated from the best-fit parameters by using equation 71 (see below).

	3[BF₄]₂	3[BF₄]₃	4[BPh₄]₂	5[OTf]₂	5[OTf]₃
α_r	1.03	1.03	0.96	1.05	1.05
$\lambda_{SO} / \text{cm}^{-1}$	-160	-160	-191	-143	-143
$\Delta_{ax} / \text{cm}^{-1}$	780	780	950	781	781
J_{ex} / cm^{-1}	-0.467	-	1.24	-0.63	-
z	-	0.89	-	-	0.84
$R / 10^{-4}$	0.45	1.67	0.34	0.15	21.55
D / cm^{-1}	35	35	36	29	29

As evidenced by the overall lower agreement factors R , the qualities of the fits are better than those obtained with the Lines model and the parameters themselves also show more reasonable values, i.e. they lie in the range expected for six-coordinated Co(II) complexes. The data of the one-electron oxidized species were successfully simulated with the same

parameter sets as for the corresponding non-oxidized dimers after introducing an overall scaling factor z , which accounts for e.g. structural deviations or measurement uncertainties. Importantly, the axial distortion parameters Δ_{ax} are rather high and positive. According to equation 42 in section 2.3.1, this corresponds to tetragonal elongation of the octahedron. The ${}^4T_{1g}$ ground state splits into the components ${}^4A_{2g}$ and 4E_g with ${}^4A_{2g}$ becoming the ground state.

Since ${}^4A_{2g}$ is an orbital singlet term, the magnetic data of **3[BF₄]₂**, **3[BF₄]₃**, **4[BPh₄]₂**, **5[OTf]₂** and **5[OTf]₃** can be treated within the spin-only formalism using $S = 3/2$ and a typical spin Hamiltonian as described by the combination of equations 3, 4 and 5:

$$\mathcal{H} = -J_{ex}\hat{S}_1\hat{S}_2 + \sum_{i=1}^2 D_i \left[\hat{S}_{z,i}^2 - \frac{5}{4} + \frac{E_i}{D_i} (\hat{S}_{x,i}^2 - \hat{S}_{y,i}^2) \right] + \sum_{i=1}^2 g_i \mu_B \hat{S}_i \vec{B} \quad (70)$$

For strictly axially distorted octahedrons as assumed in the model by Lloret, the transverse ZFS parameter E is zero. The axial ZFS parameter D is related to the parameters α_r , λ_{SO} and Δ_{ax} and for the case of strong axial distortion compared to spin-orbit coupling ($\Delta_{ax} \gg |\lambda_{SO}|$), the value of D can be estimated by equation 71¹⁹⁴:

$$D = \frac{\alpha_r^2 \lambda_{SO}^2}{\Delta_{ax}} \quad (71)$$

The D values estimated for compounds **3[BF₄]₂**, **3[BF₄]₃**, **4[BPh₄]₂**, **5[OTf]₂** and **5[OTf]₃** using equation 71 are listed in Table 13.

Since for geometrically distorted compounds usually anisotropic g -values are observed and since exchange coupling constants might also show anisotropy, simulations based on a spin Hamiltonian easily lead to extremely over-parametrized situations. For the simulations of the magnetic data of the Co(II) compounds studied in this work therefore the simplest model, i.e. employing as few fit parameters as possible, was assumed.

Satisfactory simulations of the temperature dependence of the susceptibility data were achieved by assuming isotropic g -values and exchange coupling constants (equation 70, Figure 71). The best agreements between experimental and calculated data were observed with the parameter values listed in Table 14. For **3[BF₄]₂**, the data were simulated with the same exchange coupling constant as determined before ($J_{ex} = -0.467 \text{ cm}^{-1}$) while for the other complexes slightly lower, but still comparable values were necessary. Also the values for D

are comparable to those estimated from α_r , λ_{SO} and Δ_{ax} , showing that the model by Lloret is well suited to obtain a first idea about the electronic ground state structure of sixfold coordinated Co(II) compounds. The D values for $5[OTf]_2$ and $5[OTf]_3$ were experimentally determined by far-infrared spectroscopy (see below).

The corresponding simulations of the magnetic field dependence of the magnetization data are shown on the right hand side of Figure 71. Although still reasonably acceptable, the agreement between experimental data and simulations is worse than for the temperature dependence. This is attributed to the fact that the field dependence at low temperature is more sensitive to the nature of the ground state, e.g. g -anisotropy or state-mixing due to transverse anisotropy. However, the transverse ZFS parameters E were fixed to zero to avoid over-parametrization. Also anisotropic exchange couplings might play a role, as shown by EPR-spectroscopy (see below).

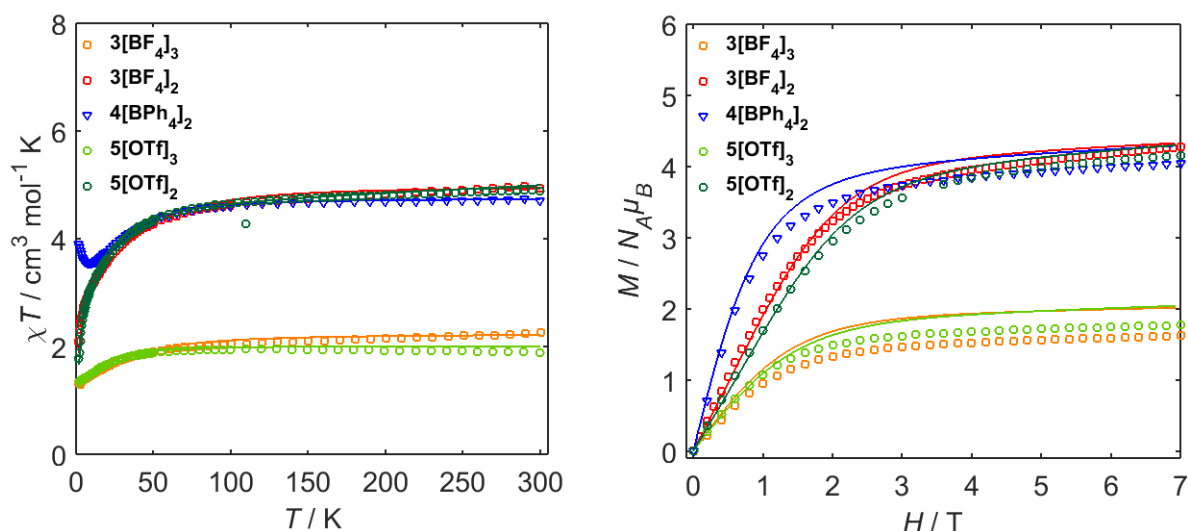


Figure 71: Temperature dependence of χT (left) and magnetic field dependence of the magnetization at 1.8 K (right) for the compounds $3[BF_4]_3$, $3[BF_4]_2$, $4[BPh_4]_2$, $5[OTf]_3$ and $5[OTf]_2$, as indicated. Solid lines correspond to simulations based on the spin-only formalism, using isotropic g -values and coupling constants.

Table 14: Simulation parameters for the dc susceptibility data of $3[BF_4]_2$, $3[BF_4]_3$, $4[BPh_4]_2$, $5[OTf]_2$ and $5[OTf]_3$ by applying the spin Hamiltonian given in equation 70.

	$3[BF_4]_2$	$3[BF_4]_3$	$4[BPh_4]_2$	$5[OTf]_2$	$5[OTf]_3$
D / cm^{-1}	43	43	37	23	23
$J_{\text{ex}} / \text{cm}^{-1}$	-0.467	-	0.760	-0.520	-
g_{iso}	2.300	2.170	2.248	2.220	2.070

Briefly summarizing this section, the magnetic properties of the cobalt dimers **3**[BF₄]₂, **3**[BF₄]₃, **4**[BPh₄]₂, **5**[OTf]₂ and **5**[OTf]₃ were analyzed by means of different models. It was shown that due to high deviations from octahedral symmetry the Lines model is not appropriate any longer. Instead, the empirical model developed by Lloret, taking into account axial distortion, provided reasonable parameter values. Importantly, for all of the studied compounds the axial distortion was shown to be positive and rather high, thus allowing the magnetic data to be interpreted in terms of a regular spin Hamiltonian. Concerning the exchange interaction, weak ferromagnetic coupling was found for the symmetrically bridged Co(II) dimer **4**[BPh₄]₂, while weak antiferromagnetic couplings were observed for the symmetrically bridged dimer **3**[BF₄]₂ as well as for the asymmetric dimer **3**[OTf]₂.

4.4.3 Spectroscopic Results and Discussion

In order to obtain more information about the anisotropy of the *g*-values and the influence of the bridging ligand on the exchange coupling constants for compounds **3**[BF₄]₂, **3**[BF₄]₃, **4**[BPh₄]₂, **5**[OTf]₂ and **5**[OTf]₃, low-temperature EPR-spectra were recorded. Furthermore, low-temperature far-infrared spectra were recorded for **5**[OTf]₂.

The obtained FIR-spectra at different applied magnetic fields as well as the corresponding normalized spectra obtained by dividing the spectra by the spectrum at highest field are shown in Figure 72. The FIR experiments were carried out by Raphael Marx and Dr. María Dörfel (Institute of Physical Chemistry, University of Stuttgart). In the normalized FIR-spectra, a field-dependent feature is visible around 47 cm⁻¹, which is attributed to single-ion zero-field splitting, i.e. it arises from transitions between the $m_S = \pm 1/2$ and $m_S = \pm 3/2$ states of the Co(II) centers. In the absence of transverse anisotropy, this corresponds to an axial ZFS parameter of $|D| \cong 23 \text{ cm}^{-1}$ and this value was therefore used for the simulations of the magnetic data (section 4.4.2) and the EPR data (see below) for both **5**[OTf]₂ and **5**[OTf]₃. Another field-dependent signal appears around 91 cm⁻¹. The observation of such a second signal is attributed to the presence of two interacting Co(II) centers per molecule. According to the ZFS term in equation 70, the possible combinations of the quantum numbers $m_S = \pm 1/2$ and $m_S = \pm 3/2$ of two $S = 3/2$ ions lead to energy levels with relative energies of $E(\pm 1/2, \pm 1/2) = 0$, $E(\pm 3/2, \pm 1/2) = 2 D$ and $E(\pm 3/2, \pm 3/2) = 4 D$. Corresponding energy level diagrams are shown in the appendix, section 8.5.3 Simulations using $D = 23 \text{ cm}^{-1}$ and the *g*-values and exchange coupling constants determined by EPR-spectroscopy (see below) are shown as dotted lines in Figure 72.

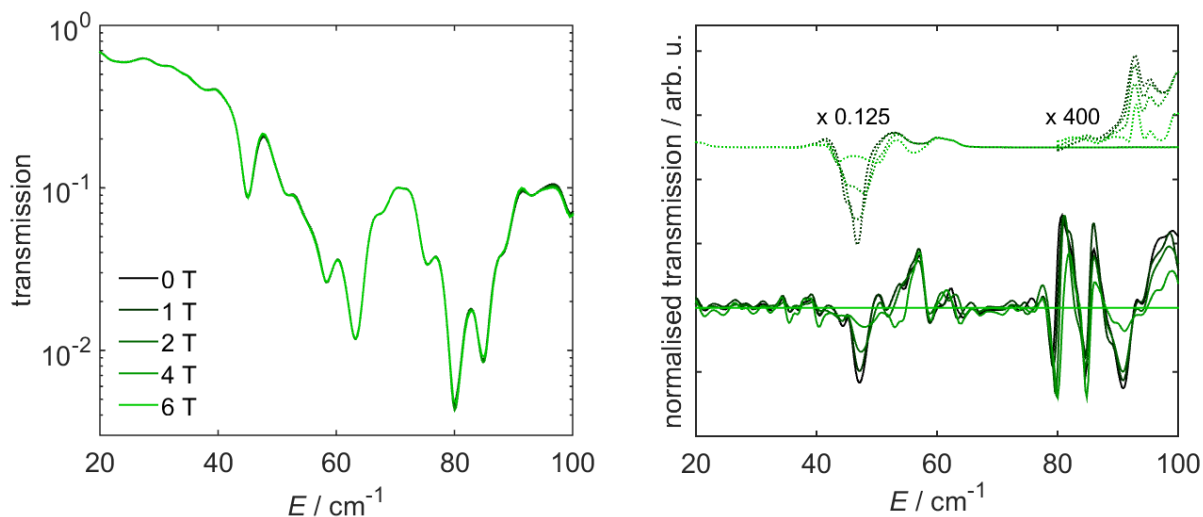


Figure 72: Left: Far-infrared transmission spectra (left) and normalized spectra (right) for $5[\text{OTf}]_2$ recorded at 9 K and various magnetic fields, as indicated. The normalized spectra were obtained by dividing the spectra by the 6 T spectrum. Dotted lines correspond to scaled simulations with $D = 23 \text{ cm}^{-1}$ (see main text). The spectra were recorded by Raphael Marx and Dr. María Dörfel.

According to these simulations, the signal corresponding to 4 D should be much weaker and scaling was necessary to make it visible in the plot. However, weak transitions can gain intensity by coupling to vibrational modes. The occurrence of vibrations in this energy range is clearly visible in the FIR transmission spectra on the left hand side of Figure 72.

EPR spectra were recorded for all of the paramagnetic dimers; however, usable spectra were only obtained for $3[\text{BF}_4]_2$, $3[\text{BF}_4]_3$ and $5[\text{OTf}]_2$. No EPR lines were observed in the spectra of $4[\text{BPh}_4]_2$, probably due to line-broadenings by fast relaxation processes that are rather common in weakly exchange-coupled dimers.¹⁹⁵ Different spectroscopic behavior for $4[\text{BPh}_4]_2$ compared to the other dimers is consistent with the fact that $4[\text{BPh}_4]_2$ is the only compound that shows ferromagnetic exchange coupling. Furthermore, the magnitude of the corresponding exchange coupling constant is higher than those of the antiferromagnetically coupled dimers.

The X-Band (9.47 GHz) EPR-spectra of $5[\text{OTf}]_3$ (appendix, section 8.5.2) displayed unexpected splittings which are too large to be solely explained by hyperfine interactions or dipolar couplings. The corresponding g -values (for $S = 3/2$) range between 1.7 and 3.2, which seems to be rather unphysical and is in contrast to the simple X-Band EPR spectra obtained for $3[\text{BF}_4]_3$ (see below). No clear transitions were observed in the HFEPR spectra. Possible explanations for this unexpected behavior include factors like structural variations, partial sample decomposition, baseline effects or impurities. The EPR experiments on $5[\text{OTf}]_3$ were carried out on a very small amount of sample that did not originate from the same batch as the

sample for the magnetic measurements. If required, the measurements should thus be repeated when a freshly synthesized and characterized sample is available. However, since the main focus of this subproject lies on the exchange coupling between the Co(II) centers, the EPR-spectra of the oxidized species are of lesser interest.

Figure 73a shows the solid-state X-band EPR-spectrum of $3[\text{BF}_4]_3$, recorded at 5 K. A rather axial spectrum is observed, showing transitions at magnetic fields around 150 and 320 mT. Within the $S = 3/2$ formalism, the best simulation is obtained using $g_{\parallel} = (2.07 \pm 0.02)$ and $g_{\perp} = (2.33 \pm 0.04)$ and an axial ZFS parameter of $D = 43 \text{ cm}^{-1}$ as estimated by SQUID magnetometry. The perpendicular component g_{\perp} being larger than the parallel component g_{\parallel} is consistent with a positive sign of D , i.e. easy-plane anisotropy. The powder EPR-spectrum was complemented by measurements on a frozen solution in butyronitrile (Figure 73b) and as expected due to weaker dipolar interactions, the corresponding spectrum displays narrower lines. The signal corresponding to g_{\parallel} exhibits a well-resolved structure arising from hyperfine coupling to the cobalt nuclear spin of $7/2$. Apart from that, the spectrum is rather similar to the solid-state spectrum, indicating the absence of intermolecular exchange pathways in the powder. The best simulation was obtained with $g_{\parallel} = (2.066 \pm 0.005)$, $g_{\perp} = (2.346 \pm 0.005)$, $D = 43 \text{ cm}^{-1}$ and a hyperfine coupling constant of $A_{\parallel} = (215 \pm 3) \text{ MHz}$.

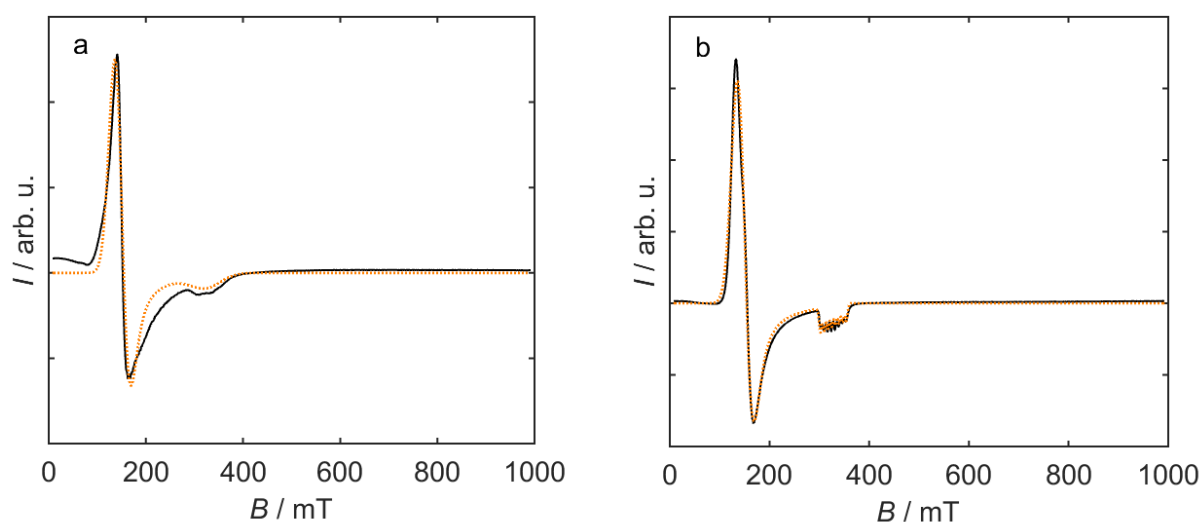


Figure 73: X-band EPR spectra of $3[\text{BF}_4]_3$ recorded on a powder sample (a) and on a frozen solution in butyronitrile (b). The measurements were performed at 5 K. Black solid lines show the experimental data while orange dotted lines depict simulations based on the spin Hamiltonian approach (see text).

A much more complicated situation was found in the X-band EPR spectrum of the non-oxidized dimer $3[\text{BF}_4]_2$ because the similar sizes of the exchange coupling and the Zeeman splittings lead to nested signals (Figure 74, left). The low-field signal seems to be split into several components and an additional signal appears at about 600 mT. Since at higher fields and frequencies g -value anisotropy is resolved better while splittings due to exchange interactions are much less affected, multi-frequency HFEPR-spectra were recorded for $3[\text{BF}_4]_2$. The spectra were recorded with the help of Raphael Marx and Dr.-Ing. Petr Neugebauer (Institute of Physical Chemistry, University of Stuttgart) and are shown on the right hand side of Figure 74. At 310.5 GHz, three well-separated lines corresponding to different g -values are located at magnetic fields around 4.3, 5.4 and 10.5 T. The exchange coupling is visible as splittings or broadening of these lines. Good simulations were only obtained when assuming not only a rhombic g -tensor but also anisotropic exchange interaction. For reasons of simplicity, the corresponding matrices were assumed to share the same axis systems but it is important to mention that in reality this is not necessarily the case.¹⁹⁶

The best agreement between simulations and experimental spectra for all applied frequencies was achieved with the following set of parameters: $D = 43 \text{ cm}^{-1}$, $g_{xx} = (2.60 \pm 0.05)$, $g_{yy} = (2.05 \pm 0.02)$, $g_{zz} = (2.10 \pm 0.03)$, $J_{xx} = (-0.077 \pm 0.003) \text{ cm}^{-1}$, $J_{yy} = (-0.215 \pm 0.003)$ and $J_{zz} = (-1.14 \pm 0.02) \text{ cm}^{-1}$.

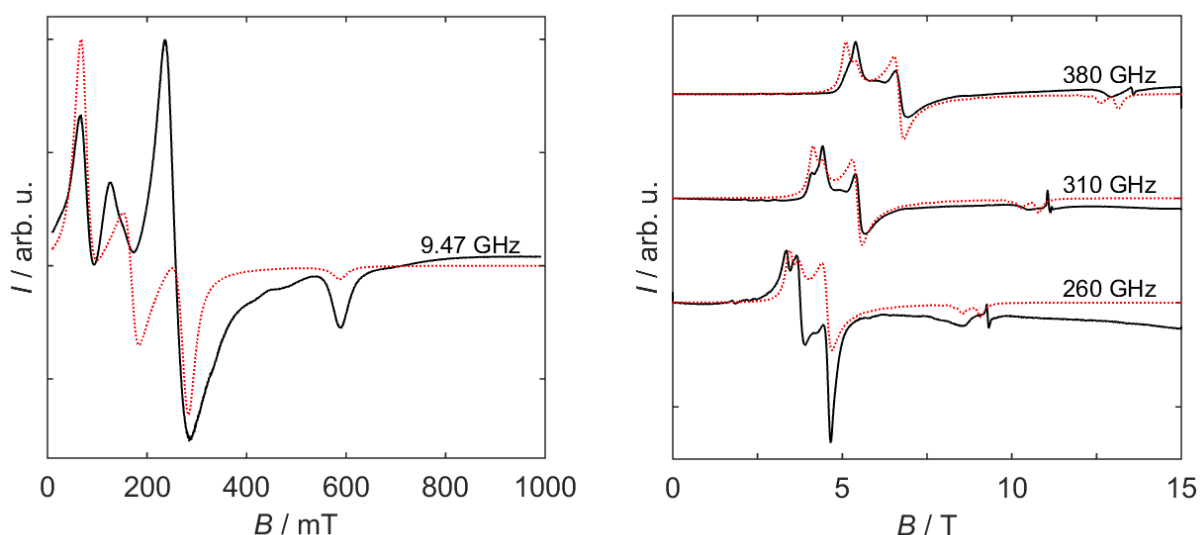


Figure 74: Solid-state EPR spectra of $3[\text{BF}_4]_2$ recorded at 5 K. Left: X-band EPR-spectrum. Right: HFEPR-spectra at different frequencies, as indicated. Black solid lines correspond to experimental spectra while red dotted lines show the simulations based on a spin Hamiltonian approach (see text). The HFEPR experiments were performed with the help of Raphael Marx and Dr.-Ing. Petr Neugebauer.

The individual g -values lie in the typical range observed for sixfold coordinated cobalt(II) centers⁴⁴ and the average g -value of $g = 2.25$ is in good agreement with $g = 2.30$ found by magnetometry. Furthermore, the average value for the exchange coupling constant is $J_{\text{ex}} = -0.48 \text{ cm}^{-1}$, in excellent agreement with the value derived from fitting the magnetic susceptibility data ($J_{\text{ex}} = -0.47 \text{ cm}^{-1}$).

The low-temperature X-band- and HFEPR-spectra of the asymmetrically bridged dimer **5[OTf]₂** are shown on the left hand side in Figure 75. Due to the small exchange coupling, the X-Band EPR-spectrum is similarly complicated as observed for **3[BF₄]₂**, showing broad and nested signals over a large magnetic field range. Simplified spectral patterns are obtained by applying higher microwave frequencies (Figure 75, right). In the 300 GHz spectrum, the most intense peaks appear at magnetic fields of about 4.1, 5.8 and 9.5 T and are attributed to three different g -values, as evidenced by different slopes in the frequency vs. field plot (Appendix, section 8.5.3). Additionally, several smaller peaks are observed that are due to transitions from slightly higher lying microstates of the exchange-coupled system. As illustrated in the frequency vs. field plots (appendix, section 8.5.3), some of these signals show the same frequency dependence as the main peaks and thus belong to the same g -values. However, the asymmetrical bridging ligand in **5[OTf]₂** complicates the simulation of the EPR data, since apart from anisotropic g - and J -tensors, the distinct Co(II) centers most likely show different sets of D , E and g -values in different axis systems, leading to an extremely over-parametrized situation.

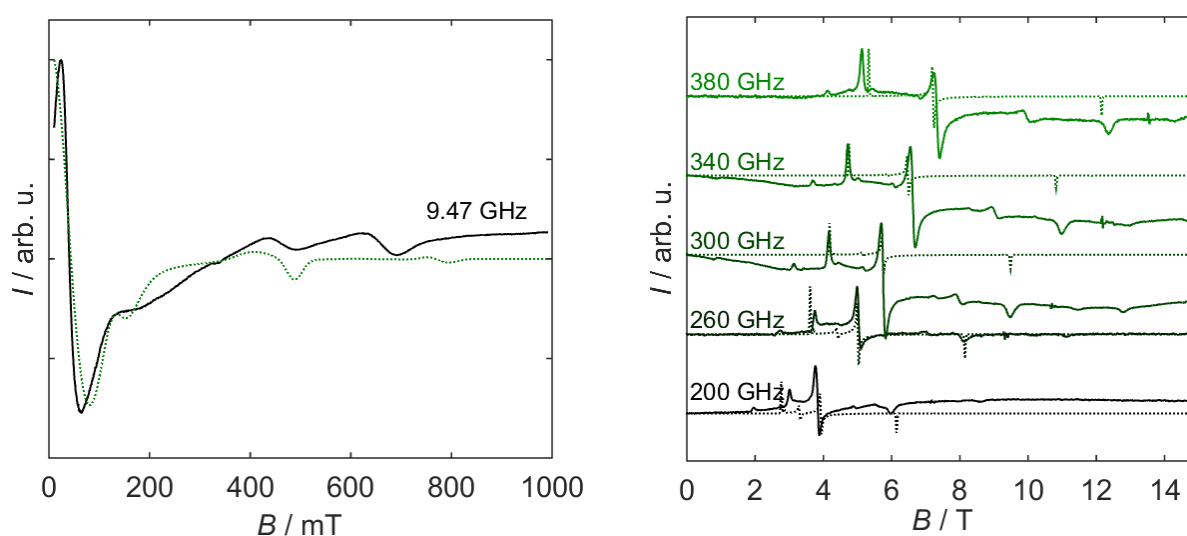


Figure 75: Left: Powder X-Band EPR-spectra of **5[OTf]₂**, recorded at 4.4 K. Right: HFEPR-spectra of a pellet of **5[OTf]₂** recorded at 5 K and various frequencies, as indicated. The HFEPR-spectra were recorded by Dr.-Ing. Petr Neugebauer. Solid lines correspond to experimental spectra while dotted lines illustrate simulations based on the model described in the text.

The simulations were thus performed in terms of a rather simplified model, using the same parameters for both Co(II) centers. The ZFS parameters were fixed to $D = 23 \text{ cm}^{-1}$ and $E = 0$, according to the ZFS gap determined by FIR-spectroscopy. The spectral main features as well as some of the smaller peaks in the HF-EPR-spectra were best simulated with $g_{xx} = (2.58 \pm 0.12)$, $g_{yy} = (2.02 \pm 0.03)$, $g_{zz} = (2.14 \pm 0.05)$, $J_{xx} = (-0.314 \pm 0.003) \text{ cm}^{-1}$, $J_{yy} = (-0.539 \pm 0.01) \text{ cm}^{-1}$ and $J_{zz} = (-0.687 \pm 0.005) \text{ cm}^{-1}$. The simulations are illustrated as dotted lines in Figure 75 while the corresponding energy level diagrams including the transitions at 300 GHz are provided in the appendix, section 8.5.3. The average g -value is 2.25 and the isotropic mean value of J is $J_{\text{ex}} = -0.51 \text{ cm}^{-1}$, in nearly perfect agreement with the values derived by SQUID magnetometry ($g = 2.22$ and $J_{\text{ex}} = -0.52 \text{ cm}^{-1}$).

Summarizing this section, the SQUID magnetometric measurements on the cobalt dimers **3[BF₄]₂**, **3[BF₄]₃**, **4[BPh₄]₂**, **5[OTf]₂** and **5[OTf]₃** were complemented by EPR-spectroscopic studies as well as by FIR-spectroscopy in the case of **5[OTf]₂**. Usable EPR-spectra were obtained for samples of **3[BF₄]₂**, **3[BF₄]₃** and **5[OTf]₂** and they were successfully simulated using the D values derived from the magnetic data and anisotropic g - and J -tensors. In the case of **5[OTf]₂**, the value for D was directly determined by FIR-spectroscopy. The EPR simulation parameters compared to the parameters derived from the magnetic susceptibility data are listed in Table 15. For **3[BF₄]₂** and **5[OTf]₂**, the average values of g and J_{ex} determined by EPR compare well to the isotropic values obtained by simulating the susceptibility data. However, for **3[BF₄]₃**, the EPR-spectroscopically determined average g -value is higher, demonstrating the well-known fact that SQUID magnetometry only allows the relatively rough estimation of g -values, e.g. due to its higher sensitivity to diamagnetic impurities.

Table 15: Comparison of the average g -values and the mean values for the exchange coupling constants J_{ex} used in the simulations of the magnetic data and the EPR-spectra of **3[BF₄]₂**, **3[BF₄]₃**, **4[BPh₄]₂**, **5[OTf]₂** and **5[OTf]₃**.

	3[BF₄]₂	3[BF₄]₃	4[BPh₄]₂	5[OTf]₂	5[OTf]₃
$J_{\text{iso, SQUID}} / \text{cm}^{-1}$	-0.47	-	0.76	-0.52	-
$J_{\text{mean, EPR}} / \text{cm}^{-1}$	-0.48	-	-	-0.51	-
$g_{\text{iso, SQUID}}$	2.30	2.170	2.248	2.220	2.070
$g_{\text{mean, EPR}}$	2.25	2.25	-	2.250	-

Comparing the exchange-coupled dimers $3[\text{BF}_4]_2$, $4[\text{BPh}_4]_2$ and $5[\text{OTf}]_2$, an interesting trend is observed: While $4[\text{BPh}_4]_2$ exhibits ferromagnetic coupling, antiferromagnetic exchange is observed for both $3[\text{BF}_4]_2$ and $5[\text{OTf}]_2$. The strength of the exchange coupling decreases in the following order: $|J_{\text{ex}}|(4[\text{BPh}_4]_2) > |J_{\text{ex}}|(5[\text{OTf}]_2) > |J_{\text{ex}}|(3[\text{BF}_4]_2)$. Intuitively, these observations are rather unexpected, since except for different substituting groups R, the bridging situations in $3[\text{BF}_4]_2$ and $4[\text{BPh}_4]_2$ are rather similar while that in $5[\text{OTf}]_2$ is different due to an asymmetric bridging ligand. Thus it can be concluded that the sign and the magnitude of the exchange coupling are extraordinarily sensitive to the nature of the bridge, including factors influenced by the substituting groups R. As mentioned in section 2.1.1, the natures of exchange couplings can be qualitatively predicted by the so-called Goodenough-Kanamori rules⁴⁰⁻⁴², taking into account the orbitals involved and the metal-ligand-metal angles. However, these rules were originally derived for rather simple bridging ligands like oxo-bridges and application to extended bridging ligands is not straightforward.

In a simplified picture, the occurrence of antiferromagnetic coupling vs. ferromagnetic coupling in similar compounds can be explained by competing exchange paths along the bonds of the bridging ligands. As illustrated in Figure 76, the anti-parallel alignment of electron spins along the meta-path results in ferromagnetic coupling of the spins of the Co(II) centers, while anti-parallel electron spin alignment along the para-path leads to anti-ferromagnetic coupling. In any case, the favored exchange path and therefore the nature of the coupling should be related to the relative geometric arrangement of the metal centers, which is mainly determined by the bridging ligands. Unfortunately, no crystal structure is available for $3[\text{BF}_4]_2$, which precludes its inclusion in the comparison of the geometric arrangements for the compounds studied in this work.

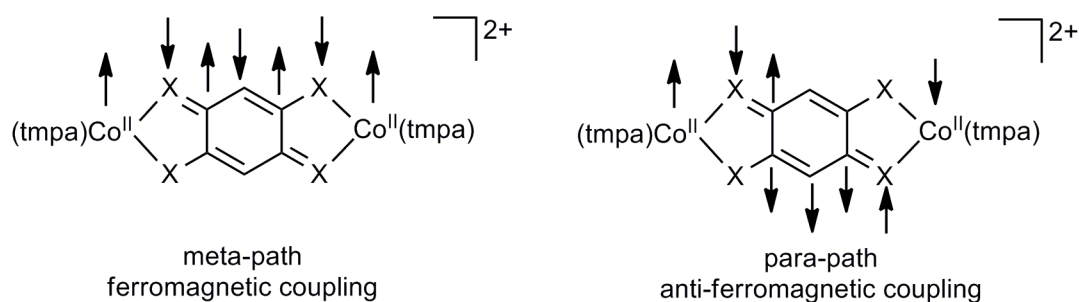


Figure 76: Schematic illustration of competing exchange paths, leading to ferromagnetic coupling (left) or anti-ferromagnetic coupling (right). Arrows depict the alignment of electron spins.

Regarding the structures of **4[BPh₄]₂** and **5[OTf]₂**, one aspect to be taken into account concerns the intra-dimer Co(II)-Co(II) distances. With 7.954 Å, this distance is shorter in **4[BPh₄]₂** than in **5[OTf]₂** (8.025 Å), providing one possible explanation for the stronger interactions in **4[BPh₄]₂**, also including stronger dipolar interaction. However, the intra-dimer distances alone are not sufficient to explain the different signs of the exchange coupling parameters. Further aspects might include e.g. the relative orientation of metal-ligand bonds or competing inter-dimer dipolar interactions. Analyzing such aspects requires comparing much more than only two structurally similar compounds.

The exchange interaction parameters found for **3[BF₄]₂**, **4[BPh₄]₂** and **5[OTf]₂** can also be compared in terms of the electron withdrawing or electron donating properties of the substituting groups R. In **3[BF₄]₂**, R² refers to 2-(methoxy)-phenyl, in **4[BPh₄]₂**, R³ stands for 2-(trifluoromethyl)-phenyl and in **5[OTf]₂**, R⁴ denotes 4-(isopropyl)-phenyl (section 4.4.1). Thus, **4[BPh₄]₂** is the only compound exhibiting an electron withdrawing group R while in **3[BF₄]₂** and **5[OTf]₂**, electron donating groups R are present, consistent with the determined signs of the exchange coupling constants. Comparing **3[BF₄]₂** and **5[OTf]₂**, slightly stronger antiferromagnetic exchange is found for **5[OTf]₂** although the electron donating properties of isopropyl groups are weaker than those of methoxy groups. Here, the different bridging situations, i.e. a symmetrical bridge with two oxygen and two nitrogen donors in **3[BF₄]₂** compared to an asymmetric bridge with three oxygen donors and only one nitrogen donor in **5[OTf]₂** might play a significant role. In order to draw final conclusions about the influence of the substituting groups and the symmetry of the bridging ligand, the studied series of symmetrically and asymmetrically bridged Co(II)-Co(II) dimers should be expanded. Symmetric and asymmetric dimers should be synthesized with the same substituents R and the same counter ions, allowing direct comparison of the influence of the donor sets. Furthermore, the series should include complexes with very strongly electron donating or electron withdrawing groups, e.g. amine or nitrile groups. In the context of molecular magnetism, ferromagnetic exchange interaction is preferred and if the trend observed in this work turns out to be correct, symmetric bridges containing strongly electron withdrawing groups could lead to enhanced ferromagnetic couplings. Also, the investigation of complexes with bridges that contain only nitrogen donors could provide very interesting results.

5 Summary and Conclusion

Since the discovery of the first single-molecule magnet in 1993,¹ the field of molecular magnetism^{2,3} has become a flourishing area of scientific research. As axial anisotropy was realized to be one of the key factors determining the energy barrier in magnetically bistable molecules, the synthesis and investigation of complexes with potentially largely anisotropic metal centers moved more and more into the focus of interest.^{9,11,21-24,28} The main questions to be answered concern for example the correlation between the molecular as well as the electronic structure and the corresponding magnetic properties, understanding aspects that control under-barrier relaxation and finally the development of rational design criteria for improved single-molecule magnets.

In this context, the contribution of the work presented here lies in the comprehensive magnetic and spectroscopic investigation of selected lanthanide and cobalt complexes exhibiting large magnetic anisotropies. The compounds were studied not only by means of magnetometry, but also by applying a range of advanced spectroscopic techniques, including far-infrared (FIR) spectroscopy, multi-frequency EPR and optical methods. Importantly, one of the main tools for complete electronic structure determinations and thus unravelling the origin of the respective dynamic properties was magnetic circular dichroism (MCD) spectroscopy. However, since the MCD-spectrometer was not part of the scientific equipment at the University of Stuttgart before, its design, setup and characterization should be considered as the first part of this work.

The MCD-spectrometer was successfully assembled by combining an Aviv Model 42 CD-spectrometer and an Oxford Instruments SM-4000-10 optical split-coil cryomagnet. The superconducting magnet provides magnetic field strengths of up to ± 10 T. It is equipped with a variable temperature insert operating at temperatures between 1.5 and 300 K, allowing for VTVH MCD measurements that are useful for electronic ground state studies. The CD-spectrometer contains a tungsten halogen lamp emitting in the near-UV, visible and near-IR regions of the electromagnetic spectrum. The light source is followed by a Cary 14 double monochromator providing an excellent spectral resolution of up to 0.1 nm, which was later on made use of for the accurate determination of f-f-transition energies in lanthanide complexes. After the monochromator, the combination of a Rochon polarizer and a photoelastic modulator generates alternately left and right circularly polarized light, which is then focused onto the sample, using appropriate optics. The sample is placed in the center of the magnetic

field and a home-built sample cell allows for studying samples as frozen solutions, mulls or thin films. Detection is carried out using a photomultiplier tube for the UV and visible range and an indium gallium arsenide photodiode for the NIR range, covering a rather wide wavelength range from 200 to 2000 nm. It is worthwhile mentioning that in MCD-spectroscopy such a large wavelength range has rarely been realized up to now, although especially high wavelengths are extremely useful for determining the energies of low-lying excited states, e.g. the levels arising from the $^4T_1(F)$ terms of four-coordinate Co(II) complexes. Wavelength calibration was performed with the help of the well-defined f-f-transitions observed in a holmium oxide standard sample¹²⁹ while CD intensity calibration was carried out making use of the well-known signal intensities of aqueous solutions of CSA¹³⁶ and nickel tartrate¹³⁶. The performance of the completely assembled MCD-spectrometer was finally tested by recording MCD-spectra of a polymer film of $K_3[Fe(CN)_6]$ and the obtained spectra agreed well with reported literature data¹³⁹⁻¹⁴². One aspect of special interest concerned the sensitivity of the MCD-spectrometer, more precisely the possibility of monolayer detection. Indeed, preliminary measurements on Langmuir-Blodgett deposited monolayers of the single-ion magnet $DyPc_2$ ²⁵ showed rather promising results, including not only the observation of clear spectra but also MCD detected hysteresis curves. These findings strongly suggest that MCD-spectroscopy provides a convenient tool for studying orientation-dependent properties of SMM monolayers, which currently requires much more sophisticated and less available techniques like synchrotron-based methods. Work in this direction is still ongoing, including e.g. studying the dependence of the hysteresis behavior on the number of stacked layers or the extension of MCD based monolayer detection to other compounds.

In conclusion, the design and setup of a high-end MCD-spectrometer at the University of Stuttgart was rather successful, as also confirmed by the substantial contributions of MCD-spectroscopy to the electronic structure elucidation of lanthanide- and cobalt-based SIMs in the further course of this work. However, since the spectrometer is not a so-called plug-and-play instrument, there will always be room for improvement or the implementation of new ideas in the future. Possible improvements concern for example the optics employed. NIR baseline artefacts due to vibrational overtones of OH groups could be minimized by replacing as many optical parts as possible by OH free analogues. The employment of achromatic lenses could minimize the currently present wavelength dependency of the focal spots of the light. Furthermore, replacing the presently used PMT by a PMT operating at wavelengths up to 1200 nm could resolve the issue of baseline artefacts around 1000 nm. Currently, work is ongoing regarding the user-friendly change of the magnet between several applications,

including MCD- and FDMR-spectroscopy. Besides the possible improvements concerning the practical performance of the MCD-spectrometer, there are a lot of further ideas regarding the application of the spectrometer, e.g. MCD-spectroscopy on oriented single crystals, measurements on air-sensitive samples or optically detected EPR (ODEPR) spectroscopy. Measurements on single crystals could be realized rather soon, requiring only improved light focusing onto the sample and an adjustable aperture. For measurements on extremely air-sensitive samples, a sealable sample cell has to be constructed, which allows preparing and transporting the sample under inert gas atmosphere. The implementation of ODEPR is a more challenging project since it requires microwave irradiation. However, due to the high sensitivity of the MCD-spectrometer, this is a rather interesting option for obtaining high-quality EPR-spectra of thin films or strongly diluted samples.

In the further course of this work, MCD-spectroscopy was employed as one of the essential tools for studying the electronic structures of selected lanthanide and cobalt complexes. Except for possible SIM properties of erbium and dysprosium complexes in general, the studied molecular tetra-carbonates²⁶ of dysprosium (**1-Dy**) and erbium (**1-Er**) were chosen mainly due to the colorlessness of the carbonate ligands, allowing for optical detection of f-f-transitions. After successful synthesis and structural characterization, the static and dynamic magnetic properties were probed by extraordinarily detailed susceptibility and magnetization measurements. Both **1-Dy** and **1-Er** are field-induced SIMs, as evidenced by clear frequency dependent maxima of the ac out-of-phase susceptibilities in the presence of an external dc bias field. Based on spectroscopic data, energy barriers of 52 cm⁻¹ for **1-Er** and 29 cm⁻¹ for **1-Dy** were determined. However, the determined magnetic relaxation behavior is rather different. While the Arrhenius plot for **1-Dy** shows a pronounced linear regime towards high temperatures, which is indicative for Orbach relaxation, the Arrhenius plot for **1-Er** is strongly curved. Further magnetic studies showed that for **1-Er**, the contributions of the direct process and the Raman process to magnetic relaxation are much higher than for **1-Dy**.

The magnetic investigations were complemented by detailed spectroscopic studies, which are not yet commonly applied in the field of molecular magnetism, but are more and more called for in recent SIM related literature.^{66,67} The combination of low temperature FIR, MCD, electronic absorption and luminescence spectroscopy allowed for the experimental determination of no fewer than 48 energy levels for **1-Er** and 55 levels for **1-Dy**, which built the foundation for the subsequent crystal field parametrization. Importantly, most of these levels were determined by electronic absorption and MCD-spectroscopy. In addition, multi-frequency EPR-spectroscopy was applied, since this method is extremely sensitive to the

nature of the lowest lying Kramers doublets and thus served as a tool for checking and fine-tuning the respective sets of determined crystal field parameters.

Crystal field analysis for **1-Dy** and **1-Er** was performed in terms of the combination of a common free-ion Hamiltonian and a crystal field Hamiltonian based on the approximate C_{2v} point symmetry of the complexes. After an iterative fitting procedure, reliable sets of crystal field parameters were found that allowed for good simulations of all the experimental data. The compositions of the wave functions of the electronic ground states described by these crystal field parameters hint at strongly mixed Kramers doublets, thus explaining the relatively poor SIM performance of **1-Dy** and **1-Er**. More quantitatively, a detailed understanding of the relaxation pathways was obtained by calculating the magnetic dipole strengths for transitions between the ground state Kramers doublets. The calculated values confirm that Orbach relaxation is prominent in **1-Dy** while under-barrier relaxation dominates in **1-Er**.

Concluding this subproject, the combination of magnetometry and advanced spectroscopic techniques allowed for the determination of the electronic structures as well as for a full understanding of the magnetic relaxation in the lanthanide-based SIMs **1-Dy** and **1-Er**. Importantly, none of the applied methods is sufficient on its own for the determination of meaningful crystal field parameters for low symmetry compounds such as **1-Dy** and **1-Er**. While magnetometry on its own unequivocally leads to over-parametrized situations, also FIR and luminescence spectra usually do not provide enough energy levels required for the unambiguous determination of crystal field parameters. They have to be complemented by optical spectra. However, energies on their own do not yield any information about the composition of the states involved, making EPR-spectroscopy essential. Thus, this work not only provides a substantial contribution to the understanding of the electronic structures of lanthanide SIMs, but also a recipe for the experimental electronic structure determination itself. However, the presented method is a rather lengthy process, not only in terms of experimental effort but also concerning the subsequent data analysis and fitting procedures. For routine investigations or for the investigation of more complicated systems, the presented recipe needs to be adapted to the individual problem and the corresponding points of interest.

Besides the lanthanide tetra-carbonates, two classes of cobalt compounds were studied, namely monometallic and bimetallic complexes. The monometallic complexes **(HNEt₃)₂2** and **(NMe₄)₂2** consist of a Co(II) central ion ligated by the nitrogen donors of two doubly deprotonated 1,2-bis(methanesulfonamido)benzene ligands, resulting in pseudo-tetrahedral coordination. Rather acute N-Co-N bite angles indicate strong axial distortions

compared to regular tetrahedrons. The static magnetic properties hinted at high energy barriers for spin reversal and rather high values for the axial zero-field splitting parameters with $D = -115 \text{ cm}^{-1}$ for **(HNEt₃)₂2** and $D = -112.5 \text{ cm}^{-1}$ for **(NMe₄)₂2** were directly determined by FIR-spectroscopy. The corresponding energy barriers are amongst the highest ever reported for first-row transition metal complexes,^{11,24,28} making **(HNEt₃)₂2** and **(NMe₄)₂2** extraordinarily interesting systems for studying SIM behavior.

Their performance as SIMs was probed by temperature and frequency dependent ac susceptibility measurements and indeed, even in the absence of a static magnetic field, clear frequency dependent maxima of the out-of-phase susceptibilities were observed. **(HNEt₃)₂2** and **(NMe₄)₂2** thus belong to the very rare examples for Co(II) based zero-field SIMs. The corresponding Arrhenius plots showed pronounced linear regimes towards high temperatures; however, the effective energy barriers derived from linear fits to these data were significantly lower than the energy barriers directly determined by FIR-spectroscopy. These findings clearly show that energy barriers derived solely from ac susceptibility data are not reliable.

The unique magnetic properties of **(HNEt₃)₂2** and **(NMe₄)₂2** were successfully explained by the analysis of spectroscopic results. The recorded HF-EPR-spectra showed no resonance lines, confirming the rather high values and negative signs of the zero-field splitting parameters D . Furthermore, the absence of EPR lines hints at rather axial electronic ground states with negligibly small transverse anisotropy, which would lead to relaxed EPR selection rules. The MCD-spectra showed intense signals arising from spin-allowed d-d-transitions from the $^4A_2(F)$ ground state to the $^4T_2(F)$, $^4T_1(F)$ and $^4T_1(P)$ excited terms of Co(II). Subsequent crystal field analysis within the D_{2d} symmetry approximation revealed that the strong axial crystal field produced by the ligands splits the first excited $^4T_2(F)$ state to such an extent that the lower 4B_2 component arising from this state closely approaches the ground state. The resulting small energy gap between the electronic ground state and the first excited state leads to increased second-order spin-orbit interactions, explaining the rather high zero-field splittings. The transitions to the $^4T_1(F)$ states were subjected to VTVH MCD measurements and the obtained curves were successfully simulated using axial g -tensors. Importantly, the corresponding signal intensities showed hysteresis with record coercive fields of 0.24 T (**(HNEt₃)₂2**) and 0.14 T (**(NMe₄)₂2**). **(HNEt₃)₂2** and **(NMe₄)₂2** thus show real magnetic bistability, caused by the strong axial ligand field generated by the bis(sulfonamide) ligands, which are able to act as both σ and π donors. The different coercive fields observed for **(HNEt₃)₂2** and **(NMe₄)₂2** hint at a strong influence of the respective counter ions and the corresponding crystal structure. For a better understanding it would be interesting to expand

the series of complexes with differing counter ions. Also, magnetic hysteresis measurements on suitable single crystals could be rather promising.

The results obtained for **(HNEt₃)₂2** and **(NMe₄)₂2** show that highly axial ground states not necessarily require linear complexes, which are a current trend in the community of molecular magnetism.^{29-31,72} Instead, four-coordinate Co(II) chelate complexes exhibiting acute bite angles and symmetry beyond the directly coordinated donor atoms can also show magnetic bistability. It is worthwhile mentioning that the Co(II) complexes presented here are fully air and moisture stable and thus much closer to practical applications than the rather exotic linear complexes reported in literature. However, in spite of their high axiality, **(HNEt₃)₂2** and **(NMe₄)₂2** still show under-barrier processes for magnetic relaxation, preventing practical application. As it was reported that quantum tunneling of the magnetization can be suppressed in exchange coupled systems,³³ one promising idea for the future concerns the conversion of the currently bidentate ligand into a tetradentate bridging ligand. Since such ligands are potentially redox active, rather strong exchange couplings could be achieved by employing the ligand in a radical form. Thus, the compounds **(HNEt₃)₂2** and **(NMe₄)₂2** provide a promising starting point for proceeding towards improved SMMs. They offer manifold possible modifications, concerning for example the choice of the counter ions, the substituents at the ligand, the denticity of the ligand or its oxidation state.

The second group of cobalt complexes studied in this work comprised dimers of distorted octahedrally coordinated Co(II) ions, bridged by quinone-based bridging ligands where one or two oxygen donors of 2,5-dihydroxy-1,4-benzoquinone are substituted by isoelectronic [NR] groups. The substitution of two oxygen donors led to the formation of the symmetrically bridged dimers **3[BF₄]₂** and **4[BPh₄]₂** with R referring to 2-(methoxy)-phenyl in **3[BF₄]₂** and 2-(trifluoromethyl)-phenyl in **4[BPh₄]₂**. The substitution of only one oxygen donor led to the asymmetrically bridged dimer **5[OTf]₂** where R stands for 4-(isopropyl)-phenyl. In all dimers, tris(2-pyridylmethyl)amine served as a co-ligand. The main interest regarding these compounds concerned the nature and strength of the exchange coupling mediated by the bridges, i.e. the influence of the bridging symmetry and the substituents R. Due to the potential non-innocent behavior of the bridges, another interesting question concerned the observation of valence tautomerism in the corresponding one-electron oxidized species that could lead to switchable magnetic properties.

The static magnetic properties were investigated by dc susceptibility and magnetization measurements and the obtained data indicated weak antiferromagnetic exchange interactions in **3[BF₄]₂** and **5[OTf]₂**, while **4[BPh₄]₂** showed ferromagnetic

exchange. No valence tautomerism was observed in the studied one-electron oxidized species **3**[BF₄]₃ and **5**[OTf]₃, showing that the potentially non-innocent bridges behave essentially innocently in these complexes. Since partially unquenched first-order orbital angular momenta in octahedral Co(II) complexes might preclude the application of a simple spin Hamiltonian, quantitative data interpretation was first performed in terms of the Lines model.⁸¹ However, since this model was originally developed for Co(II) ions in perfect octahedral symmetry, rather unreasonable fits to the susceptibility data were obtained. Instead, good agreement between calculated and experimental data as well as reasonable fit parameter values were obtained using an empirical model developed by Lloret *et al.*⁸⁵ that takes into account axial distortion in terms of the parameter Δ_{ax} . Importantly, rather high and positive values for Δ_{ax} were found, hinting at an orbital singlet ground state for Co(II), for which the spin Hamiltonian approach is appropriate. Thus, the model by Lloret is a suitable tool for obtaining a first idea about the electronic structures of cobalt complexes based on magnetic data and it can help in the decision concerning the further strategy.

Subsequently, the susceptibility data were successfully simulated using a simple spin Hamiltonian, i.e. in terms of axial ZFS parameters D , isotropic g -values and isotropic exchange coupling constants J_{ex} , with $J_{ex} = -0.47 \text{ cm}^{-1}$ for **3**[BF₄]₂, $J_{ex} = +0.76 \text{ cm}^{-1}$ for **4**[BPh₄]₂ and $J_{ex} = -0.52 \text{ cm}^{-1}$ for **5**[OTf]₂. The magnetometric measurements were complemented by multi-frequency EPR-spectroscopic studies. Simulation of the EPR data required anisotropic g -tensors and exchange couplings; however, the obtained mean values agree rather well with the values derived from the magnetic data.

Comparing the exchange coupling constants determined for **3**[BF₄]₂, **4**[BPh₄]₂ and **5**[OTf]₂, **4**[BPh₄]₂ is the only compound showing ferromagnetic exchange. At first glance this observation is rather counter-intuitive because the only difference between **4**[BPh₄]₂ and **3**[BF₄]₂ is the differing substituent R at the bridge. One possible explanation might lie in the electron withdrawing nature of the trifluoromethyl groups in **4**[BPh₄]₂ compared to the electron donating substituents in **3**[BF₄]₂ and **5**[OTf]₂. However, verifying this hypothesis requires expanding the series of studied complexes. Since in the context of molecular magnetism ferromagnetic exchange is preferred, the inclusion of bridges with strongly electron-withdrawing substituents like nitrile groups could be rather interesting. Regarding the symmetry of the bridge, the asymmetrical bridge in **5**[OTf]₂ mediates a slightly stronger antiferromagnetic exchange coupling than the symmetric bridge in **3**[BF₄]₂. However, asymmetric bridges are doubtlessly very interesting from a synthetic point of view. They potentially allow site-specific coordination to different metal centers, leading to hetero-

bimetallic complexes. For instance, one of the next steps could be the synthesis and investigation of a Co-Fe dimer. The underlying idea consists in designing a molecule which can be switched between the Co(III)-Fe(II) and Co(II)-Fe(III) species. Many iron(II) complexes show thermally activated spin-crossover^{119,197} while Co(II) exhibits large anisotropy. Thus, the combination of cobalt and iron could lead to rather interesting switchable magnetic properties.

6 Experimental Part

6.1 Film and Monolayer Preparation

6.1.1 Films of $K_3[Fe(CN)_6]$ in Poly(vinylalcohol)

Films of $K_3[Fe(CN)_6]$ in PVA were prepared according to a method described in literature¹⁴². 2.0123 g PVA (Applichem GmbH, Biochemica, *MM* ca. 72000 g mol⁻¹) were added to 40 ml doubly distilled water and heated under reflux (80 °C) and stirring until a clear solution was obtained. 0.2499 g (0.759 mmol) $K_3[Fe(CN)_6]$ (Sigma Aldrich) were dissolved in 20 ml doubly distilled water. The solutions were mixed in a volume ratio of 2 : 1 (PVA : $K_3[Fe(CN)_6]$) and the resulting mixture was put onto glass slides. After drying in the dark for several days, the films were removed with the help of a razor blade.

6.1.2 Synthesis of $(NBu_4)[Dy(Pc)_2]$ for Film Preparation

A sufficient amount of $(NBu_4)[Dy(Pc)_2]$, which was used for preparing polymer films and monolayers, was synthesized by Dr. Michael Waters (School of Chemistry, University of Nottingham), according to a literature-known procedure. A detailed description can be found elsewhere.¹⁴⁶

6.1.3 Films of $[Dy(Pc)_2]$ in Polystyrene

8.0323 g polystyrene (Aldrich Chemistry, average *MM* ca. 350000 g mol⁻¹) were dissolved in 80 ml toluene and 20.5 mg $(NBu_4)[DyPc_2]$ were dissolved in 40 ml ethanol. These stock solutions were mixed in various volume ratios and the resulting solutions were spread onto glass slides, using syringes. After drying for several days, the obtained films were peeled off. Subsequent electronic absorption and MCD measurements showed that the films almost quantitatively contained the neutral species $[Dy(Pc)_2]^0$.

For the estimation of the effective thicknesses, i.e. the numbers of molecules along the axis perpendicular to the film plane, the films were first cut into 1.5 cm diameter circles and subsequently weighed. The physical thicknesses were determined using a caliper. The effective thicknesses were then easily calculated by taking into account the respective film volumes and concentrations.

6.1.4 [Dy(Pc)₂] Monolayers

Monolayers of [Dy(Pc)₂] on (fused) quartz were fabricated by Dr. Jiří Novák, Dr. Chennan Wang and Jakub Rozbořil at the Central European Institute of Technology (CEITEC) at the Masaryk University in Brno. Deposition was performed by applying the Langmuir-Blodgett method, using solutions of (NBu₄)[DyPc₂] in chloroform (1.78 mg mL⁻¹) and surface pressures between 15 and 20 mN m⁻². Preliminary characterization by XRD measurements indicated effective layer thicknesses of 1-2 molecules. MCD-spectra of the layers showed that they consist of the neutral species [Dy(Pc)₂]⁰.

6.2 Synthesis and Structural Characterization

6.2.1 Synthesis and Characterization of the Lanthanide Tetra-Carbonates

The syntheses of **1-Er** and **1-Dy** were performed according to the method described by Goff *et al.*,²⁶ with slight modifications. Thus, 9.016 g (50.0 mmol) guanidine carbonate (Aldrich Chemistry) were dissolved in 20 ml doubly-distilled water, giving a saturated solution. For the synthesis of **1-Er**, a solution of 1.099 g (2.5 mmol) erbium(III) nitrate pentahydrate (Strem Chemicals) in 10 ml doubly-distilled water was added under stirring at room temperature. For **1-Dy**, a solution of 1.030 g (2.3 mmol) dysprosium(III) nitrate hexahydrate (Strem Chemicals) in 10 ml doubly-distilled water was used instead. A white precipitate formed, which was filtered off using a 0.45 µm syringe filter and the resulting clear solution was stored at 5°C for crystallization. After several weeks, pale pink (**1-Er**) or colorless (**1-Dy**) crystals formed, which grew rather large. Alternatively, crystallization could be speeded up by adding some drops of doubly-distilled water after several days, which then led to crystallization within 24 hours.

The easy loss of lattice water molecules complicates the elemental analyses of complexes **1-Er** and **1-Dy**. Some crystals were removed from the mother liqueur and carefully dried on filter paper in order to remove adherent solution, but avoiding the loss of lattice water. The subsequent elemental analyses performed by Barbara Förtsch (Institute of Inorganic Chemistry, University of Stuttgart) using a Perkin Elmer CHSN/O Analyzer yielded the following values:

Elemental analysis for **1-Er**:

Found (calculated for C₉H₅₂ErN₁₅O₂₃) / %: C 11.97 (11.93), H 5.80 (5.79), N 23.12 (23.19).

Elemental analysis for 1-Dy:

Found (calculated for $C_9H_{52}DyN_{15}O_{23}$) / %: C 12.09 (12.00), H 5.84 (5.82), N 23.20 (23.32).

The elemental analyses were repeated after the crystals had been exposed to air for six days. The determined compositions indicated only three water molecules per molecular unit:

Found (calculated for $C_9H_{36}ErN_{15}O_{15}$) / %: C 14.39 (14.19), H 4.68 (4.76), N 27.88 (27.58).

Found (calculated for $C_9H_{36}DyN_{15}O_{15}$) / %: C 14.50 (14.28), H 4.61 (4.79), N 27.93 (27.76).

Conventional room temperature infrared spectra of pellets of **1-Er** and **1-Dy** in KBr were recorded by Julia E. Fischer using a Bruker alpha-T spectrometer.

IR (KBr) for 1-Er:

$\tilde{\nu}$ / cm^{-1} : 668, 725, 862, 1008, 1368, 1505, 1695, 2500-3750, 3628.

IR (KBr) for 1-Dy:

$\tilde{\nu}$ / cm^{-1} : 667, 724, 862, 1007, 1368, 1517, 1652, 2550-3700.

6.2.2 Single Crystal X-Ray Analysis for the Lanthanide Tetra-Carbonates

X-Ray crystallographic analyses on single crystals of **1-Er** and **1-Dy** were performed by Dr. Wolfgang Frey (Institute of Organic Chemistry, University of Stuttgart). Large single crystals of **1-Er** and **1-Dy** were removed from the mother liquor and cut into appropriate size immediately prior to the measurements. They were characterized by X-ray diffraction studies using a Bruker Kappa APEXII Duo diffractometer, equipped with a monochromatic Mo K_{α} X-ray source ($\lambda = 0.71073 \text{ \AA}$). Data collection at 100(2) K, initial indexing and cell refinement were handled using the Bruker APEX II software suite. The structures were solved by direct methods and with the help of SHELXS-97¹⁹⁸ and they were refined anisotropically (non H-atoms) by full-matrix least squares methods on F^2 . Only a part of the hydrogen atoms could be located at different fourier map, so they were refined with fixed individual displacement parameters, using a riding model with typical d(X-H) distances. Table 16 shows the important crystallographic parameters and details about the structure refinements. Crystal structures were visualized with the help of the Mercury 2.4 crystal structure visualization software.¹⁹⁹

Table 16: Crystal data and details about structure refinement for compounds **1-Er** and **1-Dy**.

	[C(NH ₂) ₃] ₅ [Er(CO ₃) ₄] · 11 H ₂ O (1-Er)	[C(NH ₂) ₃] ₅ [Dy(CO ₃) ₄] · 11 H ₂ O (1-Dy)
formula weight / g mol ⁻¹	905.92	901.10
temperature / K	100(2)	100(2)
wavelength / Å	0.71073	0.71073
crystal system	monoclinic	monoclinic
space group	<i>P</i> 2 ₁ / <i>n</i>	<i>P</i> 2 ₁ / <i>n</i>
<i>a</i> / Å	8.8284(6)	8.7616(6)
<i>b</i> / Å	20.9625(14)	21.1384(16)
<i>c</i> / Å	19.6598(13)	19.7207(13)
α / deg	90.00	90.00
β / deg	94.266(2)	94.254(2)
γ / deg	90.00	90.00
volume / Å ³	3628.3(4)	3642.3(4)
<i>Z</i>	4	4
calculated density / g cm ³	1.658	1.603
Absorption coefficient / mm ⁻¹	2.412	2.148
<i>F</i> (000)	1852	1756
crystal size / mm	0.62 x 0.21 x 0.15	0.59 x 0.49 x 0.27
θ range for data collection / °	1.42 – 28.34	2.07 – 25.10
index ranges	-9 < <i>h</i> < 11 -27 < <i>k</i> < 26 -25 < <i>l</i> < 26	-10 < <i>h</i> < 10 -25 < <i>k</i> < 24 -23 < <i>l</i> < 22
reflections collected	34153	33026
independent reflections	8976	6439
completeness to $\theta = 28.34^\circ$	99.1 %	98.9 %
refinement method	full-matrix least squares on <i>F</i> ²	
data / restraints / parameters	8976 / 6 / 433	6439 / 138 / 498

	[C(NH ₂) ₃] ₅ [Er(CO ₃) ₄] · 11 H ₂ O (1-Er)	[C(NH ₂) ₃] ₅ [Dy(CO ₃) ₄] · 11 H ₂ O (1-Dy)
goodness-of-fit on F^2	1.044	1.048
final R indices [$I > 2\sigma(I)$]	$R1 = 0.0473$; $wR2 = 0.1311$	$R1 = 0.0742$, $wR2 = 0.1776$
R indices (all data)	$R1 = 0.0498$; $wR2 = 0.1319$	$R1 = 0.0765$, $wR2 = 0.1787$
Largest difference peak / hole / e Å ⁻³	2.502 / -1.546	3.324 / -4.501

6.2.3 X-Ray Powder Diffraction Studies on the Lanthanide Tetra-Carbonates

Some smaller crystals of **1-Er** and **1-Dy** were ground together with some drops of the respective mother liqueur and filled into 0.70 mm glass capillaries, which were then sealed in order to avoid evaporation. The measurements were performed at room temperature by Dr. Pierre Eckold at the Institute of Inorganic Chemistry at the University of Stuttgart using a STOE STADI P diffractometer with Mo $K_{\alpha 1}$ radiation (50 kV, 40 mA), equipped with a Siemens ID 3003 generator, a Germanium (111) monochromator and a DECTRIS MYTHEN 1K detector in reflection geometry. The diffractometer was operated utilizing WinXPOW software, which was also used for baseline corrections. Theoretical powder patterns were simulated with the help of the crystal structure visualization software Mercury 2.4.¹⁹⁹

6.2.4 Synthesis and Characterization of the Mononuclear Co(II) Complexes

The mononuclear Co(II) complexes (**HNEt₃)₂2** and (**NMe₄)₂2** were synthesized and structurally characterized by Dr. Margarethe van der Meer and coworkers (Institute for Chemistry and Biochemistry, Freie Universität Berlin). Details concerning the synthesis of (**HNEt₃)₂2** and the corresponding structural data can be found in ref¹⁶⁷. The molecular structures shown in section 4.3.1 were visualized with the help of the crystal structure visualization software Mercury 2.4.¹⁹⁹

6.2.5 Synthesis and Characterization of the Cobalt Dimers

The symmetrically bridged dimers **3**[BF₄]₂, **3**[BF₄]₃, **3**[BF₄]₄ and **4**[BPh₄]₂ were synthesized and structurally characterized by Dr. David Schweinfurth and coworkers (Institute for Chemistry and Biochemistry, Freie Universität Berlin). Details concerning the syntheses and the structural data can be found in ref³².

The asymmetrically bridged dimers **5**[OTf]₂, **5**[OTf]₂ and **5**[OTf]₂[BF₄]₂ were synthesized, structurally characterized and provided by Dr. Margarethe van der Meer and coworkers (Institute for Chemistry and Biochemistry, Freie Universität Berlin).

Crystal structures were visualized with the help of the Mercury 2.4 crystal structure visualization software.¹⁹⁹

6.3 Magnetic and Spectroscopic Measurements

6.3.1 SQUID Magnetometry

Magnetic measurements were performed using a MPMS 3 SQUID magnetometer (for compounds **5**[OTf]₂, **5**[OTf]₂[BF₄]₂, (HNEt₃)₂**2** and (NMe₄)₂**2**) and a MPMS-XL7 SQUID magnetometer (for compounds **1-Er**, **1-Dy**, **3**[BF₄]₂, **3**[BF₄]₃, **3**[BF₄]₄, **4**[BPh₄]₂ and **5**[OTf]₃), both from Quantum Design. Unless otherwise stated, samples were studied as slightly pressed, Teflon-wrapped powder pellets. **1-Er** and **1-Dy** were studied as mixtures with silicone grease (GE Bayer Silicones, Baysilone paste), also wrapped by Teflon tape. Temperature dependent susceptibility measurements were carried out applying static fields of 1000 – 10000 Oe. Unless otherwise stated, magnetic data were corrected for diamagnetic contributions using Pascal's constants⁹³.

6.3.2 Far-Infrared Spectroscopy

Far-infrared spectra of **1-Er**, **1-Dy** and **5**[OTf]₂ at applied magnetic fields between 0 T and 6 T were recorded on a Bruker IFS 113v FTIR-spectrometer equipped with an Oxford Instruments Spectromag SM4000 optical cryomagnet and an Infrared Laboratories pumped Si bolometer. The measurements were performed with the help of Raphael Marx and Dr. Maria Dörfel (both Institute of Physical Chemistry, University of Stuttgart). **1-Er** and **1-Dy** were studied as mulls in silicone grease (GE Bayer Silicones, Baysilone paste), while **5**[OTf]₂ was studied as a pure powder pellet.

Far-infrared spectra of $(\text{HNEt}_3)_2\mathbf{2}$ and $(\text{NMe}_4)_2\mathbf{2}$ at magnetic fields between 0 T and 11 T were recorded by Dr. Milan Orlita and Michael Hakl (both Laboratoire National des Champs Magnétiques Intenses, Grenoble). The measurements were performed on pressed powder pellets of $(\text{HNEt}_3)_2\mathbf{2}$ and $(\text{NMe}_4)_2\mathbf{2}$ dispersed in eicosane, using a Bruker IFS 66v/s FTIR spectrometer with a global source. The samples were placed inside an 11 T solenoid magnet equipped with a composite bolometer detector element.

6.3.3 Luminescence Spectroscopy

Low temperature photoluminescence experiments on mulls of **1-Er** and **1-Dy** in silicone grease (GE Bayer Silicones, Baysilone paste) grease were carried out with the help of Maren Gysler (Institute of Physical Chemistry, University of Stuttgart), Stergios Piligkos and Theis Theis Brock-Nannestad (both Department of Chemistry, University of Copenhagen) at the University of Copenhagen. The spectra were recorded using a Horiba FluoroLog3 luminescence spectrometer equipped with an Oxford Instruments helium flow optical cryostat and photomultiplier and InGaAs detectors.

6.3.4 Low Temperature Electronic Absorption and Magnetic Circular Dichroism

Magnetic circular dichroism spectra were recorded on an Aviv Model 42 CD spectrometer equipped with an Oxford Instruments SM-4000-10 optical cryomagnet. A detailed description of the experimental setup is given in section 4.1. Low temperature electronic absorption spectra were obtained by monitoring the PMT voltage keeping the photo-current constant. The baseline was corrected by means of the dynode voltage profile measured without a sample. Samples were studied either as mulls, polymer films or monolayers, as indicated in the corresponding sections.

6.3.5 Electron Paramagnetic Resonance

Conventional X-band (9.47 GHz) EPR-spectra were recorded using a Bruker EMX EPR spectrometer equipped with an Oxford Instruments continuous helium flow cryostat. The microwave power was adjusted to values that did not cause saturation effects. The samples were studied either as powders ($\mathbf{5[OTf]_2}$, $\mathbf{5[OTf]_3}$, $\mathbf{3[BF_4]_2}$, $\mathbf{3[BF_4]_3}$, $\mathbf{4[BPh_4]_2}$, $(\text{HNEt}_3)_2\mathbf{2}$ and $(\text{NMe}_4)_2\mathbf{2}$), frozen solutions in butyronitrile ($\mathbf{3[BF_4]_3}$) or mulls in Baysilone vacuum

grease (**1-Er**, **1-Dy**). The sample tubes containing the samples were evacuated immediately prior to the measurements.

High-frequency EPR (HF-EPR) spectra at frequencies between 90 and 720 GHz were recorded on a home-built spectrometer employing an Anritsu signal generator, a VDI amplifier-multiplier chain, a Thomas Keating quasi-optical bridge, an Oxford Instruments 15/17 T solenoid cryomagnet and a QMC Instruments InSb hot electron bolometer. The measurements were performed with the help of Raphael Marx and Dr.-Ing. Petr Neugebauer (both Institute of Physical Chemistry, University of Stuttgart). Samples were studied as pressed powder pellets, either of pure substance or of mixtures with eicosane. Only **1-Er** and **1-Dy** were studied as mulls in fluorolube®.

6.4 Analysis and Calculations

6.4.1 Simulation of Magnetic Data

Simulations of dc susceptibility and magnetization curves based on a spin Hamiltonian approach were performed by using the easyspin²⁰⁰ toolbox for Matlab. Part of the required scripts was provided by Raphael Marx and Philipp Lutz (both Institute of Physical Chemistry, University of Stuttgart). Simulations based on crystal field parameters were performed using the simulation software CONDON²⁰¹. Least-squares-fitting of susceptibility curves based on the Lines model⁸¹ or the empirical model by Lloret *et al.*⁸⁵ was performed by means of self-written Matlab programs. Analysis of dynamic magnetic properties, i.e. least-squares fitting of Argand plots was performed by means of self-written Matlab scripts as well. All graphs were generated with the help of Matlab.

6.4.2 Simulation of Spectroscopic Data

Simulations of far-infrared spectra based on a spin Hamiltonian approach were performed by means of the easyspin²⁰⁰ toolbox for Matlab. Part of the required scripts was provided by Raphael Marx and Philipp Lutz (both Institute of Physical Chemistry, University of Stuttgart).

Simulations of EPR-spectra using a spin Hamiltonian approach or an effective spin-1/2 approximation were performed with easyspin²⁰⁰ as well. Effective *g*-values based on crystal field parameters were calculated using the program pycf¹⁷⁶ written by Sebastian Horvath (Department of Physics and Astronomy, University of Canterbury).

VTVH-MCD curves were simulated based on the equations published by Neese and Solomon¹⁰⁸ by means of self-written Matlab scripts.

All plots showing experimental and simulated spectra or curves in this work were generated using Matlab.

6.4.3 Crystal Field Analysis

Crystal field analyses for the lanthanide compounds **1-Er** and **1-Dy** were performed by means of the f-shell program package¹⁷⁵ written by Prof. Dr. Michael F. Reid (Department of Physics and Astronomy, University of Canterbury). Calculations were performed in the intermediate coupling scheme using the full bases of states arising from the respective $4f^N$ configurations. The reported parameter uncertainties were estimated by taking the standard deviations provided by the f-shell output and modifying them by considering the effect of parameter change on the corresponding EPR simulations.

Crystal field analyses for the cobalt compounds **(HNEt₃)₂2** and **(NMe₄)₂2** were performed by means of the Crystal Field Computer Package by Yeung and Rudowicz⁸⁰, using the $\alpha SM_S LM$ basis of states and by means of a self-written Matlab script. Parameter uncertainties were estimated by qualitatively considering the effect of parameter change on the agreement between experimental and calculated energies.

All energy level diagrams shown in this work were generated using Matlab.

6.4.4 Theoretical Calculations

Theoretical calculations concerning the electronic structure and spin-phonon-couplings in **(HNEt₃)₂2** were performed by Dr. Mihail Atanasov (Max Planck Institute for Chemical Energy Conversion, Mülheim a. d. Ruhr and Institute of General and Inorganic Chemistry, Bulgarian Academy of Sciences, Sofia). Computational details as well as a detailed description of the results can be found in ref¹⁶⁷.

7 References

- 1 Sessoli, R., Gatteschi, D., Caneschi, A. & Novak, M. A. Magnetic bistability in a metal-ion cluster. *Nature* **365**, 141-143 (1993).
- 2 Kahn, O. *Molecular Magnetism*. (VCH, New York, Weinheim, Cambridge, 1993).
- 3 Gatteschi, D., Sessoli, R. & Villain, J. *Molecular Nanomagnets*. (Oxford University Press, Oxford 2006).
- 4 Friedman, J. R. & Sarachik, M. P. Single-Molecule Nanomagnets. *Annu. Rev. Cond. Mat. Phys.* **1**, 109-128 (2010).
- 5 Winpenny, R. (eds), *Single-Molecule Magnets and Related Phenomena*. (Springer Berlin, Heidelberg, 2006)
- 6 Christou, G., Gatteschi, D., Hendrickson, D. N. & Sessoli, R. Single-molecule magnets. *Mrs Bull.* **25**, 66-71 (2000).
- 7 Eppley, H. J. *et al.* Single-molecule magnets: Characterization of complexes exhibiting out-of-phase AC susceptibility signals. *Mol. Cryst. Liq. Cryst. A* **305**, 167-179 (1997).
- 8 Winpenny, R. E. P. & McInnes, E. J. L. in *Molecular Materials* (eds D. W. Bruce, D. O'Hare, & R. I. Walton) (John Wiley & Sons, Chichester, 2010).
- 9 Woodruff, D. N., Winpenny, R. E. P. & Layfield, R. A. Lanthanide Single-Molecule Magnets. *Chem. Rev.* **113**, 5110-5148 (2013).
- 10 Aromí, G. & Brechin, E. K. Synthesis of 3d Metallic Single-Molecule Magnets. *Struct. Bond.* **122**, 1-67 (2006).
- 11 Craig, G. A. & Murrie, M. 3d single-ion magnets. *Chem. Soc. Rev.* **44**, 2135-2147 (2015).
- 12 Meihaus, K. R. & Long, J. R. Actinide-based single-molecule magnets. *Dalton Trans.* **44**, 2517-2528 (2015).
- 13 Lis, T. Preparation, Structure, and Magnetic Properties of a Dodecanuclear Mixed-Valence Manganese Carboxylate. *Acta Cryst. B* **36**, 2042-2046 (1980).
- 14 Bagai, R. & Christou, G. The Drosophila of single-molecule magnetism: $[\text{Mn}_{12}\text{O}_{12}(\text{O}_2\text{CR})_{16}(\text{H}_2\text{O})_4]$. *Chem. Soc. Rev.* **38**, 1011-1026 (2009).
- 15 Ako, A. M. *et al.* A Ferromagnetically Coupled Mn_{19} Aggregate with a Record $S=83/2$ Ground Spin State. *Angew. Chem. Int. Ed.* **45**, 4926-4929 (2006).

- 16 Murugesu, M., Habrych, M., Wernsdorfer, W., Abboud, K. A. & Christou, G. Single-Molecule Magnets: A Mn_{25} Complex with a Record $S=51/2$ Spin for a Molecular Species. *J. Am. Chem. Soc.* **126**, 4766-4767 (2004).
- 17 Powell, A. K. *et al.* Synthesis, Structures, and Magnetic Properties of Fe_2 , Fe_{17} , and Fe_{19} Oxo-Bridged Iron Clusters - the Stabilization of High Ground-State Spins by Cluster Aggregates. *J. Am. Chem. Soc.* **117**, 2491-2502 (1995).
- 18 Kang, S. *et al.* A ferromagnetically coupled Fe_{42} cyanide-bridged nanocage. *Nat. Commun.* **6**, 1-6 (2015).
- 19 Waldmann, O. A criterion for the anisotropy barrier in single-molecule magnets. *Inorg. Chem.* **46**, 10035-10037 (2007).
- 20 Neese, F. & Pantazis, D. A. What is not required to make a single molecule magnet. *Faraday Discuss.* **148**, 229-238 (2011).
- 21 Zhang, P., Guo, Y. N. & Tang, J. K. Recent advances in dysprosium-based single molecule magnets: Structural overview and synthetic strategies. *Coord. Chem. Rev.* **257**, 1728-1763 (2013).
- 22 Murrie, M. Cobalt(II) single-molecule magnets. *Chem. Soc. Rev.* **39**, 1986-1995 (2010).
- 23 Sessoli, R. & Powell, A. K. Strategies towards single molecule magnets based on lanthanide ions. *Coord. Chem. Rev.* **253**, 2328-2341 (2009).
- 24 Gómez-Coca, S., Aravena, D., Morales, R. & Ruiz, E. Large magnetic anisotropy in mononuclear metal complexes. *Coord. Chem. Rev.* **289**, 379-392 (2015).
- 25 Ishikawa, N., Sugita, M., Ishikawa, T., Koshihara, S. & Kaizu, Y. Lanthanide double-decker complexes functioning as magnets at the single-molecular level. *J. Am. Chem. Soc.* **125**, 8694-8695 (2003).
- 26 Goff, G. S. *et al.* Synthesis and Structural Characterization of Molecular Dy(III) and Er(III) Tetra-Carbonates. *Inorg. Chem.* **49**, 6558-6564 (2010).
- 27 Janicki, R., Starynowicz, P. & Mondry, A. Lanthanide Carbonates. *Eur. J. Inorg. Chem.*, 3601-3616 (2011).
- 28 Frost, J. M., Harriman, K. L. M. & Murugesu, M. The rise of 3-d single-ion magnets in molecular magnetism: towards materials from molecules? *Chem. Sci.* (2016).
- 29 Zadrozny, J. M. *et al.* Magnetic blocking in a linear iron(I) complex. *Nat. Chem.* **5**, 577-581 (2013).
- 30 Zadrozny, J. M. *et al.* Slow magnetization dynamics in a series of two-coordinate iron(II) complexes. *Chem. Sci.* **4**, 125-138 (2013).

- 31 Meng, Y. S. *et al.* Observation of the single-ion magnet behavior of d^8 ions on two-coordinate Co(I)-NHC complexes. *Chem. Sci.* **6**, 7156-7162 (2015).
- 32 Schweinfurth, D. *et al.* Redox-Induced Spin-State Switching and Mixed Valency in Quinonoid-Bridged Dicobalt Complexes. *Chem. Eur. J.* **20**, 3475-3486 (2014).
- 33 Demir, S., Jeon, I. R., Long, J. R. & Harris, T. D. Radical ligand-containing single-molecule magnets. *Coord. Chem. Rev.* **289**, 149-176 (2015).
- 34 Liddle, S. T. & van Slageren, J. Improving f-element single molecule magnets. *Chem. Soc. Rev.* **44**, 6655-6669 (2015).
- 35 Dei, A., Gatteschi, D., Sangregorio, C. & Sorace, L. Quinonoid metal complexes: Toward molecular switches. *Acc. Chem. Res.* **37**, 827-835 (2004).
- 36 Bartolomé, J., Luis, F. & Fernández, J. F. (eds), *Molecular Magnets - Physics and Applications*. (Springer, Heidelberg, 2014)
- 37 Rinehart, J. D. & Long, J. R. Exploiting single-ion anisotropy in the design of f-element single-molecule magnets. *Chem. Sci.* **2**, 2078-2085 (2011).
- 38 Abragam, A. & Bleaney, B. *Electron Paramagnetic Resonance of Transition Ions*. (Oxford University Press, Oxford, 2013).
- 39 Carlin, R. L. *Magnetochemistry* (Springer, Berlin, 1986).
- 40 Goodenough, J. B. *Magnetism and the chemical bond*. (Interscience Publ., New York, 1963).
- 41 Goodenough, J. B. An Interpretation of the Magnetic Properties of the Perovskite-Type Mixed Crystals $\text{La}_{1-x}\text{Sr}_x\text{CoO}_{3-\lambda}$. *J. Phys. Chem. Sol.* **6**, 287-297 (1958).
- 42 Kanamori, J. Superexchange Interaction and Symmetry Properties of Electron Orbitals. *J. Phys. Chem. Sol.* **10**, 87-98 (1959).
- 43 Barra, A. L., Gatteschi, D. & Sessoli, R. High-frequency EPR spectra of a molecular nanomagnet: Understanding quantum tunneling of the magnetization. *Phys. Rev. B* **56**, 8192-8198 (1997).
- 44 Boča, R. Zero-field splitting in metal complexes. *Coord. Chem. Rev.* **248**, 757-815 (2004).
- 45 Ishikawa, N. Simultaneous determination of ligand-field parameters of isostructural lanthanide complexes by multidimensional optimization. *J. Phys. Chem. A* **107**, 5831-5835 (2003).
- 46 Ishikawa, N. *et al.* Determination of ligand-field parameters and f-electronic structures of double-decker bis(phthalocyaninato)lanthanide complexes. *Inorg. Chem.* **42**, 2440-2446 (2003).

- 47 Orbach, R. Spin-Lattice Relaxation in Rare-Earth Salts. *Proc. R. Soc. Lon. Ser. A* **264**, 458-484 (1961).
- 48 Singh, A. & Shrivastava, K. N. Optical-Acoustic 2-Phonon Relaxation in Spin Systems. *Phys. Stat. Sol. B* **95**, 273-277 (1979).
- 49 Shrivastava, K. N. Theory of Spin-Lattice Relaxation. *Phys. Stat. Sol. B* **117**, 437-458 (1983).
- 50 Kramers, H. A. General theory of the paramagnetic rotation in crystals. *Proc. Kon. Ned. Akad. Wetensch., C* **33**, 959-972 (1930).
- 51 Gatteschi, D. & Sessoli, R. Quantum tunneling of magnetization and related phenomena in molecular materials. *Angew. Chem. Int. Ed.* **42**, 268-297 (2003).
- 52 Friedman, J. R., Sarachik, M. P., Tejada, J., Maciejewski, J. & Ziolo, R. Steps in the hysteresis loops of a high-spin molecule. *J. Appl. Phys.* **79**, 6031-6033 (1996).
- 53 Friedman, J. R., Sarachik, M. P., Tejada, J. & Ziolo, R. Macroscopic measurement of resonant magnetization tunneling in high-spin molecules. *Phys. Rev. Lett.* **76**, 3830-3833 (1996).
- 54 Thomas, L. *et al.* Macroscopic quantum tunnelling of magnetization in a single crystal of nanomagnets. *Nature* **383**, 145-147 (1996).
- 55 Wybourne, B. G. *Spectroscopic Properties of Rare Earths*. (Interscience Publ., New York 1965).
- 56 Wybourne, B. G. & Smentek, L. *Optical Spectroscopy of Lanthanides - Magnetic and Hyperfine Interactions*. (CRC Press, Boca Raton, 2007).
- 57 Hund, F. Concerning the interpretation of complex spectra, especially the elements scandium to nickel. *Z. Phys.* **33**, 345-371 (1925).
- 58 Hund, F. *Linienspektren und periodisches System der Elemente*. (Springer, Berlin, 1927).
- 59 Pauli, W. On the connection of the arrangement of electron groups in atoms with the complex structure of spectra. *Z. Phys.* **31**, 765-783 (1925).
- 60 Görrler-Walrand, C. & Binnemans, K. in *Handbook on the Physics and Chemistry of Rare Earths* Vol. 23 (eds K. A. Gschneider & L. Eyring) (Elsevier, Amsterdam, 1996).
- 61 Nielson, C. W. & Koster, G. F. *Spectroscopic coefficients for the p^n , d^n , and f^n configurations*. (MIT Pr., Cambridge, 1963).
- 62 Dieke, G. H. *Spectra and energy levels of rare earth ions in crystals*. (Interscience Publ., New York 1968).

- 63 Dieke, G. H. & Crosswhite, H. M. The Spectra of the Doubly and Triply Ionized Rare Earths. *Appl. Optics* **2**, 675-686 (1963).
- 64 Stevens, K. W. H. Matrix Elements and Operator Equivalents Connected with the Magnetic Properties of Rare Earth Ions. *Proc. Phys. Soc. Lond. A* **65**, 209-215 (1952).
- 65 Lueken, H. *Magnetochemie*. (Teubner, Stuttgart, Leipzig, 1999).
- 66 Sorace, L., Benelli, C. & Gatteschi, D. Lanthanides in molecular magnetism: Old tools in a new field. *Chem. Soc. Rev.* **40**, 3092-3104 (2011).
- 67 Karbowski, M., Rudowicz, C. & Ishida, T. Determination of Crystal-Field Energy Levels and Temperature Dependence of Magnetic Susceptibility for Dy³⁺ in [Dy₂Pd] Heterometallic Complex. *Inorg. Chem.* **52**, 13199-13206 (2013).
- 68 Racah, G. Theory of complex spectra. II. *Phys. Rev.* **62**, 438-462 (1942).
- 69 Fano, U. & Racah, G. *Irreducible tensorial sets*. (Acad. Pr., New York, 1959).
- 70 Eckart, C. The application of group theory to the quantum dynamics of monatomic systems. *Rev. Mod. Phys.* **2**, 0305-0380 (1930).
- 71 Wigner, E. Non combined terms in the new quantum theory Part II. *Z. Phys.* **40**, 883-892 (1927).
- 72 Chilton, N. F., Goodwin, C. A. P., Mills, D. P. & Winpenny, R. E. P. The first near-linear bis(amide) f-block complex: A blueprint for a high temperature single molecule magnet. *Chem. Commun.* **51**, 101-103 (2015).
- 73 Ungur, L. & Chibotaru, L. F. Magnetic anisotropy in the excited states of low symmetry lanthanide complexes. *Phys. Chem. Chem. Phys.* **13**, 20086-20090 (2011).
- 74 Aravena, D. & Ruiz, E. Shedding Light on the Single-Molecule Magnet Behavior of Mononuclear Dy^{III} Complexes. *Inorg. Chem.* **52**, 13770-13778 (2013).
- 75 Lever, A. B. P. *Inorganic electronic spectroscopy*. (Elsevier, Amsterdam 1968).
- 76 Ballhausen, C. J. *Introduction to ligand field theory*. (McGraw-Hill Book Comp., New York 1962).
- 77 Wildner, M. Polarized electronic absorption spectra of tetrahedrally coordinated Co²⁺ ions in the new compound Ca₃Co(SeO₃)₄ and its structural characterization. *J. Sol. Stat. Chem.* **124**, 143-150 (1996).
- 78 Griffith, J. S. *The theory of transition-metal ions*. (Cambridge Univ. Press, Cambridge, 1961).
- 79 Yang, Z. Y. & Wei, Q. On the relations between the crystal field parameter notations in the "Wybourne" notation and the conventional ones for 3d^N ions in axial symmetry crystal field. *Physica B Cond. Mat.* **370**, 137-145 (2005).

- 80 Yeung, Y. Y. & Rudowicz, C. Ligand-Field Analysis of the $3d^N$ Ions at Orthorhombic or Higher Symmetry Sites. *Comput. Chem.* **16**, 207-216 (1992).
- 81 Lines, M. E. Orbital Angular Momentum in Theory of Paramagnetic Clusters. *J. Chem. Phys.* **55**, 2977-2984 (1971).
- 82 De Munno, G., Julve, M., Lloret, F., Faus, J. & Caneschi, A. 2,2'-Bipyrimidine (bipym)-bridged Dinuclear Complexes. Part 4. Synthesis, Crystal-Structure and Magnetic-Properties of $[\text{Co}_2(\text{H}_2\text{O})_8(\text{bipym})][\text{NO}_3]_4$, $[\text{Co}_2(\text{H}_2\text{O})_8(\text{bipym})][\text{SO}_4]_2 \cdot 2\text{H}_2\text{O}$ and $[\text{Co}_2(\text{bipym})_3(\text{NCS})_4]$. *J. Chem. Soc. Dalton Trans.*, 1175-1183 (1994).
- 83 Cañadillas-Delgado, L. *et al.* Unusual (μ -aqua)bis(μ -carboxylate) Bridge in Homometallic M(II) (M = Mn, Co and Ni) Two-dimensional Compounds Based on the 1,2,3,4-Butanetetracarboxylic Acid: Synthesis, Structure, and Magnetic Properties. *Inorg. Chem.* **46**, 7458-7465 (2007).
- 84 De Munno, G., Poerio, T., Julve, M., Lloret, F. & Viau, G. Synthesis, crystal structure and magnetic properties of the cobalt(II) chain $[\text{Co}(\text{bipym})(\text{H}_2\text{O})_2](\text{NO}_3)_2$ and the dinuclear compounds $[\text{Co}_2(\text{bipym})_3(\text{H}_2\text{O})_4](\text{NO}_3)_4 \cdot 2\text{H}_2\text{O}$ and $[\text{Co}_2(\text{bipym})_3(\text{H}_2\text{O})_2(\text{SO}_4)_2] \cdot 12\text{H}_2\text{O}$. *New J. Chem.* **22**, 299-305 (1998).
- 85 Lloret, F., Julve, M., Cano, J., Ruiz-García, R. & Pardo, E. Magnetic properties of six-coordinated high-spin cobalt(II) complexes: Theoretical background and its application. *Inorg. Chim. Acta* **361**, 3432-3445 (2008).
- 86 Fataftah, M. S., Zdrozny, J. M., Rogers, D. M. & Freedman, D. E. A Mononuclear Transition Metal Single-Molecule Magnet in a Nuclear Spin-Free Ligand Environment. *Inorg. Chem.* **53**, 10716-10721 (2014).
- 87 Zdrozny, J. M., Telser, J. & Long, J. R. Slow magnetic relaxation in the tetrahedral cobalt(II) complexes $[\text{Co}(\text{EPh})_4]^{2-}$ (E=O, S, Se). *Polyhedron* **64**, 209-217 (2013).
- 88 Saber, M. R. & Dunbar, K. R. Ligands effects on the magnetic anisotropy of tetrahedral cobalt complexes. *Chem. Commun.* **50**, 12266-12269 (2014).
- 89 Carl, E., Demeshko, S., Meyer, F. & Stalke, D. Triimidodisulfonates as Acute Bite-Angle Chelates: Slow Relaxation of the Magnetization in Zero Field and Hysteresis Loop of a Co^{II} Complex. *Chem. Eur. J.* **21**, 10109-10115 (2015).
- 90 Novikov, V. V. *et al.* A Trigonal Prismatic Mononuclear Cobalt(II) Complex Showing Single-Molecule Magnet Behavior. *J. Am. Chem. Soc.* **137**, 9792-9795 (2015).
- 91 Zhu, Y. Y. *et al.* Zero-field slow magnetic relaxation from single Co(II) ion: a transition metal single-molecule magnet with high anisotropy barrier. *Chem. Sci.* **4**, 1802-1806 (2013).

- 92 Zhu, Y. Y. *et al.* A Family of $\text{Co}^{\text{II}}\text{Co}^{\text{III}}_3$ Single-Ion Magnets with Zero-Field Slow Magnetic Relaxation: Fine Tuning of Energy Barrier by Remote Substituent and Counter Cation. *Inorg. Chem.* **54**, 5475-5486 (2015).
- 93 Bain, G. A. & Berry, J. F. Diamagnetic corrections and Pascal's constants. *J. Chem. Educ.* **85**, 532-536 (2008).
- 94 Cole, K. S. & Cole, R. H. Dispersion and absorption in dielectrics I. Alternating current characteristics. *J. Chem. Phys.* **9**, 341-351 (1941).
- 95 Weil, J. A. & Bolton, J. R. *Electron Paramagnetic Resonance : Elementary Theory and Practical Applications*. (Wiley-Interscience, Hoboken, NJ, 2007).
- 96 Jiang, S. D. *et al.* Direct Observation of Very Large Zero-Field Splitting in a Tetrahedral $\text{Ni}^{\text{II}}\text{Se}_4$ Coordination Complex. *J. Am. Chem. Soc.* **137**, 12923-12928 (2015).
- 97 Marx, R. *et al.* Spectroscopic determination of crystal field splittings in lanthanide double deckers. *Chem. Sci.* **5**, 3287-3293 (2014).
- 98 Görrler-Walrand, C. & Binnemans, K. in *Handbook on the Physics and Chemistry of Rare Earths* Vol. 25 (eds K. A. Gschneider & L. Eyring) (Elsevier, Amsterdam, 1998).
- 99 Judd, B. R. Optical Absorption Intensities of Rare-Earth Ions. *Phys. Rev.* **127**, 750-761 (1962).
- 100 Ofelt, G. S. Intensities of Crystal Spectra of Rare-Earth Ions. *J. Chem. Phys.* **37**, 511-520 (1962).
- 101 Bünzli, J. C. G. & Piguet, C. Taking advantage of luminescent lanthanide ions. *Chem. Soc. Rev.* **34**, 1048-1077 (2005).
- 102 Comby, S. & Bünzli, J.-C. G. in *Handbook on the Physics and Chemistry of Rare Earths* Vol. 37 (eds K. A. Gschneider, J.-C. G. Bünzli, & V. K. Pecharsky) (Elsevier, Amsterdam, 2007).
- 103 Kasha, M. Characterization of Electronic Transitions in Complex Molecules. *Discuss. Faraday Soc.*, 14-19 (1950).
- 104 Piepho, S. B. & Schatz, P. N. *Group Theory in Spectroscopy with Applications to Magnetic Circular Dichroism*. (Wiley-Interscience, New York, 1983).
- 105 Mason, W. R. *A Practical Guide to Magnetic Circular Dichroism Spectroscopy*. (Wiley-Interscience, Hoboken, NJ, 2007).
- 106 Faraday, M. Experimental Researches in Electricity. Nineteenth Series. *Phil. Trans. R. Soc. Lond.* **136**, 1-20 (1846).

- 107 Binnemans, K. & Görlner-Walrand, C. On the complementarity of absorption and MCD spectroscopy. *J. Rare Earth* **16**, 204-210 (1998).
- 108 Neese, F. & Solomon, E. I. MCD C-term signs, saturation behavior, and determination of band polarizations in randomly oriented systems with spin $S \geq 1/2$. Applications to $S = 1/2$ and $S = 5/2$. *Inorg. Chem.* **38**, 1847-1865 (1999).
- 109 McCleverty, J. A. in *Comprehensive coordination chemistry II* (Elsevier, Oxford, 2004).
- 110 Collison, D. *et al.* Optical determination of the single-ion zero-field splitting in large spin clusters. *J. Am. Chem. Soc.* **125**, 1168-1169 (2003).
- 111 McInnes, E. J. L. *et al.* Optical detection of spin polarization in single-molecule magnets $[\text{Mn}_{12}\text{O}_{12}(\text{O}_2\text{CR})_{16}(\text{H}_2\text{O})_4]$. *J. Am. Chem. Soc.* **124**, 9219-9228 (2002).
- 112 Domingo, N. *et al.* Magnetism of isolated Mn_{12} single-molecule magnets detected by magnetic circular dichroism: Observation of spin tunneling with a magneto-optical technique. *Phys. Rev. B* **69** (2004).
- 113 Solomon, E. I. *et al.* Geometric and electronic structure/function correlations in non-heme iron enzymes. *Chem. Rev.* **100**, 235-349 (2000).
- 114 Solomon, E. I., Pavel, E. G., Loeb, K. E. & Campochiaro, C. Magnetic Circular-Dichroism Spectroscopy as a Probe of the Geometric and Electronic-Structure of Nonheme Ferrous Enzymes. *Coord. Chem. Rev.* **144**, 369-460 (1995).
- 115 Bane, K., Geiger, R. A., Chabolla, S. A. & Jackson, T. A. Determination of zero-field splitting parameters for a Mn^{IV} center using variable-temperature, variable-field magnetic circular dichroism spectroscopy: Comparison to electron paramagnetic resonance spectroscopy. *Inorg. Chim. Acta* **380**, 135-140 (2012).
- 116 Krzystek, J. *et al.* Definitive spectroscopic determination of zero-field splitting in high-spin cobalt(II). *J. Am. Chem. Soc.* **126**, 2148-2155 (2004).
- 117 Görlner-Walrand, C. & Fluyt, L. in *Handbook on the Physics and Chemistry of Rare Earths* Vol. 40 (ed K. A. Gschneider) (Elsevier, Amsterdam, 2010).
- 118 Titiš, J. & Boča, R. Magnetostructural D Correlations in Hexacoordinated Cobalt(II) Complexes. *Inorg. Chem.* **50**, 11838-11845 (2011).
- 119 Sato, O., Tao, J. & Zhang, Y. Z. Control of magnetic properties through external stimuli. *Angew. Chem. Int. Ed.* **46**, 2152-2187 (2007).
- 120 Sato, O., Cui, A. L., Matsuda, R., Tao, J. & Hayami, S. Photo-induced valence tautomerism in Co complexes. *Acc. Chem. Res.* **40**, 361-369 (2007).

- 121 Sutherland, J. C. in *Modern Techniques for Circular Dichroism and Synchrotron Radiation Circular Dichroism Spectroscopy* (eds A. B. Wallace & R. W. James) (IOS Press, Amsterdam, 2009).
- 122 Planck, M. Law of energy distribution in normal spectra. *Ann. Phys. (Berlin)* **4**, 553-563 (1901).
- 123 Wedler, G. *Lehrbuch der Physikalischen Chemie*. (Wiley-VCH Weinheim, 2005).
- 124 Kingslake, R. (eds), *Optical instruments. - 2*. (Academic Press, New York, 1969)
- 125 Olsen, A. L. & McBride, W. R. Transmittance of Single-Crystal Magnesium Fluoride and IRTRAN-1* in the 0.2- 15- μ Range. *J. Opt. Soc. Am.* **53**, 1003-1005 (1963).
- 126 Dodge, M. J. Refractive Properties of Magnesium Fluoride. *Appl. Optics* **23**, 1980-1985 (1984).
- 127 <http://www.klccgo.com/mfrochon.htm> (retrieved on 02/11/2016).
- 128 Bennett, J. M. in *Handbook of Optics* Vol. 1 (eds M. Bass, E. W. van Stryland, D. R. Williams, & L. W. William) (McGraw-Hill, New York, 1995).
- 129 Travis, J. C. *et al.* Intrinsic wavelength standard absorption bands in holmium oxide solution for UV/visible molecular absorption spectrophotometry. *J. Phys. Chem. Ref. Data* **34**, 41-56 (2005).
- 130 Oxford Instruments Superconductivity Limited: *Spectromag Product Guide* (2004).
- 131 ZEMAX Optical Design Program 8.0, Focus Software, Inc.
- 132 http://www.thorlabs.de/newgrouppage9.cfm?objectgroup_id=6973&tabname=UV%20Fused%20Silica (retrieved on 02/11/2016).
- 133 Stone, J. & Walrafen, G. E. Overtone Vibrations of OH Groups in Fused-Silica Optical Fibers. *J. Chem. Phys.* **76**, 1712-1722 (1982).
- 134 Elliott, C. R. & News, G. R. Near Infrared Absorption Spectra of Silica - OH Overtones. *Appl. Spectrosc.* **25**, 378-379 (1971).
- 135 Curcio, J. A. & Petty, C. C. The near Infrared Absorption Spectrum of Liquid Water. *J. Opt. Soc. Am.* **41**, 302-304 (1951).
- 136 Tuzimura, K. *et al.* Critical Study of Measurement and Calibration of Circular-Dichroism. *Anal. Biochem.* **81**, 167-174 (1977).
- 137 Konno, T., Meguro, H., Murakami, T. & Hatano, M. A Critical-Study on Circular-Dichroism Measurement in Longer Side of Visible Region. *Chem. Lett.*, 953-956 (1981).
- 138 Osborne, G. A., Cheng, J. C. & Stephens, P. J. Near-Infrared Circular-Dichroism and Magnetic Circular-Dichroism Instrument. *Rev. Sci. Instrum.* **44**, 10-15 (1973).

- 139 Schatz, P. N., McCaffery, A. J., Suëtaka, W., Henning, G. N. & Ritchie, A. B. Faraday Effect of Charge-Transfer Transitions in $\text{Fe}(\text{CN})_6^{3-}$, MnO_4^{4-} , and CrO_4^{2-} . *J. Chem. Phys.* **45**, 722-734 (1966).
- 140 Kobayashi, H., Shimizu, M. & Kaizu, Y. Magnetic Circular Dichroism of $\text{Fe}(\text{CN})_6^{3-}$. *Bull. Chem. Soc. Jpn.* **43**, 2321-2325 (1970).
- 141 Gale, R. & J., M. A. Evidence for C Terms in Magnetic Circular-Dichroism of $\text{Fe}(\text{CN})_6^{3-}$. *J. Chem. Soc., Chem. Commun.*, 832-833 (1972).
- 142 Upton, A. H. P. & Williamson, B. E. Magnetic Circular-Dichroism and Absorption-Spectra of Hexacyanoferrate(III) in a Poly(Vinyl Alcohol) Film. *J. Phys. Chem.* **98**, 71-76 (1994).
- 143 Mack, J., Stillman, M. J. & Kobayashi, N. Application of MCD spectroscopy to porphyrinoids. *Coord. Chem. Rev.* **251**, 429-453 (2007).
- 144 Muranaka, A. *et al.* Definitive assignments of the visible-near-IR bands of porphyrin-naphthalocyanine rare-earth sandwich double- and triple-decker compounds by magnetic circular dichroism spectroscopy. *Inorg. Chem.* **44**, 3818-3826 (2005).
- 145 Kobayashi, N. & Nakai, K. Applications of magnetic circular dichroism spectroscopy to porphyrins and phthalocyanines. *Chem. Commun.*, 4077-4092 (2007).
- 146 Waters, M. *Synthesis, Characterisation and Magnetic Studies of Substituted Lanthanide (Bis) Phthalocyanine Single Molecule Magnets* PhD thesis, University of Nottingham, (2013).
- 147 Gonidec, M., Davies, E. S., McMaster, J., Amabilino, D. B. & Veciana, J. Probing the Magnetic Properties of Three Interconvertible Redox States of a Single-Molecule Magnet with Magnetic Circular Dichroism Spectroscopy. *J. Am. Chem. Soc.* **132**, 1756-1757 (2010).
- 148 Fischer, J. E. *Synthesis and Investigation of Molecular Rare-Earth Carbonates* Diploma thesis, University of Stuttgart, (2012).
- 149 Rechkemmer, Y. *et al.* Comprehensive Spectroscopic Determination of the Crystal Field Splitting in an Erbium Single-Ion Magnet. *J. Am. Chem. Soc.* **137**, 13114-13120 (2015).
- 150 Fujita, J., Martell, A. E. & Nakamoto, K. Infrared Spectra of Metal Chelate Compounds .VIII. Infrared Spectra of Co(III) Carbonato Complexes. *J. Chem. Phys.* **36**, 339-345 (1962).
- 151 Kutlu, I. & Meyer, G. Basic carbonates of dysprosium: $\text{Dy}_2\text{O}_2(\text{CO}_3)$ and $\text{Dy}(\text{OH})(\text{CO}_3)$. *Z. Anorg. Allg. Chem.* **625**, 402-406 (1999).

- 152 Kutlu, I. *et al.* Potassium lanthanoid carbonates, $\text{KM}(\text{CO}_3)_2$ ($\text{M} = \text{Nd, Gd, Dy, Ho, Yb}$). *Z. Anorg. Allg. Chem.* **623**, 1753-1758 (1997).
- 153 Michiba, K., Tahara, T., Nakai, I., Miyawaki, R. & Matsubara, S. Crystal structure of hexagonal $\text{RE}(\text{CO}_3)\text{OH}$. *Z. Kristallogr.* **226**, 518-530 (2011).
- 154 Tahara, T., Nakai, I., Miyawaki, R. & Matsubara, S. Crystal chemistry of $\text{RE}(\text{CO}_3)\text{OH}$. *Z. Kristallogr.* **222**, 326-334 (2007).
- 155 Jiang, S. D., Wang, B. W., Sun, H. L., Wang, Z. M. & Gao, S. An Organometallic Single-Ion Magnet. *J. Am. Chem. Soc.* **133**, 4730-4733 (2011).
- 156 Hernández, J. M. *et al.* Field tuning of thermally activated magnetic quantum tunnelling in Mn_{12} -Ac molecules. *Europhys. Lett.* **35**, 301-306 (1996).
- 157 Guo, Y. N., Xu, G. F., Guo, Y. & Tang, J. K. Relaxation dynamics of dysprosium(III) single molecule magnets. *Dalton Trans.* **40**, 12941-12941 (2011).
- 158 Lin, P. H. *et al.* An unsymmetrical coordination environment leading to two slow relaxation modes in a Dy_2 single-molecule magnet. *Chem. Commun.* **47**, 10993-10995 (2011).
- 159 Blagg, R. J. *et al.* Magnetic relaxation pathways in lanthanide single-molecule magnets. *Nat. Chem.* **5**, 673-678 (2013).
- 160 Das, C. *et al.* Origin of SMM behaviour in an asymmetric Er(III) Schiff base complex: a combined experimental and theoretical study. *Chem. Commun.* **51**, 6137-6140 (2015).
- 161 Liu, C. M., Zhang, D. Q. & Zhu, D. B. A single-molecule magnet featuring a parallelogram $[\text{Dy}_4(\text{OCH}_2)_4]$ core and two magnetic relaxation processes. *Dalton Trans.* **42**, 14813-14818 (2013).
- 162 Martin-Ramos, P. *et al.* Single-Ion Magnetism in a Luminescent Er^{3+} beta-Diketonato Complex with Multiple Relaxation Mechanisms. *Eur. J. Inorg. Chem.* **2014**, 511-517 (2014).
- 163 Rinehart, J. D., Meihaus, K. R. & Long, J. R. Observation of a Secondary Slow Relaxation Process for the Field-Induced Single-Molecule Magnet $\text{U}(\text{H}_2\text{BPz}_2)_3$. *J. Am. Chem. Soc.* **132**, 7572-7573 (2010).
- 164 Car, P. E. *et al.* Giant field dependence of the low temperature relaxation of the magnetization in a dysprosium(III)-DOTA complex. *Chem. Commun.* **47**, 3751-3753 (2011).

- 165 Habib, F. *et al.* The Use of Magnetic Dilution To Elucidate the Slow Magnetic Relaxation Effects of a Dy₂ Single-Molecule Magnet. *J. Am. Chem. Soc.* **133**, 8830-8833 (2011).
- 166 Ishikawa, N., Sugita, M. & Wernsdorfer, W. Nuclear spin driven quantum tunneling of magnetization in a new lanthanide single-molecule magnet: Bis(phthalocyaninato)holmium anion. *J. Am. Chem. Soc.* **127**, 3650-3651 (2005).
- 167 Rechkemmer, Y. *et al.* A four-coordinate cobalt(II) single-ion magnet with coercivity and a very high energy barrier. *Nat. Commun.* **7** (2016).
- 168 Comby, S. & Bünzli, J.-C. G. in *Handbook on the Physics and Chemistry of Rare Earths* Vol. 37 (eds K. A. Gschneider, J.-C. G. Bünzli, & V. K. Pecharsky) (Elsevier, Amsterdam, 2007).
- 169 de Bettencourt-Dias, A. in *Luminescence of Lanthanide Ions in Coordination Compounds and Nanomaterials* (ed A. de Bettencourt-Dias) (John Wiley and Sons, Ltd, Chichester, 2014).
- 170 Flanagan, B. M., Bernhardt, P. V., Krausz, E. R., Luthi, S. R. & Riley, M. J. Ligand-field analysis of an Er(III) complex with a heptadentate tripodal N₄O₃ ligand. *Inorg. Chem.* **40**, 5401-5407 (2001).
- 171 Bünzli, J. C. G. Lanthanide Luminescence for Biomedical Analyses and Imaging. *Chem. Rev.* **110**, 2729-2755 (2010).
- 172 Kang, J. G., Kim, T. J., Park, K. S. & Kang, S. K. Structural and optical properties of Er(III) complex with ODA and phen (ODA = oxydiacetate, phen=1,10-phenanthroline). *Bull. Kor. Chem. Soc.* **25**, 373-376 (2004).
- 173 Martin-Ramos, P. *et al.* Novel erbium(III) complexes with 2,6-dimethyl-3,5-heptanedione and different N,N-donor ligands for ormosil and PMMA matrices doping. *J. Mater. Chem. C* **1**, 5701-5710 (2013).
- 174 Martin-Ramos, P. *et al.* Slow magnetic relaxation and photoluminescent properties of a highly coordinated erbium(III) complex with dibenzoylmethane and 2,2'-bipyridine. *New J. Chem.* **39**, 1703-1713 (2015).
- 175 Reid, M., F. *f-shell empirical programs* (University of Canterbury, Christchurch, New Zealand, 1984).
- 176 Horvath, S. & Reid, M. F. *pycf* (University of Canterbury, Christchurch, New Zealand, 2015).

- 177 Rudowicz, C. & Bramley, R. On Standardization of the Spin Hamiltonian and the Ligand-Field Hamiltonian for Orthorhombic Symmetry. *J. Chem. Phys.* **83**, 5192-5197 (1985).
- 178 Rudowicz, C., Chua, M. & Reid, M. F. On the standardization of crystal-field parameters and the multiple correlated fitting technique: Applications to rare-earth compounds. *Physica B* **291**, 327-338 (2000).
- 179 Burdick, G. W., Gruber, J. B., Nash, K. L., Chandra, S. & Sardar, D. K. Analyses of $4f^{11}$ Energy Levels and Transition Intensities Between Stark Levels of Er^{3+} in $\text{Y}_3\text{Al}_5\text{O}_{12}$. *Spectrosc. Lett.* **43**, 406-422 (2010).
- 180 Heisenberg, W. Über den anschaulichen Inhalt der quantentheoretischen Kinematik und Mechanik. *Z. Phys.* **43**, 172-198 (1927).
- 181 Breitgoff, F. D. *Bistable molecules? Magnetic and Spectroscopic Studies on Iron and Cobalt Complexes* MSc thesis, University of Stuttgart, (2015).
- 182 Chen, L. *et al.* Slow magnetic relaxation in mononuclear seven-coordinate cobalt(II) complexes with easy plane anisotropy. *Dalton Trans.* **44**, 11482-11490 (2015).
- 183 Colacio, E. *et al.* Slow Magnetic Relaxation in a $\text{Co}^{\text{II}}\text{-Y}^{\text{III}}$ Single-Ion Magnet with Positive Axial Zero-Field Splitting. *Angew. Chem. Int. Ed.* **52**, 9130-9134 (2013).
- 184 Rajnák, C., Titiš, J., Fuhr, O., Ruben, M. & Boča, R. Single-Molecule Magnetism in a Pentacoordinate Cobalt(II) Complex Supported by an Antenna Ligand. *Inorg. Chem.* **53**, 8200-8202 (2014).
- 185 Huang, X. C., Zhou, C., Shao, D. & Wang, X. Y. Field-Induced Slow Magnetic Relaxation in Cobalt(II) Compounds with Pentagonal Bipyramid Geometry. *Inorg. Chem.* **53**, 12671-12673 (2014).
- 186 Herchel, R., Váhovská, L., Potočňák, I. & Trávníček, Z. Slow Magnetic Relaxation in Octahedral Cobalt(II) Field-Induced Single-Ion Magnet with Positive Axial and Large Rhombic Anisotropy. *Inorg. Chem.* **53**, 5896-5898 (2014).
- 187 Banci, L., Bencini, A., Benelli, C., Gatteschi, D. & Zanchini, C. in *Structures versus Special Properties* 37-86 (Springer Berlin Heidelberg, Berlin, Heidelberg, 1982).
- 188 Ruamps, R. *et al.* Ising-type magnetic anisotropy and single molecule magnet behaviour in mononuclear trigonal bipyramidal Co(II) complexes. *Chem. Sci.* **5**, 3418-3424 (2014).
- 189 Peremykin, I. *Auf Chinonliganden basierte schaltbare molekulare Magneten* teacher thesis, University of Stuttgart, (2013).

- 190 Min, K. S., DiPasquale, A. G., Golen, J. A., Rheingold, A. L. & Miller, J. S. Synthesis, structure, and magnetic properties of valence ambiguous dinuclear antiferromagnetically coupled cobalt and ferromagnetically coupled iron complexes containing the chloranilate(2-) and the significantly stronger coupling chloranilate(3-) radical trianion. *J. Am. Chem. Soc.* **129**, 2360-2368 (2007).
- 191 Tao, J., Maruyama, H. & Sato, O. Valence tautomeric transitions with thermal hysteresis around room temperature and photoinduced effects observed in a cobalt-tetraoxolene complex. *J. Am. Chem. Soc.* **128**, 1790-1791 (2006).
- 192 Carbonera, C., Dei, A., Letard, J. F., Sangregorio, C. & Sorace, L. Thermally and light-induced valence tautomeric transition in a dinuclear cobalt-tetraoxolene complex. *Angew. Chem. Int. Ed.* **43**, 3136-3138 (2004).
- 193 Min, K. S., DiPasquale, A. G., Rheingold, A. L., White, H. S. & Miller, J. S. Observation of Redox-Induced Electron Transfer and Spin Crossover for Dinuclear Cobalt and Iron Complexes with the 2,5-Di-tert-butyl-3,6-dihydroxy-1,4-benzoquinonate Bridging Ligand. *J. Am. Chem. Soc.* **131**, 6229-6236 (2009).
- 194 Papánková, B. *et al.* Magneto-structural relationships for a mononuclear Co(II) complex with large zero-field splitting. *Inorg. Chim. Acta* **363**, 147-156 (2010).
- 195 Bencini, A. & Gatteschi, D. *Electron paramagnetic resonance of exchange coupled systems* (Springer, Berlin; Heidelberg 1990).
- 196 Boer, A. B. *et al.* A Spectroscopic Investigation of Magnetic Exchange Between Highly Anisotropic Spin Centers. *Angew. Chem. Int. Ed.* **50**, 4007-4011 (2011).
- 197 Gaspar, A. B., Seredyuk, M. & Gütllich, P. Spin crossover in iron(II) complexes: Recent advances. *J. Mol. Struct.* **924**, 9-19 (2009).
- 198 Sheldrick, G. M. *SHELX-97, Program for Crystal Structure Refinement* (Göttingen, Germany, 1997).
- 199 Macrae, C. F. *et al.* Mercury: visualization and analysis of crystal structures. *J. Appl. Cryst.* **39**, 453-457 (2006).
- 200 Stoll, S. & Schweiger, A. EasySpin, a comprehensive software package for spectral simulation and analysis in EPR. *J. Magn. Reson.* **178**, 42-55 (2006).
- 201 Schilder, H. & Lueken, H. Computerized magnetic studies on d, f, d-d, f-f, and d-S, f-S systems under varying ligand and magnetic fields. *J. Magn. Magn. Mater.* **281**, 17-26 (2004).

8 Appendix

8.1 Appendix A: Background

8.1.1 Energy Level Calculations for Pr(III)

Table A 1: Matrix elements for the Coulomb repulsion in Pr(III). F^2 , F^4 and F^6 are adjustable free-ion parameters.

<i>LS</i> term	Energy
^3H	$-0.1111 F^2 - 0.0468 F^4 - 0.0018 F^6$
^3F	$-0.0444 F^2 - 0.0303 F^4 - 0.0388 F^6$
^3P	$+0.2000 F^2 + 0.0303 F^4 - 0.1748 F^6$
^1G	$-0.1333 F^2 + 0.0891 F^4 + 0.0106 F^6$
^1D	$+0.0844 F^2 - 0.0909 F^4 + 0.0971 F^6$
^1I	$+0.1111 F^2 + 0.0083 F^4 + 0.0001 F^6$
^1S	$+0.2667 F^2 + 0.1818 F^4 + 0.2331 F^6$

Table A 2: Energy matrices for the combined Coulomb and spin-orbit interactions in Pr(III). $E(^{2S+1}L)$ refers to the energies given in Table A 1.

J	Energy matrix
0	$\begin{pmatrix} E(^3P) - \zeta & -2\sqrt{3}\zeta \\ -2\sqrt{3}\zeta & E(^1S) \end{pmatrix}$
1	$\left(E(^3P) - \frac{1}{2}\zeta \right)$
2	$\begin{pmatrix} E(^3P) + \frac{1}{2}\zeta & \frac{3}{2}\sqrt{2}\zeta & 0 \\ \frac{3}{2}\sqrt{2}\zeta & E(^1D) & -\sqrt{6}\zeta \\ 0 & -\sqrt{6}\zeta & E(^3F) - 2\zeta \end{pmatrix}$
3	$\left(E(^3F) - \frac{1}{2}\zeta \right)$
4	$\begin{pmatrix} E(^3F) + \frac{3}{2}\zeta & \frac{\sqrt{33}}{3}\zeta & 0 \\ \frac{\sqrt{33}}{3}\zeta & E(^1G) & -\frac{\sqrt{30}}{3}\zeta \\ 0 & -\frac{\sqrt{30}}{3}\zeta & E(^3H) - 3\zeta \end{pmatrix}$
5	$\left(E(^3H) - \frac{1}{2}\zeta \right)$
6	$\begin{pmatrix} E(^3H) + \frac{5}{2}\zeta & \frac{\sqrt{6}}{2}\zeta \\ \frac{\sqrt{6}}{2}\zeta & E(^1I) \end{pmatrix}$

Table A 3: Comparison of the eigenvalues and eigenvectors obtained for Pr(III) applying the Russel-Saunders coupling or the intermediate coupling scheme. Only the electrostatic and the spin-orbit perturbations were considered. The free-ion parameters were set to $F^2 = 68995 \text{ cm}^{-1}$, $F^4 = 56119 \text{ cm}^{-1}$, $F^6 = 38864 \text{ cm}^{-1}$ and $\zeta_{4f} = 737 \text{ cm}^{-1}$. The ground state energies were set to zero.

Russell-Saunders coupling		Intermediate coupling	
Eigenvector	Energy / cm^{-1}	Eigenvector	Energy / cm^{-1}
$ ^3H_4\rangle$	0	$-0.0282 ^3F_4\rangle + 0.1523 ^1G_4\rangle + 0.9879 ^3H_4\rangle$	0
$ ^3H_5\rangle$	1843	$ ^3H_5\rangle$	2044
$ ^3H_6\rangle$	4054	$0.9985 ^3H_6\rangle - 0.0540 ^1I_6\rangle$	4206
$ ^3F_2\rangle$	5027	$0.0132 ^3P_2\rangle - 0.1444 ^1D_2\rangle - 0.9894 ^3F_2\rangle$	4761
$ ^3F_3\rangle$	5929	$ ^3F_3\rangle$	6129
$ ^3F_4\rangle$	7403	$-0.8634 ^3F_4\rangle + 0.4943 ^1G_4\rangle - 0.1009 ^3H_4\rangle$	6796
$ ^1G_4\rangle$	8785	$0.5037 ^3F_4\rangle + 0.8558 ^1G_4\rangle - 0.1175 ^3H_4\rangle$	10001
$ ^1D_2\rangle$	17073	$-0.3059 ^3P_2\rangle + 0.9415 ^1D_2\rangle - 0.1415 ^3F_2\rangle$	17037
$ ^3P_0\rangle$	20542	$0.9964 ^3P_0\rangle + 0.0850 ^1S_0\rangle$	20525
$ ^1I_6\rangle$	20709	$0.0540 ^3H_6\rangle + 0.9985 ^1I_6\rangle$	20959
$ ^3P_1\rangle$	20911	$ ^3P_1\rangle$	21111
$ ^3P_2\rangle$	21648	$0.9520 ^3P_2\rangle + 0.3046 ^1D_2\rangle - 0.0317 ^3F_2\rangle$	22348
$ ^1S_0\rangle$	50235	$-0.0850 ^3P_0\rangle + 0.9964 ^1S_0\rangle$	50653

8.1.2 Free Ion Terms of Co(II)

Table A 4: Energies of the LS states of free Co(II) ions dependent on the Racah parameters B and C . The energy of the ground term was set to zero. The 2D terms are not included because state-mixing leads to off-diagonal matrix elements.^{75,78}

LS term	Term energy
4F	0
4P	$15B$
2G	$4B + 3C$
2H	$9B + 3C$
2P	$9B + 3C$
2F	$24B + 3C$

8.1.3 Lines Equations for Octahedral Co(II) Compounds

The temperature dependent g value $g(T)$ appearing in section 2.3.1, equation (37) can be evaluated by solving the equations below:^{81,82}

$$[g(T)]^2 = G/P \quad (\text{A1})$$

$$G = G_1 + G_2 E_1 + G_3 E_2 \quad (\text{A2})$$

$$P = 1 + 2E_1 + 3E_2 \quad (\text{A3})$$

$$G_1 = \frac{1}{9}(10 + 3k_r)(10 + 3k_r - 15b) - \frac{40}{81} \left(\frac{k_B T}{k_r \lambda_{SO}} \right) (4 + 3k_r)(4 + 3k_r - 6a) \quad (\text{A4})$$

$$G_2 = \frac{2}{45}(22 - 6k_r)(22 - 6k_r - 33a) + \frac{352}{2025} \left(\frac{k_B T}{k_r \lambda_{SO}} \right) (4 + 3k_r)(4 + 3k_r - 6a) \quad (\text{A5})$$

$$G_3 = \frac{7}{5}(6 - 3k_r)(6 - 3k_r - 9a) + \frac{8}{25} \left(\frac{k_B T}{k_r \lambda_{SO}} \right) (4 + 3k_r)(4 + 3k_r - 6a) \quad (\text{A6})$$

$$E_1 = e^{\frac{9k_r\lambda_{SO}}{k_B T}} \quad (\text{A7})$$

$$E_2 = e^{\frac{6k_r\lambda_{SO}}{k_B T}} \quad (\text{A8})$$

$$a = \frac{1}{3}[(m-1)J + mz'J'](\langle\hat{S}_z\rangle/\mu_B H_0) \quad (\text{A9})$$

$$b = \frac{1}{3}mz'J'(\langle\hat{S}_z\rangle/\mu_B H_0) \quad (\text{A10})$$

$$(\langle\hat{S}_z\rangle/\mu_B H_0) = f(T)g(T)F_m(T)/(mk_B T) \quad (\text{A11})$$

$$f(T)g(T) = Q/P \quad (\text{A12})$$

$$Q = Q_1 + Q_2 E_1 + Q_3 E_2 \quad (\text{A13})$$

$$Q_1 = \frac{5}{9}(10 + 3k_r - 15b) - \frac{80}{81}\left(\frac{k_B T}{k_r\lambda_{SO}}\right)(4 + 3k_r - 6a) \quad (\text{A14})$$

$$Q_2 = \frac{44}{90}(22 - 6k_r - 33a) + \frac{704}{2025}\left(\frac{k_B T}{k_r\lambda_{SO}}\right)(4 + 3k_r - 6a) \quad (\text{A15})$$

$$Q_3 = \frac{21}{5}(6 - 3k_r - 9a) + \frac{16}{25}\left(\frac{k_B T}{k_r\lambda_{SO}}\right)(4 + 3k_r - 6a) \quad (\text{A16})$$

where $z'J'$ is the inter-cluster interaction parameter and $\langle\hat{S}_z\rangle$ is the ensemble average of the z component of the real spin. The remaining parameters have the meanings indicated in the main text.

8.1.4 Coefficients for the Empirical Function $G(T)$ for Co(II) Compounds

Table A 5: Coefficients for the empirical function $G(T)$ for Co(II) ions with positive values for Δ_{ax} .⁸⁵

i	j	k	$A_{i,j,k}$	$B_{i,j,k}$	i	j	k	$A_{i,j,k}$	$B_{i,j,k}$
0	1	0	-31.4024	-36.9817	2	2	2	-0.00631052	-0.928186
1	1	0	11.4908	41.6005	0	3	2	32205.9	-16265.5
2	1	0	71.9869	35.7858	1	3	2	-335.544	170.975
0	2	0	111.573	59.8737	2	3	2	-0.487717	0.189062
1	2	0	11460.3	6119.7	0	1	3	1.02469	-0.207265
2	2	0	-11.2863	-6.03483	1	1	3	-2.50702	0.460394
0	3	0	-82967.2	-34354.1	2	1	3	0.956274	-0.175258
1	3	0	440.416	474.428	0	2	3	-0.00665916	-0.00414581
2	3	0	21.4078	13.5402	1	2	3	-324.118	-197.96
0	1	1	-33.7561	-12.3045	2	2	3	0.803836	0.620907
1	1	1	56.5288	22.6914	0	3	3	57884.3	-30611.1
2	1	1	4.54432	-2.07764	1	3	3	111.254	214.729
0	2	1	0.512707	0.0714365	2	3	3	0.0144809	0.852149
1	2	1	-170.335	-404.422	0	1	4	0.91277	0.360746
2	2	1	2.78275	4.82052	1	1	4	-0.525757	-0.263315
0	3	1	-69056.8	-37392.1	2	1	4	0.0439463	0.0444235
1	3	1	-1652.05	-986.141	0	2	4	0.00400556	0.002843
2	3	1	15.1483	6.90786	1	2	4	226.742	158.056
0	1	2	-7.51043	5.1506	2	2	4	0.0740832	0.0558193
1	1	2	19.5103	-13.7685	0	3	4	6847.9	5865.39
2	1	2	-6.42675	4.8863	1	3	4	54.8031	47.4865
0	2	2	0.328464	0.2038	2	3	4	0.135804	0.117873
1	2	2	2590.92	1937.83					

Table A 6: Coefficients for the empirical function $G(T)$ for Co(II) ions with negative values for Δ_{ax} .⁸⁵

i	j	k	$A_{i,j,k}$	$B_{i,j,k}$	i	j	k	$A_{i,j,k}$	$B_{i,j,k}$
0	1	0	-8.83931	-3.26017	2	2	2	0.909855	0.346467
1	1	0	50.8544	12.3893	0	3	2	5289.88	-5812.68
2	1	0	-58.9366	-7.26867	1	3	2	-312.294	40.1274
0	2	0	19.9218	17.315	2	3	2	17.5616	-10.8844
1	2	0	-5352.7	-721.601	0	1	3	-3.7011	0.611175
2	2	0	-9.77682	1.15632	1	1	3	9.89952	-1.63939
0	3	0	141620.0	-84735.8	2	1	3	-1.88878	0.435113
1	3	0	3194.56	291.68	0	2	3	1.18422	1.04366
2	3	0	15.1231	0.948339	1	2	3	-371.058	-333.315
0	1	1	-8.4209	3.18606	2	2	3	0.0578633	0.339444
1	1	1	51.1638	-12.8675	0	3	3	35221.5	-46048.2
2	1	1	-60.5534	7.6182	1	3	3	-444.267	-111.534
0	2	1	-20.1838	-16.7859	2	3	3	1.08479	-1.1117
1	2	1	5438.06	831.944	0	1	4	1.19231	0.480371
2	2	1	9.95306	-1.10216	1	1	4	-0.614334	-0.271946
0	3	1	142707.0	92184.0	2	1	4	0.185207	0.0680986
1	3	1	3236.8	-228.766	0	2	4	0.877155	0.622096
2	3	1	15.3423	-0.633181	1	2	4	-251.966	-178.488
0	1	2	-22.0928	14.6699	2	2	4	0.111552	0.0845378
1	1	2	49.9673	-35.1699	0	3	4	17726.2	14307.9
2	1	2	3.78754	1.97382	1	3	4	-27.8511	-15.6474
0	2	2	11.3007	8.30419	2	3	4	-0.0345936	-0.0160334
1	2	2	-3284.37	-2456.07					

8.1.5 Energy Levels of Axially Distorted Tetrahedral Co(II) Compounds

Table A 7: Energies of the $S = 3/2$ term energies in axially distorted tetrahedral Co(II) compounds relative to the tetrahedral terms as zero (exclusive of configurational interaction).⁷⁵

Term	Term energy
${}^4B_1 ({}^4F)$	$+7 Dt$
${}^4B_2 ({}^4F)$	$+7 Dt$
${}^4E ({}^4F)$	$-7/4 Dt$
${}^4A_2 ({}^4F)$	$-4 Ds + 2 Dt$
${}^4E ({}^4F)$	$+2 Ds + 3/4 Dt$
${}^4A_2 ({}^4P)$	$+2 Ds - 8 Dt$
${}^4E ({}^4P)$	$-Ds - 3 Dt$

8.2 Appendix B: MCD Design and Setup

8.2.1 Optical Layout and Spot Diagrams for the First Version of the MCD Setup

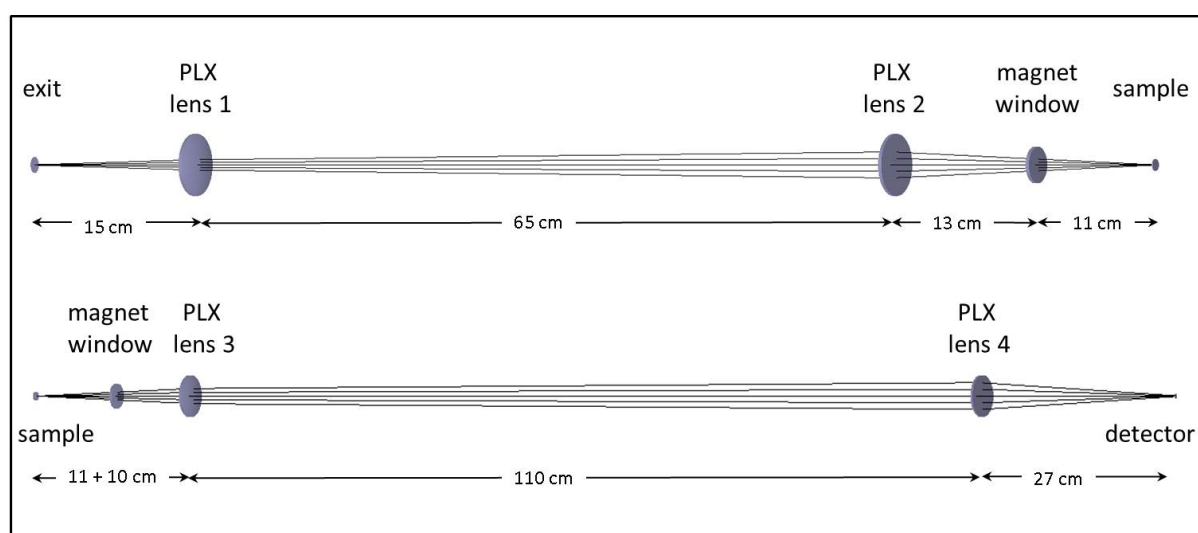


Figure A 1: Simulated optical layout for the MCD-spectrometer using four plano-convex (PLX) lenses. Top: Light path from the spectrometer exit to the sample. Bottom: Light path from the sample to the detector. For reasons of clarity, only five rays corresponding to one field point (center) and one wavelength (1000 nm) are shown.

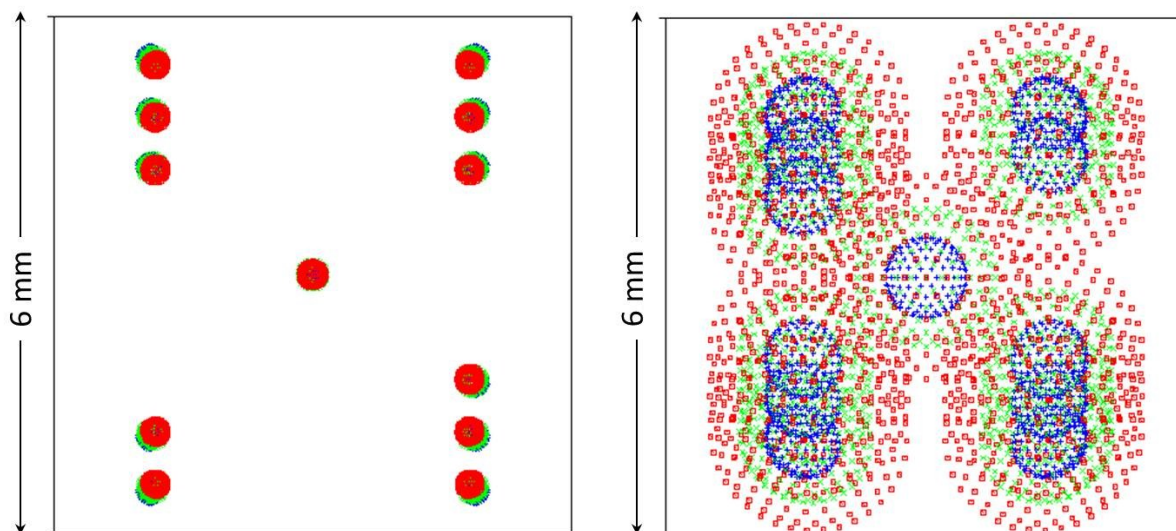


Figure A 2: Simulated full field spot diagrams corresponding to the optical layout shown in Figure A 1. Left: Sample surface. Right: Detector position. Different colors represent different wavelengths: 1000 nm (blue), 1500 nm (green) and 2000 nm (red).

8.2.2 CD Calibration Measurements on CSA

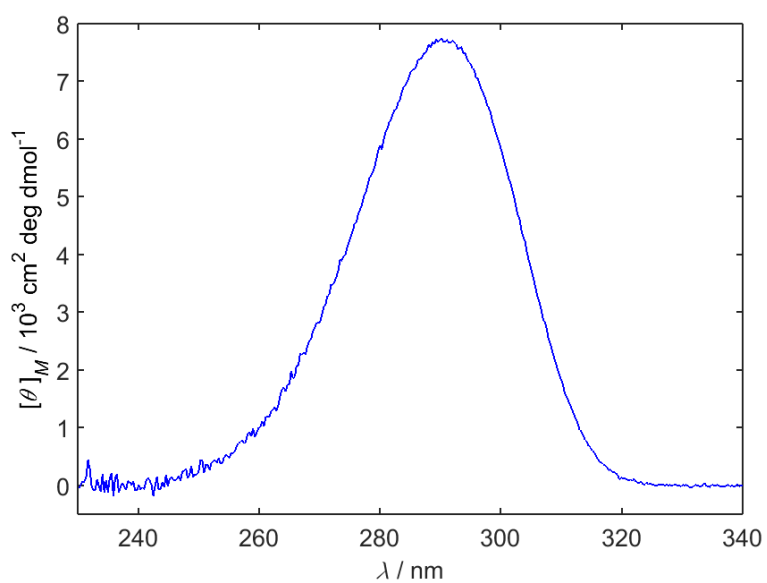


Figure A 3: Room temperature CD-spectrum of an aqueous solution of CSA (1.006 g L^{-1}) in a 1cm cuvette.

8.2.3 Electronic Absorption of [Dy(Pc)₂] in Polystyrene

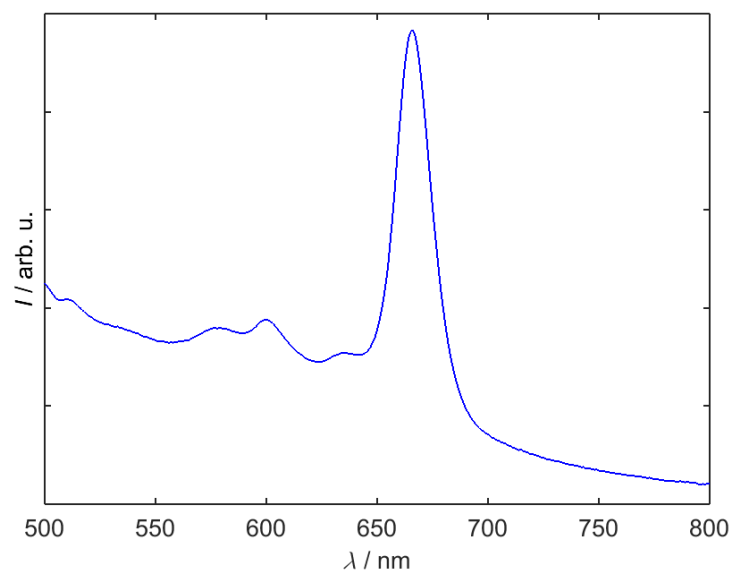


Figure A 4: Room temperature electronic absorption spectrum of a film of [Dy(Pc)₂] in polystyrene.

8.3 Appendix C: Lanthanide Tetra-Carbonates

8.3.1 Infrared Spectra

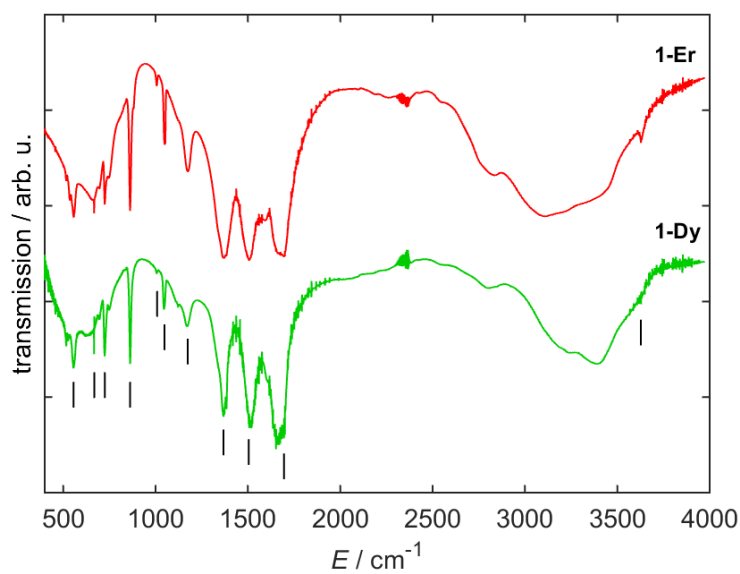


Figure A 5: Room temperature IR-spectra of pellets of **1-Er** and **1-Dy** in KBr. The measurements were performed by Julia E. Fischer.

Table A 8: Assignment of the signals observed in the infrared spectra of **1-Er** and **1-Dy**.^{27,150}

energy / cm ⁻¹		assignment
1-Er	1-Dy	
668 and 725	667 and 724	CO in-plane bending deformation
862	862	CO out-of-plane bending deformation
1008	1007	symmetric CO stretching
1368 and 1505	1368 and 1517	asymmetric CO stretching
1695	1652	NH ₂ and OH ₂ deformations
2500 - 3750	2550 - 3700	NH/OH oscillations, CO/NH ₂ /OH ₂ overtones
3628	-	OH oscillations of weaker bound H ₂ O

8.3.2 Ac Susceptibilities of Dried Samples

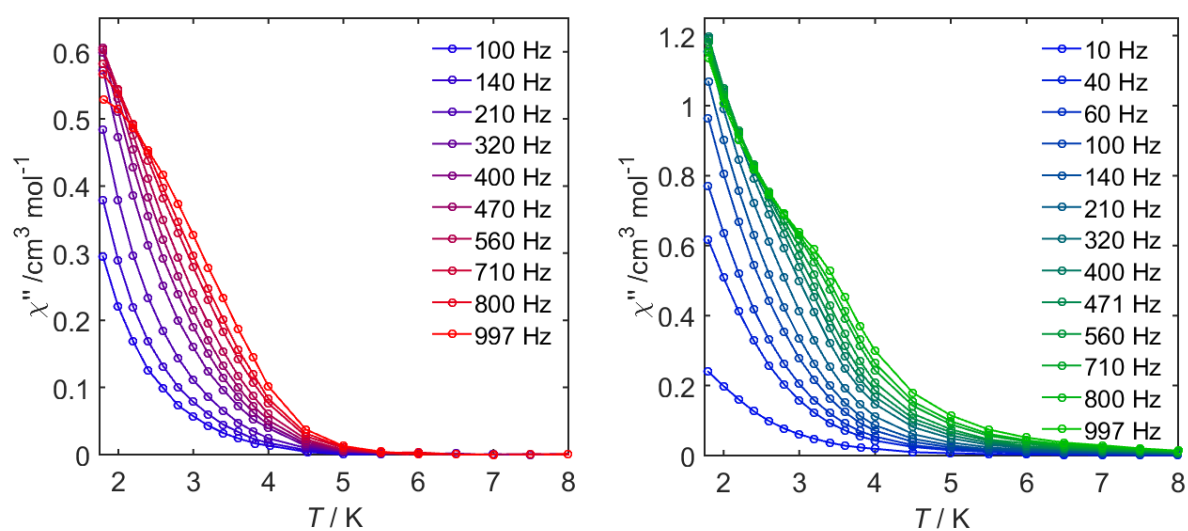


Figure A 6: Temperature dependence of the out-of-phase ac susceptibilities of **1-Er** and **1-Dy** at an applied dc field of 1000 Oe. Left: Results obtained for a finely ground sample of **1-Er** dried on filter paper. Right: Results for a vacuum-dried sample of **1-Dy**.

8.3.3 Parameters Extracted from the Argand Plots

Table A 9: Parameters obtained by least-squares fitting of the Argand plots of **1-Er** at an applied dc field of 1000 Oe and at various temperatures.

T / K	$\chi_2 / \text{cm}^3 \text{mol}^{-1}$	$\chi_1 / \text{cm}^3 \text{mol}^{-1}$	$\chi_0 / \text{cm}^3 \text{mol}^{-1}$	$\tau_{\text{fast}} / 10^{-5} \text{ s}$	α_{fast}	$\tau_{\text{slow}} / 10^{-5} \text{ s}$	α_{slow}
1.8	2.13	1.28	0.0000	12.4	0.300	2722.6	0.032
2.0	1.94	1.17	0.0000	10.6	0.274	2199.8	0.037
2.2	1.77	1.06	0.0000	9.3	0.238	1727.2	0.040
2.4	1.66	1.01	0.0000	7.5	0.219	1231.1	0.038
2.6	1.53	0.96	0.0027	6.3	0.209	776.2	0.027
2.8	1.43	0.90	0.0029	5.1	0.181	452.6	0.026
3.0	1.35	0.87	0.0035	4.2	0.200	246.9	0.011
3.2	1.28	0.80	0.0039	3.7	0.085	127.7	0.009
3.4	1.23	0.74	-	-	-	66.9	0.032
3.6	1.16	0.70	-	-	-	35.1	0.031
3.8	1.11	0.67	-	-	-	19.4	0.017
4.0	1.08	0.67	-	-	-	8.6	0.131

Table A 10: Parameters obtained by least-squares fitting of the Argand plots of **1-Dy** at an applied dc field of 1000 Oe and at various temperatures.

T / K	$\chi_{\infty} / \text{cm}^3 \text{mol}^{-1}$	$\chi_0 / \text{cm}^3 \text{mol}^{-1}$	α	$\tau / 10^{-5} \text{s}$
1.8	1.936	5.064	0.19244	6940.9
2.0	1.8849	4.526	0.14927	5890.4
2.2	1.7429	4.0714	0.11981	5217.8
2.4	1.6977	3.7441	0.097531	4524.4
2.6	1.6660	3.5030	0.079178	3834.5
2.8	1.5481	3.2206	0.066748	3090.1
3.0	1.4671	3.0016	0.057754	2310.7
3.2	1.4128	2.8349	0.052499	1590.2
3.4	1.3518	2.6781	0.04646	1026.3
3.6	1.2835	2.5275	0.040387	636.9
3.8	1.2295	2.4012	0.035953	388.0
4.0	1.1796	2.2914	0.029503	239.0
4.17	1.1346	2.1926	0.023971	161.0
4.5	1.0541	2.0351	0.018611	77.7
4.75	1.0118	1.9395	0.012725	47.2
5.0	0.96909	1.8539	0.011238	29.7
5.25	0.94127	1.7805	0.0098202	19.2
5.5	0.89477	1.7017	0.013054	12.6
5.75	0.88594	1.6383	0.013608	8.9
6.0	0.85106	1.5806	0.01039	6.2
6.25	0.86884	1.5246	0.0070702	4.6

8.3.4 Arrhenius Plots

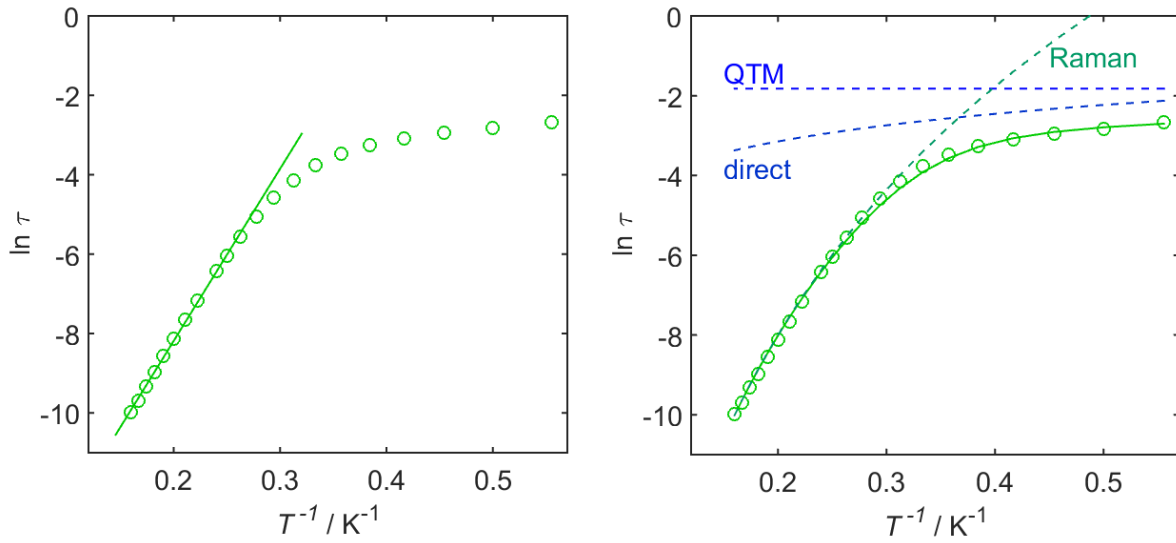


Figure A 7: Left: Linear fit to the Arrhenius plot for **1-Dy**, yielding an effective energy barrier of $U_{\text{eff}} = 30 \text{ cm}^{-1}$. Right: Simulation of the Arrhenius plot for **1-Dy** without including any Orbach process. Dashed lines illustrate the contributions of the different relaxation mechanisms while the solid line corresponds to the sum of these contributions. The simulation is based on the following set of parameters: $A_{\text{direct}} = 466 \text{ T}^{-2} \text{ K}^{-1} \text{ s}^{-1}$, $B_1 = 9.82 \text{ s}^{-1}$, $B_2 = 58.3 \text{ T}^{-2}$ and $C_{\text{Raman}} = 0.0015 \text{ K}^{-9} \text{ s}^{-1}$.

8.3.5 Dc Field Dependence of the Relaxation Rates

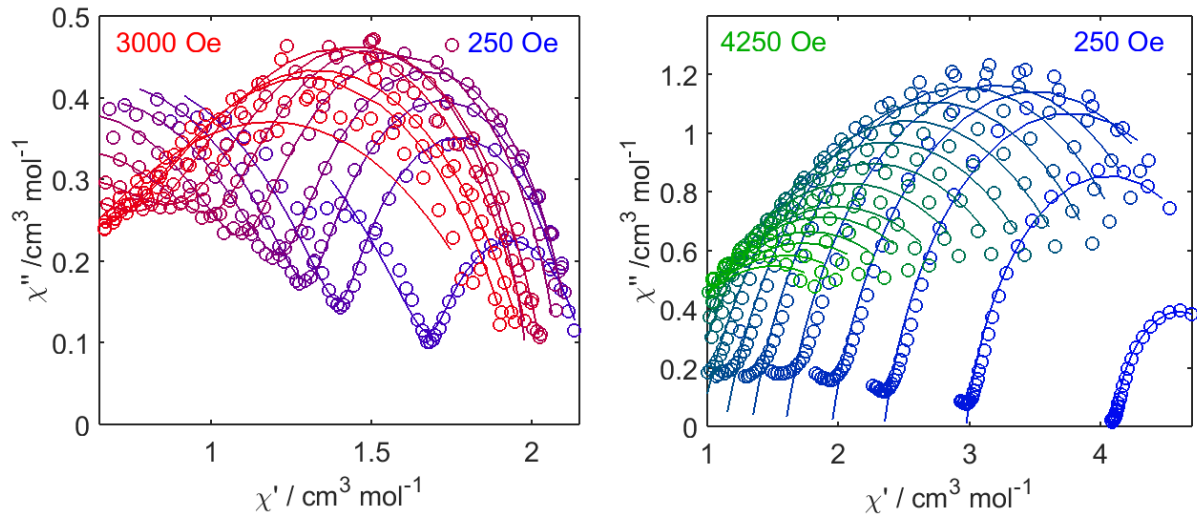


Figure A 8: Argand diagrams generated for **1-Er** (left) and **1-Dy** (right) at 1.8 K and at various dc fields. Solid lines correspond to the best fits with the parameters given in Table A 11 and Table A 12.

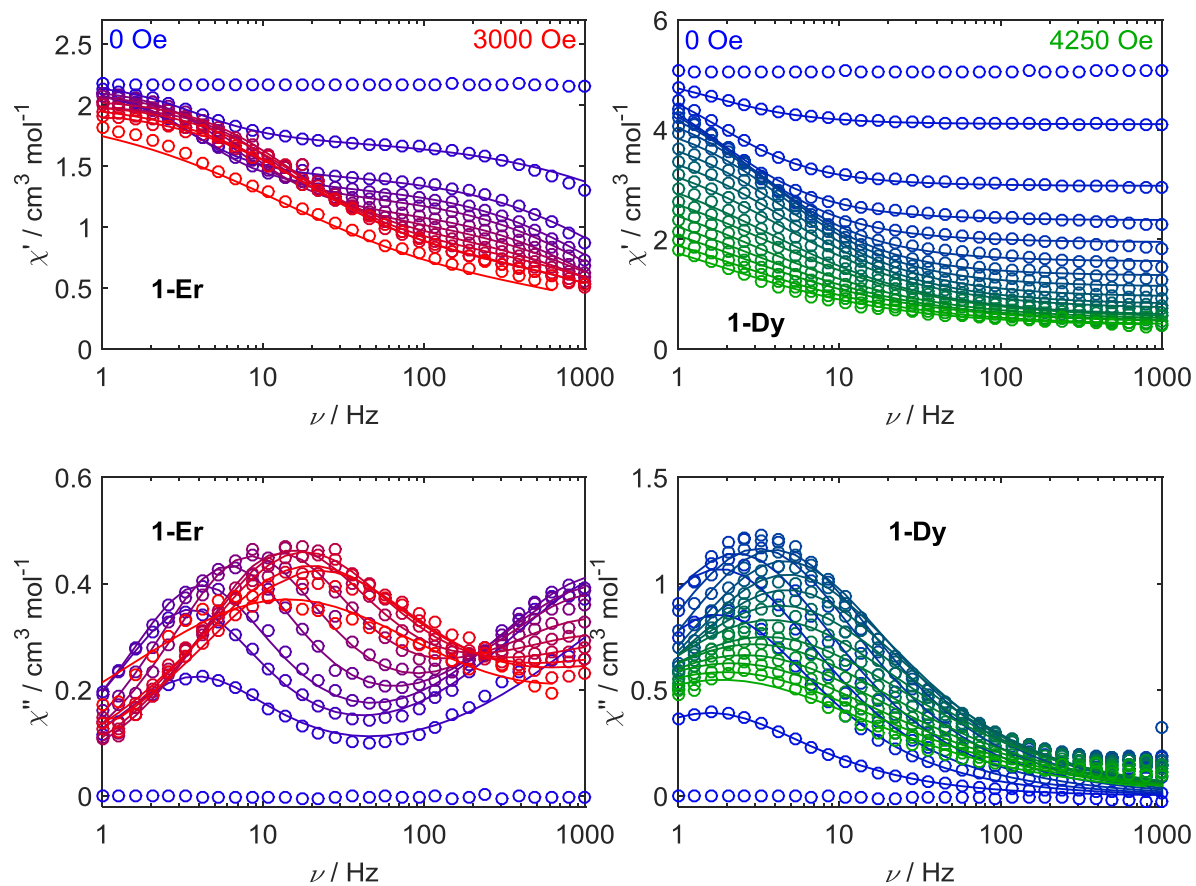


Figure A 9: Frequency dependence of the ac susceptibilities of **1-Er** (left) and **1-Dy** (right) recorded at 1.8 K and various dc fields. Solid lines correspond to simulations obtained with the parameters given in Table A 11 and Table A 12.

Table A 11: Parameters obtained by least-squares fitting of the Argand plots obtained for **1-Er** at 1.8 K and various dc fields.

H / Oe	$\chi_2 / \text{cm}^3 \text{ mol}^{-1}$	$\chi_1 / \text{cm}^3 \text{ mol}^{-1}$	$\chi_0 / \text{cm}^3 \text{ mol}^{-1}$	$\tau_{\text{fast}} / 10^{-5} \text{ s}$	α_{fast}	$\tau_{\text{slow}} / 10^{-5} \text{ s}$	α_{slow}
250	2.19	1.73	0	2.3	0.422	4371.6	0.065
500	2.14	1.45	0	8.8	0.329	4670.4	0.024
750	2.14	1.35	0	11.8	0.300	4000.0	0.030
1000	2.13	1.28	0	12.4	0.300	2722.6	0.032
1250	2.10	1.15	0	12.9	0.270	2000.0	0.070
1500	2.00	1.10	0	11.6	0.333	1337.4	0.063
1750	2.06	0.99	0	10.5	0.339	1136.5	0.146
2000	2.03	0.85	0	7.4	0.316	960.5	0.210
2250	2.03	0.72	0	6.5	0.299	882.3	0.285
2500	1.99	0.70	0	7.2	0.313	1008.5	0.289
3000	2.00	0.40	0	5.2	0.170	1190.2	0.454

Table A 12: Parameters obtained by least-squares fitting of the Argand plots obtained for **1-Dy** at 1.8 K and various dc fields.

H / Oe	$\chi_{\infty} / \text{cm}^3 \text{mol}^{-1}$	$\chi_0 / \text{cm}^3 \text{mol}^{-1}$	α	$\tau / 10^{-5} \text{s}$
250	4.10	5.11	0.158	10112
500	2.98	5.15	0.152	8966.8
750	2.35	5.18	0.177	8789.3
1000	1.95	5.05	0.192	6886.4
1250	1.60	4.80	0.200	5052.3
1500	1.34	4.57	0.209	4020.1
1750	1.14	4.34	0.230	3456.3
2000	0.95	4.14	0.263	3326.4
2250	0.81	3.94	0.293	3381.1
2500	0.73	3.79	0.324	3724.4
2750	0.60	3.58	0.355	4216.0
3000	0.56	3.42	0.386	4596.8
3250	0.53	3.24	0.381	5411.2
3500	0.49	3.07	0.395	6167.6
3750	0.48	2.98	0.410	7420.8
4000	0.43	2.78	0.415	8116.8
4250	0.42	2.58	0.404	8552.5

8.3.6 Luminescence Spectroscopy

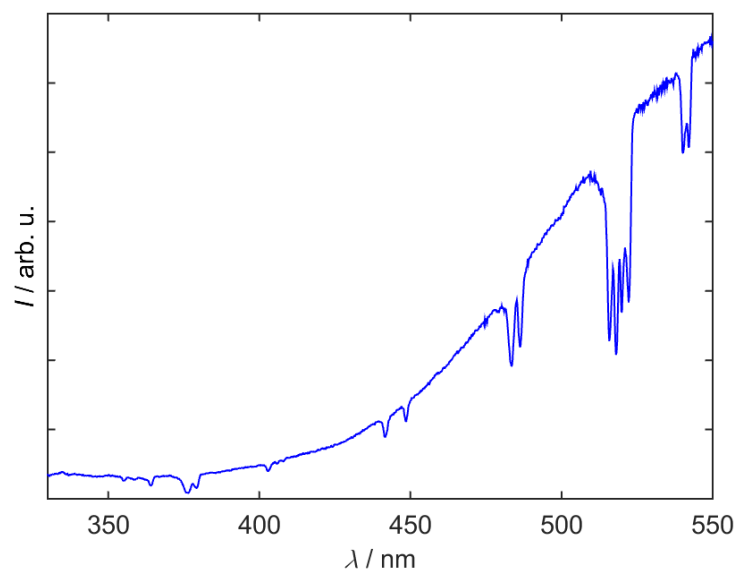


Figure A 10: Example of a luminescence spectrum of **1-Er** recorded at 20 K using an excitation wavelength of 290 nm. Instead of the expected sharp and positive luminescence peaks, a rather broad feature exhibiting negative dips is observed. The dips are located at wavelengths that correspond to the absorption maxima of **1-Er**. The spectra were recorded with the help of Maren Gysler, Dr. Stergios Piligkos and Theis Brock-Nannestad.

8.3.7 Electronic Absorption and MCD-Spectra

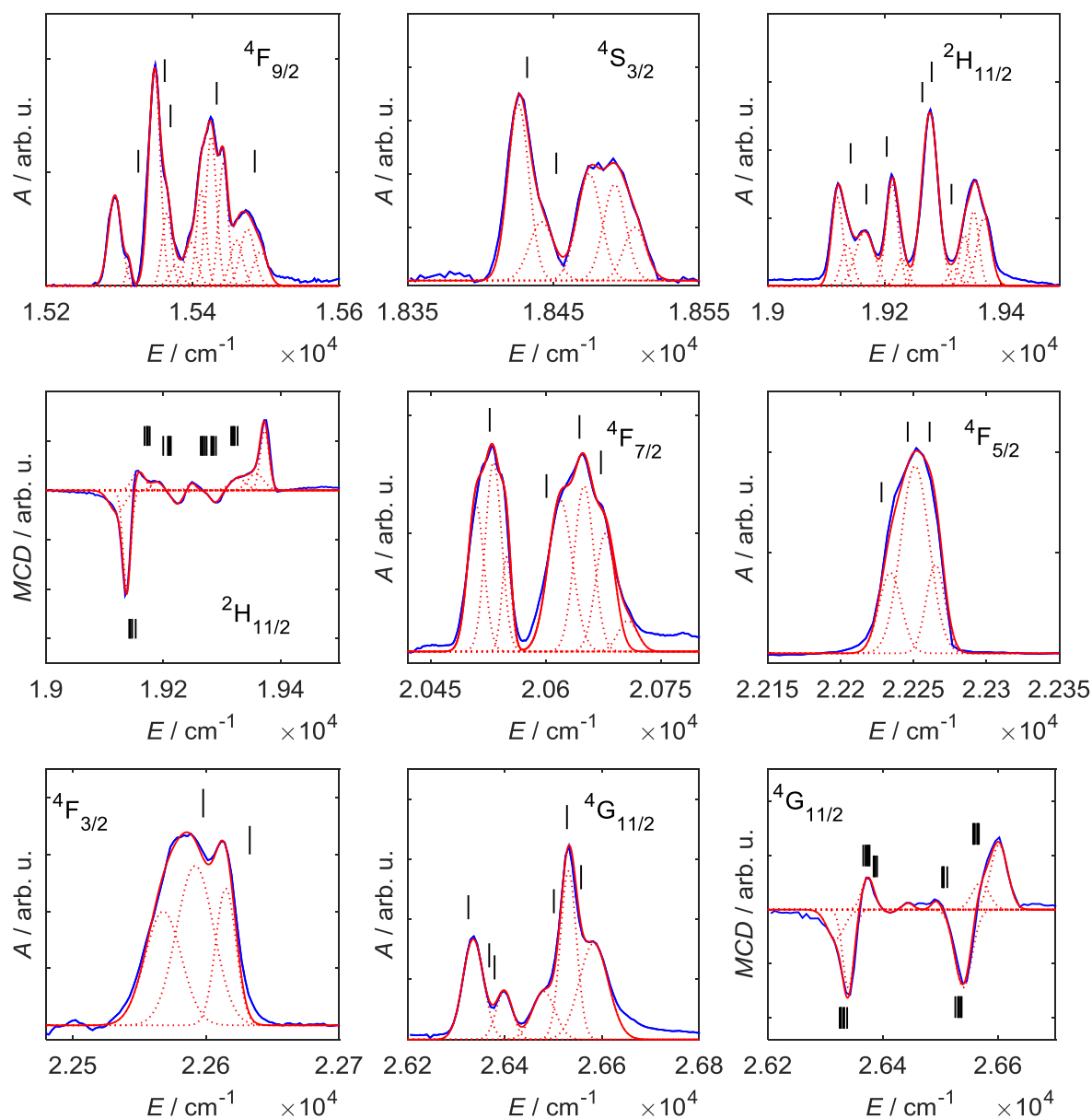


Figure A 11: Further electronic absorption and MCD-spectra of **1-Er**, recorded at 2 K and 3 T. Experimental spectra are shown in blue while red lines illustrate the deconvolution into individual Gaussians (dotted) and their sums (solid). Black bars indicate calculated transition energies based on the results of the crystal field analysis.

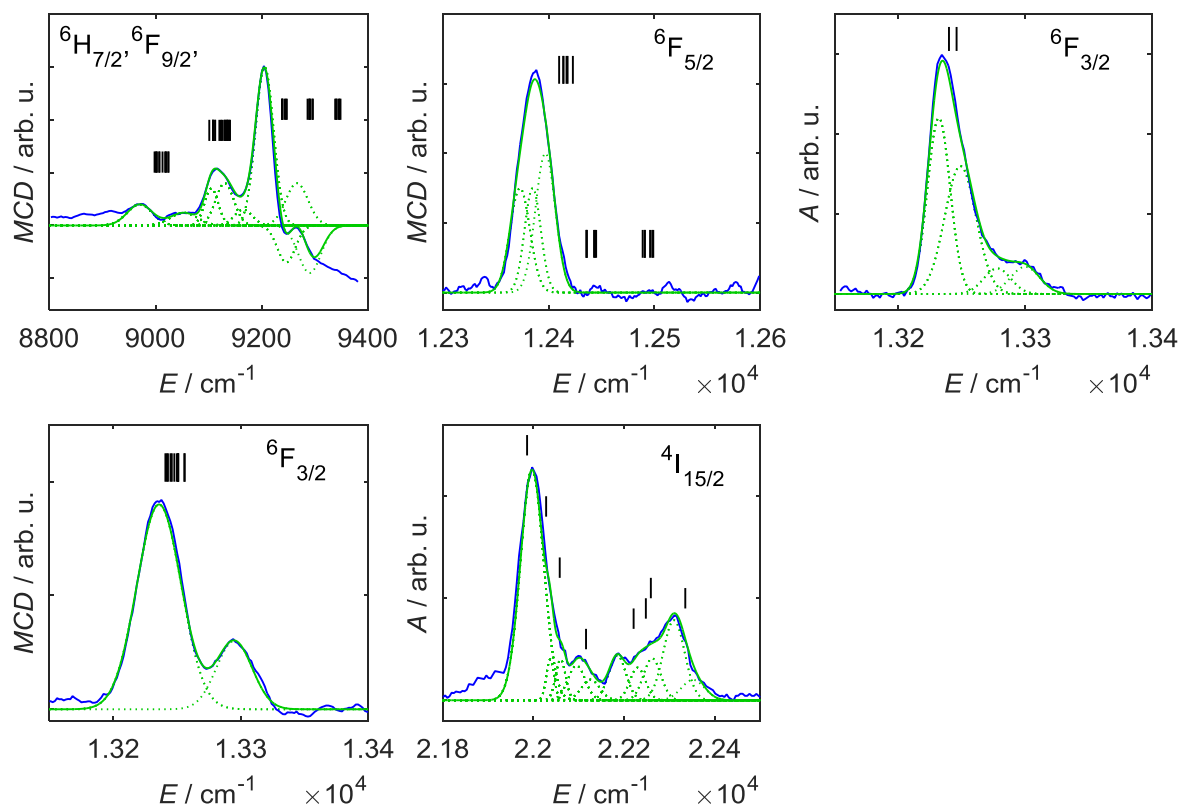


Figure A 12: Further electronic absorption and MCD-spectra of **1-Dy**, recorded at 2 K and 3 T. Experimental spectra are shown in blue while green lines illustrate the deconvolution into individual Gaussians (dotted) and their sums (solid). Black bars indicate calculated transition energies based on the results of the crystal field analysis.

8.3.8 Energy Levels

Table A 13: Experimentally observed and calculated transition energies for **1-Er**. Regarding MCD, the calculated values correspond to the orientational mean values for the transitions from the lowest Zeeman state to the respective Zeeman sublevels of the excited states.

$^{2S+1}L_J$	$E_{\text{exp}}/\text{cm}^{-1}$ (0 T)	$E_{\text{calc}}/\text{cm}^{-1}$ (0 T)	$E_{\text{exp}}/\text{cm}^{-1}$ (3 T)	$E_{\text{calc}}/\text{cm}^{-1}$ (3 T)
$^4I_{15/2}$	0	0	0	0
	52	44	-	48
	84	91	-	95
	105	112	-	116
	-	280	-	284
	-	325	-	330
	-	437	-	441
	-	462	-	467
$^4I_{13/2}$	-	6583	6580	6588
	-	6603	6608	6608
	-	6640	-	6645
	-	6689	6695	6694
	-	6744	6749	6748
	-	6775	6784	6780
	-	6818	6818	6824
	$^4I_{11/2}$	-	10249	-
-		10263	-	10268
-		10303	-	10307
-		10316	-	10321
-		10337	-	10342
-		10358	-	10364
$^4I_{9/2}$		12362	12353	-
	12482	12481	-	12489

$^{2S+1}L_J$	$E_{\text{exp}}/\text{cm}^{-1}$ (0 T)	$E_{\text{calc}}/\text{cm}^{-1}$ (0 T)	$E_{\text{exp}}/\text{cm}^{-1}$ (3 T)	$E_{\text{calc}}/\text{cm}^{-1}$ (3 T)
	12538	12510	-	12515
	12651	12656	-	12661
	12722	12719	-	12724
$^4\text{F}_{9/2}$	15294	15326	15314	15331
	15348	15362	15362	15366
	-	15370	15388	15376
	15426	15433	15439	15437
	15475	15485	15492	15490
$^4\text{S}_{3/2}$	18426	18432	-	18437
	18475	18452	-	18457
$^2\text{H}_{11/2}$	19119	19142	19138	19146
	19167	19169	19158	19174
	19213	19204	19224	19209
	-	19265	19249	19269
	19278	19281	19289	19286
	19337	19315	19328	19320
$^4\text{F}_{7/2}$	20532	20527	-	20533
	20619	20601	-	20605
	20650	20644	-	20649
	20678	20672	-	20677
$^4\text{F}_{5/2}$	22234	22228		22233
	22251	22246		22250
	22265	22261		22266
$^4\text{F}_{3/2}$	22598	22598	-	22603
	22615	22633	-	22638
$^2\text{H}_{9/2}$	24470	24466	-	24471

$^{2S+1}L_J$	$E_{\text{exp}}/\text{cm}^{-1}$ (0 T)	$E_{\text{calc}}/\text{cm}^{-1}$ (0 T)	$E_{\text{exp}}/\text{cm}^{-1}$ (3 T)	$E_{\text{calc}}/\text{cm}^{-1}$ (3 T)
	24561	24567	-	24572
	24595	24604	-	24509
	24705	24710	-	24715
	24774	24769	-	24775
$^4G_{11/2}$	26335	26325	26338	26330
	-	26368	26374	26372
	26399	26379	-	26384
	26480	26501	26493	26506
	26531	26528	26540	26532
	26583	26557	26595	26562
rms / cm^{-1}		16		18

Table A 14: Experimentally observed and calculated transition energies for **1-Dy**. Regarding MCD, the calculated values correspond to the orientational mean values for the transitions from the lowest Zeeman state to the respective Zeeman sublevels of the excited states.

$^{2S+1}L_J$	$E_{\text{exp}}/\text{cm}^{-1}$ (0 T)	$E_{\text{calc}}/\text{cm}^{-1}$ (0 T)	$E_{\text{exp}}/\text{cm}^{-1}$ (3 T)	$E_{\text{calc}}/\text{cm}^{-1}$ (3 T)
$^6\text{H}_{15/2}$	0	0	-	0
	29	29	-	35
	94	105	-	110
	144	138	-	144
	211	182	-	188
	289	302	-	307
	334	348	-	355
	416	385	-	391
$^6\text{H}_{13/2}$	3522	3520	-	3526
	3568	3556	-	3561
	3586	3573	-	3579
	3635	3617	-	3622
	3647	3632	-	3638
	3687	3677	-	3686
	3726	3714	-	3720
$^6\text{H}_{11/2}$	-	5867	5875	5872
	-	5910	5905	5915
	-	5940	5940	5946
	-	5957	5953	5964
	-	5978	5978	5984
	-	6009	6008	6015
	-			
$^6\text{H}_{11/2}, ^6\text{H}_{9/2}$	-	7587	7577	7592
	-	7647	7645	7653
	-	7693	7700	7699

$^{2S+1}L_J$	$E_{\text{exp}}/\text{cm}^{-1}$ (0 T)	$E_{\text{calc}}/\text{cm}^{-1}$ (0 T)	$E_{\text{exp}}/\text{cm}^{-1}$ (3 T)	$E_{\text{calc}}/\text{cm}^{-1}$ (3 T)
-	-	7744	7732	7749
-	-	7769	7764	7775
-	-	7814	7803	7820
-	-	7849	7840	7854
-	-	7870	7865	7877
-	-	7929	7938	7935
-	-	7960	-	7967
-	-	7998	-	8004
${}^6\text{H}_{7/2}, {}^6\text{F}_{9/2}$	-	8997	8970	9003
-	-	9014	9053	9019
-	-	9103	9105	9108
-	-	9122	9130	9128
-	-	9129	9165	9136
-	-	9236	9246	9242
-	-	9285	9290	9291
-	-	9337	-	9343
-	-	9417	-	9423
${}^6\text{H}_{5/2}$	-	10226	-	10232
-	-	10294	-	10299
-	-	10380	-	10386
${}^6\text{F}_{7/2}$	-	10996	-	11002
-	-	11043	-	11049
-	-	11101	-	11106
-	-	11114	-	11120
${}^6\text{F}_{5/2}$	12404	12411	12397	12416
	12442	12434	-	12440

$^{2S+1}L_J$	$E_{\text{exp}}/\text{cm}^{-1}$ (0 T)	$E_{\text{calc}}/\text{cm}^{-1}$ (0 T)	$E_{\text{exp}}/\text{cm}^{-1}$ (3 T)	$E_{\text{calc}}/\text{cm}^{-1}$ (3 T)
	12486	12488	-	12494
$^6F_{3/2}$	13232	13240	13236	13245
	13249	13246	-	13252
$^6F_{1/2}$	-	13782	-	13788
$^4F_{9/2}$	20904	20886	-	20892
	21023	21020	-	21025
	21086	21062	-	21068
	21138	21153	-	21159
	21217	21251	-	21257
$^4I_{15/2}$	21997	21986	-	21991
	22037	22028	-	22034
	22060	22058	-	22064
	22126	22116	-	22122
	22185	22221	-	22226
	22230	22248	-	22252
	22262	22259	-	22266
	22352	22335	-	22342
rms (all data) / cm^{-1}		18		

8.4 Appendix D: Mononuclear Cobalt Complexes

8.4.1 Parameters Extracted from the Argand Plots

Table A 15: Parameters obtained by least-squares fitting of the Argand plots for **(HNEt₃)₂2** with and without an external dc field and at various temperatures.

<i>T</i> /K	<i>H</i> _{dc} = 0 Oe				<i>H</i> _{dc} = 1000 Oe			
	$\chi_0/\text{cm}^3\text{mol}^{-1}$	$\chi_\infty/\text{cm}^3\text{mol}^{-1}$	α	$\tau/10^{-5}$ s	$\chi_0/\text{cm}^3\text{mol}^{-1}$	$\chi_\infty/\text{cm}^3\text{mol}^{-1}$	α	$\tau/10^{-5}$ s
5.0	-	-	-	-	0.575	0.141	0.000	26330.6
5.5	0.650	0.050	0.529	1635.4	0.545	0.043	0.000	17674.2
6.0	0.590	0.060	0.462	1575.3	0.531	0.039	0.000	10569.7
6.5	0.540	0.055	0.419	1292.9	0.500	0.034	0.000	6422.5
7.0	0.513	0.024	0.446	917.3	0.468	0.026	0.013	4000.7
7.5	0.463	0.055	0.331	793.3	0.439	0.020	0.021	2626.2
8.0	0.428	0.065	0.256	658.3	0.411	0.019	0.008	1819.8
8.5	0.400	0.061	0.224	524.0	0.388	0.016	0.014	1288.3
9.0	0.376	0.058	0.193	422.5	0.367	0.014	0.013	944.9
9.5	0.357	0.055	0.177	341.5	0.349	0.014	0.008	716.9
10.0	0.339	0.052	0.164	277.6	0.331	0.012	0.009	553.3
10.5	0.325	0.047	0.168	224.7	0.317	0.013	0.008	435.9
11.0	0.310	0.045	0.158	187.6	0.303	0.010	0.016	348.6
11.5	0.297	0.041	0.154	156.9	0.290	0.010	0.018	282.2
12.0	0.280	0.042	0.147	130.0	0.279	0.009	0.021	232.0
12.5	0.270	0.039	0.145	110.0	0.269	0.008	0.028	192.9
13.0	0.259	0.037	0.142	97.7	0.258	0.007	0.029	161.7
13.5	0.249	0.033	0.139	84.5	0.248	0.005	0.038	136.4
14.0	0.241	0.032	0.136	73.9	0.240	0.005	0.041	115.9
14.5	0.232	0.030	0.132	64.7	0.231	0.005	0.040	100.2
15.0	0.223	0.027	0.132	56.5	0.223	0.004	0.044	86.7
15.5	0.216	0.027	0.126	50.3	0.217	0.003	0.053	75.1
16.0	0.210	0.026	0.119	45.1	0.210	0.003	0.050	65.6

T/K	$H_{dc} = 0$ Oe				$H_{dc} = 1000$ Oe			
	$\chi_0/\text{cm}^3\text{mol}^{-1}$	$\chi_\infty/\text{cm}^3\text{mol}^{-1}$	α	$\tau/10^{-5}$ s	$\chi_0/\text{cm}^3\text{mol}^{-1}$	$\chi_\infty/\text{cm}^3\text{mol}^{-1}$	α	$\tau/10^{-5}$ s
16.5	0.205	0.025	0.119	39.8	0.203	0.003	0.051	57.7
17.0	0.199	0.025	0.113	35.5	0.198	0.003	0.054	50.7
17.5	0.193	0.025	0.109	31.9	0.192	0.003	0.055	44.6
18.0	0.188	0.025	0.108	28.6	0.188	0.003	0.058	39.3
18.5	0.182	0.024	0.101	25.6	0.182	0.003	0.060	34.5
19.0	0.178	0.022	0.104	22.5	0.177	0.003	0.058	30.5
19.5	0.173	0.023	0.104	20.0	0.173	0.004	0.057	27.2
20.0	0.169	0.021	0.107	17.6	0.169	0.002	0.066	23.3
20.5	0.165	0.017	0.111	15.1	0.165	0.002	0.070	20.3
21.0	0.161	0.015	0.112	13.0	0.162	0.000	0.076	17.2
21.5	0.158	0.012	0.115	11.1	-	-	-	-
22.0	0.154	0.004	0.124	8.9	-	-	-	-
22.5	0.152	0.003	0.138	7.2	-	-	-	-
23.0	0.149	0.001	0.143	6.1	-	-	-	-
23.5	0.144	0.001	0.090	5.2	-	-	-	-
24.0	0.142	0.000	0.090	4.8	-	-	-	-
24.5	0.138	0.001	0.075	3.8	-	-	-	-

Table A 16: Parameters obtained by least-squares fitting of the Argand plots for $(\text{NMe}_4)_2\mathbf{2}$ with and without an external dc field and at various temperatures.

T/K	$H_{\text{dc}} = 0 \text{ Oe}$				$H_{\text{dc}} = 1000 \text{ Oe}$			
	$\chi_0/\text{cm}^3\text{mol}^{-1}$	$\chi_\infty/\text{cm}^3\text{mol}^{-1}$	α	$\tau/10^{-5} \text{ s}$	$\chi_0/\text{cm}^3\text{mol}^{-1}$	$\chi_\infty/\text{cm}^3\text{mol}^{-1}$	α	$\tau/10^{-5} \text{ s}$
3.5	1.161	0.020	0.709	3526.1	0.225	0.048	0.000	17490
4.0	0.979	0.106	0.654	3263.7	0.382	0.033	0.000	23490
4.5	0.858	0.166	0.588	2851	0.575	0.045	0.000	21120
5.0	0.728	0.225	0.444	2459	0.635	0.035	0.000	14040
5.5	0.653	0.247	0.321	2000	0.610	0.034	0.000	8285
6.0	0.594	0.228	0.254	1438	0.586	0.013	0.067	4709
6.5	0.548	0.178	0.269	900.0	0.540	0.014	0.056	2933
7.0	0.510	0.158	0.246	642.8	0.502	0.012	0.053	1933
7.5	0.477	0.131	0.248	454.7	0.468	0.013	0.039	1339
8.0	0.447	0.110	0.248	329.4	0.440	0.012	0.039	952.1
8.5	0.418	0.110	0.201	281.4	0.413	0.014	0.029	704.0
9.0	0.397	0.099	0.196	223.3	0.390	0.014	0.023	532.7
9.5	0.375	0.098	0.162	192.2	0.370	0.012	0.024	412.4
10.0	0.354	0.086	0.156	155.0	0.352	0.012	0.023	323.7
10.5	0.339	0.086	0.136	134.3	0.335	0.011	0.023	259.1
11.0	0.322	0.076	0.132	110.2	0.320	0.011	0.023	211.2
11.5	0.310	0.078	0.111	97.1	0.306	0.011	0.021	174.0
12.0	0.296	0.067	0.119	80.2	0.294	0.011	0.019	144.9
12.5	0.284	0.061	0.119	67.1	0.282	0.011	0.019	121.9
13.0	0.274	0.061	0.101	60.2	0.271	0.012	0.012	104.7
13.5	0.264	0.060	0.090	53.4	0.261	0.011	0.016	88.50
14.0	0.255	0.054	0.092	45.8	0.252	0.012	0.009	77.0
14.5	0.246	0.053	0.085	40.8	0.244	0.013	0.009	66.5
15.0	0.237	0.054	0.065	37.5	0.236	0.012	0.011	57.6
15.5	0.230	0.047	0.076	32.0	0.229	0.012	0.007	50.5

T/K	$H_{dc} = 0 \text{ Oe}$				$H_{dc} = 1000 \text{ Oe}$			
	$\chi_0/\text{cm}^3\text{mol}^{-1}$	$\chi_\infty/\text{cm}^3\text{mol}^{-1}$	α	$\tau/10^{-5} \text{ s}$	$\chi_0/\text{cm}^3\text{mol}^{-1}$	$\chi_\infty/\text{cm}^3\text{mol}^{-1}$	α	$\tau/10^{-5} \text{ s}$
16.0	0.223	0.048	0.065	29.2	0.221	0.012	0.004	44.6
16.5	0.216	0.049	0.050	26.7	0.215	0.011	0.010	38.2
17.0	0.210	0.050	0.032	24.7	0.209	0.010	0.012	33.2
17.5	0.204	0.049	0.030	22.0	0.203	0.014	0.000	30.2
18.0	0.198	0.052	0.012	20.6	0.197	0.014	0.000	26.1
18.5	0.193	0.048	0.020	17.9	0.192	0.012	0.006	22.4
19.0	0.188	0.047	0.014	16.0	0.188	0.015	0.000	19.8
19.5	0.184	0.050	0.015	14.5	0.183	0.018	0.000	17.5
20.0	0.179	0.049	0.000	13.1	0.178	0.019	0.000	15.1
20.5	0.175	0.058	0.000	12.7	0.174	0.020	0.000	13.1
21.0	0.171	0.051	0.005	10.4	0.170	0.022	0.000	11.2
21.5	0.167	0.055	0.002	9.4	0.166	0.025	0.000	9.8
22.0	0.163	0.052	0.000	8.1	0.162	0.036	0.000	9.1
22.5	0.160	0.065	0.000	8.0	0.160	0.041	0.000	7.8
23.0	0.157	0.066	0.000	7.1	0.155	0.049	0.012	7.0
23.5	0.153	0.076	0.017	6.8	-	-	-	-
24.0	0.151	0.056	0.046	4.3	-	-	-	-
24.5	0.147	0.093	0.000	7.1	-	-	-	-

8.4.2 Energies of Spin-Allowed Transitions

Table A 17: Comparison between experimentally observed and calculated transition energies (D_{2d} symmetry) for $(\text{HNEt}_3)_2\mathbf{2}$ and $(\text{NMe}_4)_2\mathbf{2}$. Only the spin-allowed transitions are taken into account.

	$(\text{HNEt}_3)_2\mathbf{2}$		$(\text{NMe}_4)_2\mathbf{2}$	
	$E_{\text{exp}} / \text{cm}^{-1}$	$E_{\text{calc}} / \text{cm}^{-1}$	$E_{\text{exp}} / \text{cm}^{-1}$	$E_{\text{calc}} / \text{cm}^{-1}$
$(^4\text{B}_1(^4\text{A}_2(^4\text{F})))$	0	0	0	0
$(^4\text{B}_2(^4\text{T}_2(^4\text{F})))$	-	1300	-	1400
$(^4\text{E}(^4\text{T}_2(^4\text{F})))$	6211	5914	6671	6323
$(^4\text{E}(^4\text{T}_1(^4\text{F})))$	7236	7016	7722	7491
$(^4\text{A}_2(^4\text{T}_1(^4\text{F})))$	8217	7882	8688	8116
$(^4\text{A}_2(^4\text{T}_1(^4\text{P})))$	18083	18067	18083	18134
$(^4\text{E}(^4\text{T}_1(^4\text{P})))$	18622	18469	18450	18311

8.5 Appendix E: Cobalt Dimers

8.5.1 Diamagnetic Susceptibility of $5[\text{OTf}]_2[\text{BF}_4]_2$

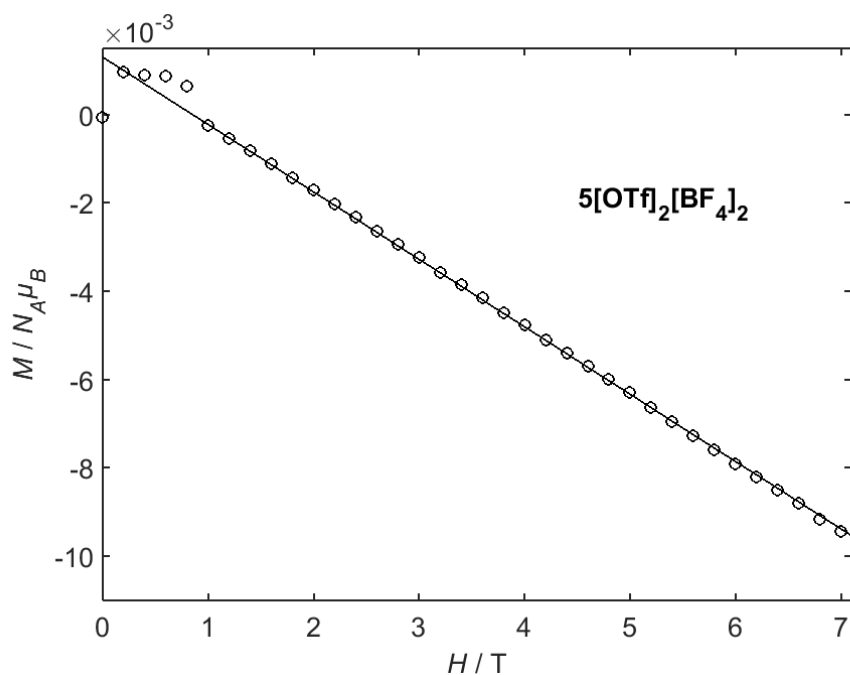


Figure A 13: Magnetic field dependence of the molar magnetization of $5[\text{OTf}]_2[\text{BF}_4]_2$, measured at 300 K. Open circles depict experimental data points while the solid line corresponds to a linear fit. The experimentally determined diamagnetic susceptibility is $\chi_{\text{dia}} = -852 \cdot 10^{-6} \text{ cm}^3 \text{ mol}^{-1}$ and thus very close to the value estimated by means of the Pascal's constants ($\chi_{\text{dia}} = -742 \cdot 10^{-6} \text{ cm}^3 \text{ mol}^{-1}$).

8.5.2 X-Band EPR-Spectroscopy

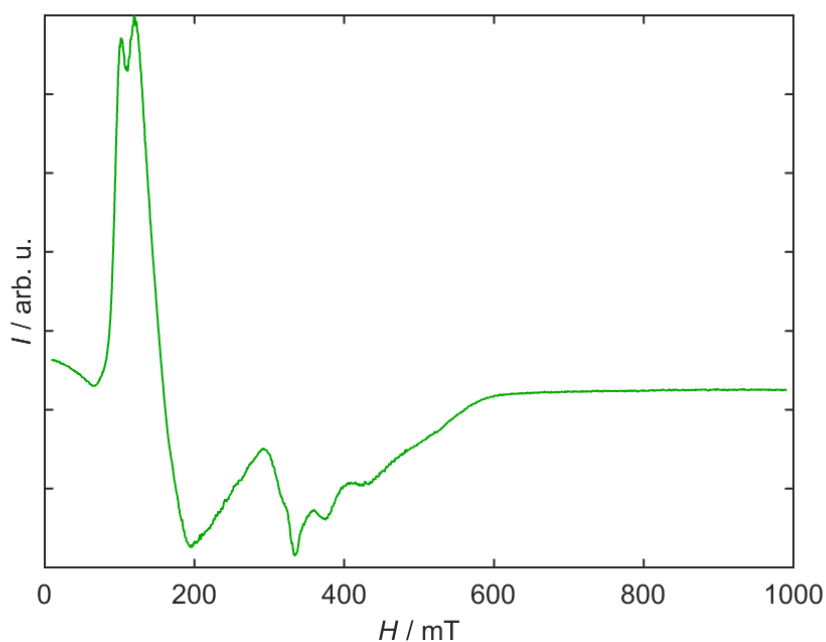


Figure A 14: Solid state X-Band EPR spectrum of $5[\text{OTf}]_3$ recorded at 4.4 K.

8.5.3 Analysis of HFEPR-Spectra

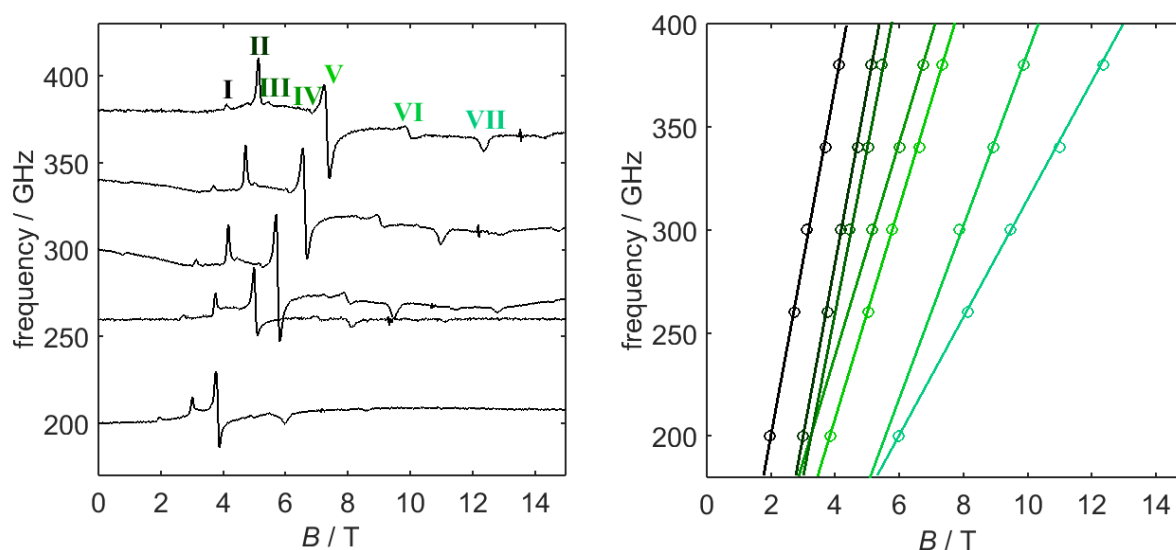


Figure A 15: Left: HFEPR-spectra of $5[\text{OTf}]_2$, recorded at 5 K and various frequencies, as indicated. The spectra were recorded by Dr.-Ing. Petr Neugebauer. Right: Frequency vs. field plot extracted from the frequency dependence of the resonance fields for the individual peaks. Parallel lines correspond to transitions belonging to the same g -values.

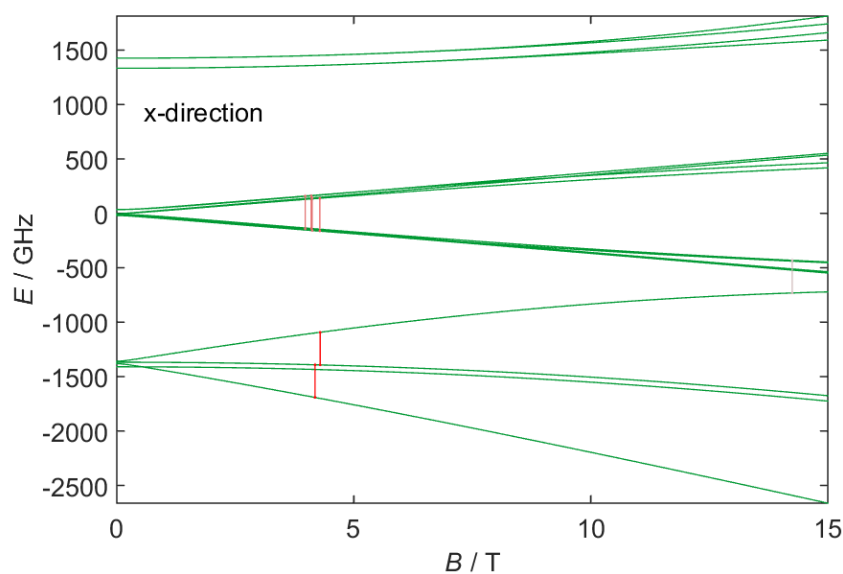


Figure A 16: Energy level diagram (x-direction) for $5[\text{OTf}]_2$, generated with the simulation parameters given in the main text. Green lines correspond to the magnetic field dependent energy levels while red vertical lines illustrate allowed EPR transitions at 300 GHz.

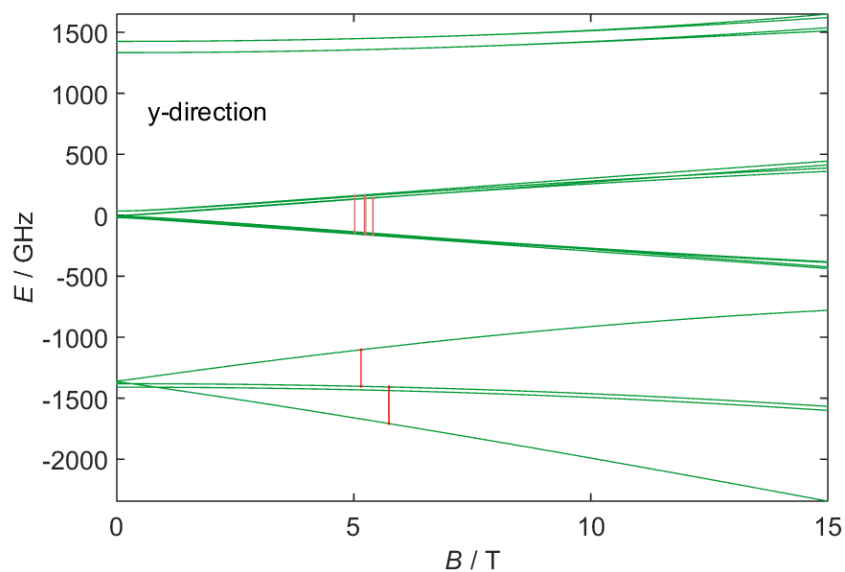


Figure A 17: Energy level diagram (y-direction) for $5[\text{OTf}]_2$, generated with the simulation parameters given in the main text. Green lines correspond to the magnetic field dependent energy levels while red vertical lines illustrate allowed EPR transitions at 300 GHz.

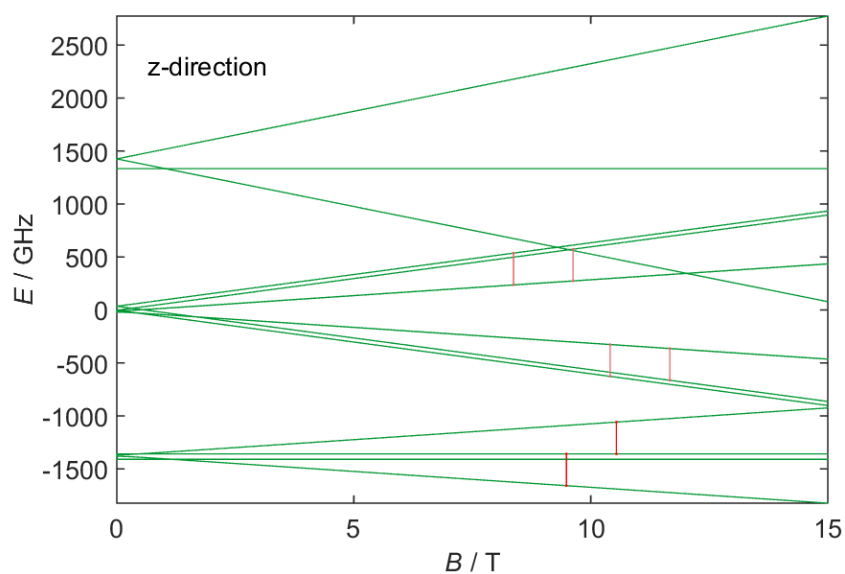


Figure A 18: Energy level diagram (z-direction) for $5[\text{OTf}]_2$, generated with the simulation parameters given in the main text. Green lines correspond to the magnetic field dependent energy levels while red vertical lines illustrate allowed EPR transitions at 300 GHz.

9 Curriculum Vitae

Persönliche Daten

Name Yvonne Rechkemmer
Geburtsdatum 09. 09. 1986 in Sinsheim, Deutschland

Ausbildung

1997 – 2006 Besuch des Gymnasiums Eppingen.
06/2006 Erlangung der allgemeinen Hochschulreife (Gesamtnote 1,3).
2006 – 2011 Studium der Chemie (Diplom) an der Universität Stuttgart.
2011 Anfertigung der Diplomarbeit am Institut für Physikalische Chemie der Universität Stuttgart unter Betreuung von Prof. Dr. Joris van Slageren.
Titel der Diplomarbeit: *Untersuchungen an heteronuklearen molekularen Magneten.*
09/2011 Erwerb des Diplomtitels in Chemie (mit Auszeichnung bestanden).
2011 – 2016 Promotion am Institut für Physikalische Chemie der Universität Stuttgart unter Betreuung von Prof. Dr. Joris van Slageren. Thema der Arbeit: *Spectroscopic Investigations of the Magnetic Anisotropy of Lanthanide- and Cobalt-Based Molecular Nanomagnets.*

Preise und Auszeichnungen

2009 Erhalt des BASF-Förderpreises 2009 für exzellente Vordiploms-Studienleistungen in der Fakultät Chemie der Universität Stuttgart.
2012 Erhalt des Preises der Vereinigung von Freunden der Universität Stuttgart für besondere wissenschaftliche Leistungen.
2016 Erhalt des Preises für den drittbesten Vortrag beim 12. Koordinationschemietreffen in Kiel.

Wissenschaftliche Publikationen

- 1.) S. Eslami, J.G.Gibbs, Y. Rechkemmer, J. van Slageren, M. Alarcón-Correa, T.C. Lee, A.G. Mark, G.L.J.A. Rikken, P. Fischer
Chiral Nanomagnets
ACS Photonics, **1**, 1231-1236 (2014).
- 2.) D. Schweinfurth, Y. Rechkemmer, S. Hohloch, N.Deibel, I. Peremykin, J. Fiedler, R. Marx, P. Neugebauer, J. van Slageren, B.Sarkar
Redox-Induced Spin-State Switching and Mixed Valency in Quinonoid-Bridged Dicobalt Complexes
Chem. Eur. J., **20**, 3475 – 3486 (2014).
- 3.) M. van der Meer, Y. Rechkemmer, I. Peremykin, S. Hohloch, M.G. Sommer, J. van Slageren, B. Sarkar
(Electro)catalytic C-C Bond Formation Reaction with a Redox-Active Cobalt Complex
Chem. Commun., **50**, 11104 - 11106 (2014).
- 4.) Y. Rechkemmer, J. E. Fischer, R. Marx, M. Dörfel, P. Neugebauer, S. Horvath, M. Gysler, T. Brock-Nannestad, W. Frey, M. F. Reid
Comprehensive Spectroscopic Determination of the Crystal Field Splitting in an Erbium Single-Ion Magnet
J. Am. Chem. Soc.; **137**, 13114–13120 (2015).
- 5.) Y. Rechkemmer, F. D. Breitgoff, M. van der Meer, M. Atanasov, M. Hakl, M. Orlita, P. Neugebauer, F. Neese, B. Sarkar, J. van Slageren
A four-coordinate cobalt(II) single-ion magnet with coercivity and a very high energy barrier
Nat. Commun.; **7**, 10467 (2016).
- 6.) M. Gysler, F. El Hallak, L. Ungur, R. Marx, M. Hakl, P. Neugebauer, Y. Rechkemmer, Y. Lan, I. Sheikin, M. Orlita, C. E. Anson, A. K. Powell, R.Sessoli, L. F. Chibotaru, J. van Slageren
Multitechnique investigation of Dy₃ - Implications for Coupled Lanthanide Clusters
Chem. Sci., **2016**, DOI: 10.1039/C6SC00318D.

-
- 7.) J. Rozbořil, Y. Rechkemmer, D. Bloos, F. Münz, C. N. Wang, P. Neugebauer, J. Čechal, J. Novák and J. van Slageren
Magneto-optical investigations of molecular nanomagnet monolayers
Dalton Trans., **45**, 7555-7558 (2016).
- 8.) M. van der Meer, Y. Rechkemmer, F. D. Breitgoff, S. Dechert, R. Marx, M. Dörfel, P. Neugebauer, J. van Slageren, B. Sarkar
Probing bistability in Fe^{II} and Co^{II} complexes with an unsymmetrically substituted quinonoid ligand
Dalton Trans.; **2016**, DOI: 10.1039/c6dt00757k.